Imperial College London

Technologies for the Conversion of External Heat to Power with Reciprocating Motion

Aly Ibrahim Taleb

Department of Chemical Engineering

Imperial College London

Supervised by Dr. Christos N. Markides
Collaborating academic: Prof. Amparo Galindo

A thesis submitted for the degree of

Doctor of Philosophy

March 2017

Publications

To date these are the publications that have been presented to the public domain in relation to the works herein.

Refereed Journals

- AI Taleb, C Barfuß, P Sapin, D Fabris, and CN Markides, The influence of real-gas effects on thermally induced losses in reciprocating compression and expansion machines, *in progress*.
- C Kirmse, OA Oyewunmi, AI Taleb, AJ Haslam, and CN Markides, A two-phase single-reciprocating-piston heat conversion engine: Non-linear dynamic modelling, *Applied Energy*, 186(3):359–375, 2017.
- AI Taleb, MAG Timmer, MY El-Shazly, A Samoilov, VA Kirillov, and CN Markides, A single-reciprocating-piston two-phase thermofluidic prime-mover *Energy*, 104:205–265, 2016.
- OA Oyewunmi, AI Taleb, AJ Haslam, and CN Markides, On the use of SAFT-VR Mie for assessing large-glide fluorocarbon working-fluid mixtures in organic Rankine cycles, *Applied Energy*, 163:263–282, 2016.
- K Palanisamy, AI Taleb, and CN Markides, Optimizing the Non-Inertive-Feedback Thermofluidic Engine for the conversion of low-grade heat to pumping work, *Heat Transfer Engineering*, 36(14–15):1304–1321, 2015.
- OA Oyewunmi, AI Taleb, AJ Haslam, CN Markides. An assessment of working-fluid mixtures using SAFT-VR Mie for use in organic Rankine cycle systems for waste-heat recovery. *Computational Thermal Sciences*, 6(4):301–316, 2014.

Refereed Proceedings

- AI Taleb, P Sapin, C Barfuß, D Fabris, and CN Markides, CFD analysis of thermally induced thermodynamic losses in the reciprocating compression and expansion of real gases, *Proceedings of the 1st International Seminar on Non-Ideal Compressible-Fluid Dynamics for Propulsion and Power*, October 2016, Varenna, Italy.

- AI Taleb, C Barfuß, P Sapin, AJ White, C Willich, D Fabris, and CN Markides, The influence of real gas effects on thermally induced losses in reciprocating piston-cylinder systems,*Proceedings of the 12th International Conference on Heat Transfer, Fluid Mechanics, and Thermodynamics*, July 2016, Malaga, Spain.

- P Sapin, AI Taleb, C Barfuß, AJ White, D Fabris, and CN Markides, Thermodynamic losses in a gas spring: comparison of experimental and numerical results, *Proceedings of the 12th International Conference on Heat Transfer, Fluid Mechanics and Thermodynamics*, July 2016, Malaga, Spain.

- AI Taleb, P Sapin, C Barfuß, AJ White, D Fabris, and CN Markides, Wall temperature and system mass effects in a reciprocating gas spring, *Proceedings of the 29th International Conference on Efficiency, Cost Optimization, Simulation, and Environmental Impact of Energy Systems*, June 2016, Portoroz, Slovenia.

- P Sapin, AI Taleb, AJ White, D Fabris, and CN Markides, Experimental analysis of loss mechanisms in a gas spring, *Proceedings of the ASME Power and Energy Conference*, June 2016, Charlotte, USA.

- CJW Kirmse, AI Taleb, OA Oyewunmi, AJ Haslam, and CN Markides, Performance comparison of a novel Thermofluidic organic-fluid heat converter and an organic Rankine cycle heat engine, *Proceedings of the 3rd International Seminar on ORC Power Systems*, October 2015, Brussels, Belgium.

- CJW Kirmse, AI Taleb, OA Oyewunmi, AJ Haslam, and CN Markides, A two-phase single-reciprocating-piston heat conversion engine, *Proceedings of the 11th International Conference on Heat Transfer, Fluid Mechanics and Thermodynamics*, July 2015, Kruger National Park, South Africa.

- AI Taleb, CJW Kirmse, OA Oyewunmi, A Samoilov, VA Kirillov, and CN Markides, Modelling investigation of a new phase-change reciprocating-piston heat engine, *Proceedings of the Sustainable Thermal Energy Management Network*, July 2015, Newcastle, United Kingdom.

- OA Oyewunmi, AI Taleb, AJ Haslam, and CN Markides, An assessment of working-fluid mixtures for use in organic Rankine cycles for waste-heat recovery using SAFT-VR, *Proceedings of the 13th UK Heat Transfer Conference*, September 2013, London, United Kingdom.

- A Samoilov, VA Kirillov, N Kuzin, AE Kronberg, M Gloushenkov, AI Taleb, and CN Markides, An external combustion heat engine with phase-change working fluid, *Proceedings of the 13th UK Heat Transfer Conference*, September 2013, London, United Kingdom.

Statement of Originality

I hereby certify that, to the best of my knowledge, the content of this thesis is original and the result of my own work. All of the assistance I received and the sources I used have been properly acknowledged

Aly Ibrahim Taleb

July 4, 2017

Copyright Declaration

The copyright of this thesis rests with the author and is made available under a Creative Commons Attribution Non-Commercial No Derivatives licence. Researchers are free to copy, distribute, or transmit the thesis on the condition that they attribute it, that they do not use it for commercial purposes and that they do not alter, transform, or build upon it. For any reuse or redistribution, researchers must make clear to others the licence terms of this work.

I would like to dedicate this thesis to my loving parents

Acknowledgements

I would like to thank

- Dr. Christos Markides for his excellent supervision of my research and his invaluable help as a mentor.
- The Skolkovo Foundation and BP for providing the funding for my work.
- Dr. Drazen Fabris who, during his academic visit at Imperial, provided me with invaluable help in my research.
- MSc students Mohammad Elshazly, Micheal Timmer, and especially Christoph Barfuß for their invaluable research work with me
- The members of the CEP Laboratory: Jae, Alexandros, Martin, Ahmad, Maria Anna, Alba, Solomos, and Micheal.
- Also James, Christoph, Vincent, Ilaria, Oyeniyi, and Paul for all the great fun and late hours we spent in the department
- Niccolo, his parents, and his *Nonna* Lucia for inviting me to their homes in Florence and Tuscany.
- My cousins Rama, Reem and Rama's husband, Daniel, for taking me out to so many great restaurants around London and also making sure I am well fed.
- My uncle Ahmad and his lovely wife Lubna for visiting London so many times and thereby providing me with support and care.
- My best friend, Adam Hafez, for providing me with a roof under which I would beat him playing FIFA. Also, his lovely family for inviting me countless times for dinner.
- Naima Ali for making Imperial a place I enjoyed commuting to every day and for our discussions of curly hair products (among other things).
- My sister, Shaimaa, for her love, care, support, and for surprising me with a visit at Imperial on my birthday.

I would like to express my greatest gratitude to my parents, Zeinab and Ibrahim, for their boundless love, patience, support for the past thirty years. Additional thanks goes to my mother, Zeinab, for cooking me excellent meals (breakfast, lunch, and dinner) while I was focussing on my writing.

"This shouldn't take you longer than a couple of hours."

– Dr. Christos Markides

Abstract

Reciprocating energy-conversion devices, such as ORCs using reciprocating expanders or Thermofluidic Oscillators (TFOs), are promising technologies for the conversion of low- or medium-grade heat from waste heat, solar, or geothermal sources at power outputs below 100 kW. In this thesis, three topics associated with reciprocating machines are investigated. Firstly, a novel two-phase TFO engine concept, named ERPE, is modelled using a linear dynamic approach. Secondly, the use of working-fluid mixtures in ORCs is examined. Thirdly, unsteady heat-transfer losses associated with reciprocating motion are investigated.

The ERPE is a theoretical TFO concept especially well-suited as a prime-mover in combined heat and power applications with power outputs below 10 kW. Based on thermal/fluid-electrical analogies, the theoretical engine is conceptualized in the electrical analogy domain as a linearized closed-loop active circuit model. By comparing model calculations with measurements of an existing prototype that is similar to the concept, it has been shown that the linear model provides realistic results. The effects of liquid inertia, viscous drag, hydrostatic pressure, vapour compressibility, and two-phase heat transfer in the various engine components/compartments are examined. Measures for improving engine performance are provided which demonstrate how this engine concept can outperform competing TFO solutions. The methodological approach implemented in this study can be used to guide the early-stage design and verification of these engines, while offering important guidelines for optimizing performance.

For the second topic of the thesis, the use of working fluid mixtures in ORCs and their influence on thermodynamic performance is investigated. Mixtures can potentially reduce exergy losses due to their non-isothermal phase-change behaviour. The efficiency, power output, and cost are calculated as a function of working-fluid mixture composition in a mathematical model of a sub-critical, non-regenerative ORC. A new version of the statistical associating fluid theory equation of state is used to predict unavailable thermodynamic property data required for the ORC model. When unlimited quantities of cooling water are used, cycles with the lighter pure working fluid exhibit the highest efficiencies and power outputs and lowest costs. Only at low evaporation pressures do the investigated mixtures perform better than pure fluids. When the quantity of cooling

water is constrained by the application, overall performance deteriorates and mixtures emerge as the optimal working fluids. A general conclusion from this work is that the choice of the optimum working fluid (pure or mixture) depends in a non-trivial and occasionally counter-intuitive fashion on the particular external heat source and heat sink conditions.

The third topic revolves around unsteady heat-transfer losses which occur in reciprocating energy-conversion devices. These exergy losses occur even if the overall time-averaged heat transfer between the gas and the cylinder wall are zero. The specific aim is to compare the behaviour of real gases (such as those used in ORCs) to ideal gases by simulating an oscillating gas-spring in CFD . Results show that unsteady heat-transfer losses are not negligible as they can reach up to 30 % of the work required to compress the gas. Further results indicate that simple mono- and diatomic gases exhibit negligible differences between ideal and real-gas models. However, when considering heavier (organic) molecules, the ideal gas-models overestimate the pressure by as much as 20 % and underestimate the unsteady heat-transfer losses by 25 %. The increase in loss is caused by different compressibility factors of the gas during compression and expansion.

Contents

Contents . . . xiii
List of Figures . . . xvi
List of Tables . . . xxiv
Nomenclature . . . xxvi
I Introduction . . . 1
I.1 Motivation . . . 1
I.1.1 The Challenge of Increasing Emissions . . . 1
I.1.2 Future Energy Scenarios . . . 3
I.1.3 The Potential of Waste Heat . . . 3
I.2 Converting External Heat Using Reciprocating Motion . . . 4
I.2.1 Two-Phase Thermofluidic Oscillators . . . 6
I.2.2 Organic Rankine Cycle . . . 7
I.3 Thesis Overview . . . 13
II Model Development for the Evaporative Reciprocating-Piston Engine . . . 15
II.1 Background . . . 15
II.1.1 Objective . . . 16
II.1.2 Overview of Chapter . . . 16
II.2 Non-Inertive-Feedback Thermofluidic Engine . . . 17
II.3 TFO Prototype . . . 20
II.4 Linear Modelling of the ERPE . . . 22
II.4.1 Horizontal (Connection) Tubes . . . 24
II.4.2 Liquid Columns and Pistons . . . 26
II.4.3 Gas Springs . . . 27
II.4.4 Solid Free Pistons . . . 28
II.4.5 Slide Bearing of Solid Free Piston . . . 31
II.4.6 Liquid Column Below Piston . . . 33
II.4.7 Liquid Column Above Piston . . . 35

II.4.8 Phase-Change/Thermal Domain and Heat Exchangers 36
II.4.9 Load Model 39
II.5 ERPE Configuration and Operation 42
II.5.1 Physical Representation of the ERPE 42
II.5.2 Solution 46
III Results and Discussion of the Linear ERPE Model 51
III.1 Comparison of Model and Experiments 51
III.2 Parametric Study 54
III.2.1 Load-Free Engine 56
III.2.2 Loaded Engine 58
III.3 Thermodynamic Cycle Diagrams 60
III.4 Summary 65
IV Model Development for Organic Rankine Cycles using Working Fluid Mixtures 67
IV.1 Background 67
IV.1.1 Objective 69
IV.2 Organic Rankine Cycle Model 70
IV.2.1 Thermodynamic Model of the Cycle 71
IV.2.2 Case Study: Waste-Heat Source and Heat-Rejection Medium . . . 75
IV.2.3 Costs for Economic Evaluation 76
IV.3 Thermodynamic Properties of Working Fluids with SAFT-VR Mie . . . 77
IV.3.1 SAFT Equation of State 77
IV.4 Validation of SAFT Predictions 80
IV.4.1 Thermodynamic Properties of Pure Working Fluids 81
IV.4.2 Thermodynamic Properties of Binary-Mixture Working Fluids . . 83
V Results and Discussion of ORCs using Working Fluid Mixtures 88
V.1 Boundary Conditions 88
V.2 Power Output 90
V.2.1 Specific Power Output 90
V.2.2 Net Power Output 90
V.3 Thermal Efficiency 92
V.4 Cost Comparisons 97
V.4.1 Variations of ORC Costs with Power Output 97
V.4.2 Variations of ORC Costs with Mixture Composition 99
V.5 Constrained Cooling Flows 99
V.6 Summary 103

VI Model Development for Calculating Thermally Induced Losses Associated with Reciprocating Motion . . . 106
VI.1 Background . . . 106
VI.1.1 Objective . . . 107
VI.1.2 Overview of Chapter . . . 108
VI.2 Previous Work . . . 108
VI.3 Background of Computational Fluid Dynamics . . . 110
VI.3.1 Discretisation using the Finite Volume Method . . . 110
VI.3.2 Accuracy and Errors of Discretisation . . . 115
VI.3.3 Numerical Solution of the Navier-Stokes Equations . . . 116
VI.4 Numerical Model . . . 120
VI.4.1 Problem Setup . . . 121
VI.4.2 Geometry and Mesh . . . 123
VI.4.3 Solver . . . 124
VI.4.4 Initial and Boundary Conditions . . . 125
VI.4.5 Convergence Study . . . 125
VI.5 Estimation of Turbulence . . . 133
VI.6 Fluid Thermodynamic and Transport Properties . . . 134
VI.6.1 Real-Gas Equation of State . . . 135
VI.6.2 Thermodynamic and Transport Properties . . . 135
VII Results and Discussion of Thermally Induced Losses Associated with Reciprocating Motion . . . 138
VII.1 Pressure, Temperature, and Heat Transfer . . . 138
VII.2 Flow Structure . . . 142
VII.3 Influence of Real-Gas on Effects Temperature and Pressure . . . 143
VII.4 Influence of Real-Gas Effects on Thermally Induced Losses . . . 146
VII.5 Comparison of Thermally Induced Losses of Alkanes . . . 152
VII.6 Thermally Induced Losses of Real-gas Mixtures . . . 154
VII.7 Summary . . . 155
VIII Summary of Thesis Findings . . . 159
VIII.1 Evaporative Reciprocating-Piston Engine . . . 159
VIII.2 Organic Working-Fluid Mixtures in ORCs . . . 162
VIII.3 Unsteady Heat-Transfer Losses Associated with Reciprocating Motion . 164
References . . . 166

List of Figures

I.1 Contour plot of maximum cycle efficiency η for a heat engine operating between a heat source and heat sink stream with varying temperatures. The horizontal axis is the inlet temperature of the heat source stream $T_{\text{hot,in}}$ and the vertical axis is the temperature drop of the heat source stream normalized by the inlet temperature $\Delta T_{\text{hot}}/T_{\text{hot,in}}$. The inlet temperature of the heat sink stream is constant $T_{\text{cold,in}} = 20$ °C. The white curve is a locus of the maximum power output at each value of $T_{\text{hot,in}}$. Taken from Markides [10] 5

I.2 (a) Schematic diagram of an ORC engine. (b) Exemplary sub-critical, non-regenerative, and ideal ORC cycle on a T-s diagram. The temperature of State 2 is exaggerated for clarity 8

I.3 T-s diagrams of Rankine cycles with different working fluids to show the significance of condensation behaviour. (a) wet fluid, water; (b) isentropic fluid, R11; (c) dry fluid, pentane 9

II.1 Schematic diagram of the NIFTE device. HHX and CHX are the hot and cold heat exchangers. The vapour spaces above the liquid in the power and displacer cylinder are part of the adiabatic vapour-volume. The horizontal dashed line indicates the equilibrium (time-mean) liquid-vapour interface position in the two vertical cylinders [27]. 17

II.2 Temperature-entropy (T-s) phase diagram of the working fluid (pentane) used in the NIFTE prototype (dashed, black line) and T-s diagram of typical linearised thermodynamic cycle undergone by the working fluid inside the NIFTE (solid, blue line). Taken from Ref. [27]. 19

II.3 Electronic circuit representation of the NIFTE where the subscripts 'th' and 'hx' denote components related to the heat exchangers, 'ad' denotes the adiabatic vapour volume, 'l' denotes the load line, 'p' denotes the power cylinder, 'f' denotes the feedback connection, and 'd' denotes the discplacer cylinder. The pressure and volumetric flow-rate are denoted by P and U respectively. A capacitor is represented by C, an inductor is represented by L, and a resistor is represented by R. 20

II.4 Schematic description of the BIC prototype. The slide valve and slide bearing are encircled in red. 21

II.5 Fluid flow and the resulting velocity profile in connection tube. The inner radius of the tube is denoted by R, the length of the tube by l, and r and z are cylindrical coordinates. 24

II.6 Schematic of piston and leakage model. The piston height is denoted by h_p while d_p and d_c are the piston and cylinder diameter respectively. The pressure at the top of the piston is P_1 and P_2 at the bottom. The leakage flow is referred to as U_l while U_p is the flow-rate of the piston, and k is the spring constant. 29

II.7 Electric circuit representation of piston and leakage model. 31

II.8 Schematic diagram of slide bearing design in two-phase TFO with two channels to divert flow of working fluid. 32

II.9 Electric circuit representation of piston and leakage model including slide bearing. 34

II.10 Linear temperature profile along the height of the cold and hot heat exchangers (CHX and HHX) in the LTP model. T_hx is the wall temperature which varies linearly with the vertical height y of the heat exchangers. . 37

II.11 Heat flux profile along the height of the heat exchangers in the DHX model. $\dot{Q}_\mathrm{hx}$ is the heat flux which varies linearly with the vertical height y of the heat exchangers. 39

II.12 Power spectrum (in the frequency domain) of the amplitude ratio downstream and upstream of the valve $|P_\mathrm{down}/P_\mathrm{up}|$ from intermediate pressure (11.8 bar) measurements on the BIC prototype (blue). The fitted load model according to Eq. II.60 is also shown (pink, triangular markers). . 40

II.13 Schematic description of the ERPE. The dashed and coloured borders denote different components or domains of the engine; these correspond to the highlighted sections in the electronic circuits of Figs. II.14 and II.15. The main physical differences between the ERPE and BIC prototype from Fig. II.4 are the missing slide valve and a single connection tube between the two cylinder. 43

II.14 Electronic circuit model of the ERPE with no load. The colours of the borders correspond to the borders in the schematic of the physical representation of the engine in Fig. II.13. 44

II.15 Electronic circuit model of the ERPE with the BIC prototype load (subscript 'lo' and magenta coloured border). As with the load-free version from Fig. II.14, the colours of the borders correspond to the borders in the schematic of the physical representation of the engine in Fig. II.13. . 44

II.16 Closed-loop representation of the ERPE where $G(s)$ is the modelled forward-loop transfer function between P_{th} and P_{d} and k_i is the feedback gain where i can be either LTP or DHX. 49

III.1 Variations in the (a) oscillation frequency f and (b) heat-input rate gradient $\mathrm{d}\dot{Q}_{\mathrm{hx}}/\mathrm{d}y$ in the load-free engine at a mean pressure of 3.6 bar calculated with the DHX model as functions of the normalized parameters listed in the legend. Parameters not presented here have low or negligible influence on the frequency or heat-input gradient. 56

III.2 Variations in the: (a) the oscillation frequency f; (b) the exergy efficiency η_{ex}; (c) the heat-input rate gradient $\mathrm{d}\dot{Q}_{\mathrm{hx}}/\mathrm{d}y$; (d) product of exergy efficiency and frequency $\eta_{\mathrm{ex}} \cdot f$ (proportional to power output per unit heat input) in engine with a load with a mean pressure of 18.1 bar as functions of normalized parameters listed in the legend. 59

III.3 Linearized pressure-volume diagrams relating pressure $P_{\mathrm{lo},1}$ to the volume displacement $V_{\mathrm{lo},1}$ in the load for 5 times (dashed lines) and one fifth (solid lines) of nominal values of: (a) C_{hx}, (b) C_{v}, (c) L_{c}, and (d) R_{th}. The dash-dotted lines represent the nominal case. The area enclosed by the Lissajous curves represent the work output per oscillation. For all cases, the time-averaged pressure is 18.1 bar, and the exergy input rate into the engine is constant. 62

III.4 Linearized T-s cycle diagrams for 5 times and one fifth of nominal values of C_{v} ((a) and (b)); and L_{c} ((c) and (d)). The areas enclosed by the T_{hx} curves (solid and dash-dotted lines) represent the net exergy made available to the device in one oscillation; the areas enclosed by the T_{v} curves (dashed lines and dotted lines) represent the net exergy gained by the working fluid in one oscillation. The difference between both cycles amounts to the exergy destruction due to irreversible heat transfer between the heat exchangers and the working fluid. The temperature values on the vertical axes are not absolute temperatures but temperature differences to the respective equilibrium temperatures. 64

IV.1 (a) Schematic diagram of an ORC engine. (b) Exemplary sub-critical, non-regenerative, and ideal ORC cycle on a T-s diagram. The temperature of State 2 is exaggerated for clarity. 71

IV.2 Selected thermodynamic properties of n-perfluorobutane (n-C_4F_{10}) and n-perfluorodecane (n-$C_{10}F_{22}$). Vapour-liquid T-ρ coexistence envelopes and density isobars (at pressures indicated in the legend) for (a) n-perfluorobutane and (b) n-perfluorodecane. Temperature dependence of the isobaric heat capacity c_{p} of (c) n-perfluorobutane and (d) n-perfluorodecane. Comparison of experimental data from NIST (symbols) with the description obtained using SAFT-VR Mie EoS (solid curves). The singularities in (c) for 20 and 40 bar are due to the phase change. . . . 82

IV.3 Selected thermodynamic properties of n-butane (n-C_4H_{10}) and n-decane (n-$C_{10}H_{22}$). Vapour-liquid T-ρ coexistence envelopes and density isobars (at pressures indicated in the legend) for (a) n-butane and (b) n-decane. Temperature dependence of the isobaric heat capacity c_{p} of (c) n-butane and (d) n-decane. Comparison of experimental data from NIST (symbols) with the description obtained using SAFT-VR Mie EoS (solid curves). The singularities in (c) for 20 and 40 bar are due to the phase change. The singularities in (c) and (d) at higher pressures are due to the phase change. 84

IV.4 Vapour-liquid equilibria of selected fluid mixtures. (a) Pressure-temperature (P-T) phase boundaries (bubble-point curves) at different mixture compositions ($x_{C_4H_{10}}$) predicted by SAFT-VR Mie (solid curves). The symbols indicate validation data from the NIST database for n-butane and n-decane and from Refs. [80, 81] for mixtures. (b) Isothermal pressure-composition (P-x) phase boundaries (saturation curves) as predicted by SAFT-VR Mie (solid curves) and validation data from Ref. [82] are represented by the symbols. (c) Pressure-temperature phase boundaries for pure n-perfluorobutane ($x_{C_4F_{10}} = 1$) and n-perfluorodecane ($x_{C_4H_{10}} = 0$) and intermediate binary mixtures with validation data taken from the NIST database for the pure compounds. 85

IV.5 Phase boundaries in the T-s and P-h spaces as predicted using SAFT-VR Mie for pure working fluid and mixtures. (a) T-s envelopes for pure n-perfluorobutane, pure n-perfluorodecane, and intermediate binary mixtures composed of 30 mol%, 60 mol%, 80 mol%, and 90 mol% n-perfluorobutane. (b) P-h envelopes for pure n-perfluorobutane, pure n-perfluorodecane, and intermediate binary mixtures composed 30 mol%, 50 mol%, and 80 mol% n-perfluorobutane. (c) T-s envelopes for pure n-butane, pure n-decane, and intermediate binary mixtures composed of 30 mol%, 50 mol%, and 80 mol% n-butane. (d) P-h envelopes for pure n-butane, pure n-decane, and intermediate binary mixtures composed 30 mol%, 50 mol%, and 80 mol% n-butane. 87

V.1 Power output per unit mass flow-rate at different evaporation pressures P_{23} based on: (a) non-superheated cycles ($d_{SH} = 0$), and (b) maximum superheated cycles ($d_{sh} = 1$) as functions of n-butane mole fraction $x_{C_4H_10}$; (c) non-superheated cycles ($d_{sh} = 0$), and (d) maximum superheated cycles ($d_{sh} = 1$) as functions of n-perfluorobutane mole fraction $x_{C_4F_10}$. The dashed lines, representing the cases of sub-atmospheric expansion (to the dew-point pressure at 30 °C), are provided for comparison. 91

V.2 Maximum absolute net power output $\dot{W}$ based on: (a) non-superheated cycles ($d_{\mathrm{sh}} = 0$), and (b) maximum superheated cycles ($d_{\mathrm{sh}} = 1$) as functions of n-butane mole fraction $x_{\mathrm{C_4H_{10}}}$; (c) non-superheated cycles ($d_{\mathrm{sh}} = 0$), and (d) maximum superheated cycles ($d_{\mathrm{sh}} = 1$) as functions of n-perfluorobutane mole fraction $x_{\mathrm{C_4F_{10}}}$; maximum power output over all degrees of superheat as functions of (e) n-butane mole fraction and (f) n-perfluorobutane mole fraction. 93

V.3 Thermal efficiency η_{th} of: (a) non-superheated cycles ($d_{\mathrm{sh}} = 0$), and (b) maximum superheated cycles ($d_{\mathrm{sh}} = 1$) as functions of n-butane mole fraction $x_{\mathrm{C_4H_{10}}}$; (c) non-superheated cycles ($d_{\mathrm{sh}} = 0$), and (d) maximum superheated cycles ($d_{\mathrm{sh}} = 1$) as functions of n-perfluorobutane mole fraction $x_{\mathrm{C_4F_{10}}}$. 94

V.4 (a) Pure butane cycle and (b) equivalent cycle of 50 mol% butane-decane mixture (right) in T-s space. Also shown are the saturation curves of the corresponding working fluids (black). 96

V.5 Performance (power output) and cost of ORC systems in the investigated case study. (a) Overall costs of the cycle against the power output for alkane mixtures. (b) Costs per unit power output against the power output for alkane mixtures. The colour range in all plots reflects the thermal efficiency of different cycles. 98

V.6 ORC systems costs for cycles designed for maximum power output. Total cost with (a) n-butane + n-decane and (b) n-perfluorobutane + n-perfluorodecane working-fluid mixtuers. Cost per unit power output (£/kW) with: (c) n-butane + n-decane (corresponding to power output in Fig. V.2(e)) and (d) n-perfluorobutane + n-perfluorodecane working-fluid mixtures (corresponding to power output in Fig. V.2(f)). 100

V.7 Performance of ORCs with restricted cooling water using n-butane + n-decane working fluid mixtures at maximum power output: (a) maximum absolute net power $\dot{W}$, (b) temperature glide in evaporator (solid lines) and condenser (dashed line, diamond markers), (c) thermal efficiency η_{th}, and (d) ORC system costs per unit power output. 101

VI.1 Control volume with centroid P and face normal vector $\vec{n}$ with the vector's space point F. 111

VI.2 Schematic of piston-cylinder geometry 121

VI.3 Modelled wedge geometry and definition of the aspect ratio. Left-hand diagram shows the wedge in a perspective view. Right-hand diagram shows a top view of the geometry (not to scale). 123
VI.4 Mesh movement during an expansion stroke of a 30×30 mesh. A grading factor increases resolution near the walls. 124
VI.5 (a) Conservation of mass at 1000 RPM case with a mesh resolution of 120×120 cells and $Co = 0.05$. (b) Wall heat flux calculated with Fourier's law (solid blue) and with first law of thermodynamics (dashed red). . . 126
VI.6 Log-log plot of the fractional error in the net mechanical work for different mesh resolutions at 1000 RPM and $Co = 0.05$ 129
VI.7 Variation of the time step increment for different crank angles. Irregular jumps of the time step increments occur around TDC or 0° (1000 RPM, mesh resolution 200×200, and $Co = 0.1$). 130
VI.8 Effect of fluctuation in the time increment on the heat flux estimation for a case with 1000 RPM, mesh resolution 200×200, and $Co = 0.1$ . . 130
VI.9 Stabilized time step control with one additional internal PISO loop for 1000 RPM, mesh resolution 200×200, and $Co = 0.1$ 131
VI.10 Appropriate mesh resolutions and Courant numbers over the range of piston frequencies between 0.5–10000 RPM. The y-axis is the number of cells that should be chosen for the x and z direction. A mesh resolution should be chosen which lies between the upper and lower limit. 133

VII.1 Pressure evolution during one cycle with an initial pressure at BDC of 3 bar, a wall temperature of 350 K with a frequency of (a) 1 RPM or $Pe = 1.8$ and (b) 750 RPM or $Pe = 1340$ (solid blue curve). The evolutions of the pressure during isothermal ($pV = \text{const}$) (dashed red curve) and adiabatic ($pV^\gamma = \text{const}$) (green dashdotted curve) compression are also included. TDC corresponds to 0 °, BDC corresponds to -180 ° and 180 °. The products of pV and pV^γ are initially calculated from the time-averaged values for pressure and volume from the CFD simulation. From these (time-averaged values) we calculated the pressure trend as a function of the crank angle. 139
VII.2 Evolution of temperature difference ΔT_{wall} between bulk gas and wall (solid blue curve) and gas-to-wall heat flux $\dot{Q}$ (dashed red curve) during one cycle. Gas spring initial pressure 3 bar, $T_{\text{wall}} = 350$ K with a frequency of (a) 1 RPM or $Pe = 1.8$ and (b) 750 RPM or $Pe = 1340$.) . 140

VII.3 (a) Evolution of temperature difference ΔT_{wall} between bulk gas and wall (solid blue curve) and gas-to-wall heat flux $\dot{Q}$ (dashed red curve) during one cycle. Helium gas spring with initial pressure of 3 bar, $T_{\text{wall}} = 350$ K with a frequency of 100 RPM. (b) Temperature profiles as functions of radius r of same case. The wall temperature $T_{\text{wall}} = 350$ K. 141

VII.4 Streamlines with contours of the axial velocity u_z during compression and expansion. The centre plot is at TDC, while the plots at the very left and very right are at BDC. 142

VII.5 (a): T–V diagram and (b): P–V diagram for helium at 250 RPM for the ideal-gas model with constant thermophysical properties, $Pe = 446$ (solid blue); ideal-gas model with temperature-dependent properties, $Pe = 502$ (dashed red); and real-gas model with temperature and density dependent properties $Pe = 457$ (dotted green). 144

VII.6 (a): T–V diagram and (b): P–V diagram for nitrogen at 25 RPM for the ideal-gas model with constant thermophysical properties, $Pe = 371$ (solid blue); ideal-gas model with temperature-dependent properties, $Pe = 355$ (dashed red); real-gas model using Peng-Robinson equation of state with temperature and density dependent properties and , $Pe = 355$ (dotted green); and model which uses empirical data tables for temperature, pressure, density, and physical properties, $Pe = 368$ (dash-dotted yellow). . 145

VII.7 (a): T–V diagram and (b): P–V diagram for propane at 10 RPM for the ideal-gas model with constant thermophysical properties, $Pe = 545$ (solid blue); ideal-gas model with temperature-dependent properties, $Pe = 442$ (dashed red); real-gas model with temperature and density dependent properties, $Pe = 382$ (dotted green); and model which uses empirical data tables for temperature, pressure, density, and physical properties, $Pe = 506$ (dash-dotted yellow). 145

VII.8 Compressibility Z over a cycle for nitrogen and propane for the case of maximum loss at $Pe \approx 10$. 146

VII.9 (a) Loss parameter ψ as defined in Eq. VI.34 and (b) loss parameter ψ_{k} as defined in Eq. VI.35 as a function of Pe for a helium gas spring. . . . 147

VII.10 (a) Loss parameter ψ as defined in Eq. VI.34 and (b) loss parameter ψ_{k} as defined in Eq. VI.35 as a function of Pe for a nitrogen gas spring. . . 148

VII.11 (a) Loss parameter ψ as defined in Eq. VI.34 and (b) loss parameter ψ_{k} as defined in Eq. VI.35 as a function of Pe for a propane gas spring. . . 148

VII.12 Ratio of real-gas model heat-transfer loss to ideal-gas model heat-transfer loss $\oint P\mathrm{d}V|_{\mathrm{RG}}/\oint P\mathrm{d}V|_{\mathrm{IG}}$ for varying Peclet numbers for the propane gas spring. The two real gas models are considered (look-up tables and Peng-Robinson). 149
VII.13 Plot of $\lambda = 1 - Z$ against volume over a cycle with propane ($Pe \approx 10$). 149
VII.14 Plot of normalized loss difference between real and ideal-gas simulations of the propane gas-spring plotted as a function of the integral Λ_i as a measure of the asymmetry in gas behaviour between compression and expansion. 151
VII.15 Loss ψ as a function of Pe for the alkanes propane (blue, solid), butane (red, dashed), pentane (green, dotted) and hexane (yellow, dash-dotted). The predictions were calculated with simulations using look-up tables. . 152
VII.16 Peak loss for different alkanes as a function of the time-averaged absolute heat capacity $\overline{C_p}$. 153
VII.17 Fluctuating component of the temperature over one cycle for the alkanes propane (blue, solid), butane (red, dashed), pentane (green, dotted) and hexane (yellow, dash-dotted) for $Pe \approx 10$ (peak loss). The predictions were calculated with simulations using look-up tables. 153
VII.18 Compressibility Z over a cycle for the alkanes propane, butane, pentane and hexane for the case of maximum loss at $Pe \approx 10$, time-averaged temperature 485 K, time-averaged pressure 7.5 bar. 154
VII.19 Loss ψ as a function of Pe for the alkanes propane (blue, solid), butane (red, dashed), pentane (green, dotted) and hexane (yellow, dash-dotted). The predictions were calculated with simulations using look-up tables. . 155
VII.20 Peak loss as a function of the mass ratio of propane in propane-hexane mixtures. 156

List of Tables

II.1 Electrical analogies for the ERPE model. RLC relations and their respective nominal values at a mean pressure of 11.8 bar. 47

II.2 Working fluid properties for saturated water (working fluid) at a mean pressure of 18.1 bar. 49

III.1 Left: operating conditions, experimentally measured frequency and empirically approximated gradients of BIC prototype. Right: calculated frequencies and temperature/heat-input rate gradients of the LTP and DHX model. 53

III.2 Nominal values and investigated ranges for the parameters in Table II.1 . 55

IV.1 Coefficients of 3rd order polynomials used to correlate the ideal-gas specific heat capacities c_{p}^{0}(J mol^{-1} K^{-1})$= a_0 + a_1 T + a_2 T^2 + a_3 T^3$ as functions of absolute temperature (in Kelvin) for n-C_4H_{10}, n-$C_{10}H_{22}$, n-C_4F_{10}, and n-$C_{10}F_{22}$. The heat capacities are take from the NIST database. The coefficients are valid between 200 K and 800 K. 79

IV.2 Model parameter values for the pure compounds estimated from experimental single phase and phase equilibrium data using SAFT-VR Mie EoS. Values for the alkanes and n-C_4F_{10} are taken from Ref. [75]. Values for n-$C_{10}F_{22}$ were generated for this study starting from the same λ_{a} value as that of n-C_4F_{10} and λ_{r} was tuned to best match experimental data. . . . 81

V.1 Ranges of investigated variables. 89

VI.1 Scalar variable and associated diffusivity for conservation equations derived from the general transport equation 111

VI.2 Gas spring dimensions in mm 121

VI.3 Engine frequencies and Peclet numbers of considered frequency range in the convergence study 126
VI.4 Mesh resolutions on which the Richardson extrapolation is based for each tested piston frequency. 128
VI.5 Estimated continuum value of the net work W^* and the fractional error ϵ_W for different frequencies and Courant numbers 132

Nomenclature

Abbreviations

BDC bottom dead centre

BIC Boreskov Institute of Catalysis

CAMD computer-aided molecular design

CEP Clean Energy Processes Laboratory

CHX cold heat exchanger

EoS equation of state

ERPE Evaporative Reciprocating-Piston Engine

FVM finite volume method

HHX hot heat exchanger

NIFTE Non-Inertive-Feedback Thermofluidic Engine

ODE ordinary differential equation

ORC organic Rankine cycle

PDE partial differential equation

PISO pressure implicit with splitting of operator

RPM revolutions per minute

SAFT statistical associating fluid theory

SIMPLE semi-implicit method for pressure linked equations

TDC top dead centre

TFO Thermofluidic Oscillator

Greek characters

α scaling factor [-]

α thermal diffusivity [m^2/s]

ϵ depth of potential well [m^2kg/s^2]

ϵ fractional error [-]

η efficiency [-]

η_{ex} exergy efficiency [-]

γ ratio of specific heats [-]

Γ_ϕ diffusivity of transport equation

λ_a, λ_r attractive and repulsive exponents [-]

μ dynamic viscosity [kg/ms]

ω angular velocity [s^{-1}]

ω_z acentric factor [-]

ϕ general scalar quantity of transport equation

ρ density [kg/m^3]

σ segment size in SAFT model [$\AA$]

θ angular coordinate in a cylindrical coordinate system [rad]

θ crank angle [rad]

Latin characters

A area [m^2]

a Helmholtz free energy

a acceleration [m/s^2]

a attraction parameter [J/mol]

b	van der Waals covolume [m^3/mol]
C	capacitance [m^4s^2/kg]
c_p	isobaric specific heat capacity [J/kg·K]
c_v	isochoric specific heat capacity [J/kg·K]
d	diameter [m]
F_R	frictional force [N]
g	gravitational acceleration constant [m/s^2]
Δh	latent heat of vaporization [J/kg]
H	enthalpy [J]
h	heat transfer coefficient [W/m^2·K]
k	mechanical spring constant [N/m]
k	thermal conductivity [W/m·K]
k	thermal conductivity [W/m·K]
k_c	convergence order [-]
L	inductance [kg/m^4]
l	length [m]
$\dot{m}$	mass flow-rate [kg/s]
M	molar mass [kg/mol]
m	number of cells in axial direction [-]
n	number of cells in radial direction [-]
$N_{m\times n}$	total number of cells in mesh [-]
P	pressure [bar]
Pe	Peclet number [-]
Q	heat [J]
R	universal gas constant [J/K·mol]
R	resistance [kg/m^4s]
r	radius or radial coordinate in a cylindrical coordinate system [m]
r_p	pressure ratio [-]
r_v	volume ratio [-]
Re	Reynolds number [-]
Re_δ	boundary-layer Reynolds number [-]
Δs_{fg}	entropy of vaporization [J/kg·K]
S	surface area [m^2]
s	specific entropy [J/kg·K]
s^{-1}	Laplace variable [1/s]
T	temperature [K]
t	time [s]
U	voluemtric flow-rate [m^3/s]
u	flow velocity [m/s^2]
V	volume [m^3]
v	molar volume [m^3/mol]
Z	compressibility factor [-]
Z	impedance, $Z = \frac{\Delta P}{U}$ [kg/m^4s]
z	axial coordinate in a cylindrical coordinate system [m]
Z_{tot}	total impedance of ERPE circuit [kg/m^4s]

Subscripts and indices

$\bullet^0$	ideal gas quantity
$*$	continuum value for an infinitely high mesh resolution
0	time-mean value

ap	pertaining to liquid column above piston in ERPE
b	pertaining to slide bearing in ERPE
bp	pertaining to liquid column below piston in ERPE
bub	bubble point
c	pertaining to connection tube in ERPE
c	pertaining to cylinder
c	value at critical point
cold	pertaining to heat sink stream
cs	condensing stream
d	pertaining to displacer cylinder in ERPE
dew	dew point
g	pertaining to gas spring in ERPE
hot	pertaining to heat source stream
hs	hot stream
hx	pertaining to heat exchangers in ERPE
in	inlet
l	pertaining to leakage flow around piston
l	pertaining to leakage flow in ERPE
lo	pertaining to load in ERPE
out	outlet
p	pertaining to piston
r	reduced value
ss	stainless steel
th	pertaining to thermal domain in ERPE
v	pertaining to vapour gas spring in ERPE
w	pertaining to working cylinder in ERPE
wf	working fluid

Chapter I

Introduction

I.1 Motivation

I.1.1 The Challenge of Increasing Emissions

Humans have been burning fossil fuels before the beginning of recorded history, but it is with the advent of the industrial revolution that the combustion of fossil fuels began to have a massive effect on the planet. Fossil fuels have a high energy density and therefore release large quantities of energy on combustion. They are hence ideal for use in heat engines which convert heat to work subsequently used to generate electricity or to produce motion for transportation. In the European Union, fossil fuels accounted for almost 75 % of all consumed primary energy sources in 2013 [1].

Fossil fuel combustion releases oxides of carbon (CO_x), nitrogen (NO_x), sulfur (SO_x) and water vapour. Additionally, unburnt hydrocarbons and particulate matter (e.g. soot) are produced if the combustion is imperfect. Water vapour, carbon dioxide (CO_2), ozone and to a lesser extent nitrous oxide (N_2O) and methane are the primary green house gases in earth's atmosphere [2]. Carbon dioxide accounted for more than 99 % of the mass of all green house gas emissions and 80 % of the global warming potential of all green house gas emissions from the European Union from 1990 to 2014 [3]. Therefore, carbon dioxide emissions and green house gases are often used interchangeably in the context of global warming. Climate change is the most significant and imminent danger currently posed by fossil fuel combustion.

At the 21st Conference of the Parties of the United Nations Framework Convention for Climate Change (UNFCC), 195 countries adopted and shortly thereafter signed the

so-called Paris Agreement to combat climate change. The main aims of the treaty are stated in Article 2 as [4]:

(a) Holding the increase in the global average temperature well below 2 °C above pre-industrial levels and to pursue efforts to limit the temperature increase to 1.5 °C above pre-industrial levels, recognizing that this would significantly reduce the risks and impacts of climate change;

(b) Increasing the ability to adapt to adverse impacts of climate change and foster climate resilience and low greenhouse gas emissions development, in a manner that does not threaten food productions;

(c) Making finance flows consistent with a pathway towards low greenhouse gas emissions and climate-resilient development.

The 2 °C threshold resulted from decades of international and mainly political discussions. It is often put forward as a level of climate change that would avoid the most serious effects of global warming while ensuring sustainable food production and economic development. However, there is little scientific evidence that supports the claim that 2 °C is still a safe level of climate change. Moreover, the measures and targets promised by the individual nations are insufficient to prevent global warming by 2 °C, let alone 1.5 °C, according to recent studies such as those by Rogelj et al. or Jeffery et al. [5, 6]. If all nations adhere to their intended contributions, a median warming of 2.6–3.1 °C will be reached by 2100.

Although greenhouse gas emissions through fossil fuel combustion may have the most far-reaching consequences, fossil fuel emissions also have other effects. Acid rain is a result of increased sulfur dioxide and nitrogen oxide emissions. Nitrogen oxides are also a component in the formation of smog along with other fossil fuel emissions such as unburnt hydrocarbons and particulate matter. The air pollution caused by fossil fuel combustion can have serious health effects on local populations. Due to these dangers and effects, a growing body of research, policy, and legislation is dedicated to the reduction of combustion emissions, especially CO_2.

The finite nature of the resources is an additional driving force pushing towards sustainable energy production. Declining reserves are leading to higher energy prices in the long run which often go hand-in-hand with economic slow-downs and recessions. Although in highly developed countries energy consumption is decreasing, it is still increasing around the world. Additionally, the world population continues to rise putting further pressure on resources and increasing fears over energy security. In summary,

dwindling resources, rising energy prices, health risks due to excessive air pollution, and an impending climate disaster are fuelling efforts by industry, governmental and non-governmental organizations, and the scientific community to establish energy efficiency schemes and to proliferate the use of renewable energy sources.

I.1.2 Future Energy Scenarios

Two opposing energy production scenarios are often proposed to tackle these challenges. The first one is a centralized power generation system where electricity is produced mainly from renewable sources at large point sources or power plants and distributed via a grid to the domestic level. This is essentially a decarbonized upgrade of current power generation settings across the globe. The second scenario is a decentralized system of distributed power where electricity and heat are generated at smaller and local scales, e.g. at the level of a single household, groups of households, large buildings, small communities, industrial plants, or small energy farms. Heat and power is produced to match local demand. Large-scale centralized plants will retain an edge in plant efficiency compared to small-scale systems. However, this advantage is compromised by the transmission and distribution losses associated with a centralized system which can amount to a reduction in plant efficiency of up to 10 %. Small-scale, decentralized systems cannot benefit from economies of scale as large systems and plants do. Therefore, costs will often be a limiting factor for the applicability of small-scale technologies. Nonetheless, decentralization is slowly becoming more dominant as the EU, US, and the rest of the world implement policies to increase decentralized power generation capacities [7, 8]. In the decentralized scenario, co-generation – the simultaneous generation and distribution of heat and electricity – will become more necessary, and it will be achieved mainly through renewable sources, such as wind, solar, or geothermal. This will inevitably involve the conversion of low- and medium-grade heat. In this thesis, low temperature or low grade heat describes heat sources with temperatures below 200 °C while medium-grade heat is between 200 °C and 500 °C.

I.1.3 The Potential of Waste Heat

Apart from renewable heat sources, waste heat is also an important and abundantly available (low or medium-grade) heat source. Waste heat is normally emitted to the surroundings in the form of flue-gas exhausts, cooling streams, etc., and it is produced in the industrial, commercial, domestic, and transport sector. Wasted heat accounts for

approximately 60% of all consumed net primary energy. The European Union consumed a total of 67.8 EJ in 2011 of which 41.9 EJ was wasted. The figures for the US have similar proportions: total consumption was 102.6 EJ of which 58.7 EJ was wasted. Worldwide, 500 EJ of primary energy were consumed of which 290 EJ were wasted [9]. The most important feature of waste heat is that it virtually does not carry any costs compared to fossil fuels. In the past, however, making use of waste heat has not been economically feasible. This is because waste heat is often intermittent, and the low temperature relative to fossil fuel heat sources meant that any conversion to electricity will have a low efficiency and low power output such that the necessary capital and operating costs were too high. Due to the long-term rise of fossil fuels costs and government policies pushing to reduce CO_2 emissions, waste heat recovery and conversion now makes economic sense and is in many cases becoming a necessity.

I.2 Converting External Heat Using Reciprocating Motion

It is essential to understand what type of systems are appropriate for the conversion of low and medium-grade heat. Figure I.1 shows a contour plot of the power output normalized by the overall heat input of an infinite series of Carnot engines operating between a heat source and sink with varying temperatures (taken from Ref. [10]). It can be understood as the highest efficiency achievable for a heat engine operating between heat sources and heat sinks with varying temperatures. This is opposed to the classical understanding of the Carnot engine which operates between two constant-temperature heat reservoirs. An infinitesimal amount of heat $\mathrm{d}\dot{Q}_{\mathrm{hot}}$ is transferred from the heat source stream to the working fluid at each Carnot engine which reduces the enthalpy and temperature of the hot stream by $\mathrm{d}\dot{H}_{\mathrm{hot}} = -\mathrm{d}\dot{Q}_{\mathrm{hot}}$ and $\mathrm{d}T_{\mathrm{hot}}$. The hot stream enters the hot heat exchanger with an inlet temperature of $T_{\mathrm{hot,in}}$ and experiences a total temperature drop of ΔT_{hot} and an enthalpy reduction of $\Delta\dot{H}_{\mathrm{hot}} = \dot{m}c_{\mathrm{p}}\Delta T_{\mathrm{hot}}$. Similarly, the heat sink stream has an inlet temperature of $T_{\mathrm{cold,in}}$ and a total temperature and enthalpy increase of ΔT_{cold} and $\Delta\dot{H}_{\mathrm{cold}} = \dot{m}c_{\mathrm{p}}\Delta T_{\mathrm{cold}}$. The horizontal axis in Fig. I.1 is the inlet temperature of the hot stream $T_{\mathrm{hot,in}}$; the vertical axis is the overall temperature drop of the hot stream normalized by the inlet temperature $\Delta T_{\mathrm{hot}}/T_{\mathrm{hot,in}}$. For simplicity, the heat duty $\dot{m}c_{\mathrm{p}}$ in the hot and cold stream are assumed equal. The inlet temperature of the cooling stream $T_{\mathrm{cold,in}}$ is 20 °C for all cases. In addition to the contour plot, the locus of the maximum power output at each value of $T_{\mathrm{hot,in}}$ is shown.

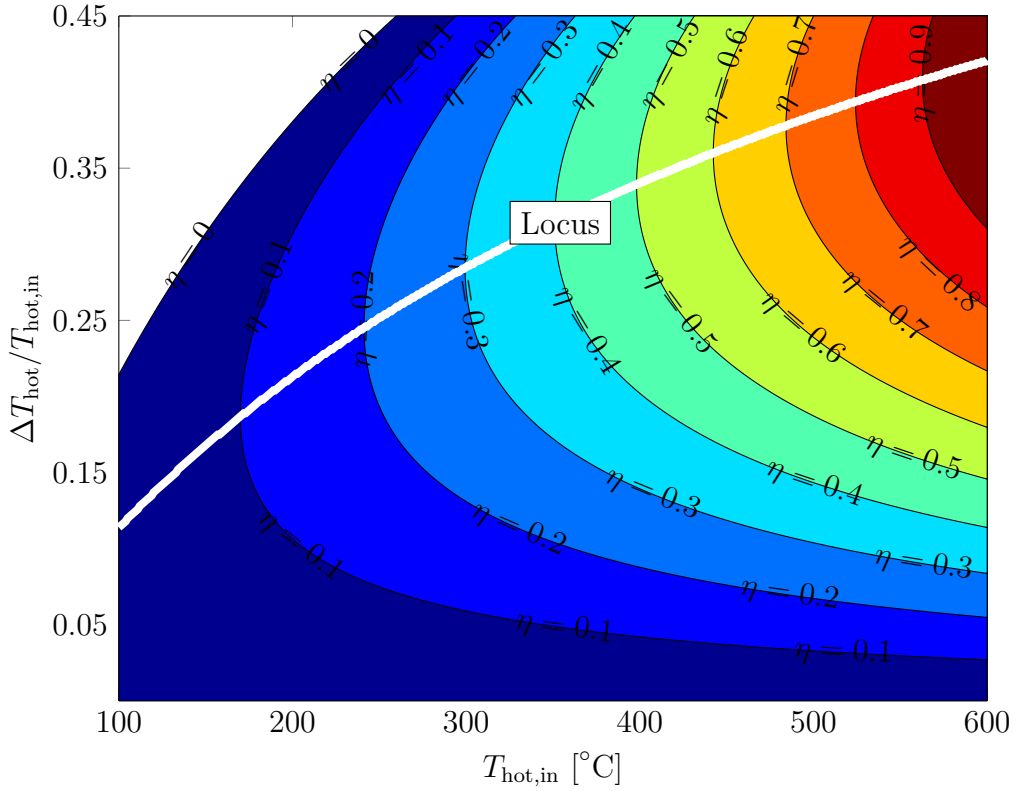


Figure I.1: Contour plot of maximum cycle efficiency η for a heat engine operating between a heat source and heat sink stream with varying temperatures. The horizontal axis is the inlet temperature of the heat source stream $T_{\text{hot,in}}$ and the vertical axis is the temperature drop of the heat source stream normalized by the inlet temperature $\Delta T_{\text{hot}}/T_{\text{hot,in}}$. The inlet temperature of the heat sink stream is constant $T_{\text{cold,in}} = 20$ °C. The white curve is a locus of the maximum power output at each value of $T_{\text{hot,in}}$. Taken from Markides [10]

An important observation from this analysis is that the ideal conversion of heat at high temperatures also requires a high temperature drop in the hot heat exchanger while the opposite is true for low inlet temperatures. For example, if $T_{\text{hot,in}} = 100$ °C, the maximum power output is achieved at a (normalized) temperature drop of $\Delta T_{\text{hot}}/T_{\text{hot,in}} = 0.12$ or $\Delta T_{\text{hot}} = 45$ °C. At a higher temperature inlet temperature of $T_{\text{hot,in}} = 600$ °C, the ideal cycle has a temperature drop of $\Delta T_{\text{hot}}/T_{\text{hot,in}} = 0.42$ or $\Delta T_{\text{hot}} = 370$ °C. For a given heat duty ($\dot{m}c_{\text{p}}$) through the hot and cold heat exchangers, the second system will be more than 8 times larger in terms of heat input and more than 20 times larger in terms of power output due to the higher efficiency. This means that for low and medium temperature heat sources, small-scale (and therefore decentralized) power generation systems are thermodynamically more suitable. Additionally, when converting low- and medium-grade

heat organic compounds are often preferred over water as working fluids. Generally, water (at normal temperature and pressure) has a much greater specific enthalpy than the vast majority of organic fluids, hence it requires a much higher heat intake per unit mass of working fluid. This has the effect of shifting the ideal operation of heat engines to higher temperatures and therefore to larger systems.

As an external heat source, we will be mainly considering applications with waste heat-sources. The technologies discussed in this thesis are compatible with heat regardless of its origin, however the type of heat source has implications regarding costs and the most significant figure-of-merit. Specifically, the energy source in waste-heat conversion applications is virtually free when compared to fossil fuel applications. Therefore, when converting waste heat, the net power output is more significant than thermal efficiency as a figure-of-merit.

The research presented in this thesis focuses on two emerging types of energy conversion systems based on thermodynamic two-phase heat engine cycles which use reciprocating motion to produce work. The first class of heat engine is the two-phase thermofludic oscillator (TFO) and the second is the organic Rankine cycle (ORC). ORCs are a well-established, mature technology. They are suitable for heat source temperatures up to 400 °C and can reach efficiencies in excess of 25 % especially at higher temperatures. The power output is in the range from few kilowatts to tens of megawatts. Current efforts focus on improving effiency and power output. An ORC does not necessarily use reciprocating motion when converting heat, in fact most commercial ORCs today use turbomachines or screw expanders. However, reciprocating-piston expanders have several advantages over these machines, that they can considerably improve performance and reduce costs of ORCs.

TFOs are a much more recent, almost nascent development. They are aimed at the affordable conversion of heat to hydraulic work from sources at 40 °C to 200 °C. The power output is intended to be up to hundreds of watts with thermal efficiencies of just a few percentage points. TFOs and ORCs are complementary systems, and they have the potential to be widely used for distributed power generation.

I.2.1 Two-Phase Thermofluidic Oscillators

Fluidics is defined as "a field of technology concerned with using small interacting flows and jets of fluid in systems of tubes, nozzles, and cavities that have few or no moving parts, to carry out operations characteristic of electronics, such as amplification and switching" [11]. Joyce [12] defines it as a technology which provides "sensing, computing, and con-

trolling functions with fluid power through the interaction of fluid streams. Fluidics can perform these functions without mechanical moving parts". Thermofluidics is a term coined by Smith [13] in 2006 which he defines as "a field of fluidics in which fluid flows are coupled with transient heat flows to or from an external source." Furthermore, he defines a thermofluidic oscillator to be "a system in which a fluid interacts with heat to produce sustained oscillations in the presence of stationary solid boundaries." With this definition, thermofluidic oscillators encompass such devices as thermoacoustic engines [14–16]; Fluidyne and free piston Stirling engines [17–22]; pulse-tube refrigerators [23, 24]; and two phase TFOs such as the Non-Inertive-Feedback Thermofluidic Engine (also known as NIFTE) [13, 25–31], the Evaporative Reciprocating-Piston Engine (ERPE) [32], and the Up-THERM engine [33, 34]

Thermacoustic engines use stationary hot and cold heat exchangers to induce pressure oscillations and convert thermal energy to acoustical energy whereby the working-fluid gas undergoes a Stirling cycle. In pulse-tube refrigerators, a pressure oscillation is imposed on a gas and heat addition and rejection are timed in such a manner such that heat pumping or refrigeration is achieved. Fluidyne engines are Stirling engines which use liquid pistons rather than solid pistons. Two-phase thermofluidic engines are similar to Fluidyne engines with the added feature that they take advantage of phase change to improve heat transfer and increase the pressure ratio of compression and expansion. What all thermofluidic oscillators have in common is that they have no or fewer mechanical parts compared to their conventional equivalents. Engines with solid pistons require additionally sliding mechanical seals. Therefore, thermofluidic engines require less maintenance and have lower costs.

I.2.2 Organic Rankine Cycle

An established heat engine for the conversion of heat up to 400 °C is the organic Rankine cycle which boasts a relatively long history of application and development starting in the 1960s. According to a recent market survey [35], there are currently over 2700 MW of cumulative electrical output produced in over 560 ORC power plants worldwide. An additional capacity of 500 MW in 75 plants is currently in planning or under construction [10, 35]. The organic Rankine cycle bears many similarities to the conventional Rankine cycle, which is the conventional steam cycle used in nuclear, coal, and petroleum power plants. They differ mainly in the working fluid, where the organic Rankine cycle replaces water with organic working fluids, such as hydrocarbons and refrigerants. Useful work and electricity can be generated from a broad range of thermal energy sources. Common

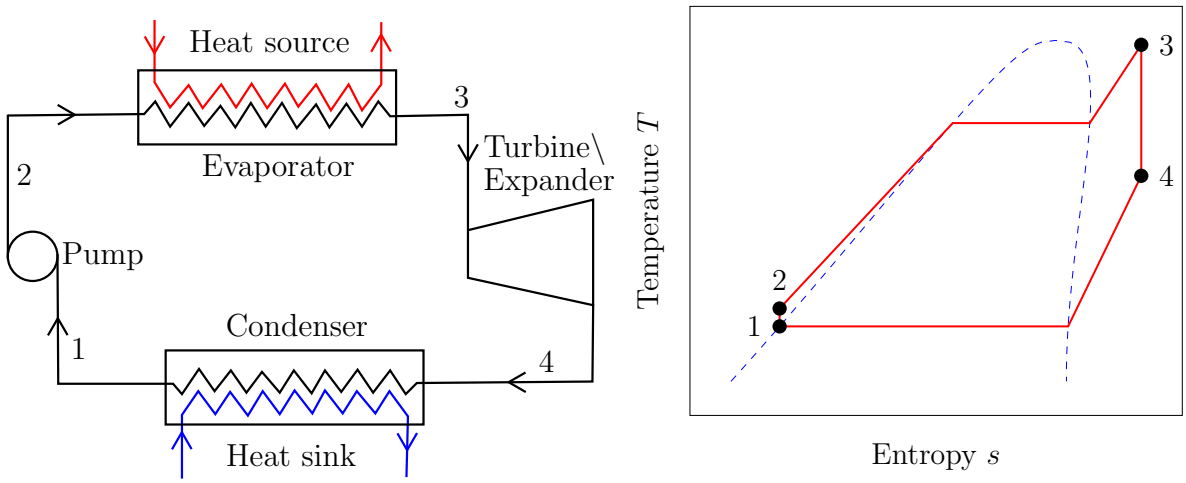


Figure I.2: (a) Schematic diagram of an ORC engine. (b) Exemplary sub-critical, non-regenerative, and ideal ORC cycle on a T-s diagram. The temperature of State 2 is exaggerated for clarity

sources are hot fluid streams from geothermal resources, low or non-concentrating solar collectors, recovered heat from biomass and biogas cogeneration, or waste heat from industrial and commercial settings.

The typical layout of a subcritical, non-regenerative organic Rankine cycle is shown in Fig. I.2(a) and a corresponding T-s cycle diagram in Fig I.2(b) (ideal cycle). The main components of such heat engines are the pump, evaporator (consisting possibly of several heat exchanger elements, including superheater), an expander or turbine, and a condenser (possibly de-superheater).

The ideal ORC cycle consist of the same four thermodynamic processes of the conventional Rankine cycle:

- $1 \rightarrow 2$ isentropic compression in a pump
- $2 \rightarrow 3$ isobaric heat addition in a boiler
- $3 \rightarrow 4$ isentropic expansion in an expander
- $4 \rightarrow 1$ isobaric heat rejection in a condenser

ORCs have two or three key advantages which make them more suitable for low- or medium-temperature applications than the conventional Rankine cycle. Firstly, many organic working fluids exhibit dry or isentropic phase change behaviour. This means that they have a positively sloped or vertical vapour curve. This is in contrast to water – a

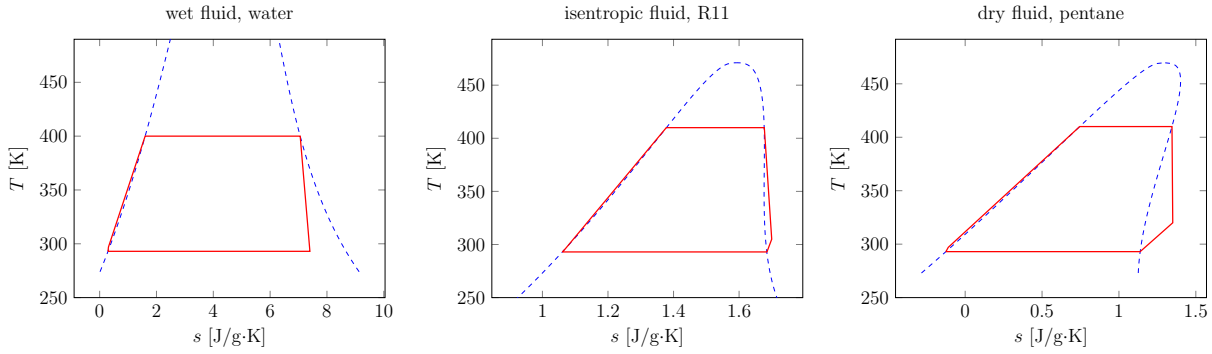


Figure I.3: T-s diagrams of Rankine cycles with different working fluids to show the significance of condensation behaviour. (a) wet fluid, water; (b) isentropic fluid, R11; (c) dry fluid, pentane

wet fluid where the vapour curve is negatively sloped. The different phase behaviours are illustrated in Fig. I.3 which show examples of Rankine (water) or organic Rankine cycles with no superheating and an evaporator outlet temperature of $T_3 = 400$ K. When using a wet fluid such as water, it is necessary to superheat the working fluid to elevated temperatures. This is to prevent the expansion of the fluid into the two-phase region, as can be seen in Fig. I.3(a). Condensation and the formation of droplets in the expansion device can lead to mechanical damage (especially in turbines) and to the deterioration of the thermodynamic performance. On the other hand, when using isentropic fluids, such as R11 (Fig. I.3(b)), or dry fluids, such as pentane (Fig. I.3(c)), little or no superheating is required for the gas at the expander outlet to be purely vapour.

Secondly, it is thermodynamically advantageous for the working fluid to expand to a pressure (Number 4 in Fig. I.2(b)) such that the corresponding saturation temperature is as close as possible to that of the cold sink. This maximizes work output and efficiency. The cold sink is most often a cooling stream at ambient temperatures (20–25 °C). The condensation temperature of the working fluid would be a few Kelvin higher than this, as determined by the pinch temperature difference in the condenser. The condensation pressure of water at 30 °C is 0.04 bar, while for R11 and pentane they are 1.3 and 0.8 bar respectively. Components suitable for sub-atmospheric pressures as low as 0.04 bar are expensive and require complicated designs to avoid air ingress. Low- and medium grade heat conversion to power involves decentralized, distributed power plants with low power outputs – in the order of few kWs to few megawatts. Therefore, costs must be kept at a

minimum – complicated and sophisticated systems which are commonly encountered in large-scale centralized power plants cannot be scaled down due to financial concerns.

A final advantage is the large choice of currently available organic compounds and mixtures, each with different thermodynamic properties. This provides the engineer with flexibility to carefully select a fluid with the optimal properties fine-tuned to the external constraints and the desired system output.

Exergy Destruction in ORCs

In studies of small-scale ($\approx$ 100 W) [36] and medium-scale ORCs ($\approx$ 100 kW) [37], it has been calculated that the evaporator, expander, and condenser account for virtually all the exergy destruction in an ORC. The expander/turbine and condenser each are responsible for 20 % of the overall exergy destruction, while the evaporator accounts for 60 %. There is much potential in increasing the efficiency and performance of ORCs by improving the heat transfer in the heat exchangers or by selecting the most suitable type of expander and reducing losses in those expanders.

We addressed the issue of improving heat transfer by investigating the potential of working fluid mixtures in ORCs. Mixtures exhibit a non-constant temperature behaviour during phase change, in contrast to pure fluids. As a mixture evaporates, its temperature (of the liquid phase) increases. As a mixture condenses, the temperature of the vapour decreases. This behaviour can provide an improved thermal match to the heat source and sink and therefore improve overall ORC performance.

The issue of exergy destruction in the expander we addressed by investigating loss mechanisms occurring in reciprocating machines. The case for reciprocating machines in ORCs is discussed in the following section.

Reciprocating-Piston Expanders in ORCs

Since the expander is responsible for a large portion of the exergy destruction in ORCs, choosing the correct type of expander is a crucial decision. The criteria for the selection of an expander involve costs, thermodynamic performance, and mechanical performance. Aspects associated with the thermodynamic performance include for instance power rating, efficiency for different load ranges, speed, expansion ratio, or design temperature and pressures. The mechanical performance is defined by characteristics such as compactness, robust construction, low-cost manufacturing, non-reliance on tight tolerances, reduced number of moving parts, or low wear and maintenance requirements.

There are two main types of expanders. The first type is known as the positive displacement or volumetric expander in which the energy of expansion contained in a working fluid is converted to volumetric displacement work. Examples include reciprocating piston, screw, and scroll expanders. The second type is the turbo-machine where the enthalpy of the working fluid is converted to kinetic energy and finally to shaft work [38]. Unfortunately, expanders for small- to medium-scale ORC-based applications are either not widely available in large quantities or still at the prototype stage. Therefore, they are still relatively expensive and not fully proven.

Turbines and turbo-expanders are a more established technology in the area of energy conversion. They are a mature technology with a high energy density (i.e. compact and lightweight) and high efficiency. However, they tend to have high costs and low efficiencies at off-design conditions or low power outputs. Additionally, turbo-machines are senstive to the presence of two-phase condensate in the flow stream. Liquid droplets in the working-fluid stream can damage the blades upon impingement. In commercial ORC applications, turbines are generally used at power outputs above 50 kW_e. Below this power rating, turbine performance deteriorates and the turbines have high costs per unit power output. Additionally, operating speeds at low power outputs are so high that it is questionable if these expanders can run reliably. The operating speeds are normally above 5000 RPM, but at very low power outputs (below 10 kW_e) operating speeds can be as high as 60000 RPM [38–40].

Scroll expanders are employed for low power outputs between 1–10 kW and rotational speeds below 6000 RPM. They are selected for their high efficiency, simple manufacture, lightweight and compact design, low rotational speeds, low cost, and the capability to operate with two-phase working fluids. However, they have low capacities and high lubrication requirements. Screw expanders are suitable for capacities from 15 to 200 kW at similar speeds as scroll expanders. They perform efficiently at off-design conditions. However, they also have high lubrication requirements, their manufacture is expensive, and they require complicated sealing designs [41]. Another positive-displacement machine is the rotary vane expander which is distinguished from the other two previously machines through its low noise operation.

Finally, reciprocating piston expanders exhibit many advantages relative to turbines and positive displacement expanders. Reciprocating-piston expanders can operate across high pressure ratios which is not always the case with other expander types. Similar to turbo-machines, they are a long-established technology with a mature manufacturability. Although they are not yet commonly used in ORCs, they have the potential of having

higher efficiencies for outputs below 100–200 kW. They can adapt to a wide range of loads and can retain a higher efficiency at off-design operation relative to turbomachines. Additionally, reciprocating piston expanders can tolerate condensate and droplets in the expansion space. They generally operate with lower rotational velocities than any other expander type (normally below 2000 RPM, sometimes as high as 3500 RPM), however, reciprocating piston expanders tend to have many moving parts compared to other machines and also tend to be quite heavy [38–42].

Over the years, several researchers have gathered considerable data about commercial and prototype ORC engines, among them are Curran et al. [40], Zahoransky et al. [42], Badr et al. [38], and more recently Qiu et al. [39] and Bao and Zhao [41]. The ORC systems considered produced power from as low as 0.03 kW up to 1120 kW. Low speeds below 5000 RPM and power outputs up to 30 kW are associated with positive displacement machines. Turbines are used for high speeds and power outputs to meet greater demands although there is increasing research to deliver power as low as 0.15 kW with turbines. The data also revealed that for positive-displacement expanders the power output rises with increasing operational speed, whereas for turbines the power output decreases with speed. All types of expanders have their own set of advantages and disadvantages. Although reciprocating machines have several advantages, not many commercial ORC systems with reciprocating machines are available and most research is focused on turbines and other positive-displacement machines.

When dealing with small-scale power conversion, expanders are characterised by low mass flow-rates. Turbo-machines are designed primarily for larger systems and higher pressures and temperatures. Therefore, the efficiency of these machines is low at small power outputs (below 10 kW). Much work is being done to improve their performance at these scales, however the main problems associated with two-phase erosion and higher costs remain (turbo-machines have strict tolerance restrictions which makes their production costly). Reciprocating-piston devices do not have these disadvantages, and they tend to have a simpler design than rotary displacement machines such as screw and scroll expanders. They are an affordable and robust solution for small- to medium- scale applications and offer flexibility so that they can maintain high efficiency at off-design conditions and at part loads. Reciprocating machines can achieve higher efficiencies if the following challenges can be addressed successfully:

- Reducing the number of moving parts (for example by replacing components such as connecting rods and camshafts by pneumatic converters)

- Improving the pressure drop occurring across valves during intake and exhaust, e.g. by using novel valve concepts and maximizing the flow area
- Address the exergetic losses associated with irreversible oscillating heat transfer between the working fluid and cylinder solid walls

In summary reciprocating expanders represent a promising solution to low-power ORCs, and are clearly worthy of further investigation and development. Our research tackles the latter issue revolving around exergy losses in an effort to move towards the next generation of high-efficiency compression and expansion machines. It should noted here that the exergetic losses associated with irreversible heat transfer are also a problem occurring in Thermofluidic oscillators.

I.3 Thesis Overview

Averting the risks caused by fossil fuel emissions, reducing the dependency on depleting resources, and moving to a sustainable energy future is arguably one of the biggest challenges of our time. In this sustainable energy future, the conversion of low- and medium-grade heat will play an increasingly crucial role as it becomes more cost-effective and as societies move to more decentralized power systems. The research conducted in this PhD project aims to be a contribution in this human endeavour.

Specifically, we researched technologies which use reciprocating motion to convert low-to-medium grade heat to power. This encompassed, firstly, two-phase thermofluidic oscillators which use the reciprocating motion of a working fluid in liquid form to produce hydraulic work. A linear model based on thermal/fluid-electrical analogies is developed with which a novel two-phase thermofluidic oscillator is conceptualized. The novel engine concept is termed the Evaporative Reciprocating-Piston Engine or ERPE, and it is based on an existing TFO prototype. However, the prototype cannot be accurately represented by a linear model, so the ERPE concept is designed such that it can be fully captured by such an approach. The model provides recommendations for the early-stage design on how to improve the performance of other TFOs as well as the ERPE, and it advances our general knowledge and understanding of TFOs. Chapter II provides a short introduction to TFOs before the modelling approach for the ERPE is explained. The results and performance of the ERPE are discussed in Chapter III. A parametric study is carried out to quantify how geometric, thermodynamic, and fluid properties influence the performance of the engine concept.

The second focus of this thesis is on working-fluid mixtures used in ORCs. Mixtures have the potential of reducing the exergy losses in ORC heat exchangers. In a model of a sub-critical, non-regenerative ORC, we examine the potential of working fluid mixtures to improve performance and reduce costs. We use a state-of-art equation of state known as SAFT-VR Mie to produce property predictions of fluids for which thermodynamic property data is unavailable. In Chapter IV, the reader will find the methodology of the model where we show the governing equations of an ORC cycle. The cost-calculation methods are also introduced in this chapter. Furthermore, we introduce the reader to the new equation of state, SAFT-VR Mie. In Chapter V, we discuss the results extracted from this model. We examine how different mixture compositions, superheating, and cycle parameters influence the performance and cost of an ORC.

The third focus of this thesis revolves around exergy losses associated with oscillating heat transfer occurring which occur in reciprocating energy-conversion devices (e.g., reciprocating-piston machines, TFOs). The research aims to quantify thermally induced losses through CFD simulations of the compression and expansion process in gas springs. Gas springs will exhibit the same type of thermally induced loss occurring in piston machines, while not suffering under loss mechanism stemming from other sources, such as valve flow and mass exchange. In Chapter VI, we provide a brief overview into the theory of computational fluid dynamics. Subsequently, we discuss the simulation model of the gas spring, i.e. geometry, mesh, mesh convergence, turbulence, solver, and initial and boundary conditions. We also explain the theory in quantifying thermally induced losses. We will put emphasis on investigating the influence of real-gas effects when using organic fluids in gas springs. Previous studies in this topic only considered ideal gases. Therefore, in this chapter we present the different ideal and real-gas models used. We examine how organic fluids compare with noble gases at varying oscillation speeds with regards to pressure, temperature, and losses in Chapter VII.

The final chapter VIII provides a summary of the entire thesis and provides insight into future research work.

Chapter II

Model Development for the Evaporative Reciprocating-Piston Engine

II.1 Background

As mentioned in the previous chapter, two-phase Thermofluidic Oscillators (TFOs) take advantage of the phase change of a working fluid as opposed to their single-phase counterparts. Phase change allows the engine to extract heat from the heat source or reject heat to the heat sink more effectively (i.e. with higher heat transfer coefficients). Therefore, they can be operated at very low temperature differences between the heat source (or heat sink) and the working fluid. The defining feature of TFOs lies in their simple design and construction. They are very compact and have few or no moving parts. Hence, they do not require dynamic seals and are therefore reliable and require little maintenance. Most crucially, however, they are very cost-efficient due to their simplicity. TFOs produce very low power outputs of up to hundreds of watts or a few kilowatts. Investment costs for heat engines with power outputs below 100 kW range around 2–4 £/W_{el} with a tendency of increasing costs for lower power outputs [43]. Therefore, any heat engine in this low power range must be significantly cost-efficient. As explained earlier, TFOs are suitable for distributed power generation or as part of CHP systems (complimentary to ORCs). Additionally, they can also be used for off-grid situations – e.g. providing pumping power or for the humanitarian provision of water – due to their compact design.

TFOs (be they of the one-phase or two-phase type) consist of a network of interconnected tubes and chambers where the working fluid undergoes an unsteady periodic thermodynamic cycle. The fluid is subjected to oscillating heat transfer and flow the latter of which is converted to a useful form of work. In a two-phase TFO, the working fluid exists simultaneously in liquid and vapour form as it undergoes periodic evaporation and condensation. In many cases, liquid pistons replace solid pistons as mechanical displacers.

II.1.1 Objective

Our research in the area of two-phase TFOs involves the theoretical conceptualization and investigation of a novel engine termed the 'Evaporative Reciprocating-Piston Engine' (ERPE). The ERPE concept is based on an existing two-phase TFO prototype, developed and tested by Encontech B.V. [44] and the Boreskov Institute of Catalysis (BIC) [45]. We will use a linear dynamic model similar in principle to the NIFTE model. The advantages of a linear model, as opposed to a non-linear one, lie in its simplicity and speed of calculation. It requires significantly less computation time (by several orders of magnitude) and is therefore well suited for parametric studies and optimizations. However, the BIC prototype contains several components and effects which cannot be modelled with a linear dynamic approach due to their strong non-linear nature. Therefore, the ERPE can be seen as a 'linearized' version of the BIC prototype; we create a model of the prototype without non-linear components and effects. This linearized version is physically different to the BIC prototype and is therefore considered to be a different engine (which we call ERPE).

The linear model can be used to provide recommendations for early-stage design and can provide valuable insight into the behaviour of two-phase TFOs in general. The objective is to use the linear model of the ERPE to understand how its performance and behaviour and by extension the TFO prototype performance and behaviour can be improved. We will also be able to understand the influence of non-linearities by comparing model calculations with available prototype measurements.

II.1.2 Overview of Chapter

The chapter begins with an introduction of the NIFTE and the BIC prototype to understand the general mode of operation of TFOs. Subsequently, a detailed discussion of the ERPE circuit and the modelling approach of the different possible physical components

of a TFO is provided. Next, the engine is compared to the aforementioned existing TFO prototype. The geometric parameters and thermophysical properties of this prototype are adopted to define the values of the electronic circuit components. The results of the ERPE model are discussed in Chapter III.

II.2 Non-Inertive-Feedback Thermofluidic Engine

Research in the area of two-phase TFOs began with the NIFTE. Smith and Markides [13, 25, 46] developed and built a prototype between 2004 and 2006. Further development continued in a spin-off company called *Thermofluidics Ltd.* [47]. Theoretical studies of the NIFTE were carried out at the Clean Energy Processes (CEP) Laboratory, of which the author is a member. A model of the NIFTE, initially developed by Smith and Markides [13, 46], was further improved by Solanki et al. at the CEP Laboratory [26, 27, 30].

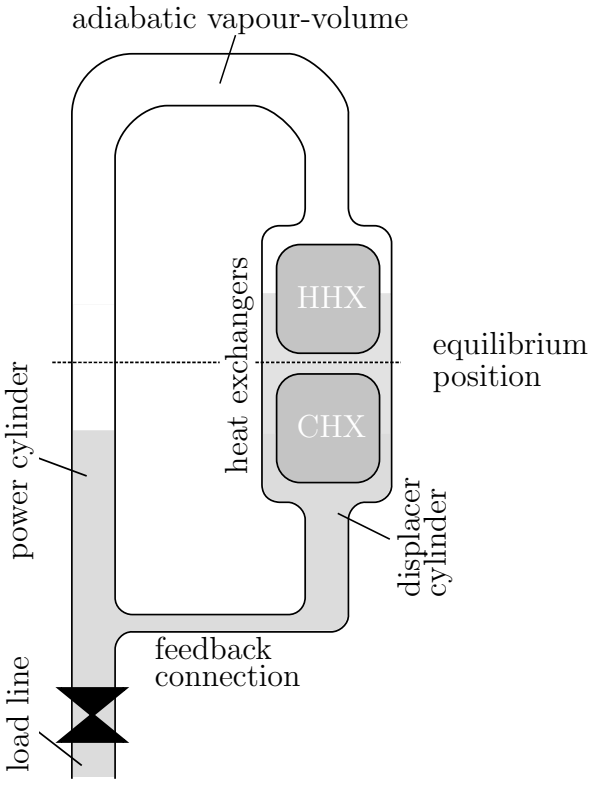


Figure II.1: Schematic diagram of the NIFTE device. HHX and CHX are the hot and cold heat exchangers. The vapour spaces above the liquid in the power and displacer cylinder are part of the adiabatic vapour-volume. The horizontal dashed line indicates the equilibrium (time-mean) liquid-vapour interface position in the two vertical cylinders [27].

Configuration and Operation

Figure II.1 shows a simplified schematic of the NIFTE. The device consists of two vertical cylinders, named displacer and power cylinder, connected by two horizontal tubes – the adiabatic vapour tube at the top and the feedback connection at the bottom. The feedback tube is completely filled with liquid. The displacer cylinder contains two heat exchanger blocks where the hot heat exchanger (HHX) evaporates the liquid working fluid and the cold heat exchanger (CHX) condenses the vaporous working fluid.

We can assume the state of the NIFTE as it is illustrated in Fig. II.1 to be the arbitrary starting point of a periodic cycle. Evaporation occurs when the vapour liquid interface is in contact with (i.e at the height of) the HHX in the displacer cylinder. The increase in the mass of vapour leads to a pressurisation of the adiabatic vapour volume at the top of the engine. The pressurisation causes the downward displacement stroke of the liquid column in the power cylinder and the downward displacement of pumped liquid into the load line. The interfaces begin moving toward the equilibrium position mid-way between both heat exchangers. However, the liquid-vapour interface in the displacer cylinder overshoots the equilibrium position due to the inertia of the liquid column and reaches the CHX. When the CHX is exposed to the vapour phase, condensation occurs causing a pressure reduction in the adiabatic vapour-volume. Additionally, the hydrostatic pressure difference between the power and displacer cylinder increases during this process which causes the downward motion of the interfaces to slow down and eventually to reverse. This leads to the upward displacement stroke of the liquid column in the power cylinder and the suction of liquid from the load line into the engine. The interface in the displacer cylinder overshoots and reaches the HHX. Once again, the hydrostatic pressure difference building up between the displacer and power cylinder stops and reverses the upward motion in the power cylinder and the interfaces move back towards their equilibrium positions. In this manner, the engine has completed a full cycle.

The thermodynamic cycle which the working fluid undergoes in the NIFTE is shown in the T-s diagram of Fig. II.2. Smith's prototype [25] had an exergy efficiency (defined as energy output divided by exergy input, see Section II.5.2) in the range of 0.4–1.7%. A heater with 125–150 W power was used as a heat source which sustained a heat source temperature of 90 °C [46], while the heat sink temperature was 4 °C. The thermal efficiency was between 0.1–0.4%.

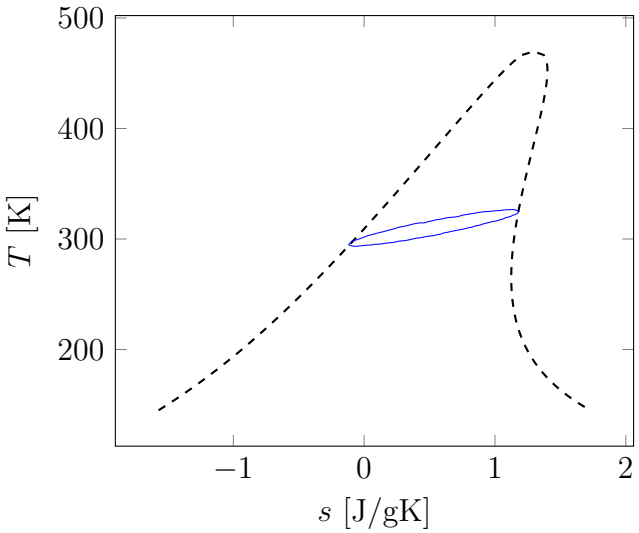


Figure II.2: Temperature-entropy (T-s) phase diagram of the working fluid (pentane) used in the NIFTE prototype (dashed, black line) and T-s diagram of typical linearised thermodynamic cycle undergone by the working fluid inside the NIFTE (solid, blue line). Taken from Ref. [27].

Linear Dynamic Model

A linear dynamic model of the NIFTE was developed to understand the behaviour of the NIFTE and other two-phase TFOs in general and to identify methods to improve its performance. It is intended for the early-stage design of the NIFTE. TFOs have dynamnic similarities with analog electric oscillators circuits and thus, electrical analogies are used to predict instability criteria and estimate first-order heat and work flows. This approach is common in the field of thermoacoustics and was employed for example by Ceperley [16] or Backhaus and Swift [14, 48] for thermoacoustic Stirling engines. The model for the NIFTE was first developed by Smith [13, 25] and was further expanded by Markides et al. [46] and Solanki et al. [26, 27, 30].

In this modelling approach, analogies are drawn between thermofluidic processes in components of the device and passive electrical components (resistors, capacitors, and inductors). The analogies are derived from linearised differential equations which relate the pressure difference across a spatially lumped component to the volumetric flow-rate. When the different electronic components are connected to reflect the connections of the physical engine, an electronic circuit is created. In Fig. II.3, the resulting circuit of the NIFTE is shown. The model was found to compute frequencies and exergy efficiencies in good agreement with the prototype. It also showed good agreement with experimental

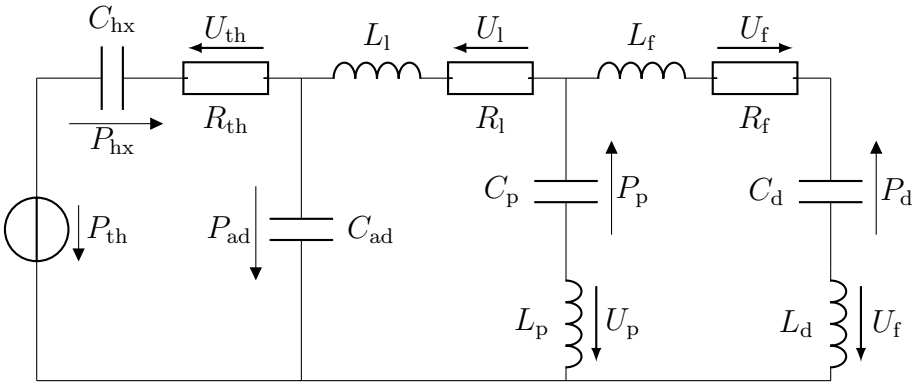


Figure II.3: Electronic circuit representation of the NIFTE where the subscripts 'th' and 'hx' denote components related to the heat exchangers, 'ad' denotes the adiabatic vapour volume, 'l' denotes the load line, 'p' denotes the power cylinder, 'f' denotes the feedback connection, and 'd' denotes the discplacer cylinder. The pressure and volumetric flow-rate are denoted by P and U respectively. A capacitor is represented by C, an inductor is represented by L, and a resistor is represented by R.

trends obtained from measurements over a certain range of conditions. In summary, this method was successfully validated against experimental data and has proven to be useful in promoting an improved understanding of the operation, performance, and also the early-stage design and optimization [27].

II.3 TFO Prototype

In Fig. II.4 a schematic of the BIC prototype is shown. It consists of a displacer cylinder, containing a solid free piston, connected to a working cylinder. The volume at the top of the displacer cylinder contains working fluid in the vapour phase, which behaves as a gas spring. This section is surrounded by the heat source which adds heat and evaporates the working fluid – in this case water. Below the heat source is the cold heat exchanger section (heat sink), which extracts heat from the working fluid and condenses it. Connected to the displacer piston is a mechanical spring which moves freely with the piston. The working cylinder, on the right-hand side, consists of an argon gas-spring entrapped by a liquid column.

The two cylinders are connected by a pair of parallel tubes which are both equipped with check valves such that the oscillating flows from the displacer cylinder to the working cylinder through one tube and returns through the other. One of the tubes is equipped with a pair of pressure sensors situated upstream and downstream of the check valve.

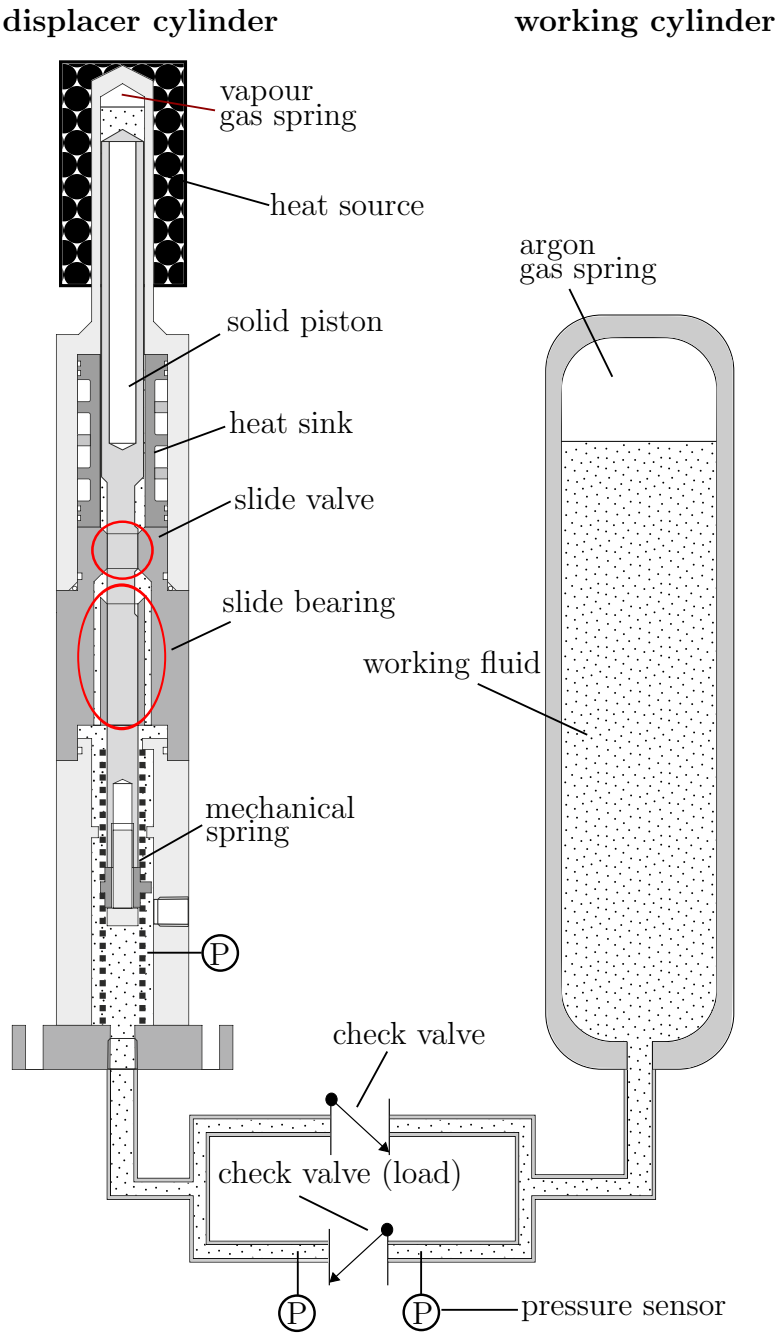


Figure II.4: Schematic description of the BIC prototype. The slide valve and slide bearing are encircled in red.

The sensors are used to assess the engine's power output by measuring the pressure drop across the adjustable check valve. When the bottom valve is completely open, the engine is considered to run without a load. Since the pressure measurements are only carried out in one of the tubes, the engine can only be considered to produce work when there is flow through the bottom connection tube. Hence, the engine only produces work during half an oscillation cycle.

The displacer cylinder additionally contains a slide bearing to fix the axial position of the free piston. The flow of the liquid working fluid is diverted into two narrow channels around the slide bearing. A short distance above that is a slide valve which closes depending on the piston position. The schematic in Fig. II.4 shows a situation where the slide valve is closed. When the valve is closed, the flow of the liquid working fluid in the displacer cylinder is stopped. The free piston is also equipped with a mechanical spring which provides restoring forces to help sustain oscillations.

II.4 Linear Modelling of the ERPE

Before introducing the physical and electrical representation of the ERPE, we will first show how common TFO components are modelled in our approach. We will then apply these sub-models to the BIC prototype where possible and thereby derive a physical and electric representation of the ERPE.

Our linear dynamic modelling approach describes a two-phase TFO with an electronic circuit which consists of a voltage/potential source and a number of resistances (R), inductances (L), and capacitances (C). A certain combination of electrical elements can represent a specific component of a TFO to a first-order approximation. For instance, a resistance, inductance, and capacitance in series can describe a liquid column while a capacitance connected to ground can describe a gas spring. These will be explained in more detail in the following section.

A set of linearized spatially lumped sub-models can be derived for components of the prototype engine, each of which describes the dominant thermal or fluid process in that particular component with an ordinary differential equation (ODE). Using electrical analogies, the resulting ODEs can be represented by a combination of passive electrical components such as resistors, inductors, and capacitors. These are then interconnected to form an electronic circuit representation of the entire device. Specifically, thermal resistance, fluid drag, and viscosity are accounted for by introducing resistors R, gravity and gas compressibility are described by capacitors C, and fluid/piston inertia by in-

ductors L. The voltage across an element represents the pressure difference ΔP at the corresponding engine component, whereas the current represents the resulting volumetric flow-rate U through it. At the heat exchangers, the voltage corresponds to a temperature difference and the current corresponds to an entropy flow-rate; both are converted into an equivalent pressure difference and volumetric flow-rate as explained in previous work [26, 27, 30, 46] and later in Section II.4.8. Applying Gauss's, Faraday's, and Ohm's laws in the electrical analogy leads to the following three fundamental equations between pressure difference ΔP and flow-rate U which, with the help of the principle of superposition, can account for more than one process or effect within a particular component:

$$\frac{\mathrm{d}(\Delta P)}{\mathrm{d}t} = \frac{1}{C}U\,, \qquad \Delta P = L\frac{\mathrm{d}U}{\mathrm{d}t}\,, \qquad \Delta P = RU\,, \tag{II.1}$$

or in the Laplace domain:

$$\Delta P = \frac{1}{sC}U\,, \qquad \Delta P = sLU\,, \qquad \Delta P = RU\,, \tag{II.2}$$

where $s = \sigma + \mathrm{i}\omega$ is the Laplace variable. Note that, in each of the relations stated above, the parameters C, L, and R represent a combination of actual physical engine parameters, i.e. geometrical dimensions or fluid and transport properties.

As two-phase TFOs are periodically oscillating devices, every thermodynamic heat and fluid flow quantity can be expressed as a decomposition of a time-averaged mean component and a fluctuating component. For example, the pressure is expressed as $P = \overline{P} + P'$ and the flow-rate $U = \overline{U} + U'$. The overline $\overline{\bullet}$ denotes mean quantities while the prime symbol $\bullet'$ represents fluctuating components. By definition, the time average of the fluctuation is zero e.g. $\overline{P'} = 0$ or $\overline{U'} = 0$. The mean pressure in a component is the equilibrium pressure while the mean flow-rate is zero. For the modelling procedure, a number of simplifications are made [27]:

1. The heat engine is a purely oscillating device and therefore only the fluctuating components around their respective time-averaged values need to be considered. The time-averaged values are also referred to as equilibrium values.

2. The time-varying quantities are assumed to exhibit small perturbations around their respective time-averaged values, e.g. $P' \ll \overline{P}$.

3. The primes are dropped from the notation in the remainder of the thesis, e.g. $P' \to P$ or $U' \to U$.

In the following sections, typical TFO components and their electrical analogy representations are discussed. When these analogies are applied to different physical components of the BIC prototype (where possible), we obtain the electronic circuit representation of the ERPE.

II.4.1 Horizontal (Connection) Tubes

Given is a horizontal tube which is completely filled with a liquid as shown in Fig. II.5. The Navier-Stokes equation (in cylindrical coordinates) is the first step in obtaining a first-order differential equation for the flow processes in a horizontal tube. We only need to consider the equation in axial direction, since the tube is horizontal and the flow is assumed axisymmetric:

$$\rho\left(\frac{\partial u_z}{\partial t}+u_r\frac{\partial u_z}{\partial r}+\frac{u_\theta}{r}\frac{\partial u_z}{\partial \theta}+u_z\frac{\partial u_z}{\partial z}\right)= \\ =-\frac{\partial P}{\partial z}+\mu\left(\frac{1}{r}\frac{\partial}{\partial r}\left(r\frac{\partial u_z}{\partial r}\right)+\frac{1}{r^2}\frac{\partial^2 u_z}{\partial \theta^2}+\frac{\partial_z^2}{\partial z^2}\right), \tag{II.3}$$

where z is the axial coordinate, r is the radial coordinate, θ is the angular coordinate, t is time, ρ is the density of the fluid, u is the flow velocity, μ is the fluid dynamic viscosity, and P is the pressure.

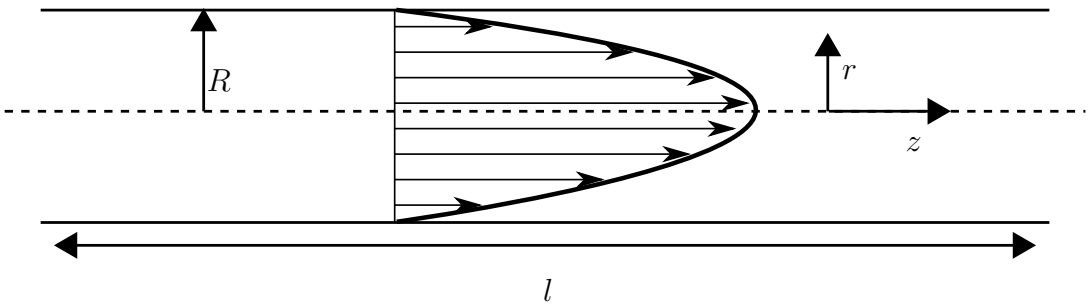


Figure II.5: Fluid flow and the resulting velocity profile in connection tube. The inner radius of the tube is denoted by R, the length of the tube by l, and r and z are cylindrical coordinates.

The flow is also assumed to be fully developed, laminar, incompressible, and without swirl. With these assumptions, Eq. II.3 is simplified to

$$\rho\frac{\partial u_z}{\partial t}=-\frac{\partial P}{\partial z}+\mu\left(\frac{1}{r}\frac{\partial}{\partial r}\left(r\frac{\partial u_z}{\partial r}\right)\right). \tag{II.4}$$

The flow in the connection tube in the z-direction is assumed to be fully developed and laminar. Therefore, a parabolic analytical expression describes the velocity profile of the fluid flow:

$$u_z(r) = ar^2 + br + c. \tag{II.5}$$

We apply the boundary conditions of zero velocity at the wall $u_z(R) = 0$ and a maximum velocity at the centreline of the tube $u_z(0) = u_{\max}$ which results in

$$u_z(r) = u_{\max}\left(1 - \frac{r^2}{R^2}\right). \tag{II.6}$$

The average velocity of the bulk flow across the tube cross-sectional area is computed to be $\overline{u} = \frac{1}{2}u_{\max}$. The volumetric flow rate U through the tube can be obtained by multiplying the average velocity with the cross-sectional area A:

$$U = \overline{u}A = \frac{1}{8}u_{\max}\pi d^2\,, \tag{II.7}$$

where d is the diameter of the tube. Solving Eq. II.7 for $u_{\max}$ gives

$$u_{\max} = \frac{8U}{\pi d^2}. \tag{II.8}$$

Combining Eq. II.6 and Eq. II.8 with Eq. II.4 and solving for the pressure gradient gives

$$\frac{\partial P}{\partial z} \approx \frac{\Delta P}{\Delta z} = -\frac{128\mu}{\pi d^4}U - \frac{4\rho}{\pi d^2}\frac{\mathrm{d}U}{\mathrm{d}t}. \tag{II.9}$$

Since Δz corresponds to the length of the tube l, Eq. II.9 becomes

$$\Delta P = -\frac{128\mu l}{\pi d^4}U - \frac{4\rho}{\pi d^2}\frac{\mathrm{d}U}{\mathrm{d}t}\,, \tag{II.10}$$

or in the Laplace domain:

$$\Delta P = -\frac{128\mu l}{\pi d^4}U - s\frac{4\rho}{\pi d^2}U\,. \tag{II.11}$$

Thanks to the principle of superposition, a horizontal tube is represented in the electrical analogy domain by a resistance R and inductance L (see Eq. II.2):

$$R = \frac{128\mu l}{\pi d^4} \quad L = \frac{4\rho l}{\pi d^2}\,. \tag{II.12}$$

The connection tubes of the BIC prototype can be modelled with these components.

II.4.2 Liquid Columns and Pistons

The approach for liquid pistons is similar as for horizontal tubes. The main difference is that the effect of gravity must be accounted for in the Navier-Stokes equation:

$$\rho\left(\frac{\partial u_z}{\partial t}+u_r\frac{\partial u_z}{\partial r}+\frac{u_\theta}{r}\frac{\partial u_z}{\partial \theta}+u_z\frac{\partial u_z}{\partial z}\right)= \\ =-\frac{\partial P}{\partial z}-\rho g+\mu\left(\frac{1}{r}\frac{\partial}{\partial r}\left(r\frac{\partial u_z}{\partial r}\right)+\frac{1}{r^2}\frac{\partial^2 u_z}{\partial \theta^2}+\frac{\partial_z^2}{\partial z^2}\right), \tag{II.13}$$

where g is the gravitational acceleration constant. The same assumptions as for horizontal tubes are made here as well. The flow is laminar, axisymmetric, incompressible, without swirl, and the velocity profile is parabolic as described in Eq. II.6. Thus, the Navier-Stokes equation becomes

$$\rho\frac{\partial u_z}{\partial t}=-\frac{\partial P}{\partial z}-\rho g+\mu\left(\frac{1}{r}\frac{\partial}{\partial r}\left(r\frac{\partial u_z}{\partial r}\right)\right), \tag{II.14}$$

and taking the same steps as for horizontal tubes leads to the following relation in the Laplace domain:

$$\Delta P=-\frac{128\mu l}{\pi d^4}U-\rho g l-s\frac{4\rho l}{\pi d^2}U\,. \tag{II.15}$$

For the term $\rho g l$, $l=\partial z$ is the varying height of the liquid piston. Bearing in mind that we are only considering fluctuating components, l can be described through

$$\frac{\partial z}{\partial t}=\frac{l}{\partial t}=\frac{U}{A}\,, \tag{II.16}$$

such that

$$l=\frac{U}{A}\partial t\,. \tag{II.17}$$

So substituting Eq. II.17 into Eq. II.15 results in

$$\Delta P=-\frac{128\mu l}{\pi D^4}U-\frac{1}{s}\frac{4\rho g}{\pi D^2}U-s\frac{4\rho l}{\pi D^2}U\,. \tag{II.18}$$

Thus, a liquid piston is represented by a superposition of a resistance, capacitance, and inductance (see Eq. II.2) where

$$R=\frac{128\mu l}{\pi D^4},\quad C=\frac{\pi D^2}{4\rho g},\quad L=\frac{4\rho l}{\pi D^2}\,. \tag{II.19}$$

For the resistance and inductance, l is the time-averaged length of the liquid piston. The displacer and working cylinder both contain liquid columns which can be modelled with these components.

II.4.3 Gas Springs

Gas springs consist of a gas enclosed by a liquid piston. In two-phase TFOs they help sustain an oscillation by storing and releasing energy through alternating compression and expansion. The prototype contains an argon gas-spring in the working cylinder, and the vapour space inside the displacer cylinder can also be considered a gas spring. The compression and expansion are assumed to be isentropic and adiabatic. The governing equation for this process is

$$PV^{\gamma} = \text{const}\,. \tag{II.20}$$

$$\implies \mathrm{d}(PV^{\gamma}) = 0\,. \tag{II.21}$$

$$\implies V^{\gamma}\mathrm{d}P + P\gamma V^{\gamma-1}\mathrm{d}V = 0\,, \tag{II.22}$$

where γ is the ratio of specific heats of the gas or vapour. For small fluctuations around the time-averaged mean values P_1 and V_1, we obtain

$$\frac{1}{P_1}\frac{\mathrm{d}P}{\mathrm{dt}} + \frac{\gamma}{V_1}\frac{\mathrm{d}V}{\mathrm{d}t} = 0\,. \tag{II.23}$$

$$\implies \frac{\mathrm{d}P}{\mathrm{d}t} = \frac{P_1\gamma}{V_1}U\,. \tag{II.24}$$

In the Laplace domain, the previous equation can be written as

$$P = \frac{1}{s}\frac{P_1\gamma}{V_1}U\,. \tag{II.25}$$

Thus, a gas spring in the electrical analogy domain is represented by a capacitor which is connected to ground. The capacitance is calculated with the equilibrium pressure and volume of the gas and the ratio of specific heats:

$$C = \frac{V_1}{\gamma P_1}\,. \tag{II.26}$$

II.4.4 Solid Free Pistons

A schematic of a solid free piston is shown in Fig. II.6. The piston has a height of h_p and a diameter d_p. We assume it is fully immersed in the liquid phase of the working fluid which flows around the piston in the gap between it and the cylinder wall. We also assume that the piston and liquid flow always move in the same direction although maybe at different speeds. These assumptions are made here to make a linear description possible. Although the prototype contains a solid free piston, it is not true that it is always fully immersed in water or that the piston and the flow always move in the same direction. Optionally, a mechanical spring with the spring constant k can be connected to the piston. To derive first-order ODEs for the leakage flow and the piston motion, the Navier-Stokes equations for the flow and a force balance (Newton's second law) on the piston are applied. A force balance on the piston gives

$$m_\mathrm{p}\ddot{z} = A_\mathrm{p}(P_2 - P_1) - m_\mathrm{p}g - kz - A_\mathrm{shell}\mu \left.\frac{\mathrm{d}u_\mathrm{z}}{\mathrm{d}r}\right|_{r=\frac{1}{2}d_\mathrm{p}} , \tag{II.27}$$

where m_p is the mass and A_p the cross-sectional area of the piston, A_shell is the cylindrical surface on the vertical sides of the piston in contact with the liquid, and z is the vertical displacement of the piston. Since only the oscillating (fluctuating) component of the motion is considered, $z' = z - \overline{z}$, $m_\mathrm{p}g$ drops out of the analysis:

$$m_\mathrm{p}\ddot{z} = A_\mathrm{p}(P_2 - P_1) - kz - \mu \left.\frac{\mathrm{d}u_\mathrm{z}}{\mathrm{d}r}\right|_{r=\frac{1}{2}d_\mathrm{p}} A_\mathrm{shell} , \tag{II.28}$$

which is an equation only for the oscillatory motion but with the prime symbols dropped as described at the beginning of Section II.4.

The axial component of the Navier-Stokes equation in cylindrical coordinates for the leakage flow is identical to Eq. II.13. It is repeated here for the convenience of the reader.

$$\begin{aligned}\rho\left(\frac{\partial u_z}{\partial t} + u_r\frac{\partial u_z}{\partial r} + \frac{u_\theta}{r}\frac{\partial u_z}{\partial \theta} + u_z\frac{\partial u_z}{\partial z}\right) = \\ = -\frac{\partial P}{\partial z} - \rho g + \mu\left(\frac{1}{r}\frac{\partial}{\partial r}\left(r\frac{\partial u_z}{\partial r}\right) + \frac{1}{r^2}\frac{\partial^2 u_z}{\partial \theta^2} + \frac{\partial_z^2}{\partial z^2}\right) .\end{aligned} \tag{II.29}$$

After ignoring gravity, as above, the same assumptions apply to the leakage flow as

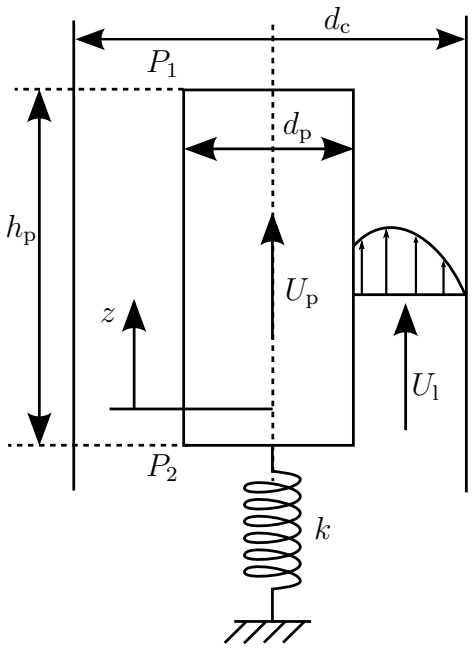


Figure II.6: Schematic of piston and leakage model. The piston height is denoted by h_p while d_p and d_c are the piston and cylinder diameter respectively. The pressure at the top of the piston is P_1 and P_2 at the bottom. The leakage flow is referred to as U_l while U_p is the flow-rate of the piston, and k is the spring constant.

before. Additionally, the flow is assumed to be quasi-steady. The Navier-Stokes equation is simplified to

$$\frac{1}{\mu}\frac{\partial P}{\partial z} = \frac{1}{r}\frac{\partial}{\partial r}\left(r\frac{\partial u_z}{\partial r}\right) . \tag{II.30}$$

Solving this differential equation for the velocity $u_z = u_l$ leads to

$$u_l = \frac{1}{4\mu}\frac{\mathrm{d}P}{\mathrm{d}z} + C_1 \ln r + C_2 . \tag{II.31}$$

To determine the constants C_1 and C_2, the boundary conditions at the cylinder wall $u_l(r = d_c) = 0$ and at the piston surface $u_l(r = d_p/2) = 4U_p/\pi d_p^2$ are applied, where U_p is the volumetric flow-rate corresponding to the piston motion (or the speed of the piston expressed in terms of m^3/s). After applying the boundary conditions and inserting u_l into the simplified Navier-Stokes equation (Eq. II.30), the following relation between

the pressure difference across the piston and the piston flow-rate is found (after some manipulation and a Laplace transformation):

$$U_\mathrm{p} = \underbrace{\left[\frac{\pi^2 d_\mathrm{p}^2 (d_\mathrm{c}^2 - d_\mathrm{p}^2) s}{-32 m_\mathrm{p} \ln\frac{d_\mathrm{p}}{d_\mathrm{c}} s^2 + 64\pi h_\mathrm{p} \mu s - 32 k \ln\frac{d_\mathrm{p}}{d_\mathrm{c}}}\right]}_{1/Z_\mathrm{p}} \Delta P_\mathrm{p}\,, \tag{II.32}$$

where s is the Laplace variable, and $\Delta P_\mathrm{p} = P_2 - P_1$ is the pressure drop across the piston. The fraction in front of ΔP_p can be considered the inverse of the solid piston impedance Z_p ($\Delta P_\mathrm{p} = ZU$). Finally, with partial fraction decomposition, Z_p can be rewritten as

$$Z_\mathrm{p} = sL_\mathrm{p} + R_\mathrm{p} + \frac{1}{sC_\mathrm{p}}\,, \tag{II.33}$$

where L_p, R_p, and C_p are described as

$$C_\mathrm{p} = \frac{\pi^2 d_\mathrm{p}^2 c_1}{32 k c_2}, \quad R_\mathrm{p} = \frac{64 h_\mathrm{p} \mu}{\pi d_\mathrm{p}^2 c_1}, \quad L_\mathrm{p} = \frac{32 c_2 m_\mathrm{p}}{\pi^2 d_\mathrm{p}^2 c_1}\,. \tag{II.34}$$

In Eq. II.34, μ is the dynamic viscosity of the working fluid; m_p is the mass of the piston; k is the spring constant of the mechanical spring; and $c_1 = d_\mathrm{c}^2 - d_\mathrm{p}^2$, $c_2 = \ln(d_\mathrm{c}/d_\mathrm{p})$, and $c_3 = c_2(d_\mathrm{c}^2 + d_\mathrm{p}^2) - c_1$ are geometric constants. Equations II.32 and II.33 prove that the solid piston can be described by an inductance L_p, resistance R_p, and capacitance C_p in series. If we integrate $u_\mathrm{l}(r)$ over the annular area between the piston and cylinder, we obtain an expression for the volumetric flow-rate of the leakage flow U_l:

$$U_\mathrm{l} = \frac{1}{Z_\mathrm{l}} \Delta P_\mathrm{p}\,, \tag{II.35}$$

where

$$\begin{aligned}\frac{1}{Z_\mathrm{l}} =& \frac{\pi\left(d_\mathrm{c}^2 - d_\mathrm{p}^2\right)\left(d_\mathrm{c}^2 - d_\mathrm{p}^2 + \ln\frac{d_\mathrm{p}}{d_\mathrm{c}}\left(d_\mathrm{c}^2 + d_\mathrm{p}^2\right)\right)}{128 h_\mathrm{p} \mu \ln\frac{d_\mathrm{p}}{d_\mathrm{c}}} + \\ &+ \frac{s\pi^2\left(d_\mathrm{c}^2 - d_\mathrm{p}^2\right)\left(d_\mathrm{c}^2 - d_\mathrm{p}^2 + 2 d_\mathrm{p}^2 \ln\frac{d_\mathrm{p}}{d_\mathrm{c}}\right)}{64 \ln\frac{d_\mathrm{p}}{d_\mathrm{c}}\left(m_\mathrm{p} \ln\frac{d_\mathrm{p}}{d_\mathrm{c}} s^2 - 2\pi h_\mathrm{p} \mu s + k \ln\frac{d_\mathrm{p}}{d_\mathrm{c}}\right)}\,.\end{aligned} \tag{II.36}$$

Similarly to before, the inverse of the impedance of the leakage flow Z_l can be written as

$$\frac{1}{Z_\mathrm{l}} = \frac{1}{R_{\mathrm{l},1}} + \frac{1}{sL_\mathrm{l} + R_{\mathrm{l},2} + \frac{1}{sC_\mathrm{l}}}\,, \tag{II.37}$$

from which it is clear that the impedance Z_l, in the electronic circuit representation, can be considered as consisting of an inductance L_l, resistance $R_{\mathrm{l},2}$ capacitance C_l in series and a resistance $R_{\mathrm{l},1}$ connected in parallel. The details of the four RLC components are

$$\begin{gathered} R_{\mathrm{l},1} = \frac{128 c_2 h_\mathrm{p} \mu}{\pi c_1 c_3}\,, \\ C_\mathrm{l} = \frac{\pi^2 c_1 (c_1 - c_2 {d_\mathrm{p}}^2)}{64 {c_2}^2 k}\,, \quad R_{\mathrm{l},2} = \frac{128 c_2 h_\mathrm{p} \mu}{\pi c_1 (c_1 - 2 c_2 {d_\mathrm{p}}^2)}\,, \quad L_\mathrm{l} = \frac{64 {c_2}^2 m_\mathrm{p}}{\pi^2 c_1 (c_1 - 2 c_2 {d_\mathrm{p}}^2)}\,. \end{gathered} \tag{II.38}$$

The overall electric circuit representation of a solid free piston with leakage flow around it is shown in Fig. II.7. Due to the coupling of the flow and solid piston motion, the flow components are functions of parameters related to the piston, and vice versa. For example, the capacitance of the leakage flow C_l depends on the mechanical spring constant k. A physical and intuitive understanding of these components in isolation is difficult. For example, the division of U_l in Fig. II.7 into two parallel branches, $U_{\mathrm{l},1}$ and $U_{\mathrm{l},2}$, cannot be understood physically, as there is no actual separation of the flow in this part of the engine. These interconnections and components are a result of algebraic manipulations of the coupled Navier-Stokes and force-balance equations.

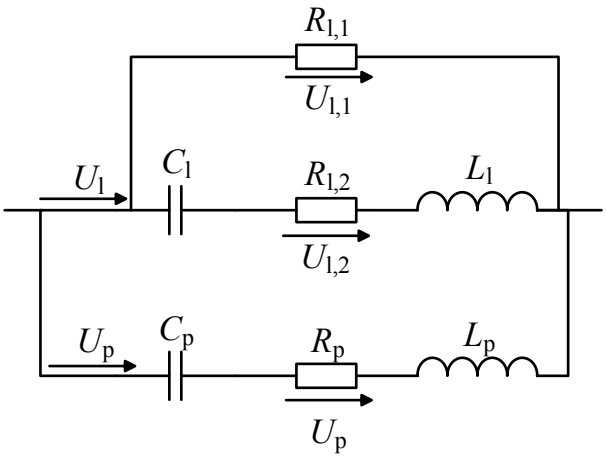


Figure II.7: Electric circuit representation of piston and leakage model.

II.4.5 Slide Bearing of Solid Free Piston

A free piston is not connected to anything outside the engine, and is often fully contained within it. If an engine contains a free piston, the radial position of the piston must be fixed. In such a case, a slide bearing can be used which fixes the radial position of the

piston and guides it vertically as it moves inside the cylinder. A schematic diagram of such a design is shown in Fig. II.8. If the slide bearing is fully contained within the engine as in the design from Fig. II.8, it will lead to additional friction on the solid piston. The working fluid itself can be used as a lubricant. Additionally, since the liquid working-fluid cannot flow around the piston at the slide bearing, it must be diverted into one or more parallel channels. Thus, the design of a slide bearing as in Fig. II.8 leads to effects which must be taken into account in the model.

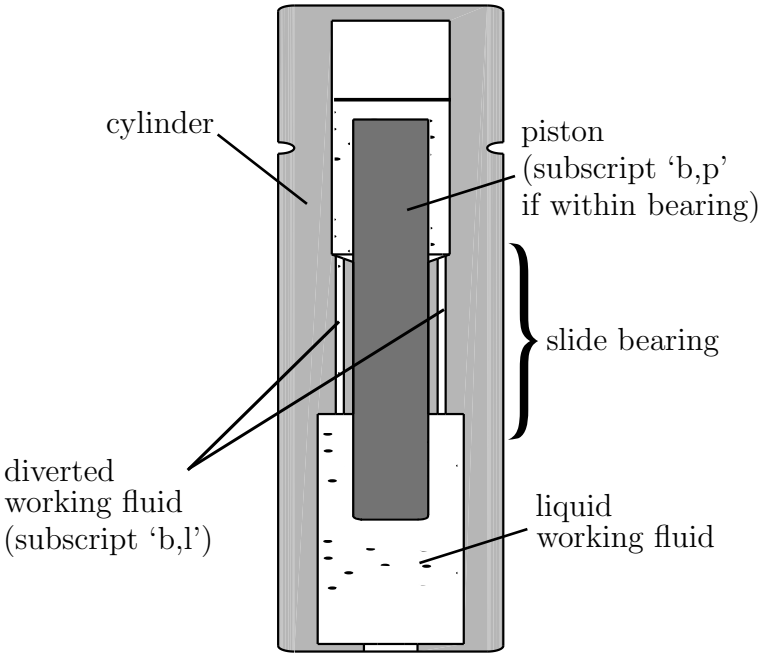


Figure II.8: Schematic diagram of slide bearing design in two-phase TFO with two channels to divert flow of working fluid.

We assume a design as in the prototype (Fig. II.4), also schematically presented in Fig. II.8, where a narrowing of the cylinder to the same diameter as the piston acts as a slide bearing to fix the piston radially. The liquid working fluid is used as a lubricant, the gap between the solid piston and slide bearing is δ, and the liquid working fluid is diverted into two narrow channels (not an annulus). The leakage flow U_l behaves like liquid columns in the channels (subscript 'b,l', see Eq. II.12). However, there is no oscillating hydrostatic pressure difference across this component (as the height of the slide bearing is constant) and, hence, no capacitance. Thus, the flow diverted past the slide bearing consists of a resistance and inductance calculated with Eq. II.12, where the diameter d is the diameter of the channels. To obtain the electric circuit representation of the piston in the slide bearing, a force balance at the piston is set up:

$$m_\mathrm{p} a_\mathrm{p} = (P_1 - P_2) A_\mathrm{p} + F_\mathrm{R}\,, \tag{II.39}$$

where a_p is the acceleration of the piston, P_2 and P_1 are the pressures at the top and bottom of the piston (in the slide bearing section), and F_R is a resistive force in the opposite direction of the piston due to viscous shear on the surface of the piston defined as:

$$F_\mathrm{R} = \mu A_\mathrm{shell} \frac{\mathrm{d}u_\mathrm{z}}{\mathrm{d}r}\,. \tag{II.40}$$

The gap between the cylinder and the piston δ is small ($\delta \ll d_\mathrm{p}$), such that we can assume the flow-velocity profile to be linear in radial direction. Thus, Eq. II.40 (with $A_\mathrm{shell} = \pi d_\mathrm{p} l_\mathrm{p}$) can be expressed as:

$$F_\mathrm{R} = -\mu \pi d_\mathrm{p} l_\mathrm{b} \frac{u_\mathrm{p}}{\delta}\,, \tag{II.41}$$

since $u_\mathrm{z}(r = 0.5 d_\mathrm{p}) = u_\mathrm{p}$ and $u_\mathrm{z}(r = 0.5 d_\mathrm{c}) = 0$. The length of the slide bearing is l_b. The velocity of the piston can be expressed with an equivalent volumetric flow-rate $u_\mathrm{p} = U_\mathrm{p}/A_\mathrm{p} = 4U_\mathrm{p}/\pi d_\mathrm{p}^2$, Eq. II.39 can be rewritten in the form:

$$P_1 - P_2 = s \frac{4\rho_\mathrm{ss} l_\mathrm{b}}{\pi d_\mathrm{p}^2} U_\mathrm{p} + \frac{16 l_\mathrm{b} \mu}{\delta \pi^2 d_\mathrm{p}^3} U_\mathrm{p}\,. \tag{II.42}$$

Thus, the piston in the slide bearing is modelled with an inductance $L_\mathrm{b,p}$ and resistance $R_\mathrm{b,p}$ where

$$L_\mathrm{b,p} = \frac{4\rho_\mathrm{ss} l_\mathrm{b}}{\pi d_\mathrm{p}^2}, \quad R_\mathrm{b,p} = \frac{16 l_\mathrm{b} \mu}{\delta \pi^2 d_\mathrm{p}^3}\,. \tag{II.43}$$

The density of the piston is ρ_ss (stainless steel). Eventually, one obtains the configuration of the piston, leakage flow, and slide bearing shown in Fig. II.9. The piston components (subscript 'b,p') are placed in the branch of the piston flow-rate U_p, while the diverted flow components are placed in the leakage flow branch U_l (one set of components $R_\mathrm{b,l}$ and $L_\mathrm{b,l}$ for each diversion flow channel).

II.4.6 Liquid Column Below Piston

If a free piston is used, the liquid below and above the piston has characteristics which must be considered. The liquid below the solid free piston is modelled by defining a control volume of fixed size moving vertically with the solid piston. This defines a control volume that contains a time-varying mass that consists of the fluid (always in the liquid

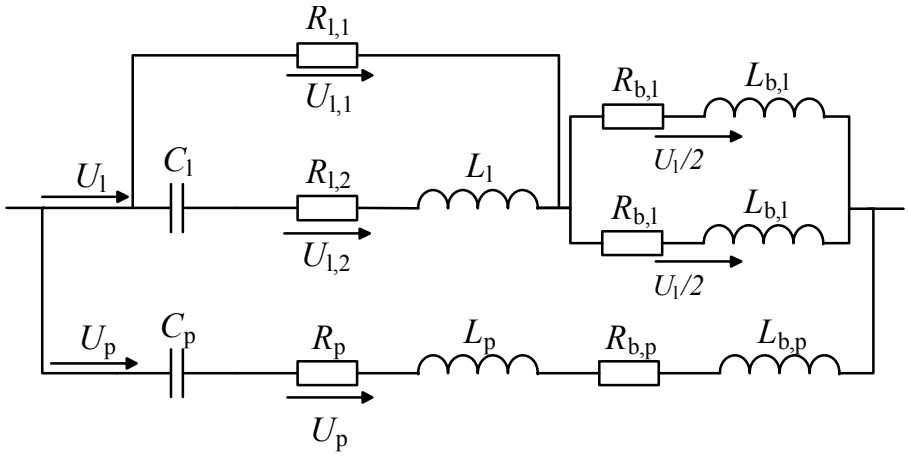


Figure II.9: Electric circuit representation of piston and leakage model including slide bearing.

phase) under the solid piston, while accounting for the different average speeds of the flow and piston. The force balance for this section takes the form:

$$\begin{aligned} m_{\mathrm{bp}} a_{\mathrm{bp}} =& P_{\mathrm{bp}} A_{\mathrm{bp}} - S_{\mathrm{bp}} \mu \left.\frac{\mathrm{d}u}{\mathrm{d}r}\right|_{\mathrm{r=r_c}} - \\ & - m_{\mathrm{bp}} g + (u_{\mathrm{rel,in}} - u_{\mathrm{rel,out}}) \frac{\mathrm{d}m_{\mathrm{bp}}}{\mathrm{d}t} \,, \end{aligned} \tag{II.44}$$

where the subscript 'bp' denotes values for the liquid column below the piston. So, e.g. m_{bp} is the (variable) mass of the liquid column in the control volume, a_{bp} is its acceleration, A_{bp} is the cross-sectional area, S_{bp} is the lateral area equal to the surface area of the cylinder, $\mathrm{d}u/\mathrm{d}r|_{\mathrm{r=r_c}}$ is the velocity gradient at the cylinder wall ($r = r_{\mathrm{c}}$) and u_{rel} is the velocity of incoming/outgoing flow (averaged across the cross-sectional area) relative to the velocity of the liquid column. The final term of the force balance accounts for the momentum of the mass being introduced into or out of the control volume. The relative velocities are given by $u_{\mathrm{rel,in}} = u - u_{\mathrm{p}}$ and $u_{\mathrm{rel,out}} = u_{\mathrm{l}} - u_{\mathrm{p}}$ where u is the velocity of the liquid flowing towards the control volume which also equals the velocity of the liquid-vapour interface at the top of the displacer cylinder. The velocity of the solid piston is u_{p} and u_{l} is the area-averaged velocity of the working fluid. Since the boundary of the variable mass control volume is moving with the piston, the velocity of the liquid column also equals u_{p}. Flow losses at sudden contractions and expansions are neglected as the flow is considered to be quasi-steady, viscous laminar, and fully developed flow. This is a reasonable approximation given the low Reynolds and Womersley numbers, i.e. low frequencies [49, 50]. Linearizing the equation, writing in terms of an equilibrium length

l_{bp}, rearranging, and taking the Laplace transform results in the following relationship between the pressure drop and the flow-rate U:

$$\begin{aligned} P_{\mathrm{bp}} = &\left(\frac{128\mu l_{\mathrm{bp}}}{\pi d_{\mathrm{bp}}^4} + \frac{\rho g}{s}\frac{1}{A_{\mathrm{p}}}\frac{Z_{\mathrm{pl}}}{Z_{\mathrm{p}}} + \right. \\ &\left. + s\rho l_{\mathrm{bp}} \left(\frac{1}{A_{\mathrm{p}}}\frac{Z_{\mathrm{pl}}}{Z_{\mathrm{p}}} + \frac{1}{A_{\mathrm{l}}}\frac{Z_{\mathrm{pl}}}{Z_{\mathrm{l}}} - \frac{1}{A_{\mathrm{bp}}} \right) \right) U \,. \end{aligned} \tag{II.45}$$

Z_{p} is the impedance of the solid piston, Z_{l} is the impedance of the leakage flow, and Z_{pl} is the combined impedance of the piston and leakage $Z_{\mathrm{pl}} = (Z_{\mathrm{l}}^{-1} + Z_{\mathrm{p}}^{-1})^{-1}$.

II.4.7 Liquid Column Above Piston

Similarly to the treatment of the section below the solid piston, the liquid column above is modelled by defining a control volume with a time-varying mass. However, in this case, the top and bottom boundaries of the liquid column are both moving independently of each other. The upper boundary is located at the liquid-vapour interface moving with velocity u and the lower boundary is located at the top of the piston moving with velocity u_{p}. The force balance on this region is written in a similar manner to that for the liquid column below the piston:

$$m_{\mathrm{ap}} a_{\mathrm{ap}} = P_{\mathrm{ap}} A_{\mathrm{ap}} - S_{\mathrm{ap}} \mu \left. \frac{\mathrm{d}u}{\mathrm{d}r} \right|_{\mathrm{r=r_c}} - m_{\mathrm{ap}} g + (u_{\mathrm{rel,in}}) \frac{\mathrm{d}m_{\mathrm{ap}}}{\mathrm{d}t} \,. \tag{II.46}$$

The subscript 'ap' denotes here values relating to the liquid column above the piston, and u_{rel} is the velocity of the incoming flow relative to the velocity of the column u. Applying the same steps as in the last section leads to the expression:

$$\begin{aligned} P_{\mathrm{ap}} = &\left(\frac{128\mu l_{\mathrm{ap}}}{\pi d_{\mathrm{ap}}^4} + \frac{\rho_{\mathrm{wf}} g}{s} \left(\frac{1}{A_{\mathrm{ap}}} - \frac{1}{A_{\mathrm{p}}}\frac{Z_{\mathrm{pl}}}{Z_{\mathrm{p}}} \right) + \right. \\ &\left. + s\rho_{\mathrm{wf}} l_{\mathrm{ap}} \left(\frac{2}{A_{\mathrm{ap}}} - \frac{1}{A_{\mathrm{p}}}\frac{Z_{\mathrm{pl}}}{Z_{\mathrm{p}}} - \frac{1}{A_{\mathrm{l}}}\frac{Z_{\mathrm{p}}}{Z_{\mathrm{l}}} \right) \right) U \,. \end{aligned} \tag{II.47}$$

Equations II.45 and II.47 obtained for the liquid column above and below the solid piston are added together to give the total pressure drop across the entire liquid column in the

cylinder (excluding the piston). When written in terms of a set of RLC parameters, they are expressed as

$$R_{\mathrm{d}} = \frac{128\mu}{\pi}\left(\frac{l_{\mathrm{ap}}}{d_{\mathrm{ap}}^4} + \frac{l_{\mathrm{bp}}}{d_{\mathrm{bp}}^4}\right), \qquad C_{\mathrm{d}} = \frac{A_{\mathrm{ap}}}{\rho g}, \tag{II.48}$$

$$\begin{aligned} L_{\mathrm{d}} =& \rho\left(l_{\mathrm{ap}}\left(\frac{2}{A_{\mathrm{ap}}} - \frac{1}{A_{\mathrm{p}}}\frac{Z_{\mathrm{pl}}}{Z_{\mathrm{p}}} - \frac{1}{A_{\mathrm{l}}}\frac{Z_{\mathrm{p}}}{Z_{\mathrm{l}}}\right) + \right. \\ &\left. + l_{\mathrm{bp}}\left(\frac{1}{A_{\mathrm{p}}}\frac{Z_{\mathrm{pl}}}{Z_{\mathrm{p}}} + \frac{1}{A_{\mathrm{l}}}\frac{Z_{\mathrm{pl}}}{Z_{\mathrm{l}}} - \frac{1}{A_{\mathrm{bp}}}\right)\right). \end{aligned} \tag{II.49}$$

II.4.8 Phase-Change/Thermal Domain and Heat Exchangers

To include the heat exchangers in the electrical analogy model, the heat transfer processes must be linked to the fluid domain. The heat exchange must be expressed in terms of a pressure difference and volumetric flow-rate. Two coupling equations are required; one between entropy flow and volumetric flow, and the other between temperature difference and pressure. During phase-change, the entropy flow $\dot{S}_{\mathrm{th}}$ can be described with the following equation, which relates it to the volumetric flow-rate U_{th}:

$$\dot{S}_{\mathrm{th}} \approx \rho_{\mathrm{v},0}\Delta s_{\mathrm{fg}} U_{\mathrm{th}}, \tag{II.50}$$

where $\rho_{\mathrm{v},0}$ is the time-averaged density of the working fluid in the vapour phase and Δs_{fg} is the entropy change due to vaporisation. U_{th} is the rate of volume change of the vapour phase. Since the volume change of the corresponding liquid phase is comparably small, it need not to be taken into account. The coupling equation between temperature and pressure is obtained by assuming the thermal processes are governed by phase change with small perturbations about a certain time-mean saturation temperature T_0 and pressure P_0:

$$T_{\mathrm{i}} = \left(\frac{\mathrm{d}T}{\mathrm{d}P}\right)_{\mathrm{sat}} P_{\mathrm{i}}, \tag{II.51}$$

where $(\mathrm{d}T/\mathrm{d}P)_{\mathrm{sat}}$ is the change in temperature with pressure along the saturation curve of the working fluid about the equilibrium point found from the Clausius-Clapeyron relation.

Linear Temperature Profile

The linear temperature profile (LTP) is one of two heat exchanger models considered in this work. In this model, the temperature profile in the heat exchangers (along the

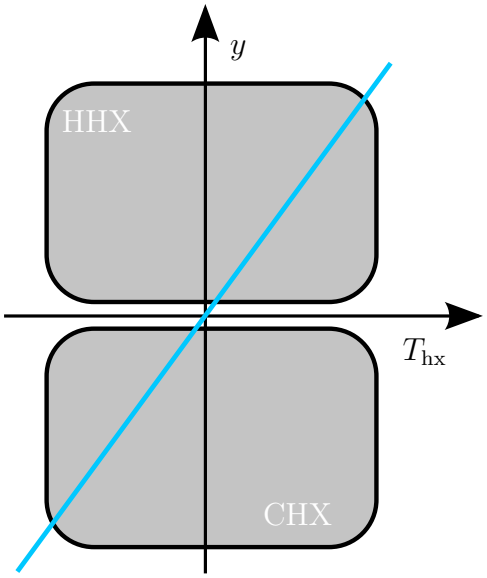


Figure II.10: Linear temperature profile along the height of the cold and hot heat exchangers (CHX and HHX) in the LTP model. T_{hx} is the wall temperature which varies linearly with the vertical height y of the heat exchangers.

vertical inner surfaces of the device) is assumed to be linear and static (i.e. does not change with time) [26, 27, 30, 46]. This is shown in Fig. II.10. We assume that the heat transfer is governed by convective heat transfer, for which all heat transferred $\dot{Q}$ goes into the phase change of the working fluid with an associated entropy flow-rate:

$$\dot{S}_{\mathrm{th}} = \frac{\dot{Q}}{T_0} = \frac{hA_{\mathrm{s}}}{T_0}\left(T_{\mathrm{hx}} - T_{\mathrm{ad}}\right) . \tag{II.52}$$

In this equation, h denotes the heat transfer coefficient, A_{s} the surface area of the heat exchanger where phase change heat transfer occurs, T_{ad} the temperature of the working fluid, and T_{hx} the temperature of the heat exchanger in contact with the fluid. It is assumed that the mean time-averaged saturation temperature of the working fluid is equal to the mean temperature of the heat exchangers and the time-averaged temperature of the working fluid: $T_0 = \overline{T}_{\mathrm{hx}} = \overline{T}_{\mathrm{ad}}$. Substituting Eq. II.50 and II.51 into Eq. II.52 leads to the first-order differential equation for the heat exchanger:

$$P_{\mathrm{th}} - P_{\mathrm{ad}} = \frac{\rho_{\mathrm{v},0} T_0 \Delta s_{\mathrm{fg}}}{hA_{\mathrm{s}}\left(\frac{\mathrm{d}T}{\mathrm{d}P}\right)_{\mathrm{sat}}} U_{\mathrm{th}} = R_{\mathrm{th}} U_{\mathrm{th}} . \tag{II.53}$$

Dynamic Heat Exchanger Model

In the LTP model, the heat exchanger walls are thermally static and have temporally constant spatial temperature profiles. The other model considered in this work is termed the Dynamic Heat Exchanger (DHX) model [27, 30]. In this model, the heat exchangers can interact thermally with the working fluid and an external heat source and sink. They have a finite capacity for periodically storing and releasing heat. The working fluid removes energy during evaporation and re-deposits energy during condensation. Contrary to the LTP model, the heat flux increases linearly along the height of the heat exchangers as illustrated in Fig. II.11. It is assumed that heat transfer to the fluid is governed by phase-change convective heat transfer as in the LTP model, while some energy is used in heating and cooling the heat exchanger blocks, such that

$$\dot{Q}_{\mathrm{hx}} - m_{\mathrm{hx}} c_{\mathrm{hx}} \frac{\mathrm{d}T_{\mathrm{hx}}}{\mathrm{d}t} = hA_{\mathrm{s}} \left(T_{\mathrm{hx}} - T_{\mathrm{ad}}\right) , \tag{II.54}$$

where m_{hx} is the mass of a fixed part of the heat exchanger wall that participates in the heat transfer process, c_{hx} is the specific heat capacity of the heat exchanger walls, and T_{hx} is the wall temperature of the heat exchangers. Using the coupling equations defined in Eqs. II.50 and II.51, we can express Eq. II.54 in the fluid domain:

$$\frac{\dot{Q}_{\mathrm{hx}}}{\rho_{\mathrm{v},0} T_0 \Delta s_{\mathrm{fg}}} = \frac{m_{\mathrm{hx}} c_{\mathrm{hx}} (\mathrm{d}T/\mathrm{d}P)_{\mathrm{sat}}}{\rho_{\mathrm{v},0} \Delta s_{\mathrm{fg}} T_0} \frac{\mathrm{P}_{\mathrm{hx}}}{\mathrm{d}t} + \frac{hA_{\mathrm{s}} (\mathrm{d}T/\mathrm{d}P)_{\mathrm{sat}}}{\rho_{\mathrm{v},0} T_0 \Delta s_{\mathrm{fg}}} (P_{\mathrm{th}} - P_{\mathrm{ad}}) . \tag{II.55}$$

With this equation, the thermal resistance and the heat exchanger capacitance can be identified with

$$U_{\mathrm{th}} = \frac{1}{C_{\mathrm{hx}}} \frac{\mathrm{d}P_{\mathrm{hx}}}{\mathrm{d}t} + R_{\mathrm{th}} \left(P_{\mathrm{th}} - P_{\mathrm{ad}}\right) , \tag{II.56}$$

or in the Laplace domain

$$U_{\mathrm{th}} = \frac{1}{sC_{\mathrm{hx}}} P_{\mathrm{hx}} + R_{\mathrm{th}} \left(P_{\mathrm{th}} - P_{\mathrm{ad}}\right) , \tag{II.57}$$

where the thermal resistance is the same as for the LTP:

$$R_{\mathrm{th}} = \frac{\rho_{\mathrm{v},0} T_0 \Delta s_{\mathrm{fg}}}{hA_{\mathrm{s}} \left(\frac{\mathrm{d}T}{\mathrm{d}P}\right)_{\mathrm{sat}}} , \tag{II.58}$$

and the heat exchanger capacitance is:

$$C_{\mathrm{hx}} = \frac{m_{\mathrm{hx}} c_{\mathrm{hx}} \left(\frac{\mathrm{d}T}{\mathrm{d}P}\right)_{\mathrm{sat}}}{\rho_{\mathrm{v},0} T_0 \Delta s_{\mathrm{fg}}} . \tag{II.59}$$

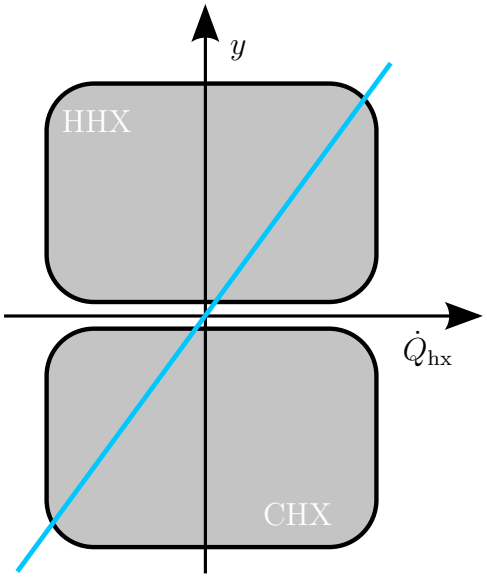


Figure II.11: Heat flux profile along the height of the heat exchangers in the DHX model. $\dot{Q}_{\mathrm{hx}}$ is the heat flux which varies linearly with the vertical height y of the heat exchangers.

II.4.9 Load Model

The engine requires a load with which its power can be assessed. This can be achieved with a device such as a hydraulic motor where the kinetic energy of the flow is converted into shaft work. The electrical analogy for such a load was developed by Kirmse et al. [33]. A simpler method is to introduce a linear resistance at the physical location where energy can be dissipated. This energy is then considered to represent useful work [26–30, 46]. The model must capture the behaviour of the actual load of the experimental prototype as closely as possible. The BIC carried out pressure measurements upstream and downstream of the adjustable load valve in their prototype that indicated that a simple resistance would not be an accurate representation. Figure II.12 depicts the ratio of the amplitudes of the measured pressures downstream and upstream of the valve $|P_{\mathrm{down}}/P_{\mathrm{up}}|$ in the frequency domain acquired with a fast Fourier transform (FFT) algorithm. A single (ideal) resistance would return a constant amplitude ratio for all frequencies. In Fig. II.12, the vicinity of the oscillation frequency observed in the prototype (0.2 Hz) is of particular interest. The spectral data in that range is found to follow the trend:

$$\frac{P_{\mathrm{down}}}{P_{\mathrm{up}}} = \xi \frac{1 + s\lambda_1}{1 + s\lambda_2}\,, \tag{II.60}$$

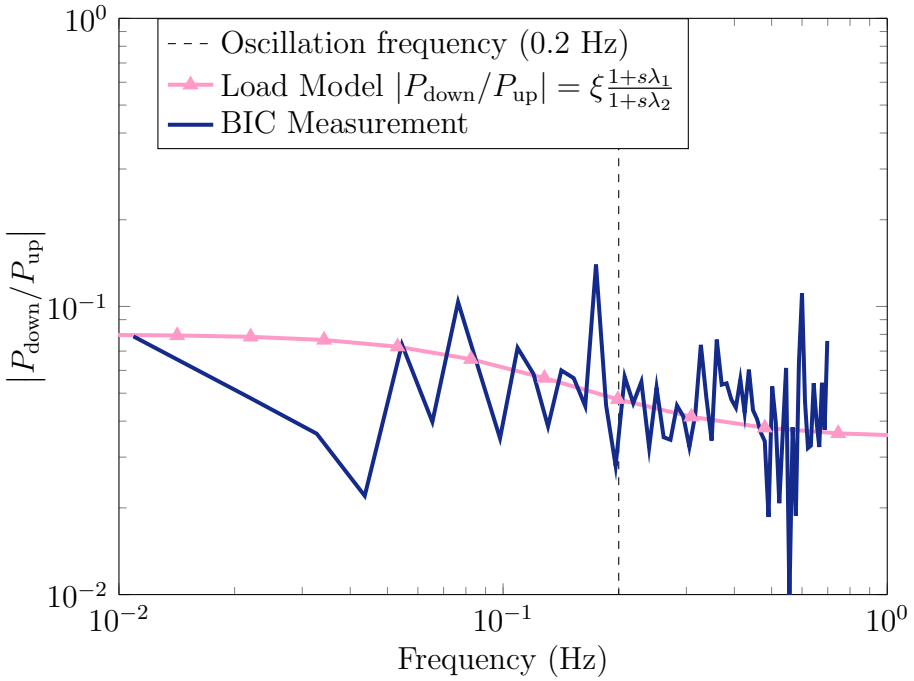


Figure II.12: Power spectrum (in the frequency domain) of the amplitude ratio downstream and upstream of the valve $|P_{\text{down}}/P_{\text{up}}|$ from intermediate pressure (11.8 bar) measurements on the BIC prototype (blue). The fitted load model according to Eq. II.60 is also shown (pink, triangular markers).

which is also represented in Fig. II.12. In Eq. II.60, $s = i\omega$ is the Laplace variable which is in this case purely imaginary as the measurements are carried out while the engine is oscillating at marginal stability (please see Section II.5.2 on the significance of stability). In addition, ξ, λ_1, and λ_2 are constants that are fitted such that the relation follows the spectral distribution as closely as possible in the vicinity of the oscillation frequency. Furthermore, pressure drop measurements across the load valve, when applying steady (non-oscillating) flows, can be used to calculate a steady-flow resistance R_{sf} value with:

$$(P_{\text{up}} - P_{\text{down}}) = U R_{\text{sf}}\,, \tag{II.61}$$

where R_{sf} is the experimentally measured steady-flow resistance. It depends solely on the valve setting and not on the operating frequency. It is the resistance to steady flow due to viscous drag in the valve. The previous equation can now be rewritten as:

$$(P_{\text{up}} - P_{\text{down}}) \left[\frac{1+s\lambda_2}{\xi(1+s\lambda_1)}\right] = U \underbrace{R_{\text{sf}} \left[\frac{1+s\lambda_2}{\xi(1+s\lambda_1)}\right]}_{R_0}\,. \tag{II.62}$$

In Eq. II.62, R_0 is a yet to be determined constant with the same unit as R_{sf}. Solving Eq. II.60 for P_{down} such that

$$P_{\mathrm{down}} = \xi \frac{1 + s\lambda_1}{1 + s\lambda_2} P_{\mathrm{up}}\,, \tag{II.63}$$

and substituting the solution into the left hand side of Eq. II.62 yields:

$$(P_{\mathrm{up}} - P_{\mathrm{down}}) \left[\frac{1 + s\lambda_2}{\xi(1 + s\lambda_1)}\right] = \frac{P_{\mathrm{up}}}{\xi} \left[\frac{1 + s\lambda_2}{1 + s\lambda_1} - \xi\right]\,. \tag{II.64}$$

The expression on the left-hand side in the square brackets in Eq. II.64 is dimensionless. From Eq. II.62 we know that

$$U = (P_{\mathrm{up}} - P_{\mathrm{down}}) \left[\frac{1 + s\lambda_2}{\xi(1 + s\lambda_1)}\right] \frac{1}{R_0}\,, \tag{II.65}$$

so if we divide both sides of Eq. II.64 by R_0, we can write

$$U = (P_{\mathrm{up}} - 0) \frac{1}{\xi R_0} \left[\frac{1 + s\lambda_2}{1 + s\lambda_1} - \xi\right]\,. \tag{II.66}$$

In summary, one can use the definition of the impedance ($U = PZ^{-1}$) to write:

$$U = \frac{P_{\mathrm{up}} - P_{\mathrm{down}}}{Z_{\mathrm{lo},1}} = \frac{P_{\mathrm{up}} - 0}{Z_{\mathrm{lo},1} + Z_{\mathrm{lo},2}}\,, \tag{II.67}$$

where $Z_{\mathrm{lo},1}$ is the impedance of the load and $Z_{\mathrm{lo},2}$ is the impedance describing all the components downstream of the load:

$$Z_{\mathrm{lo},1} = \xi R_0 \frac{1 + s\lambda_1}{1 + s\lambda_2}, \quad Z_{\mathrm{lo},2} = \xi^2 R_0 \frac{(1 + s\lambda_1)^2}{(1 + s\lambda_2)^2 - \xi(1 + s\lambda_1)(1 + s\lambda_2)}\,. \tag{II.68}$$

Finally, R_0 is evaluated from Eq. II.62 for $s \to 0$, such that

$$R_0 = \frac{R_{\mathrm{sf}}}{\xi}\,. \tag{II.69}$$

The load impedance $Z_{\mathrm{lo},1}$ from Eqs. II.67 and II.68 equals the steady-flow resistance R_{sf} where there is no oscillation and $s = 0$. Note that $P_{\mathrm{up}} - 0$ is the pressure drop across the load valve *and* the whole working cylinder including the gas spring. Thus, the sum $Z_{\mathrm{lo},1} + Z_{\mathrm{lo},2}$ accounts for the RLC components representing the valve and everything downstream of it (predominantly the working cylinder.) The two impedances are placed

in series in the electronic circuit and replace the working cylinder components (subscript 'w' and 'g', compare loaded and load-free electronic circuits Figs. II.14 and II.15).

II.5 ERPE Configuration and Operation

II.5.1 Physical Representation of the ERPE

By applying the aforementioned submodels of components to the BIC prototype we can derive a new, simpler engine which we call the ERPE. The following (non-linear) characteristics of the prototype cannot be modelled with the linear approach:

- The slide valve which opens and closes depending on the position of the piston
- Flow through different connection tubes depending on flow direction
- Work only being produced during a half-cycle
- The free piston not being fully immersed in water
- The free piston and flow sometimes moving in opposite directions
- A non-linear profile of the temperature or heat flux along the height of the heat exchangers

All of the above aspects are non-linear phenomena and therefore cannot be captured with a linear model. Therefore, the ERPE engine (physical reprensation) will not include them. A schematic of the ERPE is shown in Fig. II.13. The main differences between the ERPE and the BIC prototype are the missing slide valve and a single (instead of two) connection tube between the two cylinders. By replacing the individual ERPE components with their electric counterparts and connecting the electric components as they are connected in the physical engine, we obtain the electronic circuits of the ERPE shown in Figs. II.14 (no load) and II.15 (with load). The coloured boxes denote different components in the physical engine. The two capacitors which are connected to ground (subscripts 'g' and 'v', red and light blue borders) are the argon and vapour gas-springs. The resistance and inductance with subscript 'c' inside the yellow box represent a single horizontal connection tube between displacer and working cylinder. The components with the subscript 'l' and 'p' within the dark blue borders represent the solid free piston and leakage flow, while the adjacent components in the orange box (subscript 'b') represent

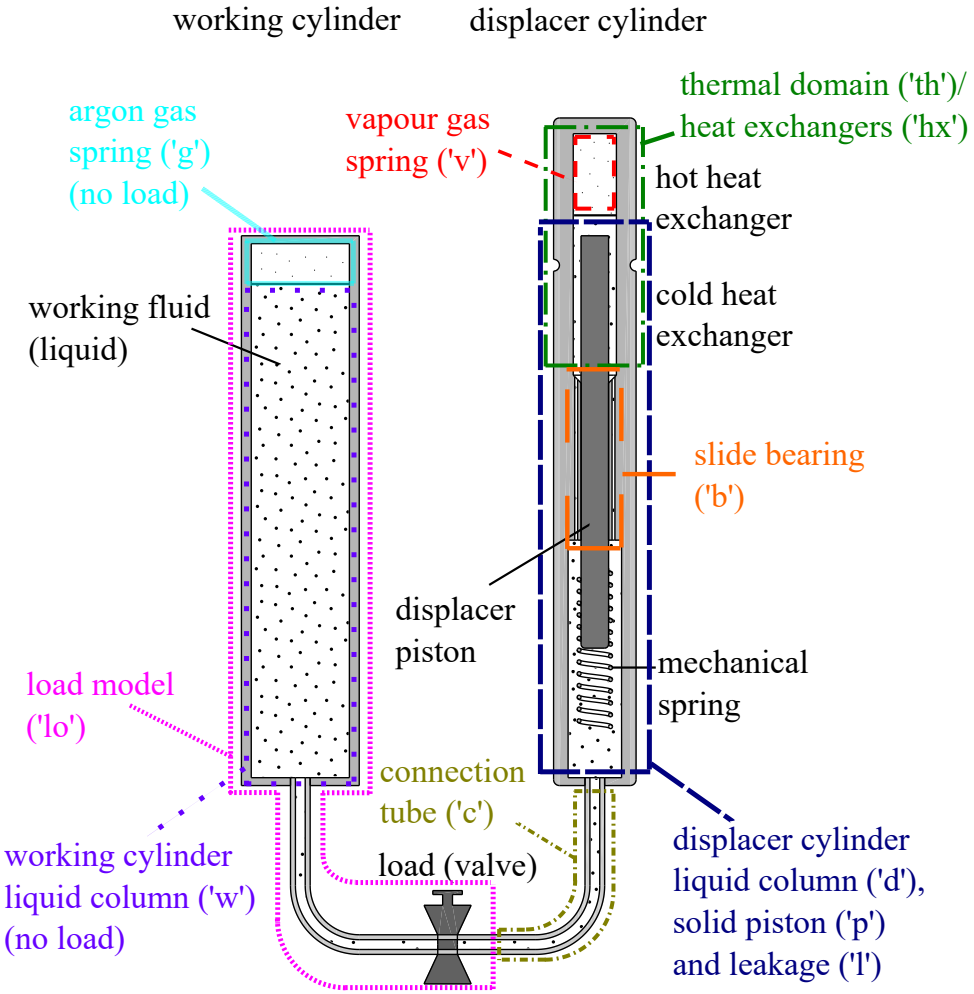


Figure II.13: Schematic description of the ERPE. The dashed and coloured borders denote different components or domains of the engine; these correspond to the highlighted sections in the electronic circuits of Figs. II.14 and II.15. The main physical differences between the ERPE and BIC prototype from Fig. II.4 are the missing slide valve and a single connection tube between the two cylinder.

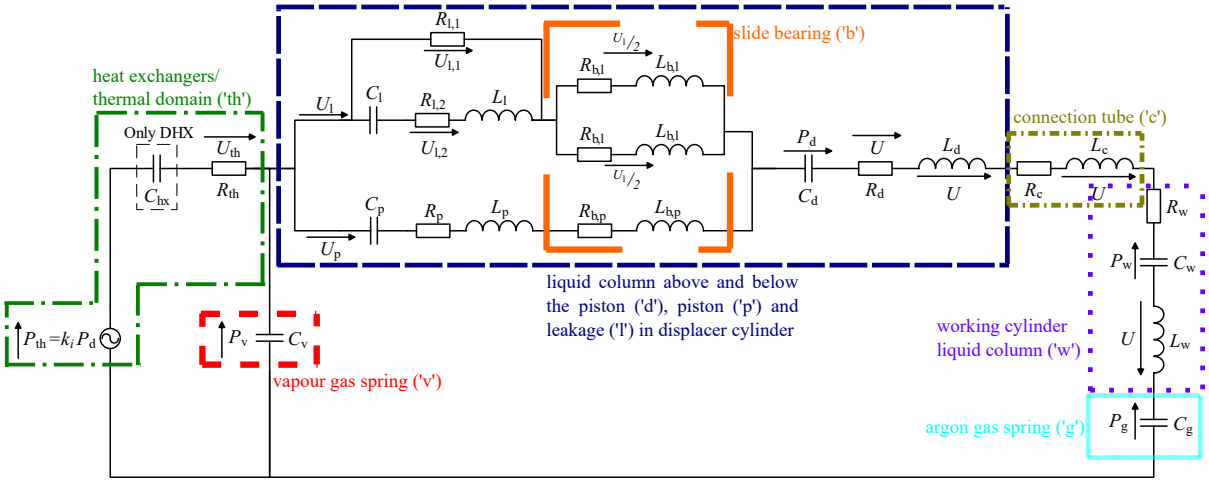


Figure II.14: Electronic circuit model of the ERPE with no load. The colours of the borders correspond to the borders in the schematic of the physical representation of the engine in Fig. II.13.

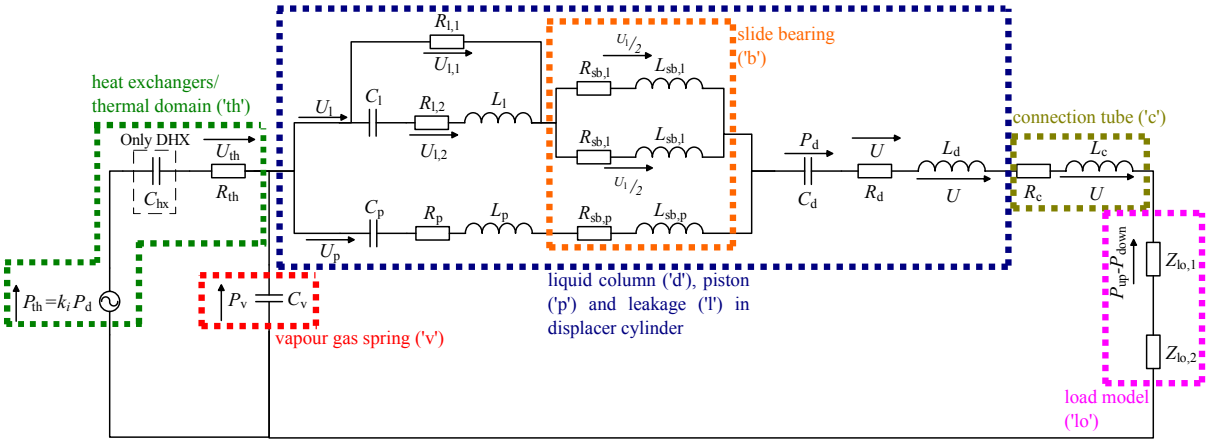


Figure II.15: Electronic circuit model of the ERPE with the BIC prototype load (subscript 'lo' and magenta coloured border). As with the load-free version from Fig. II.14, the colours of the borders correspond to the borders in the schematic of the physical representation of the engine in Fig. II.13.

a slide bearing. The remaining three components in the dark blue box with subscript 'd' are the sum of the components of the liquid columns above and below solid pistons.

Since the EPRE is an oscillator, understanding the processes undergone in one reciprocating cycle fully explains its operation. Assuming a cycle to start at the top dead center (TDC) of the solid piston, the liquid-vapour interface is in contact with the hot heat exchanger (HHX) such that heat is added to the working fluid. The working fluid evaporates, generating vapour and leading to a pressure increase in the vapour gas spring. This pressure drives a downward acceleration of the liquid level and of the displacer piston which – due to their inertia – overshoot their equilibrium positions located halfway between the two heat exchangers. The vapour-liquid interface and the displacer piston are assumed in this model to always move in the same direction albeit not necessarily at the same speeds. Nevertheless, the displacer piston is assumed to be always completely immersed in water. Water flows through the load in the connection tube – thereby dissipating work – into the working cylinder elevating its water level and compressing the gas spring. A hydrostatic pressure difference is created between the water levels of the two cylinders. Gradually, the cold heat exchanger (CHX) surfaces are exposed to the hot vapour, which begins to condense. The condensation process leads to a decrease in pressure in the vapour region. The increasing hydrostatic pressure difference between the displacer and working cylinders, the increasing compression of the mechanical and gas springs, and the decreasing pressure in the vapour region exert restoring or suction forces on the piston and the water column directed oppositely to the piston movement. However, for a limited time, the piston and water column continue their downward displacement due to their momentum, while gradually decreasing in speed.

As the displacer piston reaches bottom dead centre (BDC), the restoring hydrostatic, spring and gas compressibility forces gradually lead to a reversal of the piston and flow direction. The water level and the displacer piston accelerate upwards and overshoot their equilibrium positions due to their inertia. Once again, the hydrostatic pressure difference and the gas and mechanical springs create restoring forces; this time, in the opposite direction, thus gradually decelerating the rising piston and water level until they reach TDC where their movement is reversed. In this manner, a full cycle is completed. The BIC prototype was self-starting. By just turning on the heat input, the engine would slowly start oscillating. Therefore, it is safe to assume that the ERPE would also be self-starting.

To define the values of the components in the ERPE circuit and thereby develop a physical ERPE device, the geometric parameters and thermodynamic fluid properties

from the TFO engine prototype are adopted to the new concept [45]. Additionally, we use experimental data of pressure variations provided by BIC of their prototype as indicative values to assess if the present model predictions are realistic.

II.5.2 Solution

The electronic circuits are ultimately a set of differential equations relating pressure and volumetric flow-rate. The parameter definitions and the nominal values of each electrical model parameter (for the engine with and without a load) can be found in Table II.1.

The advantage of writing the differential equations as an electronic circuit is that one can use Kirchhoff's laws to determine a forward path transfer function $G(s)$. The input signal is the heat exchanger temperature difference represented by the pressure P_{th} while the output signal is the hydrostatic pressure in the displacer cylinder P_{d}. To close and solve the system, a feedback relation is required, namely $P_{\mathrm{th}} = k_i P_{\mathrm{d}}$ (see Fig. II.16). For the LTP model (Section II.4.8), the feedback gain $k_i = k_{\mathrm{LTP}}$ can be derived if we bear in mind that

$$P_{\mathrm{d}} = \rho g y \,, \tag{II.70}$$

and

$$P_{\mathrm{th}} = \frac{T_{\mathrm{sat}}(y)}{(\mathrm{d}T/\mathrm{d}P)_{\mathrm{sat}}} \,, \tag{II.71}$$

where y is the position or height of the liquid vapour interface and $T_{\mathrm{sat}}(y)$ is the temperature of the liquid vapour interface at y. Thus, we can write the gain as

$$k_i = k_{\mathrm{LTP}} = \frac{P_{\mathrm{th}}}{P_{\mathrm{d}}} = \frac{\mathrm{d}T_{\mathrm{hx}}/\mathrm{d}y}{\rho g (\mathrm{d}T/\mathrm{d}P)_{\mathrm{sat}}} \,. \tag{II.72}$$

For the LTP the temperature gradient at the heat exchangers is constant, such that $T_{\mathrm{sat}}/y = \mathrm{d}T_{\mathrm{hx}}/\mathrm{d}y$.

To derive the feedback gain k_{DHX} for the DHX model we begin with Eq. II.50. The entropy flow to and from the working fluid can be expressed as

$$\dot{S_{\mathrm{th}}} = \frac{\dot{Q}}{T_0} = \rho_{\mathrm{v},0} \Delta s_{\mathrm{fg}} U_{\mathrm{th}} \,, \tag{II.73}$$

$$\implies U_{\mathrm{th}} = \frac{\dot{Q}}{T_0 \rho_{\mathrm{v},0} \Delta s_{\mathrm{fg}}} \,, \tag{II.74}$$

Table II.1: Electrical analogies for the ERPE model. RLC relations and their respective nominal values at a mean pressure of 11.8 bar.

	Thermal-fluid effect	Parameter expression	Nominal Value
Resistances [kg/m^{4}s]	Thermal resistance	$R_{\mathrm{th}} = {\rho_{\mathrm{v},0}\Delta s_{\mathrm{fg}}T_0}/{hA_s(\mathrm{d}T/\mathrm{d}P)_{\mathrm{sat}}}$	2.08×10^{11}
	Displacer cylinder flow resistance	$R_{\mathrm{d}} = {128\mu}/{\pi}\left({l_{\mathrm{d,a}}}/{d_{\mathrm{d,a}}^4} + {l_{\mathrm{d,b}}}/{d_{\mathrm{d,b}}^4}\right)$	8.36×10^{2}
	Working cylinder flow resistance	$R_{\mathrm{w}} = {128\mu l_{\mathrm{w}}}/{\pi d_{\mathrm{w}}^4}$	6.08×10^{3}
	Connection tube flow resistance	$R_{\mathrm{c}} = {128\mu l_{\mathrm{c}}}/{\pi d_{\mathrm{c}}^4}$	1.11×10^{6}
	Solid piston resistance	$R_{\mathrm{p}} = {64h_{\mathrm{p}}\mu}/{\pi d_{\mathrm{p}}^2 c_1}$	1.23×10^{5}
	1st leakage flow resistance	$R_{\mathrm{l},1} = {128c_2h_{\mathrm{p}}\mu}/{\pi c_1 c_3}$	6.29×10^{7}
	2nd leakage flow resistance	$R_{\mathrm{l},2} = {128c_2h_{\mathrm{p}}\mu}/{\pi c_1(c_1 - 2c_2{d_{\mathrm{p}}}^2)}$	1.37×10^{6}
	Slide bearing piston resistance	$R_{\mathrm{b,p}} = {16\mu l_{\mathrm{b}}}/{\pi^2\delta d_{\mathrm{p}}^3}$	4.49×10^{4}
	Slide bearing flow resistance	$R_{\mathrm{b,l}} = {128\mu l_{\mathrm{b}}}/{\pi d_{\mathrm{b,l}}^4}$	2.44×10^{6}
Inductances [kg/m^4]	Displacer cylinder flow inertia	$L_{\mathrm{d}} = \rho_{\mathrm{wf}} l_{\mathrm{d,a}}\left(\frac{2}{A_{\mathrm{d,a}}} - \frac{Z_{\mathrm{pl}}}{A_{\mathrm{p}}Z_{\mathrm{p}}} - \frac{Z_{\mathrm{p}}}{A_{\mathrm{l}}Z_{\mathrm{l}}}\right) + +\rho_{\mathrm{wf}} l_{\mathrm{d,b}}\left(\frac{Z_{\mathrm{pl}}}{A_{\mathrm{p}}Z_{\mathrm{p}}} + \frac{Z_{\mathrm{pl}}}{A_{\mathrm{l}}Z_{\mathrm{l}}} - \frac{1}{A_{\mathrm{d,b}}}\right)$	1.12×10^{6}
	Working cylinder flow inertia	$L_{\mathrm{w}} = {4\rho_{\mathrm{wf}} l_{\mathrm{w}}}/{\pi d_{\mathrm{w}}^2}$	3.35×10^{5}
	Connection tube flow intertia	$L_{\mathrm{c}} = {4\rho_{\mathrm{wf}} l_{\mathrm{c}}}/{\pi d_{\mathrm{c}}^2}$	3.18×10^{8}
	Leakage flow inertia	$L_{\mathrm{l}} = {64c_2^2 m_{\mathrm{p}}}/{\pi^2 c_1(c_1 - 2c_2 d_{\mathrm{p}}^2)}$	7.11×10^{7}
	Piston inertia	$L_{\mathrm{p}} = {32c_2 m_{\mathrm{p}}}/{\pi^2 {d_{\mathrm{p}}}^2 c_1}$	7.44×10^{6}
	Slide bearing piston inertia	$L_{\mathrm{b,p}} = {4\rho_{\mathrm{ss}} l_{\mathrm{b}}}/{\pi {d_{\mathrm{p}}}^2}$	2.44×10^{6}
	Slide bearing flow inertia	$L_{\mathrm{b,l}} = {4\rho l_{\mathrm{sb}}}/{\pi d_{\mathrm{b,l}}^2}$	3.17×10^{7}
Capacitances [m^{4}s^2/kg]	Vapour gas spring capacitance	$C_{\mathrm{v}} = {V_{\mathrm{v}}}/{\gamma_{\mathrm{v}} P_{\mathrm{v,eq}}}$	2.07×10^{-11}
	Displacer hydrostatic capacitance	$C_{\mathrm{d}} = {\pi d_{\mathrm{d}}^2}/{4\rho_{\mathrm{wf}} g}$	2.60×10^{-8}
	Working hydrostatic capacitance	$C_{\mathrm{w}} = {\pi d_{\mathrm{w}}^2}/{4\rho_{\mathrm{wf}} g}$	7.31×10^{-8}
	Gas spring capacitance	$C_{\mathrm{g}} = {V_{\mathrm{g}}}/{\gamma_{\mathrm{g}} P_{\mathrm{g,eq}}}$	1.41×10^{-12}
	Piston capacitance	$C_{\mathrm{p}} = {\pi^2 d_{\mathrm{p}}^2 c_1}/{32k_{\mathrm{ms}}c_2}$	3.62×10^{-11}
	Leakage capacitance	$C_{\mathrm{l}} = {\pi^2 c_1(c_1 - c_2 d_{\mathrm{p}}^2)}/{64c_2^2 k_{\mathrm{ms}}}$	1.32×10^{-7}
	Heat exchanger capacitance	$C_{\mathrm{hx}} = {m_{\mathrm{hx}} c_{\mathrm{hx}}(\mathrm{d}T/\mathrm{d}P)_{\mathrm{sat}}}/{\rho_{\mathrm{v},0}\Delta s_{\mathrm{fg}} T_0}$	1.10×10^{-12}

where $\rho_{\mathrm{v},0}$ is the time-averaged density of the vapour. With Thevenin's theorem for AC circuits [51] we can find the equivalent current for the voltage source P_{th}, where $P_{\mathrm{th}} = U_{\mathrm{th}} Z_{\mathrm{th}}$ and $Z_{\mathrm{th}} = 1/sC_{\mathrm{hx}}$. Thus, the feedback gain can be expressed as:

$$k_i = \frac{1}{s} k_{\mathrm{DHX}} = \frac{P_{\mathrm{th}}}{P_{\mathrm{d}}} = \frac{1}{s} \frac{\mathrm{d}\dot{Q}/\mathrm{d}y}{\rho_{\mathrm{wf}} g \rho_{\mathrm{v},0} \Delta s_{\mathrm{fg}} T_0 C_{\mathrm{hx}}} \,, \tag{II.75}$$

where ρ_{wf} is the density of the liquid working fluid. For the DHX, the heat flux gradient is constant such that $\dot{Q}/y = \mathrm{d}\dot{Q}/\mathrm{d}y$.

The gain k is proportional to the constant temperature gradient $\mathrm{d}T_{\mathrm{hx}}/\mathrm{d}y$ imposed on the heat exchanger walls in the LTP model, while in the DHX model the gain is proportional to the constant heat-input rate $\mathrm{d}\dot{Q}_{\mathrm{hx}}/\mathrm{d}y$ [27, 30]. A sustained oscillation of the engine can be observed at marginal stability of the closed-loop transfer function:

$$C(s) = \frac{G(s)}{1 - k_i G(s)} \,. \tag{II.76}$$

The closed-loop representation of the ERPE is shown in Fig. II.16. The closed-loop $C(s)$ transfer function has seven poles: one real and three complex conjugate. Marginal stability occurs when one conjugate complex pole pair of the closed-loop transfer function $C(s)$ lies on the imaginary axis and all other conjugate pairs have negative real parts [26–28, 30, 32, 46]. A mathematical solver using an iterative method is used to calculate the feedback gain necessary for marginal stability. An elegant alternative to that is the Routh-Hurwitz Criterion. A whole row in Routh's table must equal zero for marginal stability [52]. It is recommended for future models that this method be used in place of the iterative method as it is much quicker and more reliable. The frequency of the marginal poles is the oscillation frequency of the engine. The values of the temperature gradient $\mathrm{d}T_{\mathrm{hx}}/\mathrm{d}y$ and the heat input rate gradient $\mathrm{d}\dot{Q}/\mathrm{d}y$ are estimated from the gains, the working fluid properties – listed in Table II.2, and the components R_{th} and C_{hx}.

The ERPE model lacks an external input to the engine. Instead, the input to the engine (defined here as the heat-source/sink temperature) is set by an internal feedback coupling (connection) to the engine's output (defined as the oscillation of the liquid in the displacer cylinder). Specifically, the heat-source temperature experienced by the working fluid as it changes phase is set by the vertical position of the liquid-vapour interface in the displacer cylinder. Owing to this internal feedback connection and lack of an external input, the linear ERPE model can only result in sinusoidal oscillations of all thermodynamic properties (P, V, T) over the cycle and also of the volumetric flow-rates

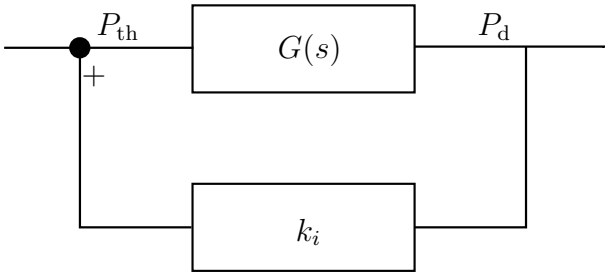


Figure II.16: Closed-loop representation of the ERPE where $G(s)$ is the modelled forward-loop transfer function between P_{th} and P_{d} and k_i is the feedback gain where i can be either LTP or DHX.

Table II.2: Working fluid properties for saturated water (working fluid) at a mean pressure of 18.1 bar.

ρ_{wf}	Working fluid density	9.95×10^2 kg/m^3
ρ_{v}	Vapour density	9.13 kg/m^3
μ	Dynamic viscosity, water	7.19×10^{-4} kg/s·m
γ_{v}	Ratio of specific heats, vapour	1.46
Δs_{fg}	Entropy of vaporization	3.97×10^3 J/kg·K
$\left(\frac{\mathrm{d}T}{\mathrm{d}P}\right)_{\mathrm{sat}}$	Change in saturation temperature with pressure in two-phase region	$2.69{\times}10^{-5}$ K/Pa

throughout the engine. Oscillations which contain more than one frequency component can only be attained by non-linearities within the device itself [28].

The average power produced or dissipated at a component x is expressed with

$$\dot{W}_{\mathrm{av}} \;=\; \overline{P_x(t)U_x(t)} = 1/2|P_x|^2/|Z_x|\cos\theta = 1/2|U_x|^2|Z_x|\cos\theta\,, \tag{II.77}$$

where $|P|$ and $|U|$ are the amplitudes of the pressure and flow-rate at the component x, Z_x is the impedance of the component x, and θ is the phase difference between the pressure and flow-rate. Bearing in mind that $\mathrm{Re}(Z) = |Z|\cos\theta$, the exergy efficiency can be calculated with the following formula [32, 46]:

$$\eta_{\mathrm{ex}} = \frac{\overline{P_{\mathrm{lo},1}(t)U(t)}}{T_{\mathrm{hx}}(t)\dot{S}_{\mathrm{hx}}(t)} = \frac{\overline{P_{\mathrm{lo},1}(t)U(t)}}{\overline{P_{\mathrm{th}}(t)U_{\mathrm{th}}(t)}} = \left|\frac{P_{\mathrm{lo},1}}{P_{\mathrm{th}}}\right|^2 \frac{\mathrm{Re}(1/Z_{\mathrm{lo},1})}{\mathrm{Re}(1/Z_{\mathrm{tot}})}\,. \tag{II.78}$$

$P_{\mathrm{lo},1}$ is the pressure at the load valve with the impedance $Z_{\mathrm{lo},1}$ and Z_{tot} is the combined impedance of all circuit components.

Chapter III

Results and Discussion of the Linear ERPE Model

In this chapter the results from the ERPE model are discussed. The first section compares the calculations with measurement values from the BIC prototype to assess the reliability of the linear model. The two different sub-models of the heat exchangers (LTP and DHX) are compared. Subsequently, a parametric study is performed in which different component characteristics are varied to examine their influence on the engine's performance indicators. Thermodynamic cycle diagrams, specifically pressure-displacement and temperature-entropy diagrams, are investigated to obtain a deeper understanding as to what influences the engine performance.

III.1 Comparison of Model and Experiments

The initial step is to draw a qualitative comparison between results from the ERPE circuit model and available experimental data from the similar, but not identical, BIC prototype. The BIC prototype differs from the ERPE in that: (1) it possesses a valve in the displacer cylinder which opens depending on the piston position; (2) it can only produce work during one half-cycle owing to the load arrangement; and (3) the piston does not necessarily always remain fully immersed underneath the water level inside the displacer cylinder. These factors cannot be added to the present ERPE circuit model because they are inherently and strongly nonlinear and thus cannot be modelled linearly with acceptable accuracy. Both engines are nonetheless similar enough in all other aspects

so that the calculations should lie in the same order of magnitude and reveal the same underlying trends observed in the measurements.

The BIC prototype was tested under eight different operating conditions, five of which had a load and three of which did not have a load. The operating conditions are summarized in Table III.1. Temperature and heat transfer measurements were not carried out along the walls of the heat exchangers. Therefore, no precise experimental values exist of the temperature gradient $\mathrm{d}T_{\mathrm{hx}}/\mathrm{d}y$ or the heat-input rate gradient $\mathrm{d}\dot{Q}_{\mathrm{hx}}/\mathrm{d}y$ applied onto the internal heat exchanger walls. However, the temperature gradient is still required as input for the LTP model, while the heat-input rate gradient is input for the DHX model. One is able to approximate their values based on the measured flow rates of air and fuel and the measured temperatures at the external wall of the heat exchangers. It is known that 465 W of thermal energy is transferred to the external wall of the heat exchanger in the three cases operated without a load, while in the remaining five cases with a load 270 W is transferred to the heat exchanger. The measured wall temperature at the top of the hot heat exchanger is approximately 600 °C and approximately 20–40 °C at the bottom of the cold heat exchanger. A linear profile is an acceptable first approximation across a portion of the heat exchanger height centred around the equilibrium position; it is assumed to be between 30 and 150 mm and not the 230 mm of the entire heat exchanger. The average oscillation height in several BIC prototype tests was around 30 mm. The results in the gradient values are listed in Table III.1.

Additionally, modelling predictions of the frequency f, temperature gradient $\mathrm{d}T_{\mathrm{hx}}/\mathrm{d}y$ for the LTP model, heat input rate gradient $\mathrm{d}\dot{Q}_{\mathrm{hx}}/\mathrm{d}y$ for the DHX model, and exergy efficiency η_{ex} are also listed in Table III.1. Considering initially the load-free case, the DHX model predicts frequencies which are two or three times higher than the direct experimental observations on the BIC prototype. This discrepancy is considered reasonable given the first-order approximation model of the ERPE and the differences between the ERPE model and the actual BIC arrangement on which the experiments were performed. The LTP model overestimates the frequency to a greater extent, while both models reasonably predict the temperature or heat-input rate gradient in the measurement range (40–200 K/cm and 60–300 W/cm) from Table III.1. Thus, the DHX model is considered a more accurate representation of the physical device in the load-free case compared to the LTP model, indicating that the heat exchanger walls are thermally dynamic.

Table III.1 also lists the remaining five cases where load is present at different pressures. The DHX and LTP models predict similar operational oscillation frequencies which are too high, especially at low pressures. Possibly, the behaviour of the non-linear valve

Table III.1: Left: operating conditions, experimentally measured frequency and empirically approximated gradients of BIC prototype. Right: calculated frequencies and temperature/heat-input rate gradients of the LTP and DHX model.

BIC prototype operating conditions		**BIC prototype measurements**			**LTP model**			**DHX model**		
	Mean pressure [bar]	f [Hz]	$\mathrm{d}T_{\mathrm{hx}}/\mathrm{d}y$ [K/cm]	$\mathrm{d}\dot{Q}_{\mathrm{hx}}/\mathrm{d}y$ [W/cm]	f [Hz]	$\mathrm{d}T_{\mathrm{hx}}/\mathrm{d}y$ [K/cm]	η_{ex} [%]	f [Hz]	$\mathrm{d}\dot{Q}_{\mathrm{hx}}/\mathrm{d}y$ [W/cm]	η_{ex} [%]
no load	3.6	0.6	≈40–200	≈60–300	6.5	192	-	1.1	190	-
	5.5	0.4			7.3	198	-	1.3	206	-
	8.2	0.6			8.5	199	-	1.6	289	-
load	9.4	0.02	≈40–200	≈35–180	1.7	122	1.5	2.0	167	0.3
	11.8	0.16			2.3	115	3.3	2.5	123	1.1
	15.8	0.24			2.5	75	7.0	2.7	139	1.6
	18.1	0.29			2.7	168	2.4	2.9	147	2.0
	22	0.2			2.2	153	1.5	2.5	160	0.01

load arrangement in the prototype is not properly captured in the linear models. The LTP and DHX models both, however, do capture the trend of the operation frequency increasing with the mean pressure before decreasing again at the highest pressure of 22 bar. Moreover, as with the load-free runs, the temperature and heat input rate gradients are within the measured ranges (40–200 K/cm or 35–180 W/cm) for both models. On the other hand, the models differ significantly in their estimations of the exergetic efficiency, with the DHX predicting lower values. The DHX predicts efficiencies between 0.01 % and 2 %, while the LTP efficiencies are between 1.5 % and 7 %. Nevertheless, both models predict high efficiencies at intermediate pressures (15.8 bar) while the lowest and highest pressures (9.4 bar and 22 bar) resulted in low efficiencies. It must be noted, however, that we do not have measurements which can provide experimental efficiency values for comparison. In summary, the DHX model is regarded in this study to be a reasonable first description of what would be expectd from a heat exchanger arrangement in a possible physical representation of an ERPE.

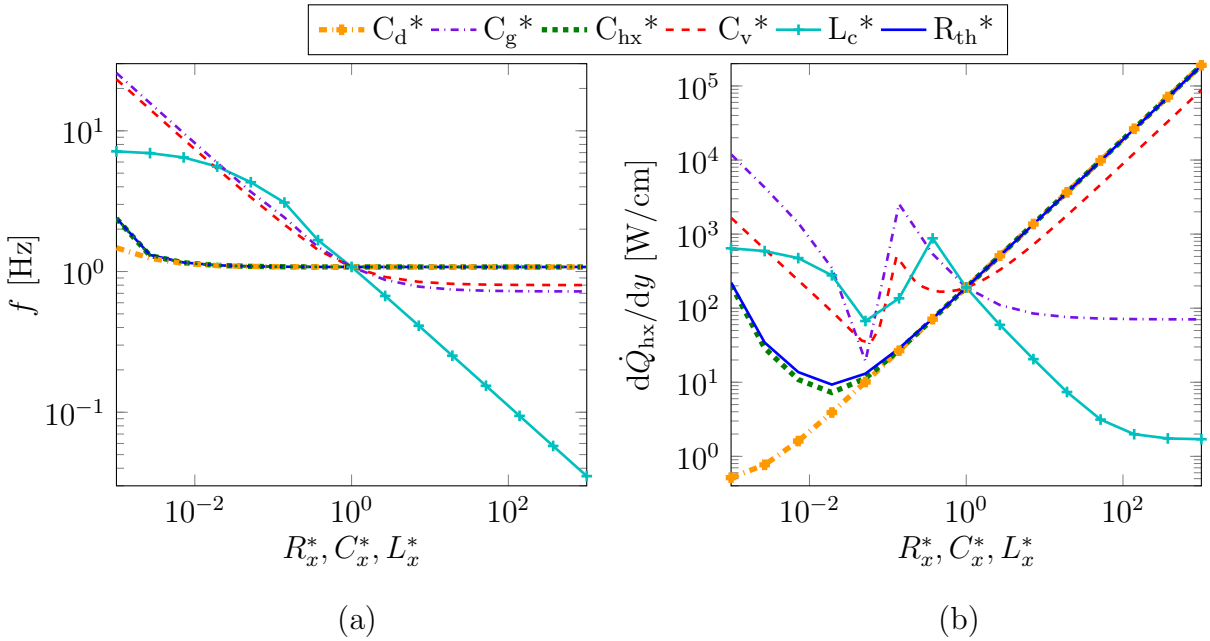
III.2 Parametric Study

In this section, the influence of the various electrical ERPE model parameters (RLC) on the: (a) operational/oscillation frequency f, (b) exergy efficiency η_{ex} (if load present), (c) heat-input rate gradient $\mathrm{d}\dot{Q}_{\mathrm{hx}}/\mathrm{d}y$, and (d) product of exergy efficiency and frequency $\eta_{\mathrm{ex}} \cdot f$ (if load is present) are examined for two engine configurations: (a) a load-free configuration at a time-averaged mean pressure of 3.6 bar that matches the lowest no-load pressure case in Table III.1, and (b) an engine configuration featuring a load with an 18.1 bar mean pressure that matches the highest (DHX) efficiency load case in Table III.1. The product of exergy efficiency and frequency $\eta_{\mathrm{ex}} \cdot f$ is proportional to the hydraulic power output per unit heat input, and therefore high values for this product are favourable. Similarly, low heat-input rates or temperature gradients are also favourable because they are measures of the thermal input/temperature difference required to sustain the operation of the device. Each RLC parameter considered here is directly linked to geometric, thermodynamic/thermophysical, or transport properties of the ERPE that result from solid materials or fluid selection decisions and the operational characteristics of the engine. The parameters are defined in Chapter II and Table II.1.

Figures III.2 and III.1 show the results of this parametric investigation, where only influential parameters are shown while parameters with negligible influence have been omitted. The RLC parameters are normalized (e.g. R^*_{th}) in these figures. The varied

Table III.2: Nominal values and investigated ranges for the parameters in Table II.1

Electrical parameter	Nominal value	Investigated range	Units
R_{th}	2.08×10^{11}	2.08×10^{8} – 2.08×10^{14}	kg m^{-4} s^{-1}
R_{d}	8.36×10^{2}	8.36×10^{-1} – 8.36×10^{5}	kg m^{-4} s^{-1}
R_{w}	6.08×10^{3}	6.08×10^{0} – 6.08×10^{6}	kg m^{-4} s^{-1}
R_{c}	1.11×10^{6}	1.11×10^{3} – 1.11×10^{9}	kg m^{-4} s^{-1}
R_{p}	1.23×10^{5}	1.23×10^{2} – 1.23×10^{8}	kg m^{-4} s^{-1}
$R_{\mathrm{l,1}}$	6.29×10^{7}	6.29×10^{4} – 6.29×10^{10}	kg m^{-4} s^{-1}
$R_{\mathrm{l,2}}$	1.37×10^{6}	1.37×10^{3} – 1.37×10^{9}	kg m^{-4} s^{-1}
$R_{\mathrm{b,p}}$	4.49×10^{4}	4.49×10^{1} – 4.49×10^{7}	kg m^{-4} s^{-1}
$R_{\mathrm{b,l}}$	2.44×10^{6}	2.44×10^{3} – 2.44×10^{9}	kg m^{-4} s^{-1}
L_{d}	1.12×10^{6}	1.12×10^{3} – 1.12×10^{9}	kg m^{-4}
L_{w}	3.35×10^{5}	3.35×10^{2} – 3.35×10^{8}	kg m^{-4}
L_{c}	3.18×10^{8}	3.18×10^{5} – 3.18×10^{11}	kg m^{-4}
L_{l}	7.11×10^{7}	7.11×10^{4} – 7.11×10^{10}	kg m^{-4}
L_{p}	7.44×10^{6}	7.44×10^{3} – 7.44×10^{9}	kg m^{-4}
$L_{\mathrm{b,p}}$	2.44×10^{6}	2.44×10^{3} – 2.44×10^{9}	kg m^{-4}
$L_{\mathrm{b,l}}$	3.17×10^{7}	3.17×10^{4} – $3.17 \times 10^{1}0$	kg m^{-4}
C_{v}	2.07×10^{-11}	2.07×10^{-14} – 2.07×10^{-8}	m^{4} s^{2} kg^{-1}
C_{d}	2.60×10^{-8}	2.60×10^{-11} – 2.60×10^{-5}	m^{4} s^{2} kg^{-1}
C_{w}	7.31×10^{-8}	7.31×10^{-11} – 7.31×10^{-5}	m^{4} s^{2} kg^{-1}
C_{g}	1.41×10^{-12}	1.41×10^{-15} – 1.41×10^{-9}	m^{4} s^{2} kg^{-1}
C_{p}	3.62×10^{-11}	3.62×10^{-14} – 3.62×10^{-8}	m^{4} s^{2} kg^{-1}
C_{l}	1.32×10^{-7}	1.32×10^{-10} – 1.32×10^{-4}	m^{4} s^{2} kg^{-1}
C_{hx}	1.10×10^{-12}	1.10×10^{-15} – 1.10×10^{-9}	m^{4} s^{2} kg^{-1}



(a) (b)

Figure III.1: Variations in the (a) oscillation frequency f and (b) heat-input rate gradient $\mathrm{d}\dot{Q}_{\mathrm{hx}}/\mathrm{d}y$ in the load-free engine at a mean pressure of 3.6 bar calculated with the DHX model as functions of the normalized parameters listed in the legend. Parameters not presented here have low or negligible influence on the frequency or heat-input gradient.

parameters (e.g. R_{th}) are divided by their respective nominal values (e.g. $R_{\mathrm{th,nom}}$). The nominal values are based on pre-defined geometric, thermodynamic/thermophysical and transport properties taken from the BIC prototype (Table II.1) in order to give the model a physically realisable starting point for this exercise. The considered variation range for each parametyer is between 10^{-3} and 10^{3} times the nominal starting value.

III.2.1 Load-Free Engine

The operational frequency of a load-free ERPE is shown in Fig. III.1(a). The capacitance of the gas spring in the working cylinder C_{g}, the capacitance of the vapour-phase gas spring at the top of the displacer cylinder C_{v} and the inductance of the liquid in the connection tube L_{c} (see Fig. II.13) are the three most influential components. All remaining parameters, including the ones shown in the plot (C_{d}, C_{hx}, R_{th}), have very little influence on the frequency of the engine. The largest magnitude of all the inductances is exhibited by L_{c} while the two gas-spring capacitances C_{c} and C_{g} have the smallest magnitudes of all the capacitances. Dominant capacitances have small values because the corresponding impedance is given by $Z = 1/sC$. Hence, variations in these parameters

have the greatest influence on the frequency of the engine as a whole. Table II.1 suggests measures that can be taken to change parameters in a desired direction. The two gas-spring capacitances must be reduced as much as possible to maximize frequency. This can be achieved by decreasing the time-mean dead volumes in these parts of the device. To reduce the connection tube inductance, the cross-sectional area of the connection tube must be increased and/or length of the tube must be shortened.

Figure III.1(b) shows the heat-input rate gradient $\mathrm{d}\dot{Q}_{\mathrm{hx}}/\mathrm{d}y$ as a function of: the hydrostatic capacitance in the displacer cylinder C_{d}, the working cylinder gas-spring C_{g}, the heat exchanger capacitance C_{hx}, the vapour gas-spring capacitance C_{v}, the connection tube inductance L_{c}, and the thermal resistance R_{th}. Decreasing all of these parameters, with the exception of C_{d} and L_{d}, below the nominal design values by approximately one order of magnitude, leads to a reduction in the required heat input. The thermal-domain parameters, i.e. the heat exchanger capacitance C_{hx} and the thermal resistance R_{th}, lead to minimal heat-input at slightly lower than nominal values. Increasing the heat-transfer area (e.g. through the addition of fins, etc.) and the heat transfer coefficient of phase change reduces the thermal resistance R_{th}, because it is inversely proportional to them. Additionally, the heat-exchanger capacitance C_{hx} depends proportionally on the heat capacity c_{hx} of the heat exchanger material and mass m_{hx} of the portion of the heat exchangers which interacts thermally with the working fluid. These can be reduced by using a heat exchanger material which has a lower specific heat capacity.

The hydrostatic capacitance in the displacer cylinder C_{d} and the inductance of the liquid in the connection tube L_{c} are the two most dominant parameters. The necessary heat input $\mathrm{d}\dot{Q}/\mathrm{d}y$ increases linearly with C_{d} in the log-log plot of Fig. III.1(b). The inductance L_{c} attains low heat inputs when increased by at least a factor of ~ 100 from its nominal value. Low heat inputs can be achieved in practice by a reduction in the cross-sectional area of the displacer cylinder, which decreases the quantity of working fluid per unit height of the heat exchanger (requiring less thermal energy for evaporation per unit height) and therefore reduces the corresponding hydrostatic capacitance C_{d}. The inductance L_{c} can be increased, for instance, by lengthening the connection tube or using a smaller tube diameter.

In Fig. III.1(b), one can also see sharp inflection points or discontinuities in the trends of C_{g}, C_{v}, and L_{c}. As explained in Section II.5.2, the closed-loop transfer function has seven poles: one real and three complex conjugate pairs. One of these pairs is purely imaginary while the others have negative real parts for marginal stability. The dominant pair of poles switches to a different pair at the discontinuities which leads to a sudden

change in the oscillating frequency and gain, and hence the heat-transfer rate gradient. Discontinuities have also been observed and discussed in linearized modelling studies of the NIFTE [28, 30].

III.2.2 Loaded Engine

A similar parametric study is carried out for an ERPE but in the following with a load and a mean pressure of 18.1 bar (this matches the highest efficiency case in Table III.1). We examine the influence of various parameters on the following performance indicators: frequency f, exergy efficiency η_{ex}, heat-input rate gradient $\mathrm{d}\dot{Q}_{\mathrm{hx}}/\mathrm{d}y$, and the product $\eta_{\mathrm{ex}} \cdot f$. Only five of the 19 variable parameters of the load case (Fig. II.15) influence the performance indicators significantly, i.e. the thermal resistance R_{th}, the heat exchanger capacitance C_{hx}, the vapour compressibility in the displacer cylinder C_{v}, the hydrostatic capacitance in the displacer cylinder C_{d}, and the inductance of the connection tube L_{c}. All other parameters affect the performance indicators only marginally, even if they are varied by several orders of magnitude. The relevant results from this parametric study are summarized in Fig. III.2.

Similarly to the load-free case, the two thermal-domain parameters R_{th} and C_{hx} influence the frequency in a similar manner, as shown in Figure III.2(a). When decreased below their nominal values, these two parameters lead to a monotonic increase in the frequency within the entire investigated parameter ranges. Moreover, as with the load-free case, a low vapour-spring capacitance C_{v} results in a significantly higher frequency, as does a low connection-tube inductance L_{c} albeit to a lesser extent.

Figure III.2(b) shows the exergy efficiency which is mainly influenced by the vapour-spring capacitance C_{v} and, to a lesser extent, the connection-tube inductance L_{c}. The exergy efficiency is shown to reach theoretical values up to 90% when the capacitance C_{v} is reduced 1000 times. However, it may be physically impossible to attain a displacer hydrostatic capacitance that low. Increasing L_{c} to approximately 100 times its nominal values increases the efficiency from 2% to 20%. The remaining three parameters discussed here only change the efficiency by a few percentage points. Although the ERPE has low efficiencies at the nominal values derived from the BIC prototype, Fig. III.2(b) shows that it is possible to substantially increase the efficiency (and also the frequency) with relatively simple measures. Reducing the volume or increasing the pressure of the vapour region in combination with increasing the length of the connection tube and reducing its diameter would increase the efficiency. The ERPE demonstrates a potential of exhibiting high exergetic efficiencies, and it is not expected to be adversely affected by the same degree

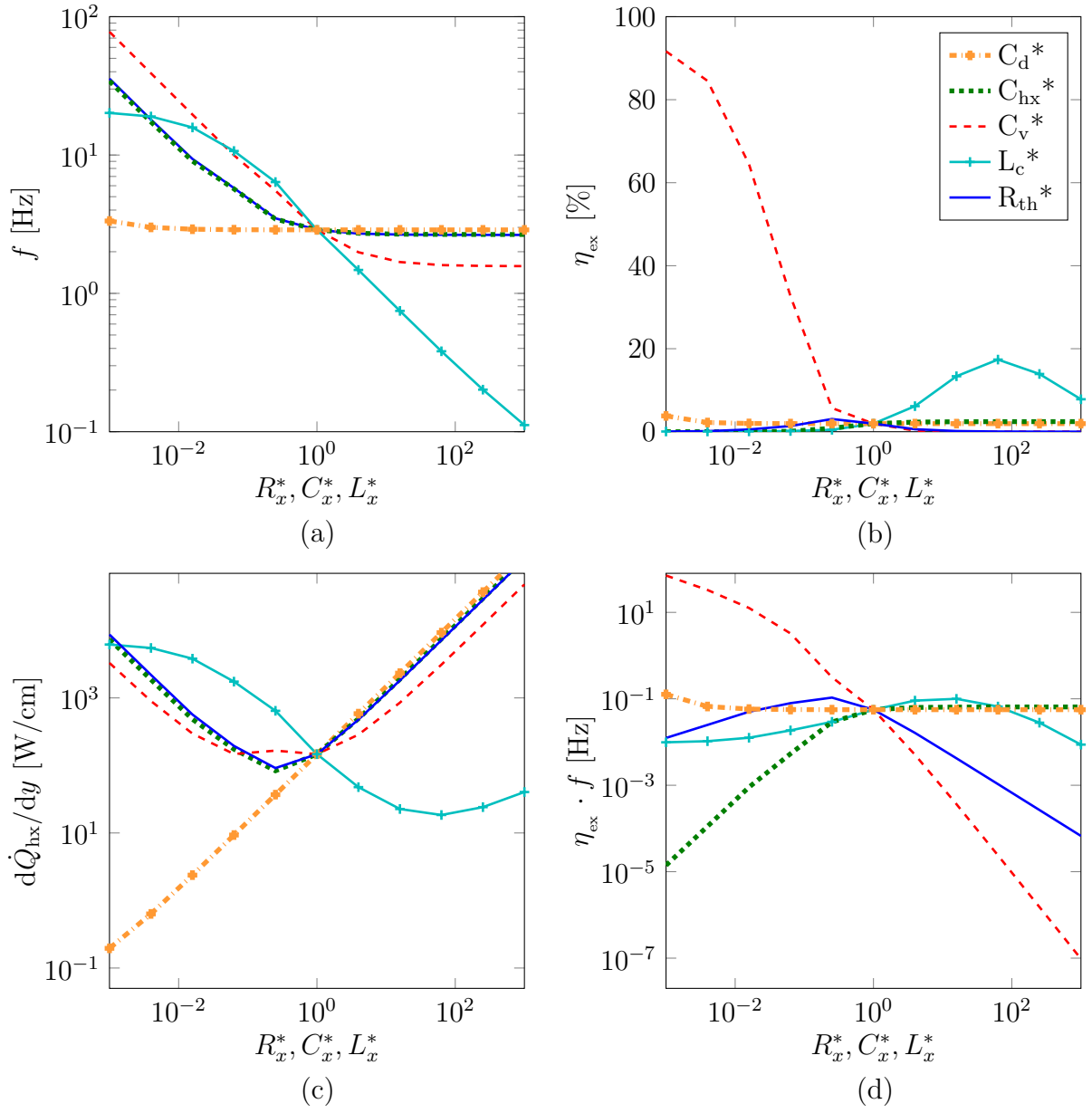


Figure III.2: Variations in the: (a) the oscillation frequency f; (b) the exergy efficiency η_{ex}; (c) the heat-input rate gradient $d\dot{Q}_{hx}/dy$; (d) product of exergy efficiency and frequency $\eta_{ex} \cdot f$ (proportional to power output per unit heat input) in engine with a load with a mean pressure of 18.1 bar as functions of normalized parameters listed in the legend.

of parasitic condensation that has been observed in other TFOs thanks to the reduced vapour region over the HHX in the displacer cylinder. All other remaining parameters have little to no effect on the exergy efficiency including all resistances. At this point we make the counter-intuitive observation that the resistances have almost negligible influence on the efficiency in comparison to the aforementioned two components. In fact, it has been observed for the NIFTE that in some cases increasing some resistances was beneficial for the exergy efficiency [26, 27, 30, 53]. These findings show that many aspects of the behaviour of TFOs is often non-trivial and counter-intuitive and underlines the value of this modelling approach. It provides a swift method to understand general trends of behaviour of the engine.

Figure III.2(c) shows the behaviour of the necessary heat-input rate gradient $\mathrm{d}\dot{Q}_{\mathrm{hx}}/\mathrm{d}y$ where the thermal resistance R_{th}, the heat exchanger capacitance C_{hx} and the vapour compressibility C_{v} all show similar behaviour: for values slightly below the employed nominal values, the necessary heat input reaches a minimum. The hydrostatic capacitance in the displacer cylinder C_{d} is once again the most influential parameter, as the necessary heat input $\mathrm{d}\dot{Q}_{\mathrm{hx}}/\mathrm{d}y$ increases as a power law for the entire investigated range around the nominal values. Moreover, the necessary heat input decreases to a minimum at a value of L_{c} which is ~ 100 times its nominal value.

Figure III.2(d) shows the behaviour of the hydraulic power output per unit heat input. Varying the inductance L_{c} has a comparatively small effect on the normalized power output while variations in C_{d} have almost no effect. The normalized power output is maximized for values of the thermal resistance R_{th} slightly below the nominal value $(0.25 \cdot R_{\mathrm{th,nom}})$ and decreases for other values of R_{th}. Furthermore, the normalized power output increases with the capacitance C_{hx} before levelling off around the nominal value. The gas spring capacitance C_{v} is the most dominant parameter with which the normalized power output decreases sharply. This parameter should therefore be kept at a minimum.

III.3 Thermodynamic Cycle Diagrams

Pressure-displacement ($P_{\mathrm{lo},1}$-$V_{\mathrm{lo},1}$) diagrams across the load are shown in Fig. III.3 while Fig. III.4 shows temperature-entropy (T-S) diagrams at the heat exchanger of the ERPE. The diagrams help explain the trends of the exergy efficiency and normalized power output in Fig. III.2(b) and (d). The areas enclosed by the P-V diagrams in Fig. III.3 represent the net work-output in one cycle that can be multiplied with the frequency to obtain the hydraulic power. The T-s diagrams in Fig. III.4 show the temperatures

of the solid heat exchanger surfaces that the fluid contacts T_{hx} and the temperatures of the working fluid T_{v} contained within the displacer cylinder that interacts with the heat exchangers. The areas enclosed by T_{hx} (solid or dotted-dashed lines) correspond to the exergy input to the engine, and the areas enclosed by T_{v} (dashed or dotted lines) represent the net exergy gained by the working fluid. Hence, the difference between the two areas is a measure of the exergy destruction due to heat transfer to or from the working fluid during one oscillation. The exergy input rate to the device was kept constant for all cases and the time-averaged pressure was 18.1 bar. The five parameters from Fig. III.2 are perturbed to 1/5 to 5 times their respective nominal values, though only those parameters which display significant variation are shown.

The P-V diagrams reflect the power output trends from Fig. III.2(d). The work output per cycle increases with increasing C_{hx} and L_{c} and with decreasing R_{th} and C_{v} similar to the behaviour of the normalized power output. The Lissajous plots provide insight into what the increase in work and power output can be attributed to. An increase in area of these curves can be caused by an increase of the amplitudes of P and V or an improvement in the phase difference between them towards an ideal of 90°. We can see from Fig. III.3(b), for example, that when C_{v} is reduced, the area and work output increase due to a slight improvement of the phase difference and, more significantly, due to a substantial elevation of the pressure amplitude (and not as much the displacement amplitude). For the remaining three parameters, especially the inductance L_{c}, the pressure and displacement increase similarly and contribute to the overall improvement of the engine's work output. For L_{c} in Fig. III.3(c), the area increases with increasing L_{c} to a greater extent than the other parameters despite the phase difference deteriorating. The phase differences are not strongly influenced by variations in the thermal domain parameters C_{hx} and R_{th}, while for the other two parameters, the ellipse symmetry axes both steepen at lower values.

In Fig. III.4, we show how variations in C_{v} and L_{c} affect the exergy input, and thereby the exergy efficiency. The area enclosed by the T_{hx}-S curve at high C_{v} values shown in Fig. III.4(b), which represents the external exergy input to the device, is large compared to the curve obtained with smaller values of C_{v} shown in Fig. III.4(a). This is primarily the result of the larger amplitudes of the entropy flow-rate. However, the area enclosed by the Lissajous T_{v} curve, which represents the net exergy transferred to the working fluid, is virtually zero due to an extremely small temperature amplitude. For $1/5 \cdot C_{\mathrm{v,nom}}$ shown in Fig. III.4, the phase difference between T_{v} and S is 73° while the phase difference is 16° for $5 \cdot C_{\mathrm{v,nom}}$. Additionally, the temperature amplitudes are higher

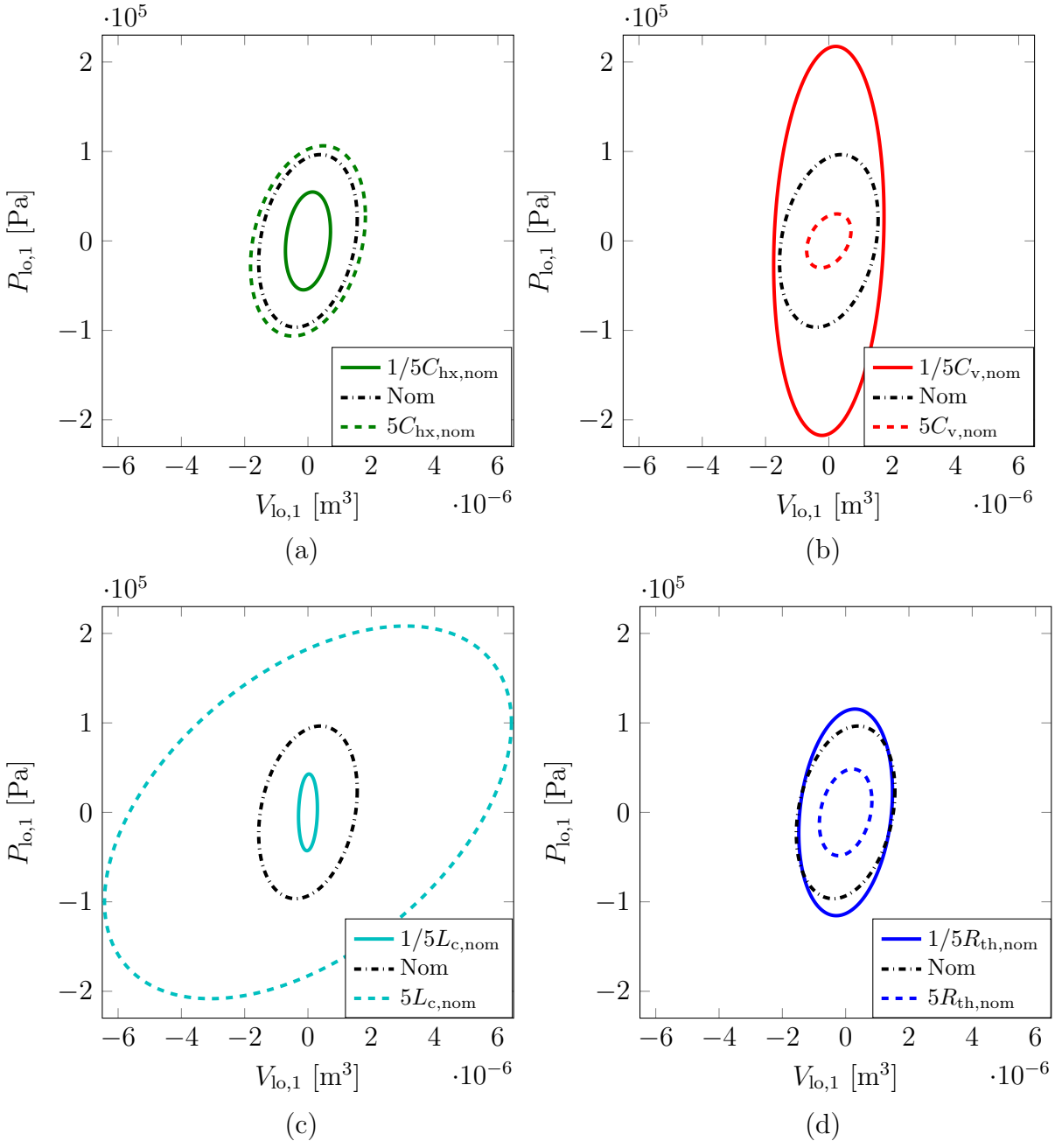


Figure III.3: Linearized pressure-volume diagrams relating pressure $P_{\mathrm{lo},1}$ to the volume displacement $V_{\mathrm{lo},1}$ in the load for 5 times (dashed lines) and one fifth (solid lines) of nominal values of: (a) C_{hx}, (b) C_{v}, (c) L_{c}, and (d) R_{th}. The dash-dotted lines represent the nominal case. The area enclosed by the Lissajous curves represent the work output per oscillation. For all cases, the time-averaged pressure is 18.1 bar, and the exergy input rate into the engine is constant.

for the smaller capacitance. Simultaneously, the area enclosed by the T_{hx} curve drops considerably thanks to a sharp drop in the entropy amplitude (although the temperature increases here also). In summary, when reducing C_{v} the two areas exhibit opposite behaviours: the T_{hx} area decreases and the T_{v} area increases meaning that the total exergy input to the system is smaller, while at the same time the net exergy transferred to the working fluid increases. This substantial reduction in exergy destruction at the heat exchanger is the reason for the sharp increase of the exergy efficiency at lower C_{v}.

An improvement in efficiency can also be achieved with a higher connection tube inductance L_{c} although the area enclosed by the T_{hx} curve enlarges (III.4(c) and (d)). From $1/5 \cdot L_{\mathrm{c,nom}}$ to $5 \cdot L_{\mathrm{c,nom}}$, the phase difference between T_{v} and S rises from 26° to 40°, while the phase difference between T_{hx} and S decreases slightly from 90° to 85°. In addition, the amplitudes of the temperature and entropy of the T_{v} curve increase, while for the T_{hx} curve only the entropy amplitude increases. Hence, the area enclosed by the T_{v} curve increases to a greater extent than that enclosed by the T_{hx} curve. This is why an improvement of the exergy efficiency is observed albeit not as substantial as by varying C_{v} because the necessary exergy input also increases. All other parameters show no significant variations in the T-S diagrams.

In summary, an efficient and high-power engine requires (a) a very low vapour gas spring capacitance C_{v} which is also the most influential parameter, (b) a thermal resistance R_{th} slightly below the nominal value, (c) a nominal heat exchanger capacitance C_{hx}, and (d) a moderately high connection tube inductance L_{c}. The capacitance C_{v} can be reduced with a small vapour space or a high mean pressure, which also leads to a high frequency. Moreover, the thermal domain components R_{th} and C_{hx} can be reduced by improving the heat transfer characteristics or heat transfer coefficient. Requirement (d) can be implemented by increasing the connection tube length and reducing the tube diameter. This also leads to an increase in frequency, however if there is a desire to increase it further, then R_{th} should be reduced instead of C_{hx} if both are at their nominal values. A decrease of C_{hx} in this case, will increase frequency but also reduce power. L_{c} should be moderately high to keep the necessary heat input low. C_{d} should be as small as possible which can be implemented with a small cross-sectional area of the cylinder. All other parameters reduce the heat input if they are slightly below their nominal values.

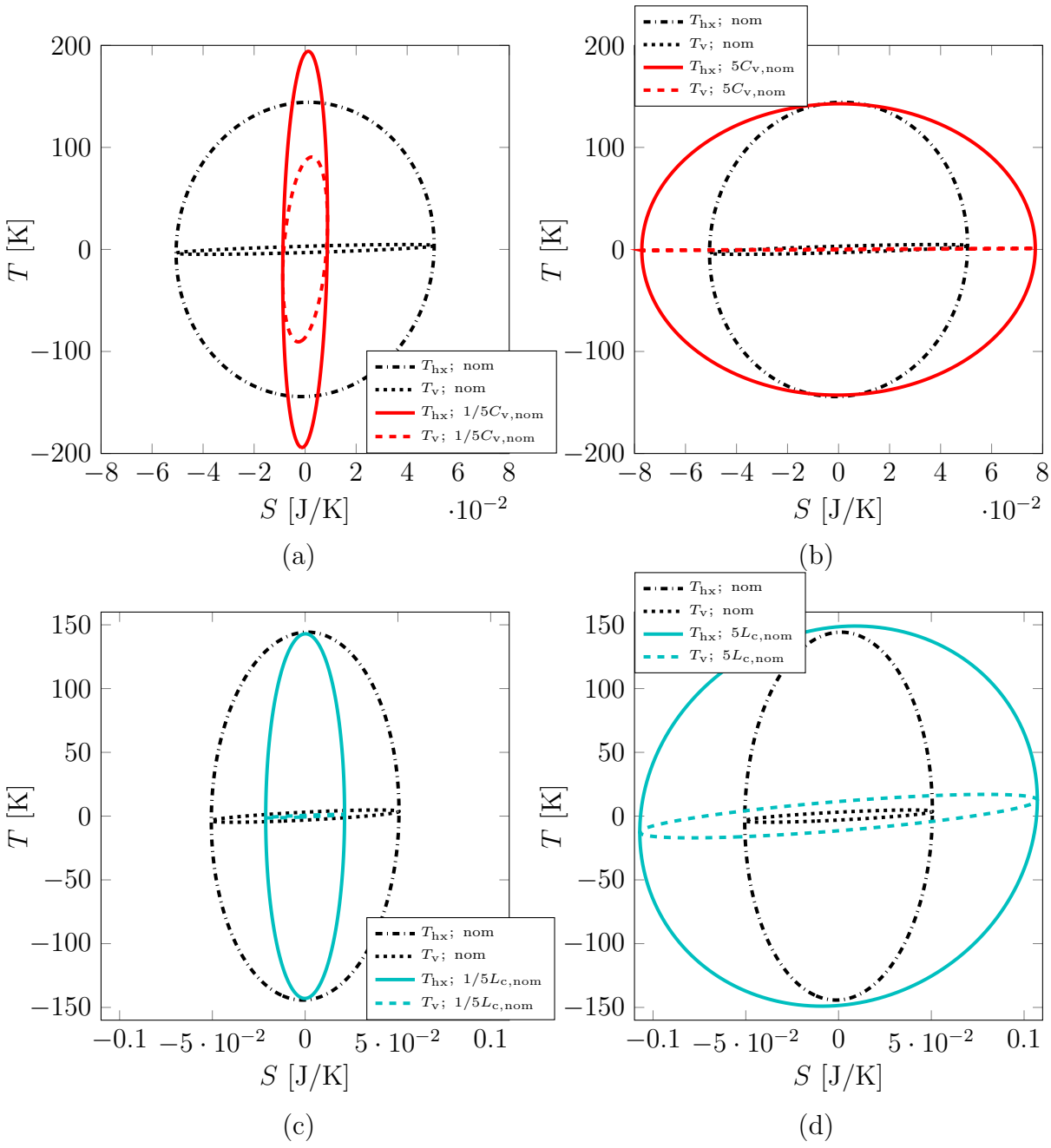


Figure III.4: Linearized T-s cycle diagrams for 5 times and one fifth of nominal values of C_v ((a) and (b)); and L_c ((c) and (d)). The areas enclosed by the T_hx curves (solid and dash-dotted lines) represent the net exergy made available to the device in one oscillation; the areas enclosed by the T_v curves (dashed lines and dotted lines) represent the net exergy gained by the working fluid in one oscillation. The difference between both cycles amounts to the exergy destruction due to irreversible heat transfer between the heat exchangers and the working fluid. The temperature values on the vertical axes are not absolute temperatures but temperature differences to the respective equilibrium temperatures.

III.4 Summary

A first-order linearized, spatially lumped dynamic model of a class of unsteady heat-engine referred to as the 'Evaporative Reciprocating-Piston Engine' (ERPE) has been developed as an electronic circuit representation based on a linearized version of an existing TFO engine prototype. This model applies electrical analogies founded on thermoacoustic and thermofluidic principles where combinations of capacitances, inductances, and resistances can represent the operation of different physical components of an engine. The circuit is used to guide the early-stage design of complex unsteady thermodynamic systems and provides suggestions on how to improve performance of the ERPE *and* the BIC prototype. The model results also provide valuable insight into the general behaviour and mode of operation of TFOs.

The concept engine consists of two vertical cylinders, displacer and working cylinder, and a free solid piston contained within the former. A pair of hot and cold heat exchangers along the walls of the displacer cylinder periodically adds and extracts heat from the working fluid in this part of the engine. During the heat rejection phase, vaporous working fluid condenses, which decreases the pressure in the vapour space. This leads to the positive displacement of the liquid column as well as the displacer piston. As the vapour liquid interface moves up to the hot heat exchanger, it begins evaporating which reverses the aforementioned process. The working cylinder contains a liquid column and a gas spring. The compressibility of the gas and vapour springs, the inertia of the liquid columns in both cylinders, and the hydrostatic pressure differences between both cylinders help sustain pressure and flow-rate oscillations of the working fluid. These flow oscillations can be harvested to produce hydraulic work in a load.

Measurements of the frequency, temperature gradients and heat input rate gradient in the prototype are used as indicative values for the calculations of the model. The developed model contains two sub-models of the heat-transfer process. One sub-model assumes a linear temperature profile (LTP) along the height of the heat exchanger walls. The other allows for dynamic heat exchange (DHX) to take place at the heat exchangers which accounts for the capacity of the heat exchanger walls to store and release heat. The models in all cases overestimate the frequency. However, the DHX model predicts realistic frequencies in the load-free case. The temperature and heat input gradients predictions, on the other hand, are all within acceptable ranges.

Parametric studies have shown that for the load-free case, the gas spring compressibility C_{g}, vapour gas spring compressibility C_{v} and connection tube inductance L_{c} have

the highest effect on increasing the frequency if kept at a minimum. Additionally, the thermal resistance R_{th}, heat exchanger capacitance C_{hx}, displacer cylinder hydrostatic capacitance C_{d}, vapour gas spring compressibility C_{v} should be low to minimize the heat input rate gradient, while the connection tube inductance L_{c} should be high.

In a loaded engine, only five parameters prove to affect the frequency, exergy efficiency, heat-input rate gradient, or power output significantly: the hydrostatic capacitance C_{d} of the displacer cylinder, the vapour compressibility C_{v}, the heat exchanger capacitance C_{hx}, the connection tube inductance L_{c}, and the thermal resistance R_{th}. The most influential parameter is C_{v}. To increase the power output, exergy efficiency and frequency, the vapour compressibility C_{v} must be minimized while the connection tube inductance L_{c} should be kept moderately high. This can be achieved by increasing the mean pressure, reducing the diameter of the connection tube or increasing its length, or decreasing the time-averaged vapour space. Furthermore, keeping the heat exchanger capacitance C_{hx} and thermal resistance R_{th} at intermediate (nominal) levels will further increase power output and efficiency. The resistance is inversely proportional to the heat transfer coefficient and heat transfer area, while the capacitance is proportional to the heat capacity of the walls and their mass. Finally, to keep the necessary heat input low, the parameters are optimal around their nominal values except for L_{c}, which should be moderately high (as before for the efficiency), and the hydrostatic capacitance in the displacer cylinder C_{d}, which should be as small as possible by decreasing the cross-sectional area of the cylinder. The insight from these results offers important suggestions and guidance for improving performance and for system optimization.

The ERPE was only investigated using water. It would be of interest for future researchers to investigate the performance of the engine when using other (organic) fluids or fluid mixtures. Such studies have been carried out for other TFOs [29, 34] for different types of pure fluids but not mixtures. Many organic fluids significantly outperform water in terms of power output and efficiency. Acquiring reliable and accurate thermodynamic data for pure fluids and mixtures is essential for this study. Unfortunately, there are many organic fluids where data is not available. For such a case, a state-of-the-art equation of state, such as SAFT-VR Mie, can be employed. SAFT-VR Mie possesses many advantages over other equations of state. It has been used for calculating properties of working fluid mixtures in ORCs discussed in the following two chapters.

Chapter IV

Model Development for Organic Rankine Cycles using Working Fluid Mixtures

IV.1 Background

As mentioned in Chapter I, there is a growing interest in the organic Rankine cycle (ORC) as it is more suitable for low-temperature heat conversion relative to conventional power cycles [10]. ORCs generally have lower thermal efficiencies than large centralized systems due to the lower temperature of the heat source, however low- or medium-grade heat sources are abundant and easily accessible, and there is great interest in their recovery and utilization. In many cases, such as with waste heat, the cost of the energy source is virtually zero compared to fossil fuel power plants where fuel costs may account for up to two-thirds of the levelized costs (total costs) of electricity generation. The aim in the development of low- or medium-grade heat conversion technologies, such as ORCs, is to maximize the power output while minimizing investment and capital costs. In waste heat recovery and conversion applications, efficiency is secondary to power output and is only significant in as much as it contributes to maximizing power and minimizing costs [10].

In an ORC system, the combined thermodynamic losses in the evaporator and condenser account for approximately 80% of the exergy destruction in the whole cycle [36, 54] due to irreversibilities associated with heat transfer between the working fluid and external heat sources or heat sinks. Conventional working fluids consisting of a single

component exhibit isothermal behaviour during isobaric phase change. The temperature difference between the working fluid and the heat source (or sink) stream reaches a local minimum at the pinch point. Away from that point, the temperature difference is considerably higher if the phase change is isothermal. Heat transfer across such large temperature differences is associated with significant exergy loss. Isothermal phase change leads to the well-known pinch point, away from which the temperature difference between heat source/sink and working fluid is considerably higher.

Therefore, there is an increased interest in the scientific community in the employment of zeotropic mixtures as working fluids. Mixtures exhibit a so-called temperature glide when changing phase. During evaporation, the temperature of the liquid working fluid increases (and during condensation the temperature decreases). Hence, there is an improved thermal match between the heat source/sink and the working fluid, and the average temperature difference between the heat source/sink stream and the working fluid stream is smaller. Therefore, the exergy loss can be reduced and the thermal efficiency and net power output can be increased. This allows for smaller and cheaper heat exchanger components [54, 55] and shifts the dominant component of the cycle's exergy destruction to the expander.

Several studies have investigated in detail the potential of employing working fluid mixtures for more efficient and power-dense ORCs. It has been shown, for example, that suitable binary mixtures may increase power output in specific applications by 20% and improve thermal efficiencies by 15% compared to single-component fluids [56]. In an experimental study of mixtures of R245fa and R152a as ORC working fluids, it has been observed that the mixtures exhibit a higher thermal efficiency and require a reduced expander size relative to employing R245fa as working fluid [57]. Yet in another theoretical study of geothermal ORCs by Heberle et al. [58], mixtures of isobutane with isopentane and R227ea with R245fa exhibited an efficiency 15% higher than the most efficient component pure fluid. Lecompte et al. [59] examined several different mixtures for ORCs and found that the exergy efficiency increased from 7.1% to 14.2%. These previous efforts suggest that working-fluid mixtures can be more effective with low-temperature heat sources than with higher-temperature sources.

Although these studies show potential advantages of working fluid mixtures, the research in the exact benefits is still in the early stages. An obstacle lies in the fact that the suitability of the working fluid is a strong function of the particular cycle which is designed for a custom application. Identifying application-specific optimal fluids is difficult especially because of the large range of potential candidates and their mixtures. A

common application case is the where an ORC is operated for producing power and has sufficiently large quantities cooling water. Where such a case is discussed, a very small temperature glide is needed in the condenser, however in any other case, the optimal working fluid is the one with the best thermal match to the temperature profile of the heat source *and* sink. The heat streams are external boundary conditions to the ORC design over which the engineer has no control. For ORC systems in CHP applications for example, energy integration, or cases where cooling fluid is scarce, a working fluid with large temperature glide is desired.

ORC development can be greatly advanced with the development of whole-system optimization platforms. Such a platform would take into account optimal cycle conditions, advanced system architectures, and the design of novel fluid substances to simultaneously optimize the working fluid (including mixtures) and the ORC design. The platform would be very powerful due to its ability to capture coupling relations and interdependencies of seemingly unrelated cycle components. Computer-aided molecular design (CAMD) [60] is a promising tool which can be employed as part of a whole-system optimization platform where it features accurate thermodynamic property prediction models for pure and mixed fluids. The platform would take into account optimal cycle conditions, advanced system architectures, and the design of novel fluid substances to simultaneously optimize the working fluid (including mixtures) and the ORC design. To this end, reliable descriptions of working fluids at a molecular level are required which also describe molecular interaction between different components. Research groups have begun to explore the use of advanced molecular models [61, 62].

IV.1.1 Objective

The primary objective of our research work discussed in this chapter to identify potential advantages of working fluid mixtures. By employing a recent version of the statistical associating fluid theory (SAFT-VR Mie) molecular-based models are developed from which the thermodynamic properties of pure organic fluids and their mixtures are calculated. The influence of mixtures and mixing ratios on the thermodynamic performance and costs of an ORC system are investigated. A mathematical model of a sub-critical, non-regenerative ORC system which converts heat from a refinery flue-gas stream calculates the thermodynamic performance as a function of the mixture composition. The cycles in this application have power outputs of up to 30 MW; the working fluid may not be expanded to below 1 bar; and the temperature of the heat sink stream cannot go below 30 °C. Two sets of mixtures are investigated to demonstrate the potential of SAFT-VR

Mie in predicting thermodynamic properties: butane-decane (n-C_4H_{10} + n-$C_{10}H_{22}$) and perfluorobutane-perfluorodecane (n-C_4F_{10} + n-$C_{10}F_{22}$) mixtures. The property predictions are validated against available experimental data

The considered compounds are environmentally benign and have low global warming potential compared to high-performance alternatives, such as CFC12 [63]. Especially perfluoroalkanes are known for being stable and having high autoignition temperatures [64, 65], and they are suitable as replacements for fluids with high ozone depletion potential and global warming potential.

This chapter explains the theory behind the research in employing working fluid mixtures in organic Rankine cycles. Firstly, the mathematical ORC model is explained in full detail followed by a discussion of SAFT-VR Mie. The results of this study are in Chapter V.

IV.2 Organic Rankine Cycle Model

The simplest form of the (ideal) organic Rankine cycle consists of four basic processes undertaken by an organic working fluid for each of which a dedicated component is required. The processes have already been explained in Section I.2.2 and are listed here once again for the reader's convenience:

- $1 \rightarrow 2$ isentropic compression in a pump
- $2 \rightarrow 3$ isobaric heat addition in a boiler/evaporator
- $3 \rightarrow 4$ isentropic expansion in an expander/turbine
- $4 \rightarrow 1$ isobaric heat rejection in a condenser

The corresponding schematic and T-s diagram are shown in Figs. IV.1(a) and IV.1(b). In a practical organic Rankine cycle, Processes $1 \rightarrow 2$ and $3 \rightarrow 4$ are not perfectly isentropic.

Apart from the four main components, additional components are usually required depending on the application, such as heat stream or coolant fluid pumps or equipment items like motors, alternator, separators, tanks, seals, etc.

With the aim of increasing the thermal efficiency, a regenerator (sometimes called a recuperator) is employed which preheats the working fluid after pressurization (before evaporation) with thermal energy from the working fluid at the outlet of the expander. This can reduce the external heat requirement. However, the additional heat exchanger component increases the complexity and costs of the ORC system. Minimizing capital and

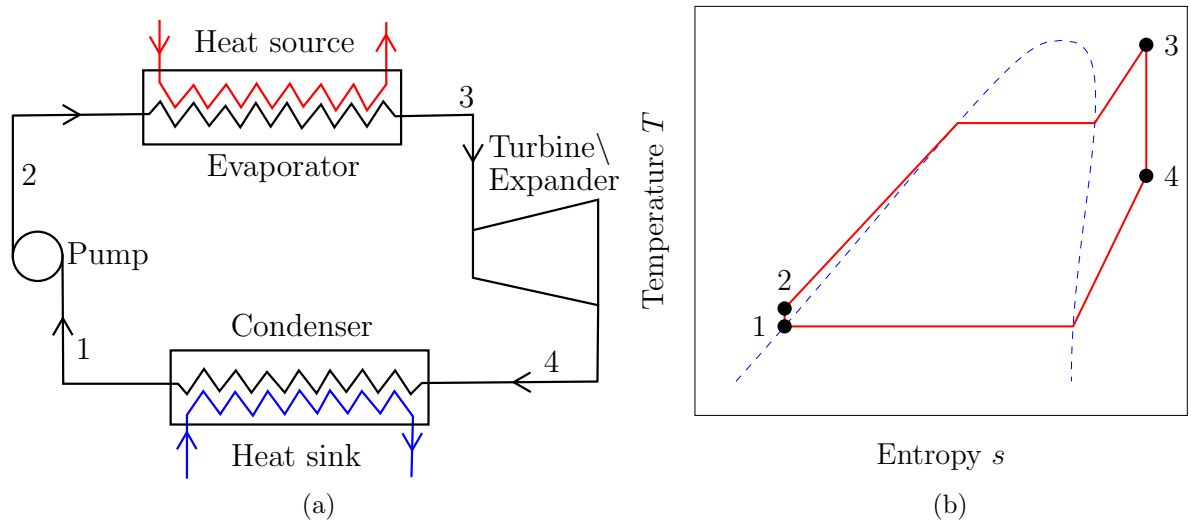


Figure IV.1: (a) Schematic diagram of an ORC engine. (b) Exemplary sub-critical, non-regenerative, and ideal ORC cycle on a T-s diagram. The temperature of State 2 is exaggerated for clarity.

investment costs is of paramount importance especially in distributed small- to medium-scale waste-heat conversion and energy integration applications. Therefore, in this study a regenerator is not considered; rather, the problem definition is to maximize the power output of a simple, non-regerative ORC, while considering indicative system costs.

IV.2.1 Thermodynamic Model of the Cycle

The ORC engine is assumed to run in steady state conditions, and therefore dynamic relations are not necessary. Steady-state energy balances suffice for a thermodynamic cycle analysis. The resulting model equations for the process depicted in Fig. IV.1(b) are stated briefly below.

Working Fluid Pump (State 1 → State 2)

The working fluid pump increases the pressure of the working fluid from a pre-defined condenser pressure to a pre-specified evaporator pressure. State 1 is assumed to be a saturated liquid at the condenser pressure, such that the fluid properties (temperature T, specific enthalpy h, and specific entropy s) for State 1 are functions of the condensing pressure and mixture composition only:

$$\{T_1, s_1, h_1\} = f(P_{41}, x)\,. \tag{IV.1}$$

State 2 is determined with the imposed evaporating pressure P_{23} and a given isentropic efficiency for the pump:

$$\eta_{\text{is,pump}} = \frac{h_{2\text{s}}(P_{23}) - h_1}{h_2 - h_1}\,, \tag{IV.2}$$

where $h_{2\text{s}}$ is the enthalpy of the working fluid following an isentropic process from State 1 to the evaporating pressure P_{23}. In this study, the isentropic efficiency for the pump is constant at 0.75. The fluid properties at State 2 are then calculated from

$$\{T_2, s_2\} = f(P_{23}, x, h_2)\,, \tag{IV.3}$$

with h_2 having been previously evaluated from Eq. IV.2. Thus, the power required to pump the working fluid from P_{41} to P_{23} (i.e., State 1 to State 2) is given by the working-fluid enthalpy change through the pump:

$$\dot{W}_{\text{pump}} = \dot{m}_{\text{wf}}(h_2 - h_1)\,, \tag{IV.4}$$

where $\dot{m}_{\text{wf}}$ is the mass flow-rate of the fluid through the pump.

Heat addition (State 2 → State 3)

The working fluid at State 2 is evaporated with heat extracted from the heat source and leaves the evaporator as a saturated vapour (at its dew point at the evaporating pressure) or a superheated vapour (State 3). The heat addition process is isobaric as the pressure drop across the heat exchanger is negligible relative to the pressure in this component (P_{23}). The temperature of the working fluid at State 3 is defined with the dew-point temperature ($T_{\text{dew},P_{23}}$) at the evaporating pressure P_{23}, plus a variable superheat temperature difference ΔT_3 set by the degree of superheating. The degree of superheating d_{sh} and is defined by

$$d_{\text{sh}} = \frac{T_3 - T_{\text{dew},P_{23}}}{T_{3,\text{max}} - T_{\text{dew},P_{23}}}\,, \tag{IV.5}$$

where $\Delta T_3 = T_3 - T_{\text{dew},P_{23}}$ and $T_{3,\text{max}}$ is the maximum possible superheat temperature (usually the heat-source temperature minus a pre-specified minimum pinch temperature-difference), such that

$$T_3 = T_{\text{dew},P_{23}} + \Delta T_3\,. \tag{IV.6}$$

All other properties of the working fluid at the evaporator exit can be found from

$$\{s_3, h_3\} = f(P_{23}, x, T_3) \tag{IV.7}$$

once State 3 is defined. The heating rate required to evaporate and superheat the working fluid is equal to the rate of heat extraction from the heat source, $\dot{Q}_{\text{in}}$ (assuming no heat losses):

$$\dot{Q}_{\text{in}} = \dot{m}_{\text{wf}}(h_3 - h_2) = \dot{m}_{\text{hs}} c_{\text{p,hs}}(T_{\text{hs,in}} - T_{\text{hs,out}})\,, \tag{IV.8}$$

where $\dot{m}_{\text{hs}}$ is the mass flow-rate of the heat-source stream, $c_{\text{p,hs}}$ is its specific heat capacity, and $T_{\text{hs,in}}$ and $T_{\text{hs,out}}$ are the inlet and outlet temperatures of this stream at the evaporator.

Expansion Machine (State 3 → State 4)

Due to irreversible thermal and mechanical losses, a real expansion process is not isentropic. Therefore, an isentropic efficiency is used to account for non-ideal expansion defined as

$$\eta_{\text{is,exp}} = \frac{h_3 - h_4}{h_3 - h_{4\text{s}}(P_{41})}\,, \tag{IV.9}$$

where $h_{4\text{s}}$ is the enthalphy at the outlet of an ideal, isentropic expander. As for the pump, the isentropic efficiency for the expander is constant at 0.75. After calculating h_4 from IV.9, all other properties at State 4 can be deduced:

$$\{T_4, s_4\} = f(P_{41,\text{x}}, \eta_{\text{is,exp}})\,. \tag{IV.10}$$

The power generated through the expansion of the working fluid from P_{23} to P_{41} is

$$\dot{W}_{\text{exp}} = \dot{m}_{\text{wf}}(h_3 - h_4)\,. \tag{IV.11}$$

Heat Rejection (State 4 → State 1)

From State 4 to State 1, the low-pressure (P_{41}) expanded fluid is condensed to a liquid state at a constant pressure typically using water at ambient conditions in the heat-sink stream. The expression for the rate of heat rejection in the condenser is similar to that of the heat input in the evaporator:

$$\dot{Q}_{\text{out}} = \dot{m}_{\text{wf}}(h_4 - h_1) = \dot{m}_{\text{cs}} c_{\text{p,cs}}(T_{\text{cs,out}} - T_{\text{cs,in}})\,. \tag{IV.12}$$

An important and novel aspect of this study is highlighted at this point. The pressure in the condenser is not permitted to fall below atmospheric pressure (approximately 1 bar). This is to prohibit the possibility of air ingress into the cycle. In large-scale,

centralized power plants, the working fluid is expanded to sub-atmospheric pressures, however this requires complicated (and therefore costly) designs and seals to prevent air ingress. As minimizing costs is of paramount importance for small- and medium-scale power generation from waste heat, we are not considering expansion below 1 bar. One may interject at this point that the cycle during heat addition has a pressure much higher than its surroundings and therefore may suffer from leakage if not designed and sealed appropriately. However, leakage is not as critical as air ingress, as leakage can be solved easily by adding more working fluid. Solving air ingress is a much more difficult problem.

Another condition imposed on the condenser is that the temperature of working fluid remains above the cooling-stream temperature (20 °C) plus a specified minimum pinch temperature difference (10 °C) to permit heat rejection. The selection of the heat-rejection conditions (in particular, of the condensation pressure and cooling-stream flow-rate) is described in Chapter V.

Degrees of Freedom and Thermodynamic Cycle Solution

Equations IV.2 to IV.12 represent the thermodynamic model of the sub-critical, non-regenerative ORC system we are considering. The equations are solved by specifying the following input parameters: working-fluid composition and mass flow-rate, evaporating and condensing pressures, pump and expander isentropic efficiency, degree of superheat, and finally, heat source and heat sink characteristics. Finally, the thermal efficiency is calculated as the ratio of net power output from the system to the ratio of heat input from the heat source:

$$\eta_{\mathrm{th,ORC}} = \frac{\dot{W}_{\mathrm{exp}} - \dot{W}_{\mathrm{pump}}}{\dot{Q}_{\mathrm{in}}} \,. \tag{IV.13}$$

Heat Exchangers

It must be guaranteed that along the length of the heat exchangers, heat is transferred from the higher to the lower temperature so as not to violate the second law of thermodynamics. This is achieved by specifying a minimum pinch-point temperature difference between the hot-side and cold-side fluid streams along the length of the heat exchangers.

The evaporator is conceptualized as consisting of three sections, one each for preheating, evaporation, and superheating. Thus, the heat input expression $\dot{Q}_{\mathrm{in}}$ from Eq. IV.8 can be rewritten as

$$\dot{Q}_{\mathrm{in}} = \dot{m}_{\mathrm{wf}} c^{P_{23}}_{\mathrm{p,wf,l}} (T_{\mathrm{bub},P_{23}} - T_2) + \dot{m}_{\mathrm{wf}} \Delta h^{P_{23}}_{\mathrm{wf}} + \dot{m}_{\mathrm{wf}} c^{P_{23}}_{\mathrm{p,wf,v}} (T_3 - T_{\mathrm{dew},P_{23}}) \,. \tag{IV.14}$$

Here, $c_{\mathrm{p,wf,l}}^{P_{23}}$ and $c_{\mathrm{p,wf,v}}^{P_{23}}$ are the specific heat capacities of the working fluid in the sub-cooled and superheated states respectively, while $\Delta h_{\mathrm{wf}}^{P_{23}}$ represents the latent heat of vaporization, and $T_{\mathrm{bub},P_{23}}$ is the bubble-point temperature (all at pressure P_{23}). The enthalpy and temperature profiles in the heat source are discretized into segments, so that one can examine the profile of the temperature difference through the heat exchanger by calculating the temperature difference at each segment. Thermal energy balance at any segment can be described by

$$\dot{m}_{\mathrm{wf}} c_{\mathrm{p,wf}}^{P_{23}} (T_i - T_{i-1}) = \dot{m}_{\mathrm{hs}} c_{\mathrm{p,hs}} (T_{\mathrm{hs},i+1} - T_{\mathrm{hs},i}) \,. \tag{IV.15}$$

Discretizing each section in 20 segments is sufficient for a smooth temperature profile. The heat capacities for each segment are selected depending on the temperature at the inlet of each segment. The pinch point in the heat exchanger is the segment with the lowest temperature difference between the heat source stream and the working fluid ($\Delta T_{\mathrm{pp}} = \min\{T_{\mathrm{hs},i} - T_i\}$). The heat exchanger is thus feasible by specifying that the pinch-point temperature difference is not lower than the stated minimum of 10 °C.

The condenser is considered to have two components, namely a desuperheating section and a condensing section. Both sections are descretized in a similar manner as the evaporator, and the pinch-point temperature difference is specified to not fall below 10 °C. From Eq. IV.12, one can write

$$\dot{Q}_{\mathrm{out}} = \dot{m}_{\mathrm{wf}} c_{\mathrm{p,wf,v}}^{P_{41}} (T_4 - T_{\mathrm{dew},P_{41}}) + \dot{m}_{\mathrm{wf}} \Delta h_{\mathrm{wf}}^{P_{41}} \,, \tag{IV.16}$$

where $T_{\mathrm{dew},P_{41}}$ is the dew-point temperature at pressure P_{41}. We assume constant specific heat capacities for both the heat source and the cooling fluids.

IV.2.2 Case Study: Waste-Heat Source and Heat-Rejection Medium

In the present study, an ORC system is considered for an industrial waste-heat application. The heat source is a flue-gas stream from a gas-fired boiler in a refinery. It has a flow-rate of 560 kg/s and a temperature of 330 °C which we know from direct measurements at the boiler exhaust. The specific heat of the flue gas is known through its constituent compounds (nitrogen, oxygen, and carbon dioxide), where c_{p} equals 1.07 kJ/kg·K. The cooling stream is a flow of water at 20 °C and atmospheric pressure.

IV.2.3 Costs for Economic Evaluation

A first estimate of the costs of the ORC system can be made by summing up the individual costs of the four major constituent components of the ORC, namely the two heat exchangers, the pump, and the expander. These are responsible for 50–70% of total installed costs in ORCs [36, 66] The ultimate goal is to investigate the effects of different working fluid mixtures on capital costs. The output of the economic evaluation is reported in terms of absolute costs in pounds (£) and in terms of pounds per unit power (£/kW), since it is the purchaser or user who decides on the optimal compromise between costs, performance, and system size.

Heat Exchanger Costs

The cost of a heat exchanger is a strong function of its size or, in other words, of the area available for heat transfer. A number of empirical correlations have been developed for estimating the costs of different type of heat exchangers. The difficulty with these correlations lies in the arriving at suitable definitions for the heat-transfer areas for the different types. The C-value method [67] cleverly circumvents this problem by defining a cost factor C as a cost per unit UA or per unit $\dot{Q}/\Delta T_{\mathrm{lm}}$ where A is the heat transfer area and U is the overall heat-transfer coefficient according to

$$\dot{Q} = UA\Delta T_{\mathrm{lm}}\,, \tag{IV.17}$$

where the logarithmic-mean temperature difference ΔT_{lm} (for the evaporator) is defined as

$$\Delta T_{\mathrm{lm}} = \frac{(T_{\mathrm{hs,in}} - T_3) - (T_{\mathrm{hs,out}} - T_2)}{\ln[(T_{\mathrm{hs,in}} - T_3)/(T_{\mathrm{hs,out}} - T_2)]}\,. \tag{IV.18}$$

To derive costs with the C-value method, we use the ESDU chart 92013 which contains tabulated values of overall heat-transfer coefficients U and cost factors C for different cold-side and hot-side fluids at fixed values of $\dot{Q}/\Delta T_{\mathrm{lm}}$. The values for $\dot{Q}/\Delta T_{\mathrm{lm}}$ are calculated from Eqs. IV.8, IV.12, IV.14, IV.16, and IV.18, and the 'U' and 'C' are obtained using a logarithmic interpolation:

$$C = \exp\left(\ln C_1 + \ln(C_1/C_2)\frac{\ln\left[(\dot{Q}/\Delta T_{\mathrm{lm}})/(\dot{Q}/\Delta T_{\mathrm{lm}})_1\right]}{\ln\left[(\dot{Q}/\Delta T_{\mathrm{lm}})_1/(\dot{Q}/\Delta T_{\mathrm{lm}})_2\right]}\right)\,. \tag{IV.19}$$

To obtain the cost of the heat exchanger, the C-value is multiplied with $\dot{Q}/\Delta T_{\mathrm{lm}}$ (the costs must still be adjusted for inflation). When using the ESDU chart, the C-values under 'Low Viscosity Organic Liquids' are used for the cold fluid side in the evaporator as this is the working fluid. For the flue gas of the heat source stream, we use 'Low Pressure Gas' as the hot fluid side in the evaporator. For the condenser, the C-values under 'Low Viscosity Organic Liquids' and 'Process Water' are used for the hot-fluid side (working fluid) and cold-fluid side (cooling water) respectively.

Expander and Pump Costs

Costs for suitable turbo-expanders and positive displacement expanders are derived from a market survey, similar to Ref. [36]. Positive displacement expanders are currently not widely commercially available for use in power generation. Therefore, costs of positive displacement expanders are based on positive displacement compressors of equivalent size. Expander costs are described as functions of the inlet volumetric flow-rate ($\dot{V}_3$) and the pressure ratio (P_{23}/P_{41}). The data surveyed covers a wide range of operating conditions: the volumetric flow-rates considered range from approximately 100 cm^3/s to 0.2 m^3/s and the inlet pressures range from 2 bar to 45 bar. A two-dimensional interpolation method is used to derive specific cost information for different operating conditions. A similar approach was used for the estimation of the pump costs.

As an alternative one can use the correlations provided in Seider et al. [68] which provide cost correlations for all types of process engineering machines and components. Regardless if one uses this source or the C-value method (for heat exchangers) [67], the costs must be adjusted for inflation using the Chemical Engineering Plant Cost Index (CEPCI) [69].

IV.3 Thermodynamic Properties of Working Fluids with SAFT-VR Mie

IV.3.1 SAFT Equation of State

Most deployed heat engines currently employ single-component fluids. Therefore, thermodynamic property modelling has always focused on pure fluids. For many compounds, reliable property data can be obtained from databases such as NIST/TRC Web Thermo Tables [70], REFPROP[71], or CoolProp [72] which contain a wide range of experimental

thermodynamic properties. However, experimental thermodynamic properties of fluid mixtures are often unavailable, especially regarding enthalpies, entropies, and heat capacities which are important parameters for modelling ORCs. In the rare cases when experimental data is available for mixtures, it is not necessarily for the mixture composition of interest. Thus, in order to model mixtures of any desired composition, a method of predicting reliable thermodynamic information is necessary.

Cubic equations of state (Eos), such as Peng-Robinson [73] and Soave-Redlich-Kwong [74], have been employed for several years especially in the oil and gas industry for modelling phase equilibrium properties. These equations are best suited for phase equilibrium properties of mixtures in the P-T-x (where x is the mixture composition), however they are not as reliable when predicting calorific properties, such as specific heat and enthalpy, for pure fluids and mixtures. These shortcomings are not surprising because cubic EoS are semi-empirical and the molecular model is based on hard spherical cores surrounded by spherically symmetrical regions of attraction, whereas molecules often take on other forms (e.g. chains).

Advances in statistical mechanics in combination with improved computational capabilities have been strong drivers for the development of an equation of state based on molecular principles which provide more realistic and accurate descriptions. The foremost example of these models is the statistical associating fluid theory (SAFT). Because the SAFT EoS is firmly grounded in statistical mechanics, it has a stronger predictive capability than cubic EoS. SAFT provides confidence in predictions outside of the experimental range used for the adjustment of the model parameters and also in predictions of parameters which were not used in the process of the model refinement.

In this study, we use the SAFT-VR Mie equation of state. An extensive discussion of SAFT-VR Mie and its advantages over cubic EoS was written by Lafitte et al. [75]. Notably, it was shown that this version of SAFT can produce accurate descriptions of each class of fluids that we considered in this study. We focus on alkanes and perfluoroalkanes as ORC working fluids in this study. SAFT-VR Mie models molecule behaviour and properties are based on the Helmholtz free energy. Fluid molecules are modelled as chains of m spherical segments that interact through a Mie (generalized Lennard-Jones) pair potential centered on each segment [75, 76]:

$$\phi(r) = \frac{\lambda_\mathrm{r}}{\lambda_\mathrm{r} - \lambda_\mathrm{a}} \left(\frac{\lambda_\mathrm{r}}{\lambda_\mathrm{a}}\right)^{\frac{\lambda_\mathrm{a}}{\lambda_\mathrm{r}-\lambda_\mathrm{r}}} \varepsilon \left[\left(\frac{\sigma}{r}\right)^{\lambda_\mathrm{r}} - \left(\frac{\sigma}{r}\right)^{\lambda_\mathrm{a}}\right] . \tag{IV.20}$$

In Eq. IV.20, r represents the separation between two interacting molecular segments, σ represents the size of the segment, ε is the depth of the potential well, and λ_r and λ_a are respectively the repulsive and attractive exponents characterizing the range of the potential. For $\lambda_\mathrm{r} = 12$ and $\lambda_\mathrm{a} = 6$, Eq. IV.20 becomes the standard Lennard-Jones potential [77]. Thus, the five parameters comprising the chain length m and the pair-potential parameters σ, ε, λ_r, and λ_a fully define the model of a non-associating fluid, such as alkanes or perfluoroalkanes.

The Helmholtz free energy a is expressed as the sum of an ideal and residual component. The latter consists of a sum of terms representing contributions due to monomer segments, the grouping of m segments into chains, and association in case of associating molecules. Hence, a simplified SAFT free energy equation can be expressed as:

$$a = a^{\mathrm{IDEAL}} + a^{\mathrm{MONO}} + a^{\mathrm{CHAIN}} + a^{\mathrm{ASSOC}} . \tag{IV.21}$$

We are not considering any associating molecules in this study, and hence $a^{\mathrm{ASSOC}} = 0$. The ideal component a^{IDEAL} is calculated with the ideal gas specific heat c_p^0 as function of the fluid temperature. The standard approach for obtaining ideal gas specific heats is to use correlations which use polynomials in temperature. A common method is to use the NASA or JANAF heat capacity polynomials (see Section VI.6 for more details) [78, 79]. However, when using SAFT-VR Mie, the current code employs a 3rd order polynomial as opposed to the 7th or 9th order polynomials from NASA. Integration of c_p^0 gives the enthalpy and integration of c_p^0/T gives the entropy from which a^{IDEAL} is obtained. The coefficients of the polynomials are listed in Table IV.1.

Table IV.1: Coefficients of 3rd order polynomials used to correlate the ideal-gas specific heat capacities c_p^0(J mol^{-1} K^{-1})$= a_0 + a_1 T + a_2 T^2 + a_3 T^3$ as functions of absolute temperature (in Kelvin) for n-C_4H_{10}, n-$C_{10}H_{22}$, n-C_4F_{10}, and n-$C_{10}F_{22}$. The heat capacities are take from the NIST database. The coefficients are valid between 200 K and 800 K.

Fluid	a_0	$a_1 \cdot 10$	$a_2 \cdot 10^4$	$a_3 \cdot 10^7$
n-C_4H_{10}	9.487	3.313	-1.108	-0.02822
n-$C_{10}H_{22}$	-7.913	9.609	-5.288	1.131
n-C_4F_{10}	46.37	6.197	-5.165	1.479
n-$C_{10}F_{22}$	64.95	17.21	-17.29	6.328

Standard thermodynamic relations are used to derive thermodynamic properties of interest once the Helmholtz free energy is defined. In SAFT-VR, the repulsive exponent

λ_r can be adjusted to suit the repulsive potential (and the spherical hardness) of the segments. This allows accurate descriptions of second derivative properties, such as heat capacities, while providing reliable representations of the phase equilibrium behaviour. This aspect is important for the current study. Mixtures are modelled with van der Waals one-fluid mixing with standard combining rules and no further adjustments or binary-interaction parameters are employed. More details on the mixure modelling can be found in Lafitte et al. [75]. The intermolecular parameters for the pure compounds are presented in Table IV.2.

To demonstrate the predictive power of the SAFT-VR Mie we consider fluorocarbon mixtures of *n*-perfluorobutane and *n*-perfluorodecane (*n*-C_4F_{10} + *n*-$C_{10}F_{22}$). There is no mixture data available in the literature, and therefore we shall use mixtures of corresponding analogue alkanes of *n*-butane and *n*-decane (*n*-C_4H_{10} + *n*-$C_{10}H_{22}$) for validating the modelling approach. The results of the fluorocarbon model are compared with the alkane model. Alkanes are particularly well suited for validation because they are common ORC working fluids and extensive experimental thermodynamic property data is available for both of the considered alkanes. Furthermore, alkanes just like perfluoroalkaness are non-associating molecules and therefore provide a good starting point before proceeding to more complex molecules.

The models for the alkanes and for perfluorobutane are already available [75]; the model development for perfluorodecane is presented in the paper by Oyewunmi et al. [76]. Model parameters are obtained by adjustment to provide the best description of experimental vapour pressures P_{sat}, saturated liquid densities ρ_{sat}, single-phase densities (subcooled liquid and superheated vapour), and the speed of sound u. A least-squares objective function comprising the sum of the residuals from each of the considered properties is minimized. Please refer to Lafitte et al. [75] or Oyewunmi et al. [76] for more details. The model parameters which resulted from the optimization are shown in Table IV.2. The pressure and temperature ranges considered for the experimental data can be found in Ref. [76].

IV.4 Validation of SAFT Predictions

The effectiveness of the SAFT modelling approach in predicting thermodynamic properties is demonstrated in Figs. IV.2–IV.5. Thermodynamic cycles are often analysed in *T*-*s* or *P*-*h* diagrams, hence experimental data in these spaces would ideally be used for validating the SAFT calculations. To the best of our knowledge, experimental data of

Table IV.2: Model parameter values for the pure compounds estimated from experimental single phase and phase equilibrium data using SAFT-VR Mie EoS. Values for the alkanes and n-C_4F_{10} are taken from Ref. [75]. Values for n-$C_{10}F_{22}$ were generated for this study starting from the same λ_a value as that of n-C_4F_{10} and λ_r was tuned to best match experimental data.

Fluid	m	σ/Å	(ε/k_B)/K	λ_r	λ_a
n-C_4H_{10}	1.8514	4.0887	273.64	13.650	6.0
n-$C_{10}H_{22}$	2.9976	4.5890	400.79	18.885	6.0
n-C_4F_{10}	2.1983	4.4495	290.49	24.761	5.7506
n-$C_{10}F_{22}$	2.8693	5.2581	382.63	26.508	5.7506

the phase equilibrium in these spaces of the compounds considered are only available for pure fluids. Additionally, we are not aware of experimental data in the P-x, T-x or P-T space of the n-C_4F_{10} + n-$C_{10}F_{22}$ mixture system. In Figs. IV.2–IV.5, symbols represent experimental data, while curves represent calculations.

IV.4.1 Thermodynamic Properties of Pure Working Fluids

In Fig. IV.2(a), we show the saturation curve in the temperature density space of n-perfluorobutane (n-C_4F_{10}) calculated with SAFT-VR Mie. Additionally, density isobars are included at the pressures P = 2, 5, 20, and 40 bar. The same type of diagram for n-perfluorodecane (n-$C_{10}F_{22}$) is shown in Fig. IV.2(b). One can also find density isobars at 1, 4, and 10 bar, while experimental data for isobars is only available from 1 to 4 bar. The agreement in fluid density between calculations and experimental values in all regions of interest – sub-critical condensed liquid, superheated vapour, and supercritical fluid – is excellent. This degree of accuracy is difficult to achieve with an analytical EoS, and we are not aware of literature where a similar degree of agreement has been reported. Especially fluorinated hydrocarbons are difficult to describe, which is partly due to the strong repulsive nature and polarizability of the electronegative fluorine in the molecules.

Specific heat capacities as functions of temperature of perfluorobutane and perfluorodecane are shown in Fig. IV.2(c) and (d) respectively. Four isobars at P = 2, 5, 20, and 40 are included in Fig. IV.2(c) which span both sub-critical and supercritical regions of the vapour and liquid. A slight disagreement near the critical region can be observed in Fig. IV.2(c), but otherwise the agreement between calculations and experimental data is very good. The predictive power of SAFT-VR Mie is well demonstrated here, since

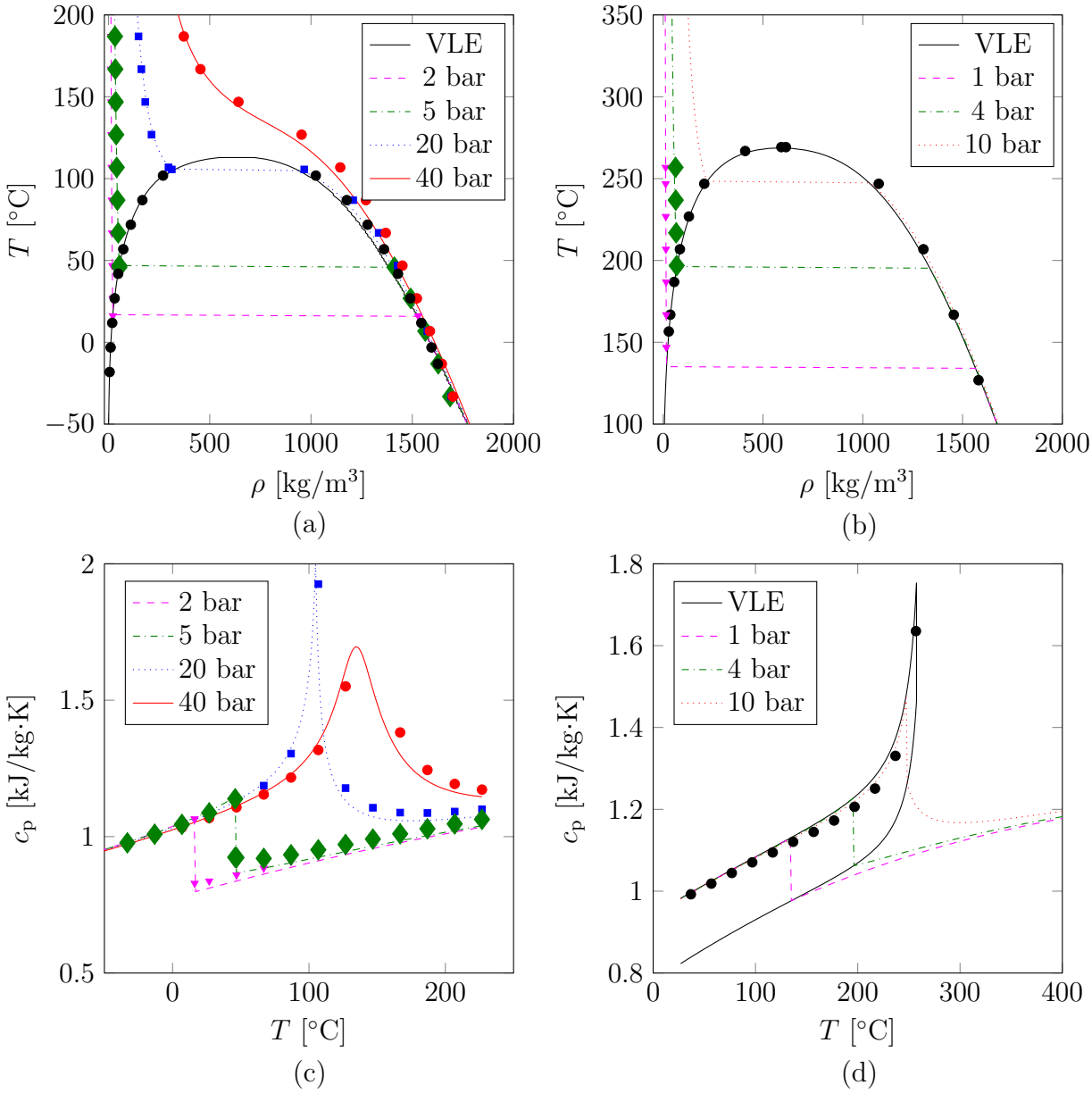


Figure IV.2: Selected thermodynamic properties of *n*-perfluorobutane (*n*-C_4F_{10}) and *n*-perfluorodecane (*n*-$C_{10}F_{22}$). Vapour-liquid T-ρ coexistence envelopes and density isobars (at pressures indicated in the legend) for (a) *n*-perfluorobutane and (b) *n*-perfluorodecane. Temperature dependence of the isobaric heat capacity c_p of (c) *n*-perfluorobutane and (d) *n*-perfluorodecane. Comparison of experimental data from NIST (symbols) with the description obtained using SAFT-VR Mie EoS (solid curves). The singularities in (c) for 20 and 40 bar are due to the phase change.

the specific heat capacity was not used for refining the model parameters. As for perfluorodecane in Fig. IV.2(d), experimental data was only available for the saturated liquid phase. Once again, the calculations are consistent with the available experimental data.

In Fig. IV.3, the properties of the alkane analogues (n-butane and n-decane) are illustrated in the T-ρ and c_p-T spaces (similar to Fig. IV.2). The descriptions of the pure fluid properties provided by SAFT-VR Mie are in good agreement with the available experimental data. In summary, Figs. IV.2 and IV.3 prove that SAFT-VR Mie provides excellent predictions of thermodynamic properties of the four pure compounds.

IV.4.2 Thermodynamic Properties of Binary-Mixture Working Fluids

In Fig. IV.4, we show SAFT-VR Mie calculations of mixtures in the P-T-x space. Available experimental data in these spaces are also included in the plot. P-T vapour pressure curves for pure n-butane ($x_{C_4H_{10}} = 1$) and n-decane ($x_{C_4H_{10}} = 0$) and bubble point curves of mixtures with constant composition x are shown in Fig. IV.4(a). The dew point curves have been omitted to maintain clarity in the figure. Experimental data is included from NIST [70] and two other sources (Ref. [80, 81]), however, the experimental data only span a section of the P-T bubble curve, whereas the SAFT-VR Mie calculations cover the entire bubble curve. This enables a better description of the transition between the two pure components. In Fig. IV.4(b), isothermal P-x envelopes calculated with SAFT-VR Mie at four different temperatures are shown which represent the bubble and dew-point descriptions. The symbols represent experimental values from Ref. [82]. From Fig. IV.4(a) and (b), we can see that SAFT-VR Mie calculations provide an excellent description of phase equilibria in the P-T-x space for pure and mixed alkanes. There are slight deviations in the critical region, as analytical EoS cannot simultaneously capture critical and sub-critical regions [83]. Nevertheless, the overall agreement between SAFT-VR Mie and the experimental data remains very good.

Pressure-temperature phase boundaries for pure n-perfluorobutane and n-perfluorodecane and for intermediate binary mixtures are shown in Fig. IV.4(c). The symbols in the plot represent experimental data taken from the NIST database. SAFT-VR Mie provides a very good description of the phase behaviour of the pure fluorocarbons. Unfortunately, there are no experimental data available for mixtures of these two compounds. However, we can see from Fig. IV.4(a) that the envelopes of the perfluoroalkanes follow a similar trend as the alkanes which have been substantiated with experimental values. Therefore,

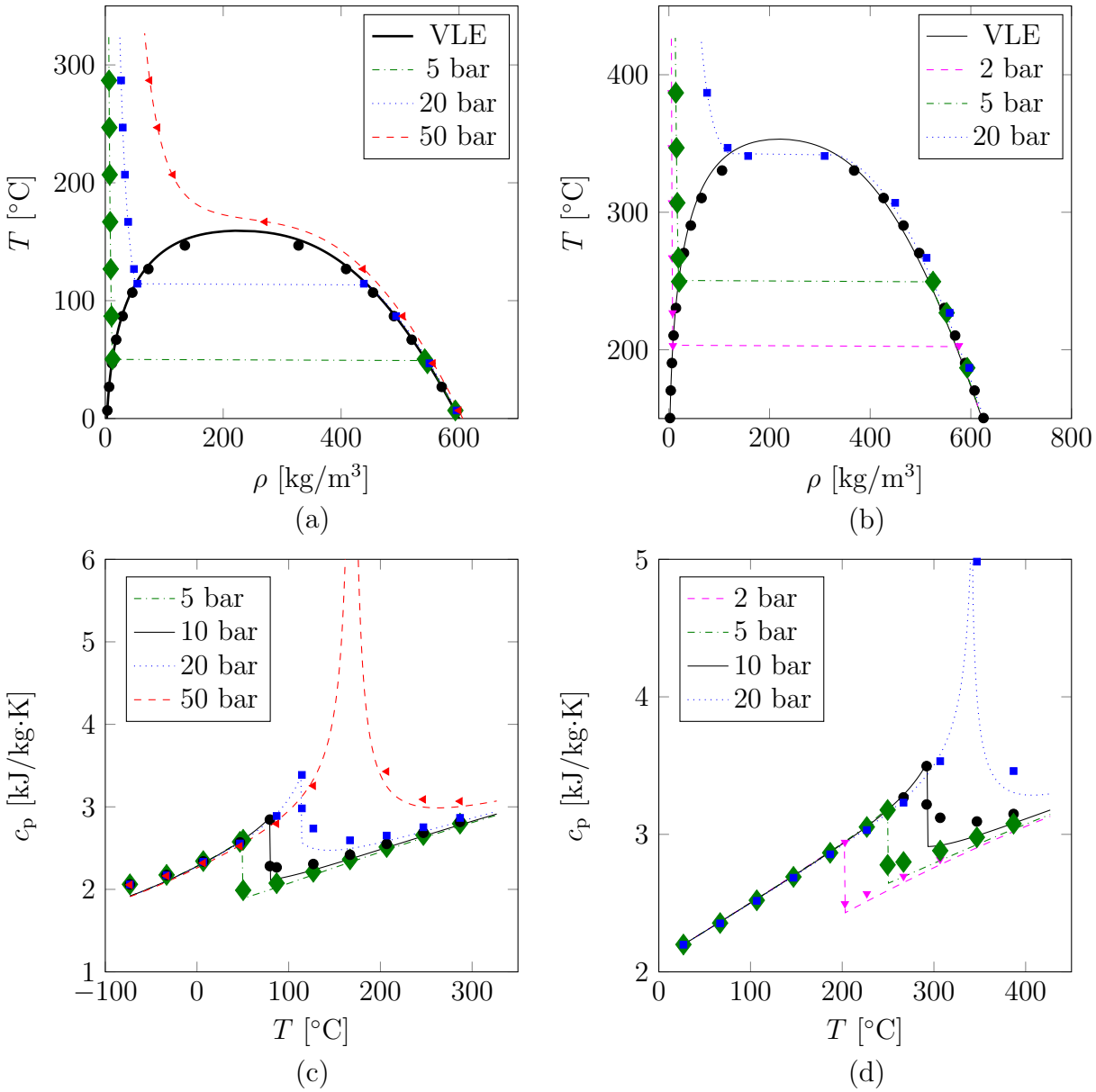


Figure IV.3: Selected thermodynamic properties of n-butane (n-C_4H_{10}) and n-decane (n-$C_{10}H_{22}$). Vapour-liquid T-ρ coexistence envelopes and density isobars (at pressures indicated in the legend) for (a) n-butane and (b) n-decane. Temperature dependence of the isobaric heat capacity c_p of (c) n-butane and (d) n-decane. Comparison of experimental data from NIST (symbols) with the description obtained using SAFT-VR Mie EoS (solid curves). The singularities in (c) for 20 and 40 bar are due to the phase change. The singularities in (c) and (d) at higher pressures are due to the phase change.

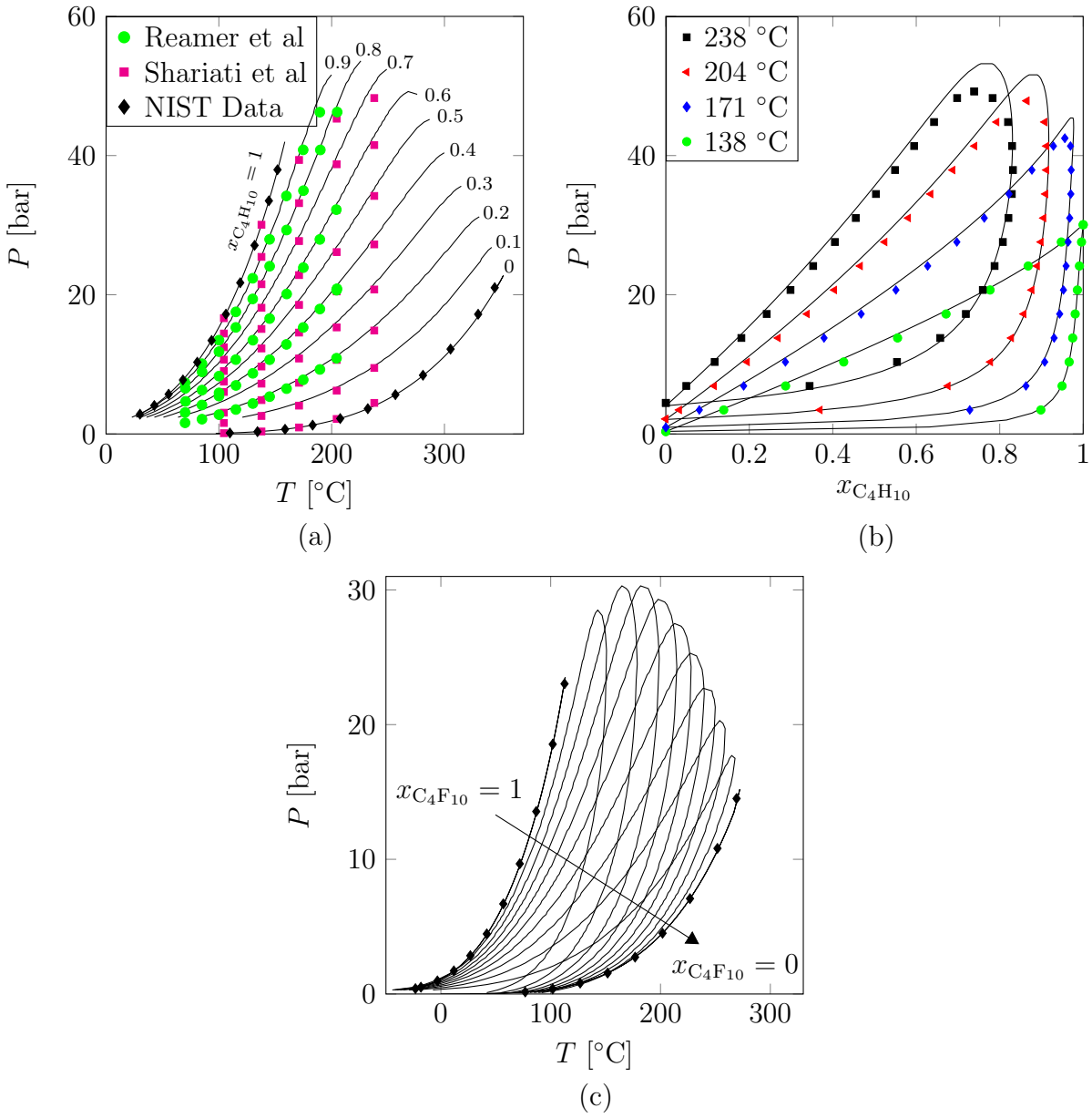


Figure IV.4: Vapour-liquid equilibria of selected fluid mixtures. (a) Pressure-temperature (P-T) phase boundaries (bubble-point curves) at different mixture compositions ($x_{C_4H_{10}}$) predicted by SAFT-VR Mie (solid curves). The symbols indicate validation data from the NIST database for n-butane and n-decane and from Refs. [80, 81] for mixtures. (b) Isothermal pressure-composition (P-x) phase boundaries (saturation curves) as predicted by SAFT-VR Mie (solid curves) and validation data from Ref. [82] are represented by the symbols. (c) Pressure-temperature phase boundaries for pure n-perfluorobutane ($x_{C_4F_{10}} = 1$) and n-perfluorodecane ($x_{C_4H_{10}} = 0$) and intermediate binary mixtures with validation data taken from the NIST database for the pure compounds.

one can be confident that vapour-liquid predictions for perfluoroalkanes mixtures are just as accurate as those for their alkane analogues.

This section concludes with a discussion of predictions in the T-s and P-h spaces which are crucial for the analysis of thermodynamic cycles. In Fig. IV.5(a) and (b), phase envelopes for pure perfluoroalkanes (n-perfluorobutane and n-perfluorodecane) and their intermediate mixtures are shown in the T-s and P-h space respectively in order to show the transition in the phase behaviour. Experimental data from NIST is also included for the pure fluids. The phase envelopes for the alkanes in the T-s and P-h spaces are shown in Fig. IV.5(c) and (d). The agreement between the SAFT-VR Mie predictions and the experimental data is very promising. It is especially remarkable if we recall that the entropy and enthalpy were not used for fine-tuning the model parameters σ, m, ε, λ_{a}, and λ_{r}.

In conclusion, the high degree of agreement between SAFT-VR Mie calculations and experimental values for pure fluids demonstrated in Figs. IV.2–IV.5 underline the predictive power of the proposed modelling approach. Moreover, the agreement between calculations and experiments for alkane mixtures in the P-T, P-h, and T-s spaces is excellent. This provides confidence in the reliability of thermodynamic property predictions for mixtures for which experimental P-h and T-s envelopes are not readily available such as the considered perfluoroalkanes. Given that the perfluoroalkanes are structural analogues of the alkanes (which were well validated) and that both chemical classes exhibited similar behaviour in Figs. IV.2–IV.5, predictions for thermodynamic properties of perfluoroalkanes mixtures are also considered to be accurate. One of the primary goals of this study is to provide a reliable method to predict properties of pure and mixed fluids, especially in the T-s and P-h spaces. The results in this section have shown that this is the case for the chemical compounds considered here as working fluids.

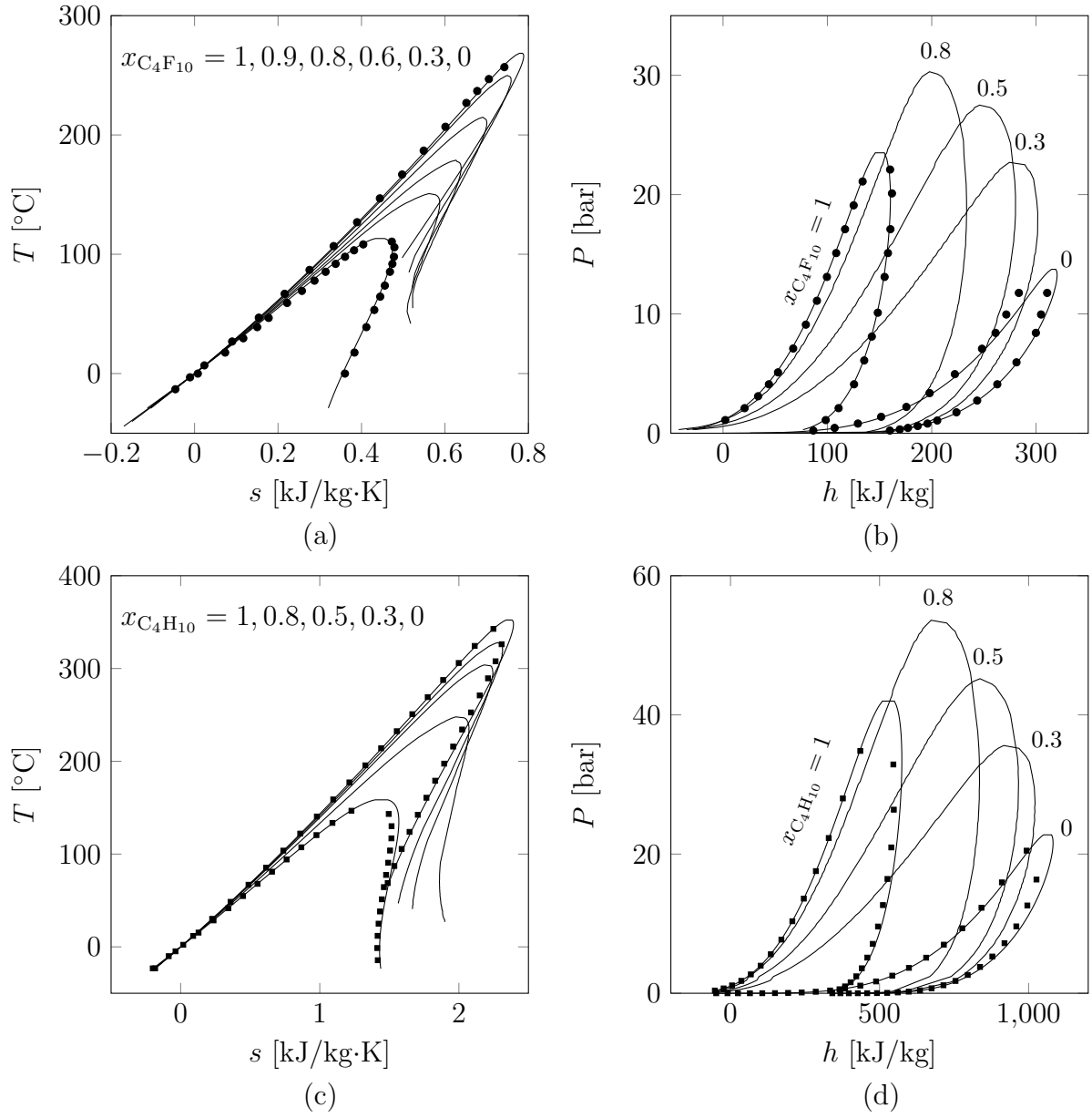


Figure IV.5: Phase boundaries in the T-s and P-h spaces as predicted using SAFT-VR Mie for pure working fluid and mixtures. (a) T-s envelopes for pure n-perfluorobutane, pure n-perfluorodecane, and intermediate binary mixtures composed of 30 mol%, 60 mol%, 80 mol%, and 90 mol% n-perfluorobutane. (b) P-h envelopes for pure n-perfluorobutane, pure n-perfluorodecane, and intermediate binary mixtures composed 30 mol%, 50 mol%, and 80 mol% n-perfluorobutane. (c) T-s envelopes for pure n-butane, pure n-decane, and intermediate binary mixtures composed of 30 mol%, 50 mol%, and 80 mol% n-butane. (d) P-h envelopes for pure n-butane, pure n-decane, and intermediate binary mixtures composed 30 mol%, 50 mol%, and 80 mol% n-butane.

Chapter V

Results and Discussion of ORCs using Working Fluid Mixtures

V.1 Boundary Conditions

Thermodynamic properties – in particular heat capacities, enthalpies, entropies, and densities – are generated for the working fluids in the P-T-x space with the SAFT approach as discussed in Chapter IV. The values are stored in lookup tables and accessed by the ORC model via interpolation. The evaporation pressure P_{23}, the mixture composition x, the degree of superheat d_{sh}, and the working-fluid mass flow-rate $\dot{m}_{\mathrm{wf}}$ are varied between an upper and lower bound shown in Table V.1. The maximum temperature $T_{3,\mathrm{max}} = 320$ °C because the flue gas has a temperature of 330 °C (mass flow-rate of hot stream of 560 kg/s) and a minimum pinch-point difference of 10 °C is applied. The primary objective in this study is to understand the effect of these variables on the power output, the power output per unit working-fluid flow-rate, the thermal efficiency, and the cost of the considered ORC application.

Figures V.1–V.3 present the specific power output $\dot{W}/\dot{m}$, absolute (net) power output $\dot{W}$, thermal efficiency η_{th} as functions of the n-butane or n-perfluorobutane mole fraction in n-butane + n-decane or n-perfluorobutane + n-perfluorodecane working-fluid mixtures. Evaporating pressures P_{41} range from 6 bar to 40 bar. However, this study aims to investigate sub-critical ORCs, and therefore only systems with evaporating pressures below 90% of the critical pressure are considered. Overall trends are similar between alkanes and perfluoroalkanes, however perfluoroalkanes tend to have much lower critical

Table V.1: Ranges of investigated variables.

Variable	Lower bound	Upper bound
P_{23}	6 bar	90% of P_{crit}
x	0	1
d_{sh}	0 ($T_3 = T_{\text{dew}}(P_{23})$)	1 ($T_3 = T_{3,\text{max}} = 320°\text{C}$)
$\dot{m}_{\text{wf}}$	0.001 kg/s	Maximum possible allowed by pinch points

pressures than alkanes such that the highest evaporation pressure considered for any of the perfluoroalkane mixtures is 22 bar.

To maximize work output and efficiency, condensing at the lowest possible temperature and pressure is generally desired. Given that the inlet temperature of the cooling stream is 20 °C and the minimum temperature difference is 10 °C, the temperature of the working fluid at State 1 (outlet of the condenser, see Fig. IV.1(a) and (b)) can only go as low as 30 °C. Another restriction in the ORC system is that the pressure is not allowed to expand below atmospheric pressure. Sub-atmospheric pressures require expensive and complex designs and sealing. Therefore, the lowest possible pressure in the cycle (condensation pressure P_{41}, see see Fig. IV.1(a) and (b)) is 1 bar. The two limitations described above can be expressed mathematically as $T_1 = T_{\text{bub}}(P_{41}) \geq 30$ °C and $P_{41} = P_1 = \max\{1 \text{ bar}, P_{\text{bub}}(T_1)\}$. We consider the idealized case of a cooling stream with an infinite flow-rate in Sections V.2–V.4. The cooling-stream temperature in this case is constant and $T_1 = \max\{30 °\text{C}, T_{\text{bub}}(1 \text{ bar})\}$ and $P_{41} = P_1 = \max\{1 \text{ bar}, P_{\text{bub}}(30 °\text{C})\}$. We also consider cases with constrained cooling streams in Section V.5.

It can be seen from Figs. V.1–V.3 that mixtures with low butane or perfluorobutane fractions have sub-atmospheric bubble-point pressures at the desired condenser outlet temperature (of the working-fluid stream) of 30 °C. However, we set a condition prohibiting the expansion below atmospheric pressure. Therefore, for alkane mixtures with $x_{C_4H_{10}}$ below 30 mol% and perfluoroalkane mixtures with $x_{C_4F_{10}}$ below 20 mol% the condensation pressure P_{41} is set to 1 bar, and the condensation temperature at the condenser exit T_1 (equal to the saturation temperature at 1 bar) is higher than 30 °C: $T_1 = T_{\text{bub}}(P_{41} = 1 \text{ bar}) \geq 30$ °C. Therefore, we distinguish between two regimes. In the first regime (Regime I), the condensation pressure is set to $P_{41} = 1$ bar and the condenser outlet temperature T_1 is above 30 °C. The second regime (Regime II) encompasses cases where the cycle is expanded to the saturation pressure corresponding to the condenser outlet temperature of $T_1 = 30$ °C, $P_{41} = P_{\text{bub}}(T_1 = 30 °\text{C})$ (which is above 1 bar). Re-

sults of when the working fluid is allowed to expand below 1 bar to reach a temperature of 30 °C, or $P_{41} = P_{\text{bub}}(T_1 = 30\ ^\circ\text{C}) < 1$ bar, are also shown for comparison and are represented by dotted lines.

V.2 Power Output

V.2.1 Specific Power Output

In Fig. V.1, the specific power output $\dot{W}/\dot{m}$ is plotted as a function of the butane (for n-butane + n-decane mixtures) or perfluorobutane (for n-perfluorobutane + n-perfluorodecane mixtures) mole fractions. For non-superheated cycles (Fig. V.1(a) and (d)), the optimal working fluid in terms of maximum specific power output has a composition of 30 mol% butane or 20 mol% perfluorobutane. Superheating increases specific power output as observed in other studies due to the increased specific enthalpy difference through the expander. For cases where the working fluid is superheated to the maximum degree allowed by the heat-source stream ($d_{\text{sh}} = 1$ and $T_3 = 320\ ^\circ\text{C}$), pure butane and pure perfluoroalkane are the optimal working fluids. Generally, the perfluoroalkanes exhibit the same behaviour as the alkanes although the specific power output is less by a factor of 4 to 5. This is due to the comparably low specific heat capacities of perfluoroalkanes. The specific power output $\dot{W}/\dot{m}$ decreases with increasing butane fraction, especially at low evaporation pressures, since butane has a lower specific enthalpy difference between State 3 and State 4 (h_{34}) compared to decane. In addition, mixtures with higher butane contents have higher dew-point pressures at 30 °C meaning that ORCs with such mixtures expand the fluid to higher pressures thereby producing lower power outputs. For the cases, where the working fluid (with a high decane content) is allowed to expand below 1 bar and 30 °C (represented by the dotted lines in Fig. V.1), the output monotonically decreases with increasing butane content. Pure decane in this case produces the highest power output due to its very low saturation pressure (0.0026 bar). However, when the condensing pressure is set to 1 bar as in Regime I, the condensing temperature of pure decane, for instance, is 173 °C. The difference in specific enthalpy h_{34} is therefore reduced significantly.

V.2.2 Net Power Output

The specific power output is a useful performance indicator because it only depends on the thermodynamic properties of the cycle but not the flow-rates of the heating and cooling

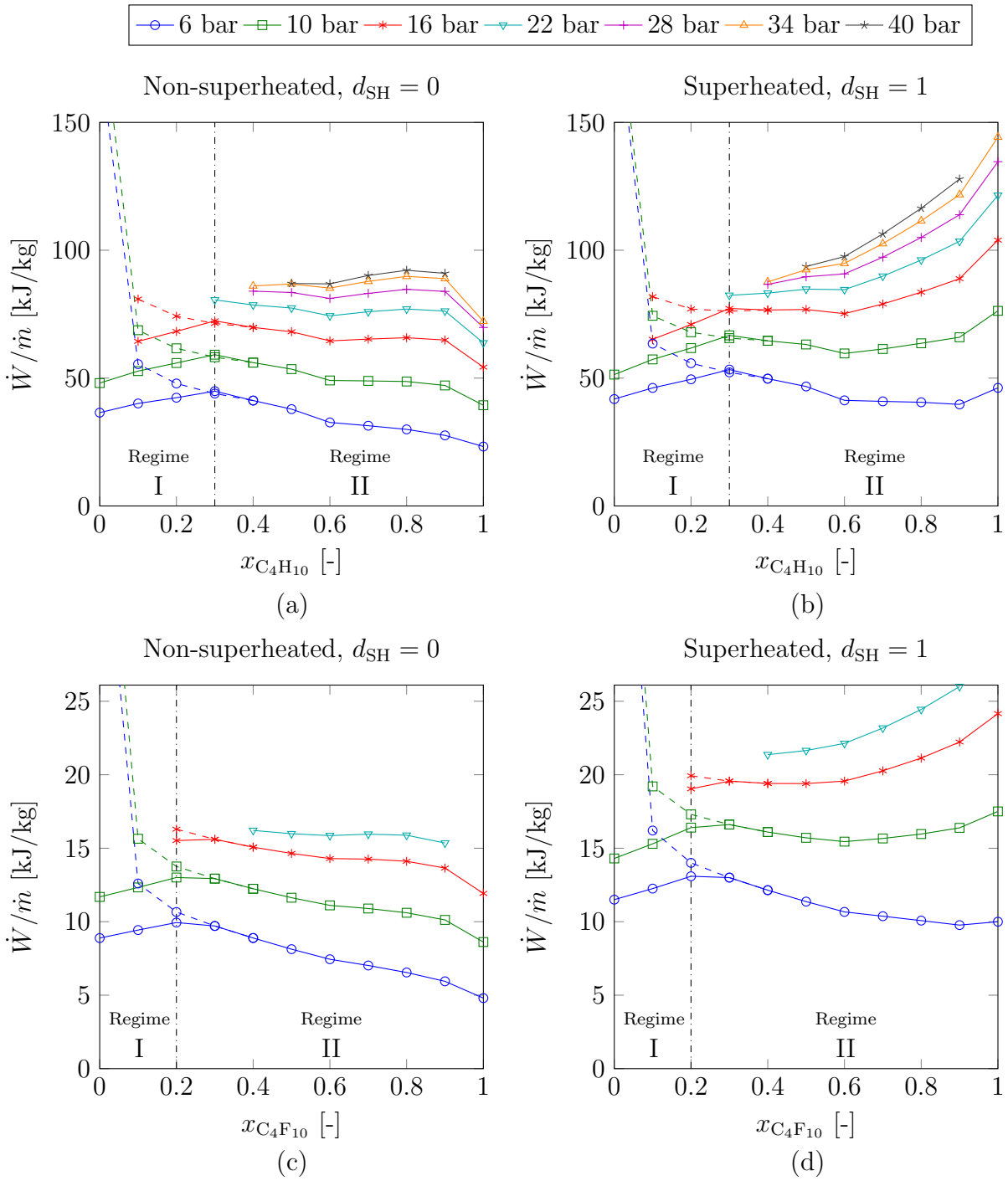


Figure V.1: Power output per unit mass flow-rate at different evaporation pressures P_{23} based on: (a) non-superheated cycles ($d_{SH} = 0$), and (b) maximum superheated cycles ($d_{sh} = 1$) as functions of *n*-butane mole fraction $x_{C_4H_10}$; (c) non-superheated cycles ($d_{sh} = 0$), and (d) maximum superheated cycles ($d_{sh} = 1$) as functions of *n*-perfluorobutane mole fraction $x_{C_4F_10}$. The dashed lines, representing the cases of sub-atmospheric expansion (to the dew-point pressure at 30 °C), are provided for comparison.

streams. However, it is not a sufficient figure-of-merit for a given ORC application if maximizing power output is the primary aim. In such a case, specific power output can be misleading in choosing an appropriate cycle design and working fluid. The maximum net power output is a more suitable measure. It accounts for the flow-rate of the working-fluid which can be calculated directly for a given cycle by increasing it until the pinch condition is met.

The net power output is plotted as a function of the butane/perfluorobutane mole-fraction for non-superheated and superheated ($d_{\mathrm{sh}} = 1$) cycles in Fig. V.2(a)-(d). The maximum power output over all degrees of superheat d_{sh} is plotted in Fig. V.2(e) and (f) for alkanes and perfluoroalkane mixtures. Perfluoroalkane cycles produce distinctly lower power outputs than cycles running with alkanes, although the trends are generally the same. Contrary to what the results in specific power output may imply, non-superheated cycles produce higher power outputs than superheated ones. Furthermore, Fig. V.2(a) and (c) are virtually identical to Fig. V.2(e) and (f) respectively demonstrating that cycles optimized for maximum power output should not be superheated. When it comes to the optimal mixture composition, 30 mol% butane and 20 mol% perfluorobutane produce the highest power at low evaporation pressures up to 6 bar. In Regime II ($x_{\mathrm{C_4H_{10}}} > 30$ mol%, $x_{\mathrm{C_4F_{10}}} > 20$ mol%), the net power is almost constant for low evaporation pressures. At high evaporation pressures, the power output increases monotonically with the mole fraction, and the highest power output is produced with pure *n*-butane/*n*-perfluorobutane.

V.3 Thermal Efficiency

In Fig. V.3, the thermal efficiencies of the cycles investigated in Figs. V.1 and V.2 are plotted. Cycles operated with pure *n*-decane/*n*-perfluorodecane working fluids have exhibited the highest efficiencies at low evaporation pressures. At high evaporation pressures, cycles with pure *n*-butane/*n*-perfluorobutane have the highest efficiency. This is valid for both non-superheated and superheated cycles. Thus, to maximize the thermal efficiency in this ORC application, mixtures should be avoided. The efficiencies of cycles running on perfluoroalkanes show efficiencies 1–2% lower than alkane cycles partly due to the lower heat capacities and enthalpies of vaporization of perfluoroalkanes.

Cycles with maximum degree of superheat (Fig. V.3(b) and (d)) exhibit a lower efficiency than non-superheated cycles ((Fig. V.3(a) and (c))). This observation may be surprising given that the average temperature of heat addition and the maximum tem-

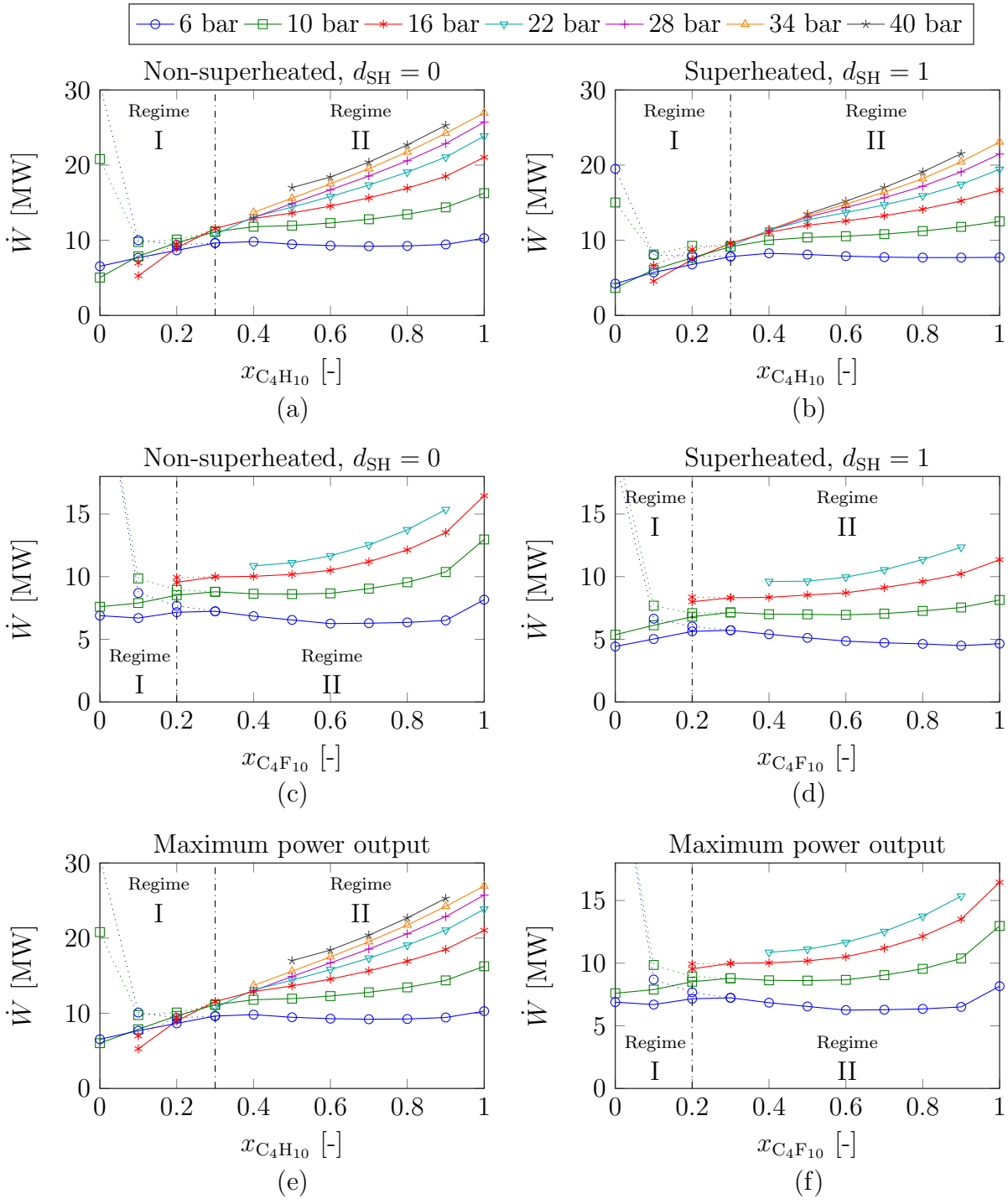


Figure V.2: Maximum absolute net power output $\dot{W}$ based on: (a) non-superheated cycles ($d_{sh} = 0$), and (b) maximum superheated cycles ($d_{sh} = 1$) as functions of *n*-butane mole fraction $x_{C_4H_{10}}$; (c) non-superheated cycles ($d_{sh} = 0$), and (d) maximum superheated cycles ($d_{sh} = 1$) as functions of *n*-perfluorobutane mole fraction $x_{C_4F_{10}}$; maximum power output over all degrees of superheat as functions of (e) *n*-butane mole fraction and (f) *n*-perfluorobutane mole fraction.

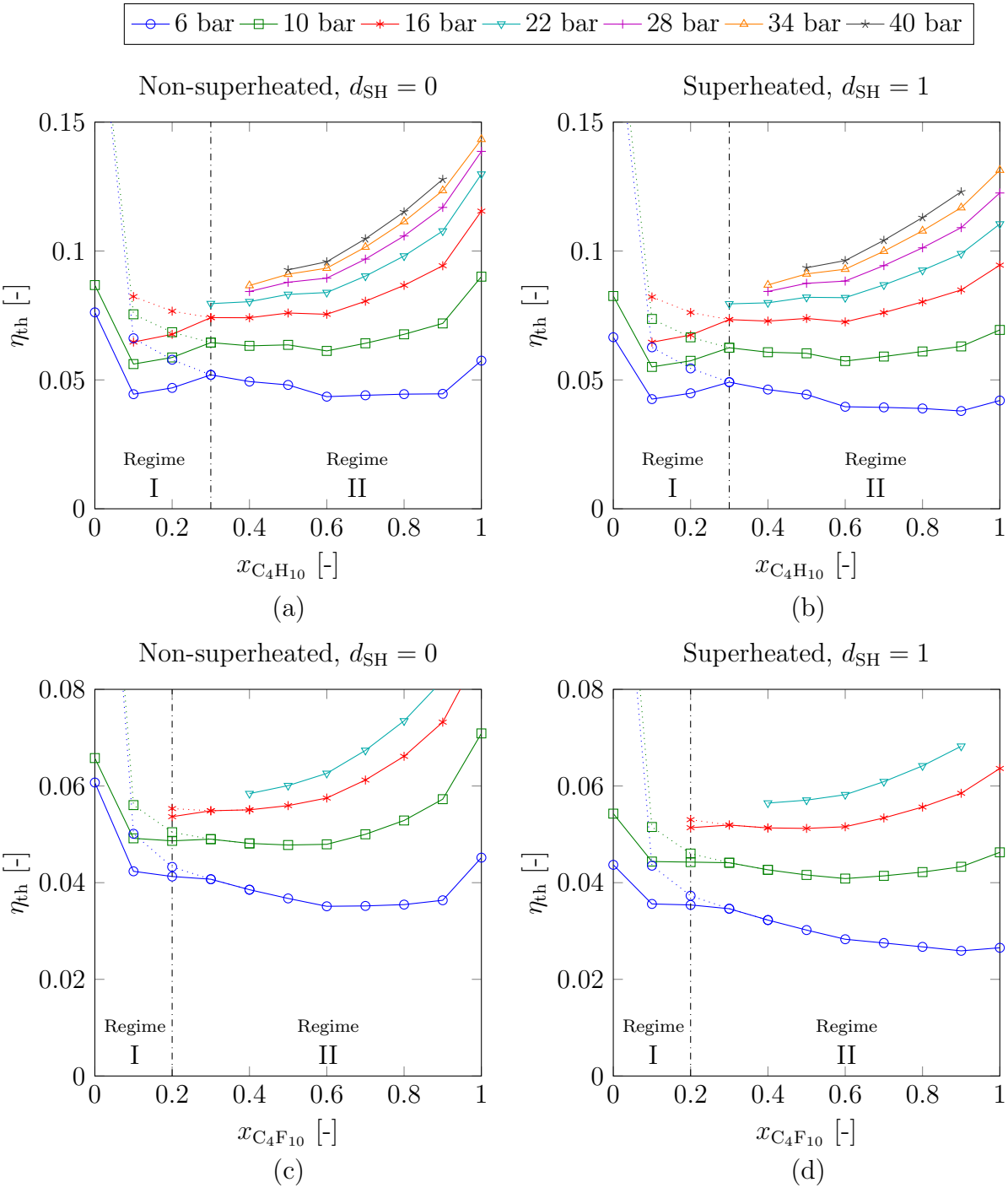


Figure V.3: Thermal efficiency η_{th} of: (a) non-superheated cycles ($d_{sh} = 0$), and (b) maximum superheated cycles ($d_{sh} = 1$) as functions of n-butane mole fraction $x_{C_4H_{10}}$; (c) non-superheated cycles ($d_{sh} = 0$), and (d) maximum superheated cycles ($d_{sh} = 1$) as functions of n-perfluorobutane mole fraction $x_{C_4F_{10}}$.

perature are higher in the superheated cycles. However, the average temperature of heat rejection is also higher in superheated cycles which reduces the efficiency. In addition, *n*-decane/*n*-perfluorodecane are 'drier' than *n*-butane/*n*-perfluorobutane such that the dryness of a mixture increases with the proportion of decane. The vapour entering the condenser is thus increasingly superheated which leads to a penalty in thermal efficiency. This also implies that superheating increases the efficiency of cycles using wet fluids. At higher evaporation pressures, the decrease in efficiency due to superheating is less pronounced.

The cost of the heat source in a waste-heat conversion-plant is very cheap relative to the cost of the heat source in a fossil-fuel power-plant. Therefore, in waste-heat recovery and energy integration applications, power output is favoured over thermal efficiency as a figure-of-merit. Thermal efficiency and power output do not necessarily give similar indications for optimal performance. An increase in efficiency leads to a decrease in power in cycles where the temperatures of the heat source and heat sink change. This is contrary to cycles where heat is added and rejected from constant-temperature heat-reservoirs [84]. This behaviour in our case has been observed for $x_{C_4H_{10}} = 0.1$ mixtures. The maximum power output for $P_{23} = 16$ bar is lower than that for $P_{23} = 10$ bar and $P_{23} = 4$ bar, although the thermal efficiency is higher. The power output is increased by an increase in the mass flow-rate. From a certain point, the working-fluid inlet temperature of the evaporator must be reduced lest the pinch condition be violated. This leads to an overall reduction of efficiency. Hence, maximum efficiency does not necessarily require the maximum amount of heat be extracted from the heat source and, therefore it does not always coincide with the highest possible power output.

The results presented in Fig. V.3 indicate that pure butane is associated with higher efficiencies than mixtures. This finding is in contrast to several observations in the literature as mentioned in Section IV.1. In theory, mixtures allow an increase in the average temperature of heat addition without violating the pinch condition, and therefore they have the potential of increasing power output and efficiency. However, mixtures may also increase average temperature of heat rejection which has an adverse effect on the performance of the cycle. This is illustrated in Fig. V.4 where we juxtapose an ORC employing pure butane as a working fluid (Fig. V.4(a)) against an ORC using a 50 mol% butane mixture (Fig. V.4(b)). The enclosed area of the cycle in the T-s diagrams is a measure of the net work output per cycle, while the ratio of the enclosed area to the area below the heat addition process is a measure of the thermal efficiency. In Fig. V.4, we can see that the non-isothermal heat rejection of the mixture decreases the enclosed area

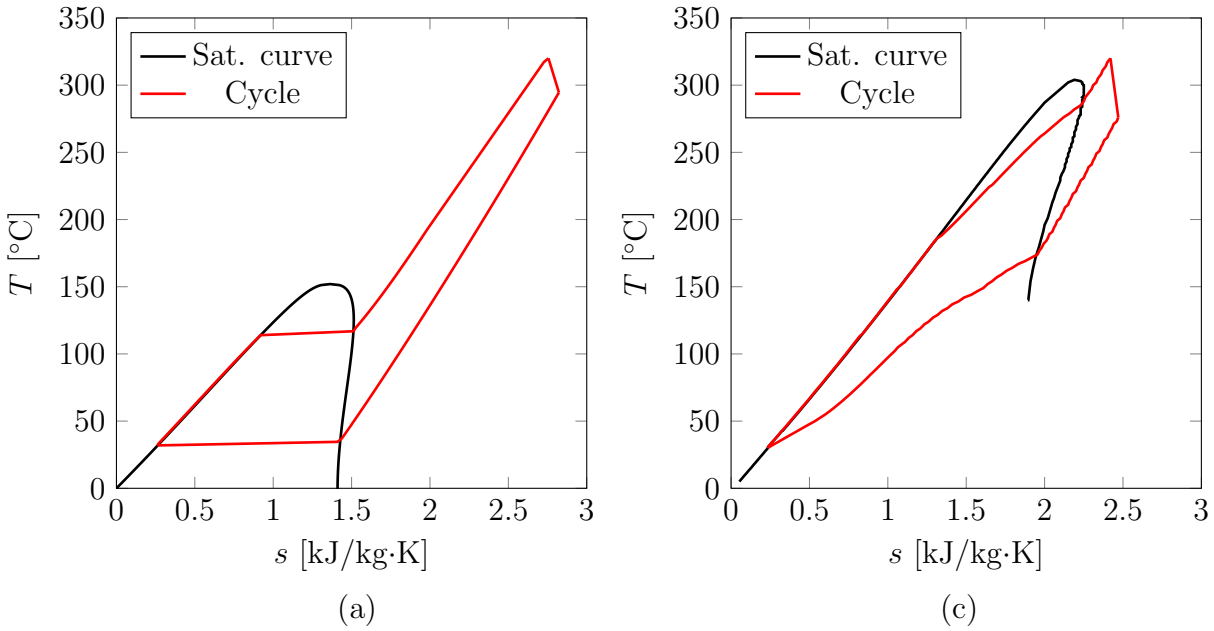


Figure V.4: (a) Pure butane cycle and (b) equivalent cycle of 50 mol% butane-decane mixture (right) in T-s space. Also shown are the saturation curves of the corresponding working fluids (black).

compared to the pure fluid cycle which is the reason for the reduced power output and efficiency of the cycle.

In conventional power generation where access to large amounts of cooling water is available (such that the heat sink has a constant temperature), an ideal mixture would exhibit an optimal temperature glide during evaporation and azeotropic behaviour during condensation. In such a case, the average temperature difference during heat addition and rejection is minimized. In ORCs employed for energy integration and combined heat and power, an optimal plant will most often require a trade-off between the temperature glides in the evaporator and condenser.

It may be interesting at this point to consider how changing the isentropic efficiency of the expander can influence the performance of the ORC and by extension change the choice of the optimal working. As mentioned in Chapter IV, the isentropic efficiency is set at 0.75. In a seperate study by Kirmse et al. [85] different isentropic efficiencies were considered for an ORC running on a variety of working fluids. The power output and thermal efficiency increased monotonically with the isentropic efficiency. A 10% increase in isentropic efficiency increased the power output by approximately 5–10% and increased thermal efficiency by less than 5%. All in all an increase in isentropic efficiency only leads

to an increase of power output of the same proportion, however it has little bearing on the choice of the optimal working fluid.

V.4 Cost Comparisons

V.4.1 Variations of ORC Costs with Power Output

In Fig. V.5, the total costs of ORCs using alkane (butane, decane, and their mixtures) working fluids are illustrated as function of the power output and thermal efficiency. The total costs are the summation of the purchasing costs of the four main components – working fluid pump, evaporator, expander or turbine, and condenser. Although the cost values are adequate for comparison, the actual installation costs of an ORC system are higher. The costs of the four main component typically represent 50–70% of the total installed costs of an engine in waste heat application [36, 66]. The costs for cycles using perfluoralkane working fluids exhibit the same trends as the alkanes illustrated in Fig. V.5 and are therefore omitted.

There is a strong correlation between the power output and the cost. For small and medium-scale ORC engines up to 100 kW, the total cost increases from £8000 for the smallest system considered (0.2 kW) to £30000–£50000 for systems with power outputs around 100 kW. The cost per unit power output drops from £40000 per kW (at 0.2 kW) to £300–£500 per kW (at 100 kW). In the CEP Laboratory, of which the author is a member, an operational ORC system rated to 1 kW had a construction cost of approximately £7000 or £7000 per kW. This value is close enough to the calculated values of £10000 per kW indicated in Fig. V.5. In this system-sized range (up to 100 kW), a 100 kW system is the most economically viable solution when the payback period is significant and the investor is capable to cover the higher capital costs.

For larger scale ORCs, with power outputs between 100 kW and 30 MW, total costs are roughly proportional to the power output. Thus, the costs per unit kW vary only slightly between £150 and £500 per kW. The increase in total costs is a direct result of the large working-fluid flow-rates which necessitate large turbines and heat exchangers. The turbine is the dominant cost factor among the individual components at large scales and the turbine costs scale with the power output. Therefore, the total costs of the system follow this trend.

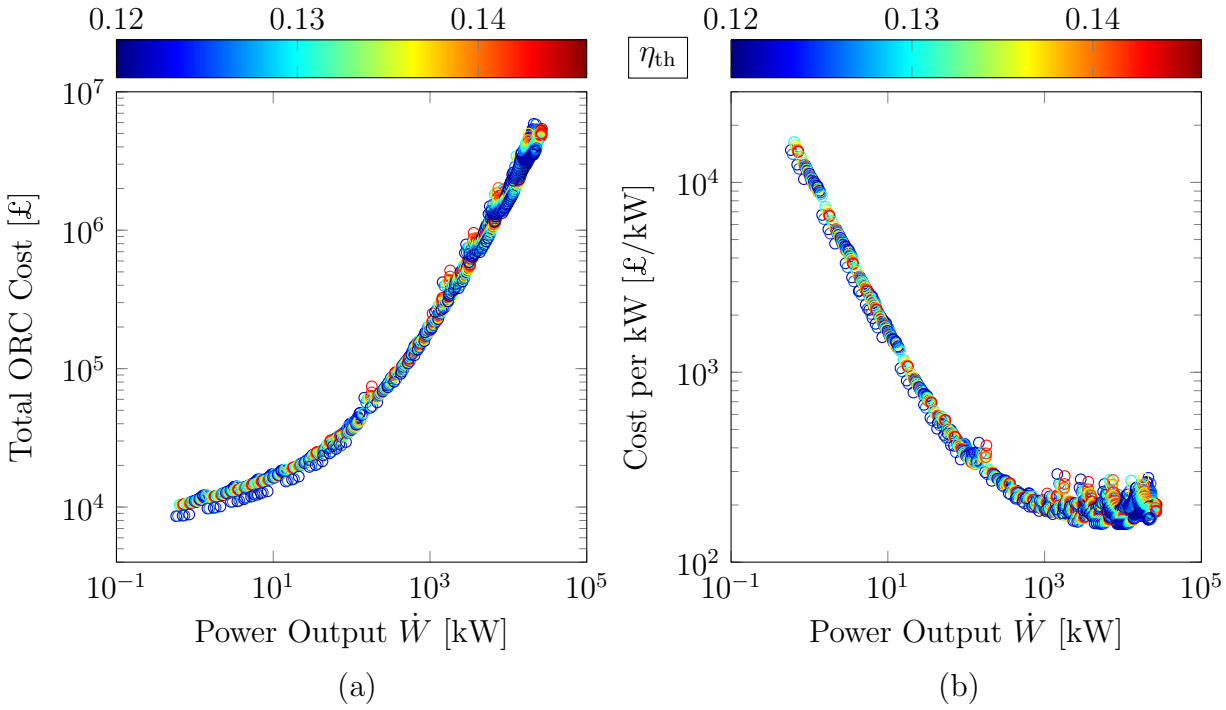


Figure V.5: Performance (power output) and cost of ORC systems in the investigated case study. (a) Overall costs of the cycle against the power output for alkane mixtures. (b) Costs per unit power output against the power output for alkane mixtures. The colour range in all plots reflects the thermal efficiency of different cycles.

V.4.2 Variations of ORC Costs with Mixture Composition

The absolute total costs (in £) and the costs per unit power output (in £/kW) are presented in Fig. V.6 for different mixture compositions of n-butane + n-decane and n-perfluorobutane + n-perfluorodecane to compare the cost effects of different mixing ratios. The data points in Fig. V.6 correspond to the maximum power output cases from Fig. V.2(e) and (f). The trends show that the total costs (Fig. V.6(a) and (b)) generally are not strongly affected by the mole fraction. At high pressures, however, there is a striking peak cost for butane fractions for $x_{C_4H_{10}} = 0.7$ or 0.8. The specific costs are shown in Fig. V.6(c) and (d) for alkanes and perfluoroalkanes respectively. On the one hand, pure butane and perfluorobutane systems are more cost-effective in terms of specific cost although they may have relatively high total cost. The low specfic cost is due to the very high power outputs associated with pure butane/perfluorobutane. On the other hand, pure decane and perfluorodecane have lower specific costs than intermediate mixtures even though they have the least power outputs (see Fig. V.2). The results indicate that pure working fluid are more cost-effective than mixtures. When using higher evaporation pressures with pure butane or perfluorobutane, the power output and cost increase in similar proportions. Therefore, the specific cost per unit power output for pure butane tends to vary around £400/kW (except at very low pressures).

V.5 Constrained Cooling Flows

In the previous section, we were discussing an idealized case where the cooling stream flow-rate is high enough such that the temperature of it is constant through the condenser. This specification typically produces maximum power output when the working-fluid flow-rate and the evaporation pressure are maximized, while simultaneously using sufficient cooling to ensure the working fluid is fully condensed and the pinch condition is not violated. Abundant amounts of cooling resources are normally available for large-scale power generation in the form of rivers or cooling towers.

For such cases, the more volatile pure working fluid is seen to perform better than working-fluid mixtures due to the improved thermal match between cooling stream and condensing pure working fluid. This is contrary to observations reported in ORC studies in the literature where working fluid mixtures produced higher power outputs than their constituent pure working fluids. The cooling streams considered in these studies are limited wherein the inlet and outlet temperatures of the cooling stream are specified (see

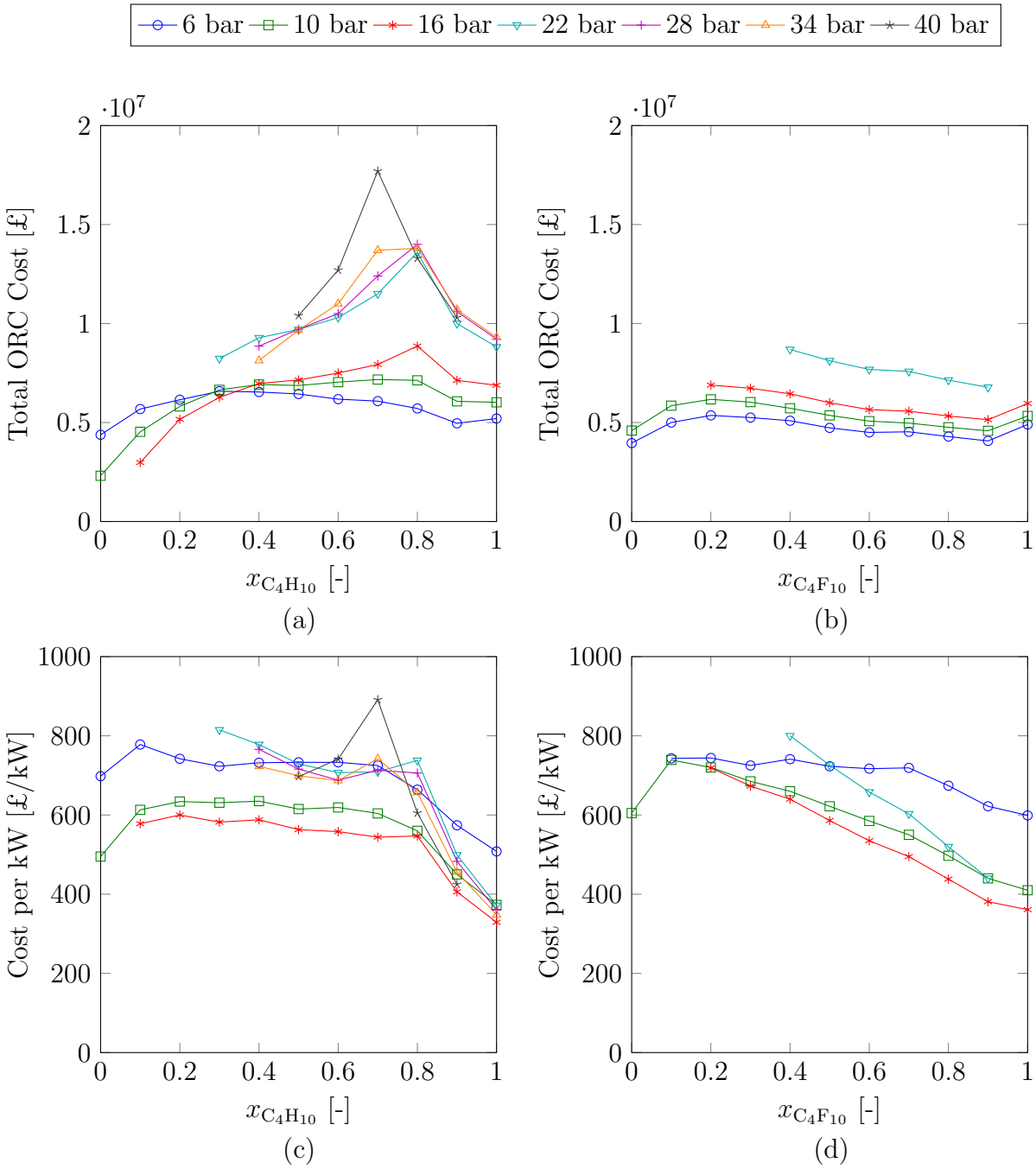


Figure V.6: ORC systems costs for cycles designed for maximum power output. Total cost with (a) *n*-butane + *n*-decane and (b) *n*-perfluorobutane + *n*-perfluorodecane working-fluid mixtuers. Cost per unit power output (£/kW) with: (c) *n*-butane + *n*-decane (corresponding to power output in Fig. V.2(e)) and (d) *n*-perfluorobutane + *n*-perfluorodecane working-fluid mixtures (corresponding to power output in Fig. V.2(f)).

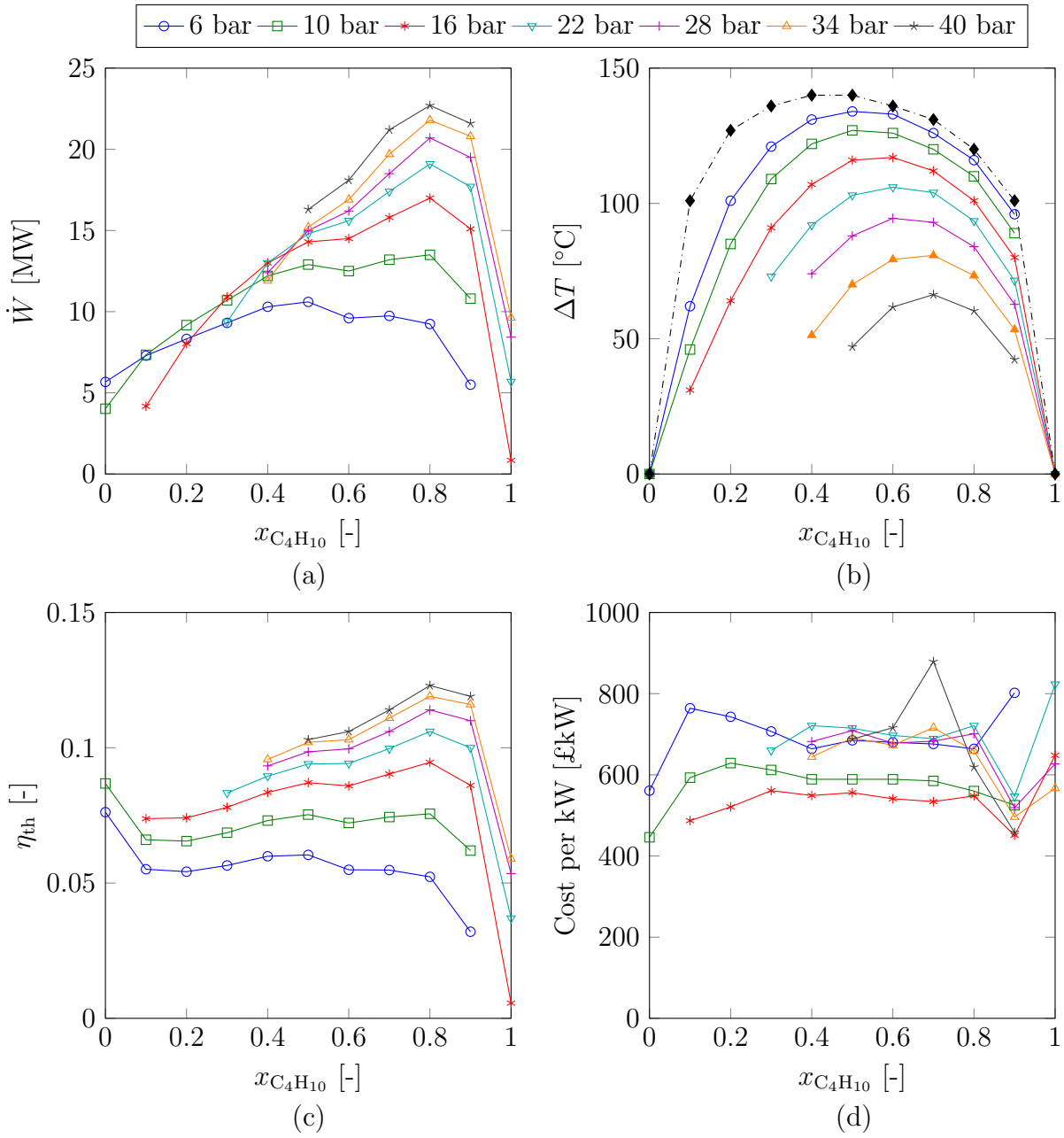


Figure V.7: Performance of ORCs with restricted cooling water using n-butane + n-decane working fluid mixtures at maximum power output: (a) maximum absolute net power $\dot{W}$, (b) temperature glide in evaporator (solid lines) and condenser (dashed line, diamond markers), (c) thermal efficiency η_{th}, and (d) ORC system costs per unit power output.

for example [56, 58, 59]). This characteristic of the cycle allows working fluid mixtures to be condensed at lower pressures by providing a temperature glide and a closer thermal match to the heat sink. Conversely, pure fluids are condensed at higher pressures to satisfy the pinch conditions caused by isothermal condensation profile. Therefore, working fluid mixtures can provide higher power outputs than pure components.

Practical applications with limited cooling resources include power generation in remote or arid areas, power generation with air condensation aided by cooling fans, or CHP applications where ORC cooling water is used for household or district heating. For the latter application, cooling water is heated from ambient temperature to close to the boiling point (90 °C) [86, 87]. Such a constrained cooling requirement presents a case for which non-azeotropic working-fluid mixtures could be deployed to a great advantage. Results from such a case are shown in Fig. V.7. The absolute power output, the temperature glides in the evaporator and condenser, the efficiency, and the specific cost per unit power output are plotted as functions of the n-butane mole fraction of n-butane + n-decane working fluid mixtures.

Relative to cycles with unconstrained cooling (Fig. V.2(e)), cycles with constrained cooling produce lower power outputs especially when using mixtures with high n-butane content. The largest difference between the two cases is observed for pure butane where the power output with constrained cooling flow is only 60% of the power output with unconstrained cooling flow. Working fluids with low n-butane content produce similar power output values in constrained and unconstrained cooling-flow cases (compare Figs. V.2(e) and V.7(a)) because the condenser pressure is predominantly 1 bar in both cases. This is not the case for mixtures with high butane content.

Overall, mixtures produce higher power outputs than both pure fluids, where the optimal composition at low evaporation pressures is $x_{C_4H_{10}} = 0.5$ and $x_{C_4H_{10}} = 0.8$ at high pressures. Temperature glides in the evaporator and condenser are given in Fig. V.7(b). Large glides up to 130 °C in the evaporator and 140 °C in the condenser are observed. Such large temperature glides provided by the mixtures allow a better thermal match to the large temperature change required in the cooling stream (from 20 °C to 90 °C). This leads to a reduction in the average temperature difference between the working-fluid mixtures and the cooling stream, a decrease of exergy losses in the condenser and thus improved efficiency and power output. Concerning the cost per unit power output of this ORC system, there is little variation between pure fluids and mixtures. The sole exception here are cycles with working fluids with high butane contents due to the significantly reduced power output produced with these mixtures (and pure butane).

V.6 Summary

One of the aims of the research presented in this chapter is to assess the potential of working-fluid mixtures, specifically alkane and fluorocarbon mixtures, in ORCs for low to medium grade heat conversion. Mixtures can provide an improved thermal match to the heat source and heat sink of a cycle thanks to their non-isothermal phase change behaviour. The average temperature difference between working fluid and heat source/sink during heat addition/rejection is reduced and therefore less exergy is destroyed during these processes. This can lead to an enhancement of the power output and thermal efficiency. We modelled a sub-critical, non-regenerative ORC which employs binary mixtures of fluorocarbons or alkanes as a working fluid with a view towards affordable, low complexity but high power ouput ORC plants. Accurate thermodynamic and phase-change property values of the working-fluid mixtures are required for this model. SAFT-VR Mie was used to acquire the relevant data. The two fluorocarbons (n-perfluorobutane and n-perfluorodecane) and alkanes (n-butane and n-decane) were chosen as they are dissimilar and therefore the property prediction of their mixtures is more challenging. Furthermore, dissimilar components of working-fluid mixtures allow for large temperature glides during heat addition and rejection which may be advantageous in some certain ORC applications.

We used SAFT-VR Mie equation of state for providing accurate thermodynamic property values of working-fluid mixtures. Employing this equation of state in an ORC model can be an attractive alternative to the more common approach of using software platforms such as the REFPROP and CoolProp property databases, especially if the fluid in question is not in the database or there are uncertainty associated with the particular fluid. The aforementioned property databases employ correlative equations of state which rely on a large number of parameters. Uncertainty can arise if the experimental data, on which the correlation is based, is scarce or if one is looking at property values which lie outside the experimental range of the data. Although experimental thermophysical property values are necessary to parametrize the molecular model of the SAFT approach, the number of parameters is much less than those required for other equations of state. Consequently, less experimental data are needed to develop an accurate model over large regions of the phase diagram. Additionally, the parameters used in SAFT-VR Mie have a physical meaning. In summary, modelling thermodynamic cycles coupled with SAFT offers a strong alternative to the common method of using REFPROP or CoolProp.

It has been long established that SAFT-VR Mie is a powerful tool in predicting the fluid in the P-T-x space. The description of the considered fluids in this space, shown in Chapter IV, is excellent. Of greater importance for thermodynamic cycle analysis are calorific values and predictions in the T-s and P-h space. The fluid representation in these spaces is also of high quality. These observations underline the fact that SAFT-VR Mie is a powerul tool for the prediction of working-fluid thermophysical behaviour for the analysis of thermodynamic cycles such as ORCs.

The case study considered in this chapter is an ORC engine which is driven by the exhaust flue gas stream of a refinery at 330 °C as heat source. The heat sink is a cooling stream with a large enough flow-rate such that the temperature in the condenser is constant. Both sets of mixtures (alkanes and perfluoroalkanes) exhibit the same general behaviour. For this application, cycles running with pure working fluids exhibit higher thermal efficiencies than those using mixed working fluids. At low evaporation pressures, the heavier component (n-decane or n-perfluorodecane) results in the most efficient cycles while at high evaporation pressures the lighter component ((n-butane or n-perfluorobutane) results in highest efficiencies. These observations are generally non-trivial.

For waste heat recovery and conversion applications, power output is a more significant performance indicator than the thermal efficiency. The energy source – waste heat – is free and abundantly available as opposed to fossil fuels for example. In order to maximize power ouput, the results have shown that superheating should be avoided. Non-superheated cycles also exhibited higher efficiencies. Cycles using pure n-butane and n-perfluorobutane produced the highest power outputs (in the supher-heated and non-superheated cases). Thus, the optimal working fluids are pure n-butane and n-perfluorobutane as they produce the highest power output for all cases *and* the highest efficiencies at pressures above 10 bar. For low pressures, mixtures with low (perfluoro-)butane concentrations (20–40 mol%) produce similarly high power outputs to pure (perfluoro-)butane, but the most efficient cycles are achieved with with pure (perfluoro-)decane. Overall, the performance of cycles employing mixtures is inferior to those using pure fluids and only in certain circumstances is a mixture to be preferred.

The total costs of the ORC increase with the mole fraction of the lighter component (n-butane or n-perfluorobutane) which is a consequence of the increased power output (which correlates with the butane content). The specific cost per unit power output increases with the mole fraction of the lighter component before sharply falling for pure

(perfluoro-)butane. In general, cycles employing pure substances (either (perfluoro-)butane or (perfluoro-)decane) are more cost-efficient than those using mixtures.

The above results have shown that the optimum working fluid strongly depends on the external heat source and heat sink conditions to the cycle in a manner that is non-trivial and sometimes counter-intuitive. Although pure fluids outperform mixtures when the cooling stream is unconstrained, this is not the case for cooling streams with restricted flow-rates. Mixtures actually become the optimal working fluids, because of the improved thermal match to the temperature profile of the cooling stream through the condenser. The best mixture composition depends on the gradient of the temperature rise and other cycle conditions, such as the evaporation pressure. However, a restricted cooling-stream flow-rate severely deteriorates the performance of the ORC relative to the unconstrained cooling-stream case. In conclusion, it is important to consider the use of working-fluid mixtures, in particular those with large temperature glides, depending on the specific application. Therefore, working fluid design must be fully integrated in the design of the whole cycle to exploit the full potential of the full range of applications of interest.

Chapter VI

Model Development for Calculating Thermally Induced Losses Associated with Reciprocating Motion

VI.1 Background

Performance losses in reciprocating-piston machines can arise from different sources, and it is essential to minimize all loss mechanisms to optimize performance. Mechanical losses can arise in piston machines due to friction in bearings, valve gears, and piston rings. Other losses occur due to leakage and pressure drops across valves. Valve losses can be minimized through adequate timing, rapid opening, and large open areas, while friction losses between stationary and moving parts are addressed with adequate lubrication. Once mechanical, leakage, and valve losses are minimized, thermally induced losses due to unsteady heat-transfer remain. These losses also occur in TFOs, and it is assumed, with good reason, that this type of loss can play a very significant role in two-phase TFOs, such as the NIFTE [27] or ERPE. As will be shown in the results Chapter VII, these losses are not negligible.

We examine gas springs as models for the compression and expansion processes and associated unsteady heat tranfer losses occurring in reciprocating energy-conversion system such as ORC engines and TFOs. In gas springs, a fixed mass of gas undergoes

sequential compression and expansion within a closed space. They do not include the complex effects of valve timing and gas exchange of reciprocating-piston devices while they retain the fluctuating heat exchange phenomena between the cylinder walls and gas.

Unsteady heat-transfer losses or thermally induced losses (we use both expressions interchangeably) can occur even if the overall process is globally adiabatic (i.e. the time-mean heat transfer is zero). The heat exchange between the gas and cylinder wall across a finite temperature difference occurs as the gas compresses and expands. This is an inherently irreversible process. Heat is transferred from the gas to the wall during compression when the gas temperature is higher than the wall temperature. During expansion, heat is returned back to the gas when its temperature falls below that of the wall. Even if heat is returned to the gas in its entirety (the net fluctuating heat transfer is zero), a finite exergetic penalty is paid. Therefore, it is important to quantify and characterize the heat exchange fluctuations between the fluid and solid.

VI.1.1 Objective

In previous work (see Section VI.2), gas springs were examined that operated using air or noble gases. Lee [88] considered gas springs with ideal gases while Kornhauser and Smith [89–91] experimented with light or noble gases such as hydrogen, helium, and argon for which the ideal-gas law is an accurate approximation. We look to expand the understanding of thermally induced losses to more complex organic working fluids than those classically investigated in gas spring systems with a view towards applications such as ORCs and two-phase TFOs. Organic Rankine cycle engines and TFOs rely on refrigerants and hydrocarbons such as pentane, HFC-245fa or HFC-134a [29, 92, 93]. Furthermore, mixtures of these working fluids are a current area of research as discussed in Chapters IV and V for their potential in improving overall system performance of ORCs. However, for organic fluids, real-gas effects may become significant for the temperature and pressure ranges encountered in low- and medium-grade heat conversion (approximately 20–600 K, 0.5–40 bar). In this study, the irreversibility due to heat transfer is quantified while accounting for real-gas effects of mixtures as well as pure fluids. One goal is to understand the impact of different equations-of-state and look-up tables which account for thermodynamic and transport property variations due to temperature and pressure (or density). Secondarily, we look to determine the general behaviour of the variation in gas performance based on the compressibility factor.

VI.1.2 Overview of Chapter

The chapter begins with a discussion of previous work and literature in the area of thermally induced losses in gas springs. This is followed by a brief summary of the theory of computational fluid dynamics (CFD), where the finite volume method, errors related to discretization, and algorithms for solving numerically the Navier-Stokes equations are introduced. Subsequently, our numerical model is explained. The geometry and mesh, convergence behaviour of the discretization, solver, and initial and boundary conditions are presented in detail and discussed. An estimation of the turbulence behaviour of our problem and a justification for the selected flow model is provided. Finally, the chapter closes with a description of the four different fluid property models and equations of state which will be compared in the results chapter (Chapter VII).

VI.2 Previous Work

In the 1940s, Pfriem [94] conducted theoretical work in which he analytically described the phase difference between the heat flux and the temperature difference between the wall and the bulk gas in a gas spring. Overbye et al. [95] in 1960s observed in experiments of internal combustion engines a similar phase lag between the heat flux at the surface of the engine cylinder walls and the temperature difference between the compression space and the cylinder walls. Subsequently, Annand [96] published a review of experimental work on internal combustion engines and concluded that the conventional heat transfer coefficient was insuitable due to this phase difference. Lee [88] described the oscillating heat flux in a valveless gas spring by developing a model for a complex Nusselt number at a low frequencies, or more specifically at low Peclet numbers (non-dimensionalized frequency, see Eq. VI.33). Lawton [97] conducted experiments on a motored diesel engine to measure the heat flux on the piston head. He observed that a slightly modified version of a correlation developed by Annand [96] accurately predicted the heat transfer and the phase difference to the temperature difference. Catto and Pratta [98] published a numerical study of instantaneous heat transfer in gas springs. The governing differential equations are expressed in a moving coordinate system and solved using the finite volume method. Helium, air, and R134a were considered as working fluids and were modelled as ideal gases. The purpose of the work was to correlate computational results with empirical expressions. The numerical analysis showed excellent agreement with Lawton's

model for the instantaneous heat flux, however the comparison with the complex Nusselt number model of Lee [88] was less good.

Extensive experiments on gas springs were conducted in the 1980s and 1990s by Kornhauser and Smith [89–91] from which they calculated the thermal loss for a wide range of Peclet numbers and different compression ratios. Additionally, they proposed empirical *Nu-Re* correlations which accounted for the aforementioned phase difference with imaginary components. The correlation was only developed for low compression and helium as a working fluid. Lekić and Kok [99] simulated Kornhauser and Smith's experiments using commercial CFD software. They obtained good agreement between predicted heat fluxes and those derived from p-V measurements. The CFD analysis also provided insight into the flow structure during compression and expansion. The dominant heat transfer mechanism is conduction during expansion and compression because the flow is highly stratified. The flow structure is disturbed when the piston approaches either of the dead centre positions, the core gas then recirculates to the wall and forces convective heat transfer. The instantaneous heat flux is not directly proportional to the temperature difference between bulk gas and wall, but also depends on the dynamics of the compression process and heat accumulation in the boundary layers.

More recently, Mathie et al. [100] proposed a heat transfer model of a gas spring which includes heat conduction inside the cylinder walls. The one-dimensional heat conduction equation inside the wall is solved simultaneously with the first law in the gas volume. Mathie et al. concluded that thermally induced losses are significantly influenced by the finite conductivity of the cylinder walls, and that (a reduced) wall thickness and material may have adverse effects on the magnitude of this loss. For the design of highly efficient reciprocating machines the full conjugate (convection in the gas, conduction in the wall) and unsteady problem must be accounted for.

Another computational fluid dynamic study of gas springs was carried out by Willich et al. [101]. They observed that the secondary flow structures which arise near the dead centre positions lead to considerable spatial variations of the heat flux over the internal surfaces. Most notably, however, Willich et al. aimed to investigate the possible impact of valve flows on the heat transfer losses by simulating gas springs containing perforated plates. These plates produce eddying motions similar to those generated by valve flows. They observed that adding these has led to a significant increase of the heat transfer loss at high Peclet numbers.

VI.3 Background of Computational Fluid Dynamics

In the following section, the discretisation of the general transport equation and the computational solution of the Navier-Stokes equations are presented. Additionally, the inaccuracies and errors resulting from the discretisation are discussed.

VI.3.1 Discretisation using the Finite Volume Method

Partial differential equations (PDE) which govern flows can be transformed into algebraic equations through spatial and temporal discretisation. The solution of the algebraic equations provide a set of values in the predetermined locations in space and time. This allows for a numerical calculation of the mass, momentum, and energy conservation equations governing fluid flow. In the current study, the conservation equations are solved and the density, velocity, temperature, and pressure fields are calculated using the finite volume method (FVM), commonly used to evaluate discretised PDEs [102].

The finite volume method is commonly used in the calculation of flow fields due to its capability of describing complex or irregular geometries. The geometry is spatially discretised into small control volumes (CVs) which in turn consist of one or more cells. Although control volumes can theoretically have any shape, they are often tetrahedral or hexahedral. The former shape is especially well-suited for creating unstructured meshes in complex geometries. Each face of the control volume is shared only by two control volumes. In Fig. VI.1, a control volume is illustrated with the centroid P and the face normal vector $\vec{n}$ with the space point F. In the FVM, the fluid transport equations are calculated in their integral form over the control volume. The temporal discretisation of the solution domain is related to the temporal discretisation of the PDE through the non-dimensional Courant number. This will be discussed in more detail later.

Equation VI.1 is the general form of the transport equation in fluid dynamics for a scalar property ϕ. The equation consists of a time derivative, a convection term, a diffusion, and a source term. The density of the fluid is referred to as ρ. Table VI.1 shows the inputs for the diffusivity Γ_ϕ and for the scalar quantity ϕ [102] when expressing the mass (continuity), momentum, or energy (enthalpy) conservation equations. The source term S_ϕ represents transport of ϕ from sources or sinks. The Navier-Stokes equations are generated with the appropriate source terms in the momentum equation. Therefore, the pressures on the surfaces of the control volumes and the volume forces on the control volumes are included in the source terms of the Navier-Stokes equation.

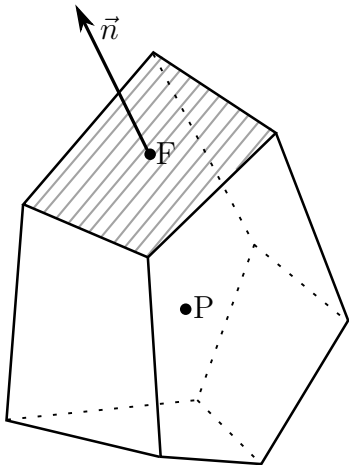


Figure VI.1: Control volume with centroid P and face normal vector $\vec{n}$ with the vector's space point F.

$$\underbrace{\frac{\partial \rho\phi}{\partial t}}_{\text{time derivative}} + \underbrace{\nabla \cdot (\rho \mathbf{U}\phi)}_{\text{convection term}} - \underbrace{\nabla \cdot (\rho \Gamma_\phi \nabla \phi)}_{\text{diffusion term}} = \underbrace{S_\phi(\phi)}_{\text{source term}} \tag{VI.1}$$

Table VI.1: Scalar variable and associated diffusivity for conservation equations derived from the general transport equation

Equation	Scalar variable	Diffusivity Γ_ϕ
Continuity	1	0
x-momentum	u_x	μ_{eff}
y-momentum	u_y	μ_{eff}
z-momentum	u_z	μ_{eff}
Enthalpy	h	$\frac{\mu_{\text{eff}}}{\sigma_h}$

The exact solution of the scalar quantity $\phi(x)$ can be expressed with Taylor series. Equation VI.2 represents a three-dimensional Taylor series expansion. The node P of the position vector $\mathbf{x}$ represents the centroid of the control volume around which the scalar quantity $\phi(x)$ varies. The expression $(\mathbf{x} - \mathbf{x}_\text{P})^n$ in Eq. VI.2 represents the n-th tensorial product of the vector $(\mathbf{x} - \mathbf{x}_\text{P})$ with itself, producing an n-th rank tensor. The operator

'$\underbrace{:::}_{n}$' is the inner product of the two n-th rank tensors creating a scalar. If only the linear terms are considered, an error of second order is introduced.

$$\begin{aligned}\phi(\mathbf{x}) = \phi_\mathrm{P} + (\mathbf{x}-\mathbf{x}_\mathrm{P})\cdot(\nabla\phi)_\mathrm{P} + \frac{1}{2}(\mathbf{x}-\mathbf{x}_\mathrm{P})^2 : (\nabla\nabla\phi)_\mathrm{P} + \\ + ... + \frac{1}{n!}(\mathbf{x}-\mathbf{x}_\mathrm{P})^n \underbrace{:::}_{n}(\underbrace{\nabla\nabla...\nabla}_{n}\phi)_\mathrm{P}\end{aligned} \tag{VI.2}$$

Integrating Eq. VI.1 over the control volume V_P around the point P gives:

$$\frac{\partial}{\partial t}\int_{V_P}\rho\phi\mathrm{d}V + \int_{V_\mathrm{P}}\nabla\cdot(\rho\mathbf{U}\phi)\mathrm{d}V - \int_{V_\mathrm{P}}\nabla\cdot(\rho\Gamma_\phi\nabla\phi)\mathrm{d}V = \int_{V_\mathrm{P}} S_\phi(\phi)\mathrm{d}V \tag{VI.3}$$

If we assume a first-order Taylor expansion of $\phi(\mathbf{x})$, then the integral of the scalar quantity over the control volume is approximated with

$$\begin{aligned}\int_{V_\mathrm{P}}\phi(\mathbf{x})\mathrm{d}V &= \int_{V_\mathrm{P}}\left[\phi_\mathrm{P} + (\mathbf{x}-\mathbf{x}_\mathrm{P})\cdot(\nabla\phi)_\mathrm{P}\right]\mathrm{d}V = \\ &= \phi_\mathrm{P}\int_{V_\mathrm{P}}\mathrm{d}V + (\nabla\phi)_\mathrm{P}\cdot\int_{V_\mathrm{P}}(\mathbf{x}-\mathbf{x}_\mathrm{P})\mathrm{d}V = \\ &= \phi_\mathrm{P}V_\mathrm{P}\,.\end{aligned} \tag{VI.4}$$

In the previous expression, P refers to the centroid of the control volume, therefore the integral of $(\mathbf{x}-\mathbf{x}_\mathrm{P})$ is zero. The approximation from Eq. VI.3 is correct if the variation of the scalar quantity is linear or constant. If the variation of ϕ is of a higher order, the approximation will have an error of the second order [102]. With Gauss' theorem (Eq. VI.5) we can transform volume integrals into surface integrals of the flux through the volume's surface area.

$$\int_V(\nabla\cdot\Psi)\mathrm{d}V = \oint_{\partial V}\Psi\cdot\mathrm{d}\mathbf{S}\,. \tag{VI.5}$$

where ∂V is the closed surface bounding the volume V and $\mathrm{d}\mathbf{S}$ represents an infinitesimal surface element with an associated outward pointing normal on ∂V. The surface integral can be transformed into a sum of integrals over all faces assuming the control volumes do not overlap and that the scalar quantity ϕ is constant on each surface of the control volume:

$$\int_V(\nabla\cdot\Psi)\mathrm{d}V = \oint_{\partial V}\Psi\cdot\mathrm{d}\mathbf{S} = \sum_f\left(\int_f\Psi\cdot\mathrm{d}\mathbf{S}\right) = \sum_f S_f\cdot\Psi\,. \tag{VI.6}$$

Thus, applying Eqs. VI.5 and VI.6 to the convection term, where $\Psi = \rho\mathbf{U}\phi$, leads to

$$\int_{V_\mathrm{P}} \nabla \cdot (\rho\mathbf{U}\phi)\mathrm{d}V = \oint_{\partial V_\mathrm{P}} (\rho\mathbf{U}\phi)\mathrm{d}S = \sum_f S_f \cdot (\rho\mathbf{U})_f \phi_f \,, \tag{VI.7}$$

and applying the same equations to the diffusion term gives

$$\int_{V_\mathrm{P}} \nabla \cdot (\rho\Gamma_\phi \nabla\phi)\mathrm{d}V = \oint_{\partial V_\mathrm{P}} (\rho\Gamma_\phi \nabla\phi)\mathrm{d}S = \sum_f (\rho\Gamma_\phi)_f S_f \cdot (\nabla\phi)_f \,, \tag{VI.8}$$

For the convection and diffusion terms, it is necessary to determine the value of ϕ on the face from the values in the control volume centres. This is done through interpolation schemes. The accuracy of the selected interpolation scheme strongly influences the overall accuracy of the FVM. The interpolation method used here is called central differencing. It is a distance weighted average and is of second order accuracy even on non-uniform meshes [103]. However, central differencing can cause unphysical oscillations in the solution. In such case, one says that the boundedness of the solution is violated. The boundedness is the property of a numerical scheme to produce physically realistic values. Equation VI.9 shows the interpolated value ϕ_f on the face between a parent control volume with the centroid P and a neighbouring control volume with centroid N. The interpolation factor λ_f is calculated from the Cartesian positions of the centroid node of the parent control volume x_P, the neighbouring control volume x_N, and x_f which corresponds to the intersection between the control volumes' centroid connection line and the shared face of the two control volumes (Eq. VI.10).

$$\phi_f = \phi_\mathrm{N}\lambda_f + \phi_\mathrm{P}(1 - \lambda_f) \tag{VI.9}$$

$$\lambda_f = \frac{x_f - x_\mathrm{P}}{x_\mathrm{N} - x_\mathrm{P}} \tag{VI.10}$$

If boundedness must be guaranteed, a first order approximation must be used, such as upwind differencing. The scalar quantity at the face f takes either the value of the parent control volume ϕ_P or of the neighbouring control volume ϕ_N depending which one is situated upstream from the face. This can be expressed mathematically in the following manner:

$$\phi_f = \begin{cases} \phi_\mathrm{P}, & \text{if } u \cdot \vec{n} > 0, \\ \phi_\mathrm{N}, & \text{if } u \cdot \vec{n} < 0\,, \end{cases} \tag{VI.11}$$

where $u \cdot \vec{n}$ represents the velocity component parallel to the face normal [103].

The source term $S_\phi(\phi)$ can be a general function of ϕ. It must be linearised for the discretisation:

$$S_\phi(\phi) = Su + Sp\phi\,, \tag{VI.12}$$

where Su and Sp can also depend on ϕ. The volume integral of the source term can be approximated in the same manner as shown in Eq. VI.3:

$$\int_{V_\mathrm{P}} S_\phi(\phi)\mathrm{d}V = SuV_\mathrm{P} + SpV_\mathrm{P}\phi_\mathrm{P}\,. \tag{VI.13}$$

Assuming a first order accurate Taylor series, the time derivative is discretized using the Euler method:

$$\rho^{n+1}\phi^{n+1} = \rho^n\phi^n + \left.\frac{\partial\rho\phi}{\partial t}\right|_\mathrm{P}\Delta t\,, \tag{VI.14}$$

where the superscript n refers to the old time-field (or current time-step) while $n+1$ represents the new time-field (or upcoming time step). Thus, substituting the individual terms from Eq. VI.3 with the expressions in Eqs. VI.7, VI.8, VI.13, and VI.14 gives the discretised transport equation:

$$V_\mathrm{P}\frac{\rho_\mathrm{P}\phi_\mathrm{P}^{n+1} - \rho_\mathrm{P}\phi_\mathrm{P}^n}{\Delta t} + \sum_f S_f\cdot(\rho\mathbf{U})_f\phi_f - \sum_f(\rho\Gamma_\phi)_f S_f\cdot(\nabla\phi)_f = SuV_\mathrm{P} + S_\mathrm{P}V_\mathrm{P}\phi_\mathrm{P}\,. \tag{VI.15}$$

For the discretized transport equation VI.15 a choice has to be made about the way the face values of ϕ and $\nabla\phi$ are evaluated. This can be done either with an explicit or implicit discretization. If the former is employed, the face values of ϕ and $\nabla\phi$ are determined from the old time-field (time-step n):

$$\phi_f = \phi_\mathrm{N}^n\lambda_f + \phi_\mathrm{P}^n(1-\lambda_f)\,. \tag{VI.16}$$

The consequence of this choice is that the scalar quantity of the new time-field ϕ_P^{n+1} is calculated solely from old time-field values. The time steps, however, are strictly limited by the Courant number Co defined as the ratio of the time step Δt to the characteristic convection time $|\mathbf{U}_f|/\Delta x$, the time required for a disturbance to be convected a distance Δx [103]:

$$Co = \frac{|\mathbf{U}_f|\Delta t}{\Delta x}\,, \tag{VI.17}$$

where $|\mathbf{U}_f|$ is the magnitude of the three dimensional velocity vector. If the Courant number is larger than unity, the explicit system becomes unstable.

When using the Euler implicit method the face values are expressed in terms of the new time-step $n+1$:

$$\phi_f = \phi_{\mathrm{N}}^{n+1}\lambda_f + \phi_{\mathrm{P}}^{n+1}(1-\lambda_f)\,. \tag{VI.18}$$

This method permits much larger time increments, but at the cost of much more computational effort. It requires to solve an additional zero point equation with a numerical scheme (e.g. Newton method). The benefit of the implicit method is that it is stable even if the Courant number limit is violated [102]. Both Euler schemes are first order accurate. Schemes with a higher order of accuracy, such as the Crank-Nicholson method can be applied. However, in this work, only the implicit Euler method is employed. Finally, Eq. VI.15 can be rearranged in terms of the new time-step quantity:

$$\phi_{\mathrm{P}}^{n+1} = \phi_{\mathrm{P}}^{n} + \frac{\Delta t}{\rho_{\mathrm{P}} V_{\mathrm{P}}}\left[-\sum_f S_f\cdot(\rho\mathbf{U}_f)\phi_f - \sum_f(\rho\Gamma_\phi)_f S_f\cdot(\nabla\phi)_f + SuV_{\mathrm{P}} + SpV_{\mathrm{P}}\phi_{\mathrm{P}}\right] \tag{VI.19}$$

VI.3.2 Accuracy and Errors of Discretisation

In the finite volume method, implementing solution schemes with an order of accuracy higher than two are difficult and require substantial computational effort. A higher order than unity carries the risk of exhibiting oscillating solutions and therefore does not strictly satisfy boundedness.

Due to the approximating character of the discretisation process, errors are introduced into the numerical solution. One type of error results from the use of discretisation schemes which have an order lower than two. This includes the numerical diffusion of the convection term which has a second order numerical error. Another type of error is caused by the discretisation of the solution domain [102]. It is known as truncation error. As an example, consider the one-dimensional Taylor series of a scalar quantity shown in Eq. VI.20:

$$\phi_{k+1,l} = \phi_{k,l} + \left(\frac{\partial\phi}{\partial x}\right)_{k,l}\Delta x + \left(\frac{\partial^2\phi}{\partial x^2}\right)_{k,l}\frac{\Delta x^2}{2} + \left(\frac{\partial^3\phi}{\partial x^3}\right)_{k,l}\frac{\Delta x^3}{6} + ... \tag{VI.20}$$

The subscripts k and l describe the positions of the nodes in x-direction and y-directions respectively. The truncation error occurs when the higher order terms are neglected. In case of a first-order solution, this includes all higher order terms (Δx^2, Δx^3, etc.). The truncation error is minimized either by taking a larger number of higher-order terms into account or by reducing the spatial difference Δx. The truncation error becomes zero if an infinite amount of terms is considered or if $\Delta x \to 0$. In practice, increasing the order

of the approximation is impractical. However, reducing Δx can be achieved by increasing the resolution of the discretisation mesh and thus reducing the cell size (or in terms of temporal discretisation, reducing the time-step). Therefore, to ensure that the truncation error does not distort the result the number of cells, i.e. the mesh resolution, must be sufficient for a given problem. An appropriate mesh resolution can be determined through a convergence study.

However, increasing the mesh resolution (i.e. decreasing Δx) is associated with a higher number of calculations. Each calculation involves round-off errors, which accumulate with every calculation step. Round-off error can be reduced by decreasing mesh resolution. This is often not an option, however, due to the truncation error. A solution to this problem is to carry out the simulation with double precision which requires more computational capacity.

In summary, the computational solution for a scalar quantity ϕ_{comp} can be considered the result of the physically correct solution ϕ_{real} subtracted by the truncation error E_{t} and the round-off error E_{r}:

$$\phi_{\text{comp}} = \phi_{\text{real}} - E_{\text{t}} - E_{\text{r}} \,. \tag{VI.21}$$

A convergence study allows to find a mesh resolution which has a sufficiently small truncation error while still maintaining a small round-off error.

VI.3.3 Numerical Solution of the Navier-Stokes Equations

Fluid flow with heat transfer is described with the temperature field T, pressure field P, and the velocity field $\mathbf{U}$ (which is a vector in each node). The conservation of mass is described with the continuity equation:

$$\frac{\partial \rho}{\partial t} + \frac{\partial(\rho u_x)}{\partial x} + \frac{\partial(\rho u_y)}{\partial y} + \frac{\partial(\rho u_z)}{\partial z} = 0 \,, \tag{VI.22}$$

where the subscript of the velocity components $\mathbf{U}$ indicates the spatial direction in cartesian coordinates. There is a momentum conservation equation (i.e. Navier-Stokes equation) for each coordinate direction. Using index notation, they can be expressed as [103]

$$\frac{\partial(\rho u_i)}{\partial t} + \frac{\partial(\rho u_j u_i)}{\partial x_j} = \frac{\partial \tau_{ij}}{\partial x_j} - \frac{\partial p}{\partial x_i} + \rho f_i \,. \tag{VI.23}$$

The subscripts i and j denote the Cartesian coordinates x, y, and z. For each direction i, all three Cartesian coordinates in j have to be included. τ_{ij} refers to the shear-stress tensor and f includes all volume forces, e.g. gravity [103].

The Navier-Stokes equations lack an independent equation for the pressure, the gradient of which is found in all three momentum equations. The continuity equation does not contain a pressure expression. This complicates the solution of the Navier-Stokes equation. One possible way to overcome this obstacle is to construct a pressure field which guarantees the validity of the continuity equation. In compressible flow, the continuity equation is solved for the density, and the pressure is subsequently determined from an equation of state [103] This approach is not suitable for incompressible or low Mach flow. Two common algorithms for solving the Navier-Stokes equations are the SIMPLE and PISO methods. They were developed to be used with incompressible as well as compressible flow.

Semi-Implicit Method for Pressure Linked Equations (SIMPLE)

SIMPLE is a pressure-velocity treatment originally formulated by Patankar [104]. The implicit time stepping of the discretised Navier-Stokes equations results in the non-linear equation (check Ref. [103] for the derivation):

$$A_{\mathrm{P}}^{u_i} u_{i,\mathrm{P}}^{n+1} + \sum_l A_l^{u_i} u_{i,l}^{n+1} = Q_{u_i}^{n+1} - \left(\frac{\partial P^{n+1}}{\partial x_i} \right) . \tag{VI.24}$$

P is the index of an arbitrary velocity node, l denotes neighbour points, and Q^{n+1} is the source term which includes all explicitly treated terms of the momentum equation. The coefficient $A_{\mathrm{P}}^{u_i}$ accumulates the constant values considering the node P in the parent CV and $A_l^{u_i}$ accumulates the face values towards adjacent CVs. The pressure gradient is treated independently in the last term on the right hand side. Equation VI.24 cannot be solved directly due to the non-linearity and coupling of the underlying differential equations. The coefficients A and the source term Q depend on the unknown solution u_i^{n+1}. Thus, the equation and the pressure can only be solved through iteration. Iterations within a time step are called outer iterations, and they are denoted with the outer index m that replaces the time step index $(n+1)$ in Eq. VI.24:

$$A_{\mathrm{P}}^{u_i} u_{i,\mathrm{P}}^{m*} + \sum_l A_l^{u_i} u_{i,l}^{m*} = Q_{u_i}^{m-1} - \left(\frac{\partial P^{m-1}}{\partial x_i} \right) . \tag{VI.25}$$

u_i^m represents the current estimate of the solution u_i^{n+1}. The algorithm is capable of solving unsteady as well as steady state problems. The SIMPLE algorithm is a predictor-corrector scheme i.e. a velocity field that does not satisfy the continuity equation is initially estimated. Subsequently, the velocity field is corrected with a pressure gradient in order to satisfy the continuity equation. The asterisk * represents the predicted, non-final solution. From Eq. VI.25, we can see that the predicted velocity field $u_{i,\mathrm{P}}^{m*}$ at the location P can be estimated with the old time-step pressure P^{m-1}.

The algorithm commonly uses a pressure correction term P' instead of the absolute pressure in order to estimate the new pressure P^m which is based on the previous iteration P^{m-1}. The final velocity u_i^m is evaluated from the predicted solution u_i^{m*} and a correction term u_i'. These corrections are shown in Eq. VI.26 for the velocity field and Eq. VI.27 for the pressure field:

$$u_i^m = u_i^{m*} + u_i' \,, \tag{VI.26}$$

$$P^m = P^{m-1} + \alpha_{\mathrm{P}} P' \,. \tag{VI.27}$$

The algorithm requires an under-relaxation factor α_{P} to improve the convergence behaviour. Substituting the pressure and velocity correction for the absolute values in Eq. VI.25 and solving for the velocity correction gives:

$$u_{i,\mathrm{P}}' = -\underbrace{\frac{\sum_l A_l^{u_i} u_{i,l}'}{A_{\mathrm{P}}^{u_i}}}_{=:\overline{u}_{i,\mathrm{P}}'} - \frac{1}{A_{\mathrm{P}}^{u_i}} \left(\frac{\partial P'}{\partial x_i}\right)_{\mathrm{P}} . \tag{VI.28}$$

This is not the velocity that would be obtained by disregarding the pressure gradient from Eq. VI.25 due to the implicit formulation [103]. The velocities must now corrected to satisfy the continuity equation:

$$\frac{\partial(\rho u_i^m)}{\partial x_i} = 0 \,. \tag{VI.29}$$

Substituting u_i^m from Eq. VI.26 and u_i' from Eq. VI.28 into the continuity equation (Eq. VI.29) gives the following equation after some manipulation with which the pressure correction P' can be estimated:

$$\frac{\partial}{\partial x_i}\left[\frac{\rho}{A_{\mathrm{P}}^{u_i}}\left(\frac{\partial P'}{\partial x_i}\right)\right] = \left[\frac{\partial(\rho u_i^{m*})}{\partial x_i}\right]_{\mathrm{P}} + \left[\frac{\partial(\rho \overline{u}_i')}{\partial x_i}\right]_{\mathrm{P}} . \tag{VI.30}$$

The velocity correction term $\overline{u}_i'$ on the right hand side is unknown, therefore it is neglected by the SIMPLE algorithm. Consequently, the solution of the Navier-Stokes equation will not converge rapidly, but convergence can be improved through selection of an appropriate under-relaxation factor. It is normally in the range of α =0.6–0.8. Subsequently, the velocity is updated with the corrected pressure P^m, because the provisional predicted velocity u_i^{m*} in combination with the corrected pressure P^m does not satisfy the momentum equation. There still remains an error in the continuity equation when the algorithm finishes with the correction of the momentum equation. Thus, this procedure is iterated until the correctors become negligibly small.

The SIMPLE algorithm can be summarised as follows [103]:

1. Start calculation of the fields at new time t_{n+1} and use u_i^n and P^n as first approximation for u_i^{n+1} and P^{n+1}

2. Solve the linearised algebraic momentum equations to obtain the predicted velocity field u_i^{m*}

3. Solve pressure-correction equation to obtain P'

4. Correct velocities and pressure to obtain velocity field u_i^m and new pressure P^m, the new velocity satisfies the continuity equation

5. return to step 2 and use u_i^m and P^m as improved estimates for u_i^{n+1} and P^{n+1}, repeat until correctors are negligibly small

6. Advance to next time step

Pressure Implicit Split Operator (PISO)

The PISO algorithm is for the most part the same as the SIMPLE algorithm. Notable differences include a more accurate pressure-correction estimation and nor requirement for under-relaxation. These advantages are qualified by the higher computational demand due to an additional correction process for the velocity field $u_{i,\mathrm{P}}''$:

$$u_{i,\mathrm{P}}'' = -\overline{u}_{i,\mathrm{P}}' - \frac{1}{A_{\mathrm{P}}^{u_i}} \left(\frac{\partial p''}{\partial x_i} \right)_{\mathrm{P}} . \tag{VI.31}$$

In the first correction step, the term $\overline{u}'_{i,\mathrm{P}}$ is neglected as is done in the SIMPLE algorithm. Substituting the $u''_{i,\mathrm{P}}$ into the continuity equation and solving for the pressure correction term gives:

$$\frac{\partial}{\partial x_i}\left[\frac{\rho}{A_{\mathrm{P}}^{u_i}}\left(\frac{\partial P''}{\partial x_i}\right)\right] = \left[\frac{\partial(\rho\overline{u}'_i)}{\partial x_i}\right]_{\mathrm{P}} . \tag{VI.32}$$

PISO generally converges more quickly than SIMPLE and is therefore more suitable for unsteady or transient problems. The algorithm can be summarised as follows [103]:

1. same as SIMPLE
2. same as SIMPLE
3. same as SIMPLE
4. same as SIMPLE
5. solve the second pressure-correction equation and correct velocities and pressure again
6. return to step 2 and use u_i^m and P^m as improved estimates for u_i^{n+1} and P^{n+1}, repeat until correctors are negligibly small
7. Advance to next time step

VI.4 Numerical Model

As stated before, we aim to expand the understanding of unsteady heat-transfer and the associated losses occurring in reciprocating piston machines and thermofluidic oscillators, especially with regards to more complex working fluids than those previously investigated in studies of heat transfer losses in gas springs (air or noble gases). A CFD model of a gas spring is developed in OpenFOAM which simulates the heat transfer and flow during the compression and expansion process. After post-processing the values for temperature, pressure, and instantaneous heat flux, we can evaluate the heat transfer losses for different operation conditions, fluid models, and working fluids. Four different fluids models are compared: an ideal-gas model with constant thermodynamic and transport properties; an ideal-gas model with temperature-dependent properties; a real-gas model using the Peng-Robinson equation of state with temperature and density-dependent properties; and a real-gas model which uses real-gas property tables to interpolate values of thermodynamic and transport properties as functions of temperature and pressure.

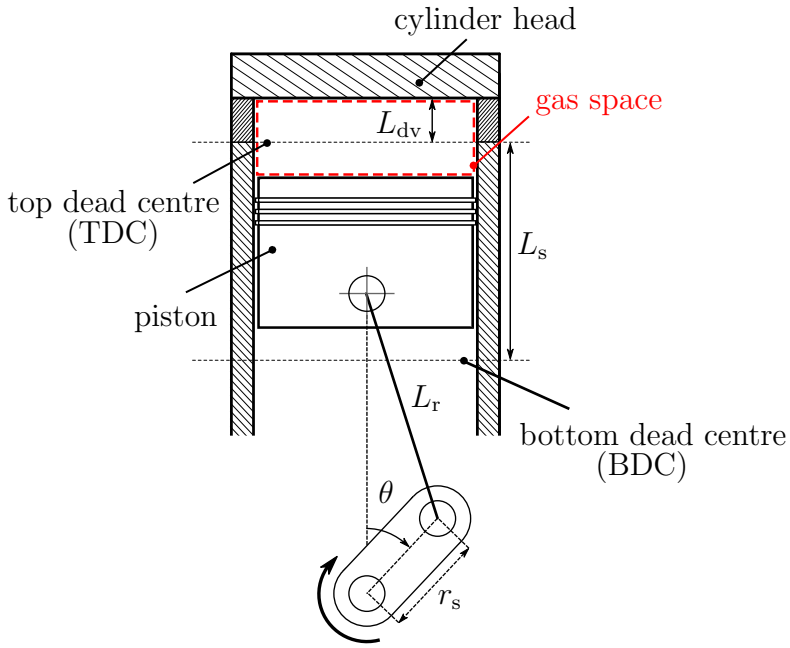


Figure VI.2: Schematic of piston-cylinder geometry

VI.4.1 Problem Setup

A gas spring system consists of a crankshaft driven piston-cylinder design. It is simulated in OpenFOAM as the cylinder space of a (single-cylinder) internal combustion engine with no combustion and no mass exchange. The engine or gas spring parameters are the crank angle θ, the stroke length L_s, and the conrod length L_r. The conrod connects the piston with the crankshaft at a radial offset from the axis of the crankshaft (crankshaft radius r_s). As a result, the stroke length L_s is twice the crank radius r_s. The remaining parameter is the bore diameter D. The characteristic engine/gas spring dimensions are summarised in Table VI.2 and illustrated in Fig. VI.2. The geometry is chosen to match an experimental apparatus which is currently being developed for testing [105–107].

Table VI.2: Gas spring dimensions in mm

Bore diameter	Con rod length	Stroke length	Dead volume height
D	L_r	$L_s = 2r_s$	L_{dv}
105	149	78	14

The oscillatory Peclet number Pe is used as a dimensionless measure for the rotational speed of the gas spring:

$$Pe = \frac{\omega D_{\mathrm{h}}^2}{4\alpha_0}\,, \tag{VI.33}$$

where ω is the angular frequency, $\alpha_0 = k/\rho c_p$ is the time and spatially-averaged thermal diffusivity, and $D_{\mathrm{h}} = 4V_{\mathrm{md}}\mathrm{A}_{\mathrm{md}}$ is the hydraulic diameter at mid-stroke (V_{md} and A_{md} are the cylinder volume and surface area at mid-stroke).

A number of parameters have been defined to quantify heat transfer losses. We use parameter ψ as defined by Faulkner [108] as the ratio of heat transfer loss $W_{\mathrm{com}} - W_{\mathrm{exp}}$(compression work minus expansion work) to the work done onto the gas just during compression W_{com}:

$$\psi = \frac{W_{\mathrm{com}} - W_{\mathrm{exp}}}{W_{\mathrm{com}}} = \frac{\oint P\mathrm{d}V}{\int_{\mathrm{BDC}}^{\mathrm{TDC}} P\mathrm{d}V}\,, \tag{VI.34}$$

where TDC stands for top dead centre and BDC for bottom dead centre. The volume is denoted by V. Another loss parameter was defined by Kornhauser and Smith [89, 109] as the heat transfer loss divided by the work for adiabatic compression for the same mean pressure, mean volume, and volume ratio:

$$\psi_{\mathrm{ad}} = \frac{W_{\mathrm{com}} - W_{\mathrm{exp}}}{W_{\mathrm{adiab}}} = \frac{\oint P\mathrm{d}V}{\frac{\rho_0 V_0}{\gamma-1}\left(\frac{1+r_{\mathrm{v}}}{2}\right)^{\gamma-1}\left(1 - r_{\mathrm{v}}^{1-\gamma}\right)}\,. \tag{VI.35}$$

Here, the subscript 0 represents cyclic mean values, r_{v} is the volume ratio, and γ is the ratio of specific heats. Expressing the adiabatic work in this manner is approximate. For a real cycle, the pressure at V_0 is different during compression and expansion. The advantage of the Faulkner's parameter ψ is its simplicity and that it can be easily understood intuitively. Kornhauser's parameter ψ_{ad} relates the loss to the maximum achievable work if there were no exergy loss (adiabatic compression). If the gas spring were adiabatic and additional there were no losses due to friction, then the expansion work equals the compression work. Thus, ψ_{ad} relates the loss to the performance limit of the gas spring or engine.

Another loss parameter, although it will not be used in this study, is the one defined by Lee [88, 109]:

$$\psi_{\mathrm{Lee}} = \frac{\oint P\mathrm{d}V}{P_0 V_0 \left(\frac{P_{\mathrm{a}}}{P_0}\right)\frac{\gamma-1}{\gamma}}\,. \tag{VI.36}$$

The amplitude of the pressure oscillation is P_{ad}. There is no simple heuristic explanation for this parameter, and there is no practical grasp to understand this loss. However, it was

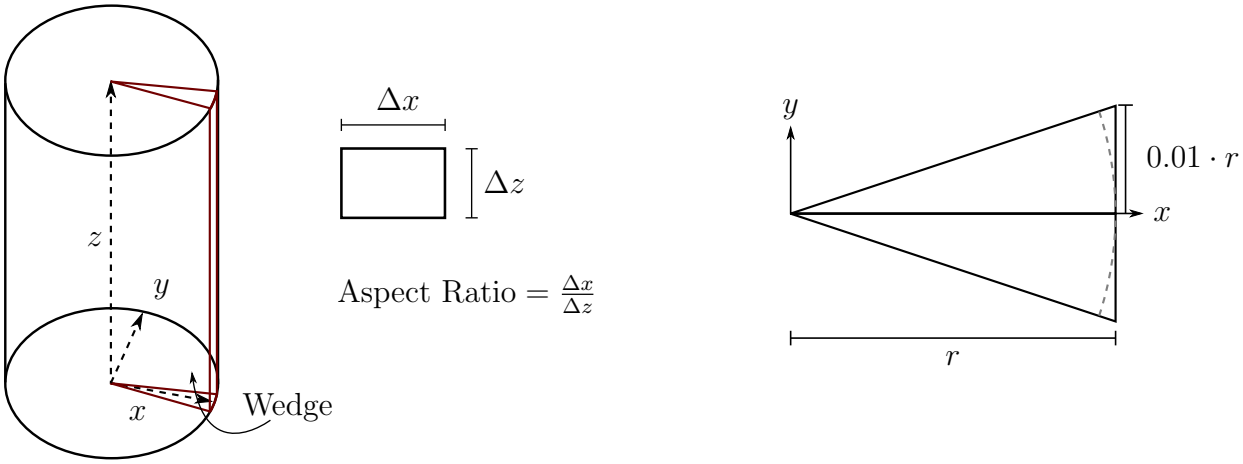


Figure VI.3: Modelled wedge geometry and definition of the aspect ratio. Left-hand diagram shows the wedge in a perspective view. Right-hand diagram shows a top view of the geometry (not to scale).

observed in experiments that the losses plotted against the Peclet number for different gases, mean pressures and geometries collapse onto approximately the same curve for a given volumetric ratio [90].

VI.4.2 Geometry and Mesh

The CFD model was developed in the open-source code OpenFOAM (v. 2.1.1 and v. 2.3.1). As the geometry is axisymmetric (Fig. VI.3), the gas spring is modelled in two spatial dimensions using a small angle wedge, and we assume that there are no non-axisymmetric three dimensional instabilities. In Section VI.5, we discuss how turbulence does not occur in the considered application. Therefore, simulating just a wedge is sufficient to capture the flow behaviour. This has also been confirmed by Lekic and Kok [110]. The simulation is performed over 10 cycles in order to reach a cyclic steady state, i.e. a state where the cycle-to-cycle variation is below 0.5%. The geometry consists of a wedge with a width of 0.02 rad and there is only one layer of cells in circumferential direction. The changing volume of the compression space is modelled with a dynamic mesh, with the moving lower boundary representing the face of the piston. Every node in the mesh compresses vertically relative to the stationary cylinder head (top boundary) and the moving piston head (bottom boundary). Nodes closer to the piston move to a greater extent than nodes closer to the cylinder head. The ratio of the vertical dimension in the compressed position compared to the expanded position is the same for all cells. The mesh distortion during compression/expansion is shown in Fig. VI.4. The mesh is modelled to have a

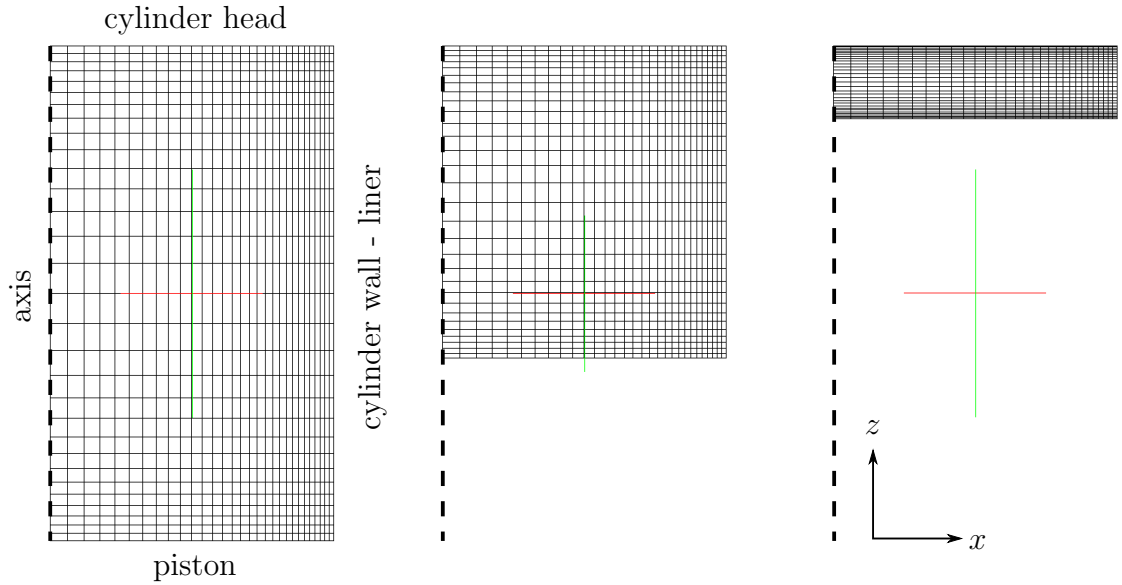


Figure VI.4: Mesh movement during an expansion stroke of a 30 × 30 mesh. A grading factor increases resolution near the walls.

cell aspect ratio of unity at mid-stroke. The size of the cells decreases linearly towards the boundaries to increase the mesh resolution inside the boundary layers near the walls. At mid-stroke, the smallest cell radial dimension is one-fourth of the largest one. The same is valid in axial direction. A convergence study was carried out to investigate the dependency of the results on the mesh resolution and the Courant number. It has been found that the optimal mesh resolution depends on the rotational speed, with the total number of cells increasing for higher speeds. For frequencies (rotational speeds) around 100 RPM, for example, the mesh is sufficiently resolved at 90 × 90 cells.

VI.4.3 Solver

The solver used is a modified version of OpenFOAM's compressible *coldEngineFoam* solver designed for reciprocating piston engines without combustion. The solution of the Navier-Stokes equations is based on the PIMPLE algorithm which is a merge between the SIMPLE and PISO algorithm specific to OpenFOAM. It uses the PISO algorithm to solve unsteady flow because of the fast convergence behaviour of inner iterations. However, it switches to the SIMPLE algorithm during portions of the engine cycle when the changes of the scalar quantity fields are small. During small changes, convergence occurs more easily and therefore the code uses the less computationally demanding SIMPLE algorithm. The aim of the PIMPLE algorithm is to optimize calculation speed.

The unsteady simulation is highly sensitive to the time increments chosen for the time stepping. Explicit schemes require small time steps to avoid calculating local minima. Furthermore, they are bound by the Courant number (Eq. VI.17) limit not to exceed unity. In the OpenFOAM simulation, the user defines a maximum time step $\Delta t_{\max}$ and a maximum Courant number $Co_{\max}$ which should be below unity to avoid instabilities. The time step is chosen such that the pre-set $Co_{\max}$ value is never exceeded. Due to the dynamic mesh, the time step needs to adapt to the changing cell size as well as the flow velocity. The maximum Courant number is set to $Co_{\max} = 0.1$ for speeds around 100 RPM.

VI.4.4 Initial and Boundary Conditions

There are only two initial conditions and one boundary condition that fully determine the thermodynamic state of the gas at cyclic steady state: the initial pressure and temperature set at bottom dead centre (which fix the mass in the cylinder) and the wall temperature. All simulations start with the piston at bottom dead centre. Adair et al. observed that the cylinder wall temperatures in reciprocating compressors oscillate by less than ± 2 K [111]. Mathie et al. [100] predicted constant internal wall temperatures if the cylinder wall thickness was low. Lekic and Kok [99] simulated Kornhauser and Smith's experiments [89–91] with constant wall temperatures and received the same values as the measurements from the experiments. Therefore, the wall temperature is assumed to be constant and uniform over all wall boundaries (cylinder head, piston head and cylinder wall). The initial gas temperature set at BDC is not an independent variable and produces a transient until the system reaches cyclic steady-state. If chosen carefully, it can be reached after few oscillations, which reduces the total computational time.

VI.4.5 Convergence Study

Background

As discussed in VI.3.2, the truncation error must be minimized to obtain physically accurate solutions. A high mesh resolution and small time step reduces the truncation error. However, these changes can greatly increase computational time. In a convergence study, the mesh resolution is sequentially increased until no more change (or negligible change) in results is seen. The same procedure is done for the time step, or in our case the maximum Courant number. Therefore, a mesh independent or continuum value must be estimated for both dimensions (time and space).

Table VI.3: Engine frequencies and Peclet numbers of considered frequency range in the convergence study

RPM	0.5	3.0	10	100	1000	10000
Co	0.3/0.2	0.2/0.1	0.2/0.1	0.2/0.1/0.05	0.1/0.05	0.05/0.03
Pe	1.40	8.42	28.06	280.62	2806.19	28061.93

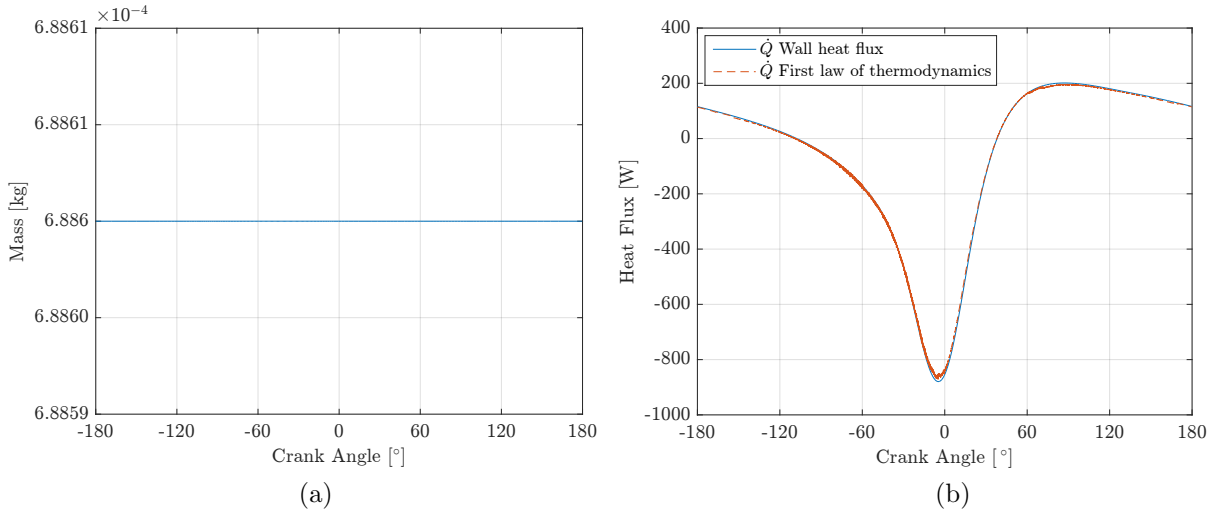


Figure VI.5: (a) Conservation of mass at 1000 RPM case with a mesh resolution of 120×120 cells and $Co = 0.05$. (b) Wall heat flux calculated with Fourier's law (solid blue) and with first law of thermodynamics (dashed red).

In the convergence study, air is used as a working fluid, and it is modelled as a constant property ideal-gas. Table VI.3 shows the range of frequencies in RPM that have been considered. In each simulation run, the gas spring process was simulated for five cycles. Cyclic steady state does not need to be reached for the convergence study, however the fifth cycle must be compared between the different resolutions. Figure VI.5(a) shows the mass conservation of the model over one cycle. The calculation of the heat flux $\dot{Q}$ based on Fourier's law and the estimation through the first law of thermodynamics coincide well which is shown in Fig. VI.5(b). These plots show that there is no mass loss and that two independent methods of calculating the heat flux calculate the same values.

By monitoring global variables, a comparison between different mesh resolutions and Courant numbers can be achieved. The net transferred heat Q, the net mechanical work W, and the loss ψ_{K} as defined by Kornhauser (Eq. VI.35) are chosen as global variables. The data of the variables are extracted from the CFD and the discrete values

are integrated over the cycle (Eqs. VI.37 and VI.38). The integration of the discrete values is carried out with a trapezoidal approximation.

$$Q = \oint \mathrm{d}Q = \oint \frac{\mathrm{d}Q}{\mathrm{d}t}\mathrm{d}t = \oint \dot{Q}\mathrm{d}t \tag{VI.37}$$

$$W = \oint P\mathrm{d}V = \oint P\frac{\mathrm{d}V}{\mathrm{d}t}\mathrm{d}t \tag{VI.38}$$

The global variables are determined for each calculated mesh resolution. In an $m \times n$ mesh, m represents the number of cells in axial or z-direction, and n represents the number of cells in radial or x-direction. We will only use meshes that have the same number of cells in both directions. The fractional error $\epsilon_{m\times n}$ of each global variable is to be estimated for each resolution. It can be calculated with:

$$\epsilon_{m\times n} = \frac{X^* - X_{m\times n}}{X^*}\,, \tag{VI.39}$$

where X represents a global variable, X^* is the continuum value of that global variable, and $X_{m\times n}$ is the value of the global calculated for a mesh resolution of $m \times n$. Should the global variable tend towards the continuum value X^* for each mesh refinement, then plotting $\epsilon_{m\times n}$ against the inverse of the number of cells $N_{m\times n}$ in a log-log plot results in a straight line. The mesh independent value represents the solution with no truncation error, i.e. the solution of a simulation with an infinite amount of cells, $N_{m\times n} \to \infty$. Thus, the following relation can be expressed between the global variables:

$$\frac{X^* - X_{m\times n}}{X^*} = \left(\frac{1}{N_{m\times n}}\right)^{k_\mathrm{c}}\,. \tag{VI.40}$$

The order of the convergence and the continuum value of the global variable X^* must be determined in order to obtain an estimate of the fractional error. This can be done with Richardson extrapolation [112]. The method uses the solution of three different mesh resolutions to define the order of convergence:

$$k_\mathrm{c} = \ln\left(\frac{X_3 - X_2}{X_2 - X_1}\right)\frac{1}{\ln r_\mathrm{eff}}\,. \tag{VI.41}$$

The subscripts of X denote different mesh resolutions where 1 represents the finest mesh and 3 represents the coarsest. The effective mesh refinement ratio r_eff is defined in Eq. VI.42, where N_1 and N_2 are the number of cells in the finer and coarser mesh respectively, and D is the number of dimensions in which the mesh is refined. In our case $D = 2$

(x and z direction). The mesh refinement ratio must be constant over all three chosen solutions, i.e. $r_{\text{eff}} = r_{\text{eff},12} = r_{\text{eff},23}$, such that

$$r_{\text{eff},12} = \left(\frac{N_1}{N_2}\right)^{1/D} = r_{\text{eff},23} = \left(\frac{N_2}{N_3}\right)^{1/D} . \tag{VI.42}$$

Finally, the continuum value X^* is extrapolated from the two finer solutions, according to Eq. VI.43 [112]:

$$X^* \approx X_1 + \frac{X_1 - X_2}{r_{\text{eff},12}^{k_c} - 1} . \tag{VI.43}$$

The slope of the extrapolation is based on three known supporting points and the extrapolation itself only on two. Therefore, it is very sensitive to the selection of the supporting points.

For each tested gas spring frequency, Table VI.4 lists the three mesh resolutions on which the Richardson extrapolations are based. If the global variable between each consecutive mesh resolution does not show a monotonic trend, the selection of the supporting points for the extrapolation are shifted towards higher resolutions. This was done for the extrapolation at 100 RPM. In Table VI.4, the number of cells in x (number of cells m) or z (number of cells n) direction are listed.

Table VI.4: Mesh resolutions on which the Richardson extrapolation is based for each tested piston frequency.

RPM	Used mesh resolutions
	m=n
0.5	20 →40→80
3.0	15 →30→60
10	30 →60→120
100	90 →120→160
1000	30 →60→120
10000	90 →120→160

In a log-log plot, e.g. Fig. VI.6, the fractional error of the global variable plotted against the inverse of the number of cells should create a straight line. However in Fig. VI.6, we can see that the slope of the trend becomes steeper as $N_{m\times n}^{-1}$ becomes smaller. This is due to the increasing round-off error at higher resolutions. Therefore,

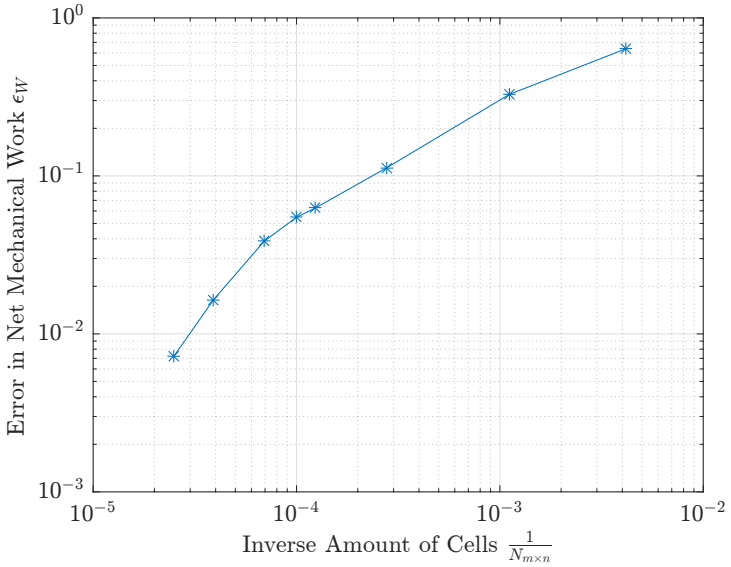


Figure VI.6: Log-log plot of the fractional error in the net mechanical work for different mesh resolutions at 1000 RPM and $Co = 0.05$

this portion is disregarded for the extrapolation. At the coarsest mesh resolutions (15×15, at the far right end of the plot), the flow field cannot be calculated accurately.

Limitations due to Numerical Instabilities

The time increments are never constant in our simulations due to the dynamic nature of the mesh. They are controlled by the Courant number. The changes in the time increments should be gradual and small between two consecutive time steps. However, in some cases, drastic jumps in the time increment were observed which caused problems for the time derivatives in the transport equations. These instabilities occurred when the piston would pass TDC for low piston frequencies and BDC at high frequencies. Figure VI.7 illustrates this phenomenon occurring shortly after the TDC position. This instability occurs at coarser grids for lower frequencies. These sudden changes in the time step size lead to wrong estimations of the time derivatives. Figure VI.8 shows an inset comparing the heat flux profiles calculated with the first law of thermodynamics and with Fourier's law (denoted by '$\dot{Q}$ wall heat flux in Fig. VI.5(b) and VI.8). As the first law uses time derivatives of the internal energy and the rate of volume change, the instabilities in the time step affect the first law calculation more significantly than Fourier's law. The small fluctuations observed in the instantaneous wall heat flux measured with the Fourier's law are much smaller than those from the first law. The first law method uses time derivatives to calculate the heat flux and therefore it is more susceptible to these

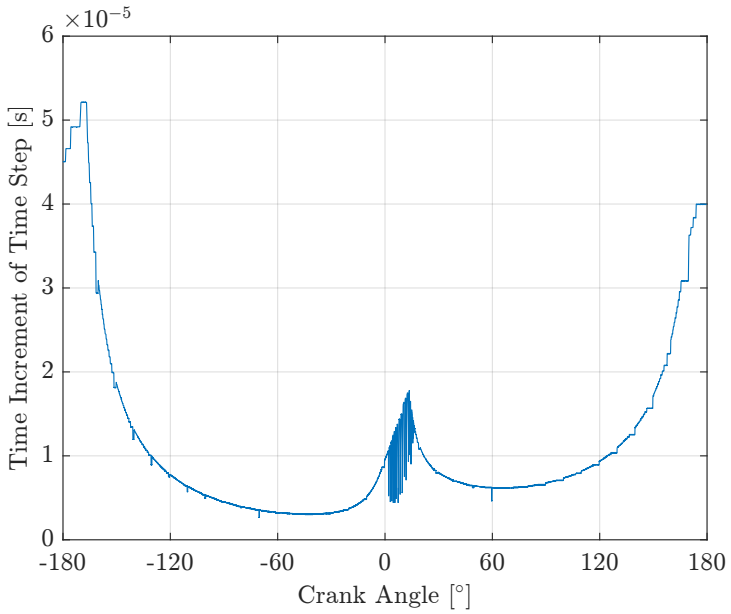


Figure VI.7: Variation of the time step increment for different crank angles. Irregular jumps of the time step increments occur around TDC or 0° (1000 RPM, mesh resolution 200×200, and $Co = 0.1$).

instabilities in the time steps. These instabilities should be avoided and they are the

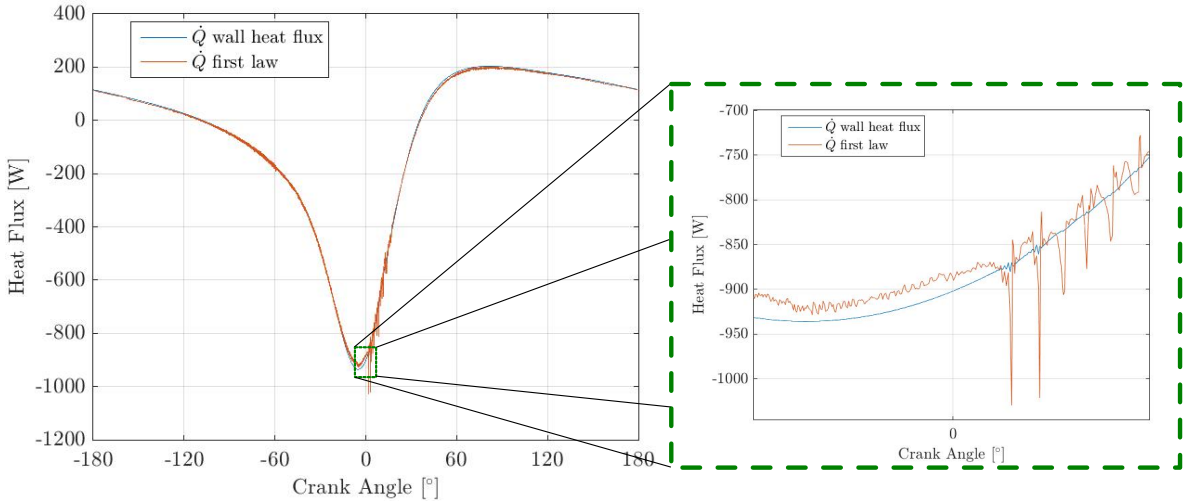


Figure VI.8: Effect of fluctuation in the time increment on the heat flux estimation for a case with 1000 RPM, mesh resolution 200×200, and $Co = 0.1$

limiting factor in increasing the mesh resolution. We have observed that these instabilities can be suppressed by decreasing the maximum Courant number (and thereby reduce the time step increments) or by increasing the number of internal correction loops of the

PISO algorithm. The improvement of the time step stability with three instead of two PISO loops (Fig. VI.8) is shown in Fig. VI.9.

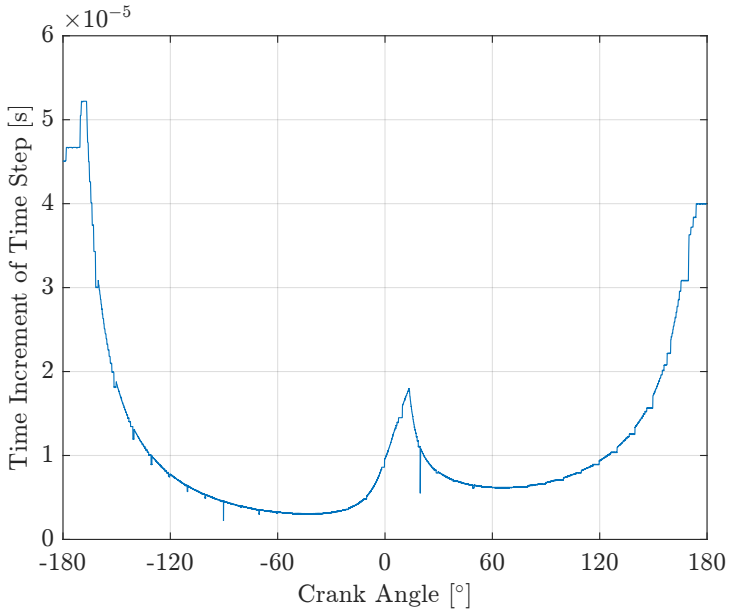


Figure VI.9: Stabilized time step control with one additional internal PISO loop for 1000 RPM, mesh resolution 200×200, and $Co = 0.1$

Convergence Study Conclusion

The net mechanical work of a cycle is assumed to be the most significant global variable because the non-dimensional loss term involves the work in its description and is therefore redundant. Additionally, the net heat transfer is very sensitive to the mesh resolution. The simulation produces very inaccurate values for this variable with coarse mesh resolutions. Consequently, it is difficult to evaluate a continuum value for the heat (the fractional error does not produce a monotonic trend in the log-log plot of VI.6).

Table VI.5 shows the evaluation of the net mechanical work with the Richardson extrapolation over the tested range of frequencies with two Courant numbers for each frequency. We compare two Courant numbers in order to estimate the influence of the temporal truncation error (as well as the spatial truncation error). Generally, the preferred Courant number is justified with a lower fractional error ϵ_W for a given frequency. The appropriate mesh resolutions are selected with the criteria of $\epsilon_W < 3\%$. Cases where numerical instabilities or excessive computational time rendered the simulation inaccurate or impractical are denoted with a dash in the fifth column in Table VI.5.

Table VI.5: Estimated continuum value of the net work W^* and the fractional error ϵ_W for different frequencies and Courant numbers

Frequency [RPM]	Courant number Co	Continuum value W^*	Fractional error ϵ_W	Converged mesh resolution m
0.5	0.3	13.5451	0.00208	-
	0.2	13.5794	0.00375	30–60
3.0	0.2	23.4099	0.00414	30–60
	0.1	23.4000	0.00150	-
10	0.20	16.4890	0.00121	-
	0.10	16.3739	0.00752	60–100
100	0.10	7.6069	0.02159	90–160
	0.05	7.4721	0.00618	90–160
1000	0.10	3.5819	0.06226	-
	0.05	3.5017	0.03869	120–200
10000	0.05	4.4640	0.73570	200–320
	0.03	1.5566	0.23943	-

At a frequency of 10 RPM, the fractional error exhibits unusual convergence behaviour when using a Courant number of $Co = 0.2$. Therefore, $Co = 0.1$ is chosen. At 100 RPM, both Courant numbers (Table VI.5) can be selected, however, the increase in accuracy of the smaller Courant number is negligible especially when considering the increase in computational time involved.

The fifth column in Table VI.5 shows the recommended mesh resolutions for a given frequency. Generally, the higher resolution should be selected for higher accuracy. However, the lower resolution in the range also provides acceptable results, and can be chosen if computational resources are limited. Figure VI.10 summarises the appropriate mesh resolutions. The upper limit of the resolutions is dictated by numerical instabilities, round-off errors, and computational errors while the lower boundary is dictated by the truncation error. For higher frequencies, a lower Courant number should be selected.

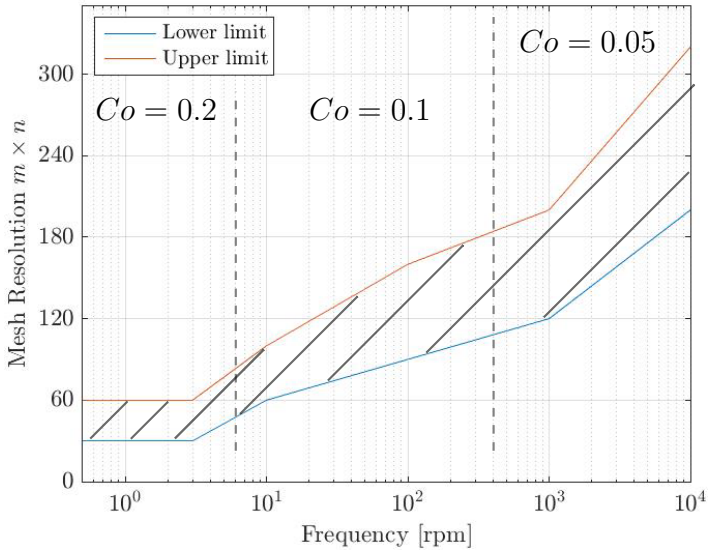


Figure VI.10: Appropriate mesh resolutions and Courant numbers over the range of piston frequencies between 0.5–10000 RPM. The y-axis is the number of cells that should be chosen for the x and z direction. A mesh resolution should be chosen which lies between the upper and lower limit.

VI.5 Estimation of Turbulence

The simulations have shown that during upstroke and downstroke the velocity profile is primarily axial and uniform. There is, however, a significant velocity gradient in radial direction near the wall due to the no-slip boundary condition. Turbulence is generated in regions of high perpendicular velocity gradients to the main flow direction (shear) which require a sufficiently high inertial force to overcome the damping effect of the viscosity. This can occur in the boundary layer during the stroke. The boundary-layer (or local) Reynolds number Re_δ can provide some insight into the transition behaviour of the boundary layer.

To the authors' knowledge, no critical Reynolds number is currently available to predict the transition from laminar to turbulent flow in the unsteady flow configuration typical to gas springs. Merkli and Thomann [113] investigated experimentally the flow transition of the Stokes boundary layer in oscillating pipe flow. Notably, no significant compression of the fluid occurs contrary to the fluid in a gas spring.. They observed a critical boundary Reynolds number of $Re_{\delta,\mathrm{c}} = 2u_{\max}/\sqrt{\nu\omega} \approx 400$.

It is proposed to use this empirical result to determine whether turbulence must be accounted for in our simulations, with an instantaneous $Re_\delta(\theta)$ defined as:

$$Re_\delta(\theta) = \frac{2u(\theta)}{\sqrt{\omega\nu(\phi)}}\,, \tag{VI.44}$$

where θ is the crank angle (representative of piston position), $u(\theta)$ is the instantaneous piston velocity equivalent to the maximum flow velocity, and $\nu(\theta)$ is the kinematic viscosity considering the variation in mean pressure. The critical Reynolds number of $Re_{\delta,\mathrm{c}} = 400$ occurs for propane gas springs at $Pe > 11000$ or at speeds over 280 RPM and for nitrogen gas springs at $Pe > 8500$ or at speeds over 680 RPM. The critical Reynolds number was not attained for gas springs using helium for the speeds considered in this study below 1000 RPM. The most relevant Pe-number range is between 0.1 and 1000 where the maximum thermally induced losses are found. However, it is highly questionable if turbulence plays any significant role at much higher speeds due to the oscillatory nature of the flow. If turbulence should develop at high speeds it would only occur for very short bursts. As the piston and the flow slow down, relaminarization occurs.

Lekic and Kok [99] carried out DNS simulations (using ANSYS CFX) of gas spring configurations similar to those of the Kornhauser experiments. The convergence study has led them to use similar cell sizes as in our simulations. Furthermore, they have not observed any turbulent flow structures in their simulations. It must be noted that for a DNS calculation, the cells are not small enough to resolve turbulent structures. Nonetheless, their calculations showed very good agreement with experimental measurements of pressure and heat transfer. Thus, it is assumed that the influence of turbulence is negative at the frequencies considered (up to 2000 RPM).

VI.6 Fluid Thermodynamic and Transport Properties

Four different fluids models are compared: an ideal-gas model with constant thermodynamic and transport properties; an ideal-gas model with temperature-dependent properties; a real-gas model using the Peng-Robinson equation of state with temperature and density-dependent properties; and a real-gas model which uses real-gas property tables to interpolate values of thermodynamic and transport properties as functions of temperature and pressure.

VI.6.1 Real-Gas Equation of State

The Peng-Robinson equation of State is expressed as [73, 77]

$$P = \frac{RT}{v-b} - \frac{a\alpha}{v\,(v+b)+b\,(v-b)}\,, \tag{VI.45}$$

where R is the universal gas constant, v is the molar volume, and a, b, and α are the attraction parameter, van der Waals covolume, and scaling factor respectively, defined as

$$a = 0.457\frac{R^2T_\mathrm{c}^2}{P_\mathrm{c}} \quad b = 0.0778\frac{RT_\mathrm{c}}{P_\mathrm{c}}\,, \tag{VI.46}$$

where T_c and P_c are the critical temperature and pressure, and

$$\alpha = \left(1+\kappa\left(1-T_\mathrm{r}^{1/2}\right)\right)^2\,, \tag{VI.47}$$

where T_r is the reduced temperature, $\kappa = 0.374 + 1.54\omega_\mathrm{z} - 0.270\omega_\mathrm{z}^2$ and ω_z is the acentric factor. For simulations using look-up tables, no equation of state is employed.

VI.6.2 Thermodynamic and Transport Properties

The temperature-dependent mole-specific heat capacity $c_\mathrm{p}^0(T)$, enthalpy $h^0(T)$ and entropy $s^0(T)$ for ideal gases are calculated with temperature-dependent polynomials often referred to as JANAF or NASA heat capacity polynomials [78, 79]:

$$c_\mathrm{p}^0(T) = R\left(a_1T^{-2} + a_2T^{-1} + a_3 + a_4T + a_5T^2 + a_6T^3 + a_7T^4\right)\,, \tag{VI.48}$$

$$h^0(T) = R\left(-a_1T^{-1} + a_2\ln T + a_3T + \frac{a_4T^2}{2} + \frac{a_5T^3}{3} + \frac{a_6T^4}{4} + \frac{a_7T^5}{5} + a_8\right)\,, \tag{VI.49}$$

$$s^0(T) = R\left(-\frac{a_1T^{-2}}{2} - a_2T^{-1} + a_3\ln T + a_4T + \frac{a_5T^2}{2} + \frac{a_6T^3}{3} + \frac{a_7T^4}{4} + a_9\right)\,. \tag{VI.50}$$

The coefficients a_i can be found in the literature for various substances [78]. With $c_\mathrm{v}^0 = c_\mathrm{p}^0 - R$, a correction of the thermodynamic properties for the density (or pressure) can be calculated with [77]:

$$c_\mathrm{v}(T,v) = c_\mathrm{v}^0(T) + T\int_v^\infty \left[\left(\frac{\partial^2 P}{\partial T^2}\right)_v\right]_T \mathrm{d}v\,, \tag{VI.51}$$

and:

$$c_{\mathrm{p}}(T,v) = c_{\mathrm{v}}(T,v) - T\frac{\left(\frac{\partial P}{\partial T}\right)_v^2}{\left(\frac{\partial P}{\partial v}\right)_T}\,. \tag{VI.52}$$

The dynamic viscosity is only temperature-dependent (and not pressure-dependent). It is calculated with Sutherland's law [114, 115]:

$$\mu(T) = \frac{A_{\mathrm{s}}\sqrt{T}}{1+\frac{T_{\mathrm{s}}}{T}}\,. \tag{VI.53}$$

where A_{s} and T_{s} are constants which can be found in the literature or can be fitted to available empirical data. Another transport property, the thermal conductivity, is calculated with the modified Eucken relation [77] which can be either just temperature-dependent or both temperature and density-dependent:

$$k(T) = \mu(T)c_{\mathrm{v}}(T)M\left(1.32 - 1.77\frac{R}{c_{\mathrm{v}}(T)}\right)\,, \tag{VI.54}$$

$$k(T,v) = \mu(T)c_{\mathrm{v}}(T,v)M\left(1.32 - 1.77\frac{R}{c_{\mathrm{v}}(T,v)}\right)\,, \tag{VI.55}$$

where M is the molar mass of the substance. The density and temperature-dependent thermal conductivity from Eq. VI.55 is used for the Peng-Robinson real-gas model while the case from Eq. VI.54 is used for the ideal-gas model with temperature-dependent properties. The previous Equations VI.48-VI.55 are not used in the look-up table model as all property values are interpolated from the tables.

Four dfferent property models are investigated and compared: (1) an ideal-gas model with constant physical properties, (2) an ideal-gas model with temperature-dependent physical properties calculated according to Eqs. VI.48, VI.53 and VI.54, (3) a real-gas model which uses the Peng-Robinson equation of state (Eq. VI.45) and temperature and density (or pressure) dependent properties calculated according to Eqs. VI.48-VI.55 and (4) a real-gas model which uses interpolated values from look-up tables of empirical data of specific heat capacity (c_{p} and c_{v}), density, enthalpy, viscosity and thermal conductivity as functions of pressure and temperature. The Peng-Robinson equation of state as it is implemented in OpenFOAM is not applicable to mixtures. Therefore, one advantage of using look-up tables is that they can be used for mixtures as well as pure fluids. The most important advantage is that data for these alkanes is highly accurate. Therefore, the look-up table simulations are used as a reference to which the other gas models are compared. The data for the look-up tables (pure fluids and mixtures) is taken from REFPROP [71].

The advantage of using more simple models such as the ideal gas one lies in a better conceptual understanding of the variation in the gas state. Additionally, using simpler fluid models is less computationally demanding. The look-up table simulation may be more accurate, however it requires about one order of magnitude longer to run.

Chapter VII

Results and Discussion of Thermally Induced Losses Associated with Reciprocating Motion

In this chapter, we discuss the results from the CFD simulations of our gas spring configurations. Firstly, we investigate how the pressure, temperature, and heat transfer behave at low and high speeds, especially with regards to the phase differences. Subsequently, we discuss the influence of real-gas effects on pressure and temperature and on thermally induced loss for pure fluids. We compare here helium and nitrogen, which are expected to behave as ideal gases, and propane, which is expected to exhibit real gas characteristics. We provide an explanation as to why real gas effects increase heat transfer losses. Finally, the chapter closes with a comparison of the heat transfer losses of light alkanes and alkane mixtures.

VII.1 Pressure, Temperature, and Heat Transfer

We consider our gas spring running with helium to show the general behaviour of the thermodynamic properties during compression and expansion. The two cases considered here are running with a frequency of 1 RPM ($Pe = 1.8$) and 750 RPM ($Pe = 1340$). Both have a wall temperature of 350 K and a starting pressure at BDC of 3 bar. This results in a time-averaged temperature and pressure of 350 K and 7.8 bar for the slow case and 396 K and 11.5 bar for the fast case. The pressure evolution during one cycle is shown in Fig. VII.1 for the two frequencies. Top dead centre corresponds to a crank angle of

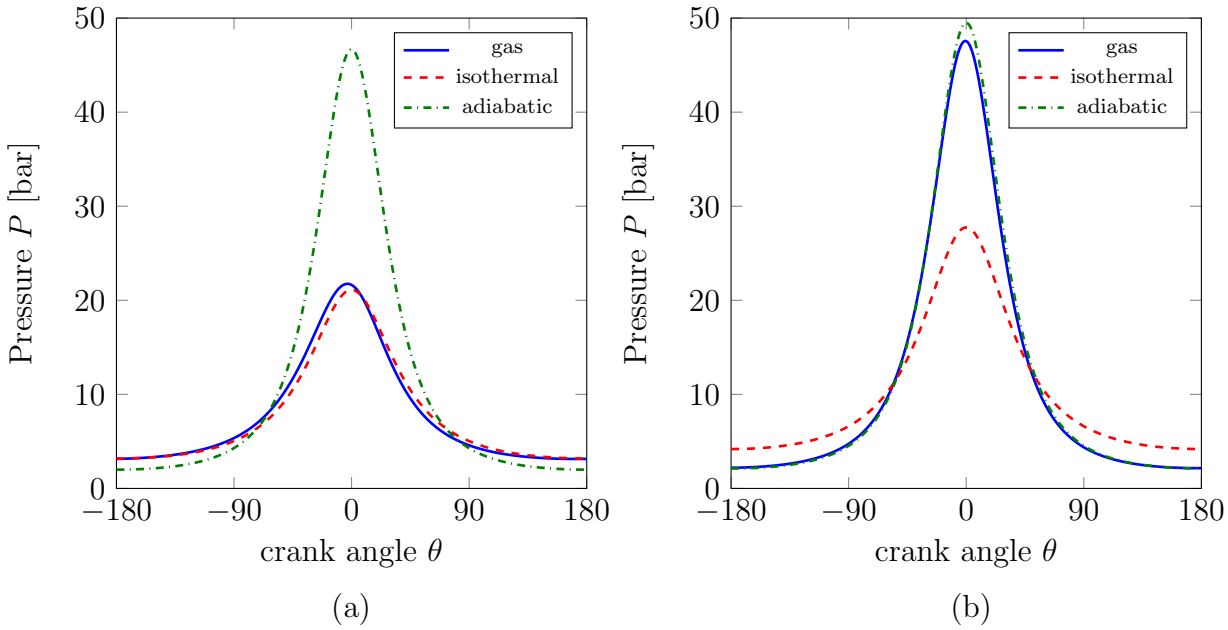


Figure VII.1: Pressure evolution during one cycle with an initial pressure at BDC of 3 bar, a wall temperature of 350 K with a frequency of (a) 1 RPM or $Pe = 1.8$ and (b) 750 RPM or $Pe = 1340$ (solid blue curve). The evolutions of the pressure during isothermal ($pV = \text{const}$) (dashed red curve) and adiabatic ($pV^\gamma = \text{const}$) (green dash-dotted curve) compression are also included. TDC corresponds to 0 °, BDC corresponds to −180 ° and 180 °. The products of pV and pV^γ are initially calculated from the time-averaged values for pressure and volume from the CFD simulation. From these (time-averaged values) we calculated the pressure trend as a function of the crank angle.

$\theta = 0$ °, while bottom dead centre is $\theta = -180$ ° and $\theta = 180$ °. In the slow case of Fig. VII.1(a), the maximum pressure is 21.8 bar while the minimum pressure is 3.1 bar, such that the pressure ratio is approximately $r_\text{p} = 7$. The fast case has a much higher pressure ratio of $r_\text{p} = 22.1$ because the minimum pressure is 2.2 bar and the maximum pressure is 47.6 bar. The maximum pressure is much higher for faster runs than slow runs. Furthermore, the minimum pressure in this case is lower than the initial pressure set at BDC of 3 bar.

Figure VII.1(a) and (b) also show the evolution of the pressure if the compression and expansion were isothermal ($pV = \text{const}$) and adiabatic respectively ($pV^\gamma = \text{const}$). The agreement with the idealized cases confirms what has been observed in previous experimental and numerical studies [90, 99, 100]. At low Peclet numbers, the oscillation frequency is small, and there is enough time for any work done by the gas to be exchanged in the form of heat with the solid walls. The gas temperature remains almost constant and equal to the wall temperature, and therefore the system undergoes isother-

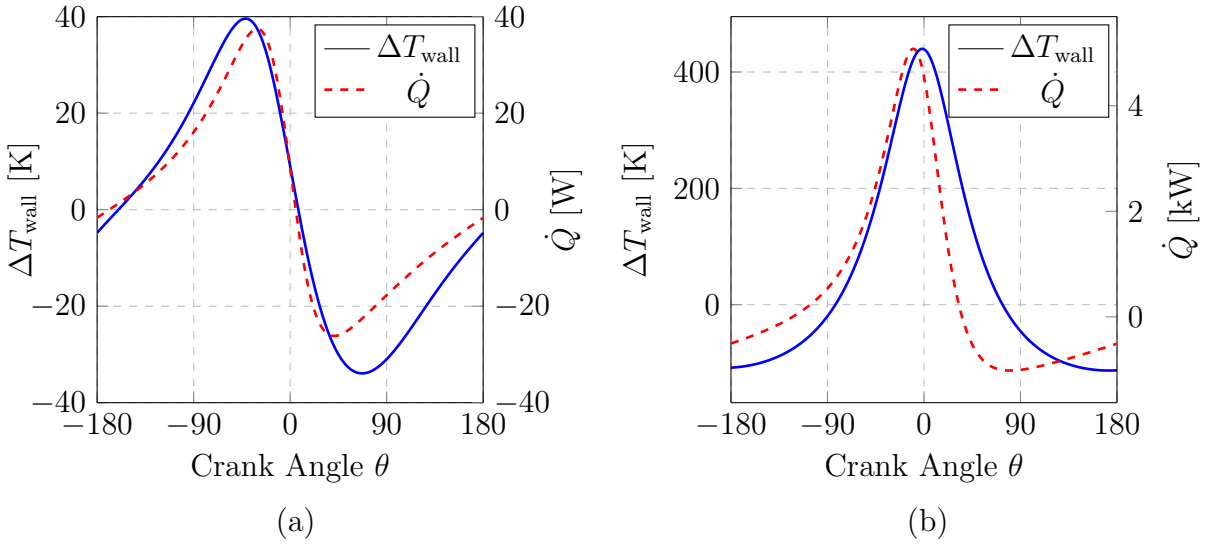


Figure VII.2: Evolution of temperature difference ΔT_{wall} between bulk gas and wall (solid blue curve) and gas-to-wall heat flux $\dot{Q}$ (dashed red curve) during one cycle. Gas spring initial pressure 3 bar, $T_{\text{wall}} = 350$ K with a frequency of (a) 1 RPM or $Pe = 1.8$ and (b) 750 RPM or $Pe = 1340$.)

mal compression. On the other hand, the oscillation frequency is high at elevated Peclet numbers. The variation between compression and expansion occurs too quickly for significant heat transfer to take place, and the system experiences near-adiabatic compression and expansion. The average pressure is much higher at higher frequencies than at lower frequencies, because for the adiabatic case pV^{γ} is constant while in the isothermal case pV is constant. In consequence, the average temperature in the adiabatic case is also higher, since from the ideal gas law we know that $pV = nRT$.

Figure VII.2 shows the evolution of the temperature difference between the bulk gas and wall for the same runs. As expected, the temperature amplitudes are very small and the mean temperature is the same as the wall temperature at low Peclet numbers. The temperature oscillates between 315 and 390 K and exhibits an almost sinusoidal trend. As for the fast run, the temperature oscillates between 237 K and 790 K. The oscillation cannot be considered sinusoidal any more. The same figure also include the gas-to-wall heat flux. The most striking feature is that at fast runs the heat transfer rate is two orders of magnitude higher than during slow runs. This is a result of the fact that slow runs have small temperature fluctuations and therefore small temperature differences with the cylinder wall.

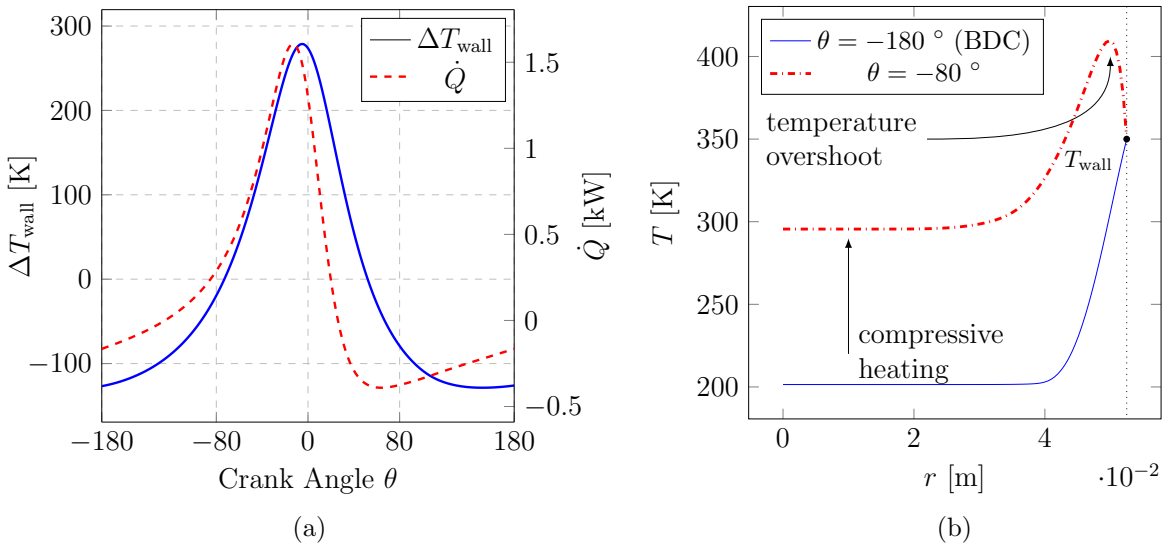


Figure VII.3: (a) Evolution of temperature difference ΔT_{wall} between bulk gas and wall (solid blue curve) and gas-to-wall heat flux $\dot{Q}$ (dashed red curve) during one cycle. Helium gas spring with initial pressure of 3 bar, $T_{\text{wall}} = 350$ K with a frequency of 100 RPM. (b) Temperature profiles as functions of radius r of same case. The wall temperature $T_{\text{wall}} = 350$ K.

From Fig. VII.2, we can also make observations of the relative phase of the temperature and heat flux evolutions. At 1 RPM shown in Fig. VII.2(a), the maximum heat flux and temperature difference occur at −31 ° and −42 ° (before TDC) respectively, while the minima are at 41 ° and 67 °. The phase difference is larger when heat is transferred from the wall to the gas during the first half of the expansion stroke (negative heat flux). At high frequencies such as 750 RPM (Fig. VII.2(b)), the peak negative temperature difference occurs close to BDC at 172 °, however the peak negative heat flux occurs at 80 °. The phase shift increases when moving to higher frequencies during the expansion stroke. However, during the compression stroke the phase differences are just as high as for low frequencies. From Fig. VII.2(b) we can see, that the phase shift between positive peaks of heat flux and temperature difference is 8 °.

The phase shift between the instantaneous wall heat flux $\dot{Q}$ and the bulk-gas-to-wall temperature difference ΔT_{wall} is observed for all rotational speeds to varying extents. This phenomenon, first predicted theoretically by Pfriem in the 1940s [94], is due to heat accumulation in the near-wall boundary layer. In Fig. VII.3(b), the temperature along the radius of a helium gas-spring running at 100 RPM is plotted. When the piston is at BDC the bulk gas is colder than the wall ($T_{\text{wall}} = 350$ K). Hence, both ΔT_{wall} and $\dot{Q}$ are negative at BDC, as shown in Fig. VII.3(a). During the compression stroke, the bulk

and near-to-wall gas is heated resulting in the temperature profile observed at $\theta > \theta_{\mathrm{BDC}}$, where a temperature overshoot is observed near the wall (in Fig. VII.3 at $\theta = -80°$). In this case, ΔT_{wall} and $\dot{Q}$ have opposite signs (Fig. VII.3(a) at $\theta = -80°$). This situation can be observed at different parts of the cycle (also during the expansion stroke with a reversed temperature overshoot) and is a characteristic feature of oscillatory heat transfer.

VII.2 Flow Structure

Figure VII.4 shows the streamlines during an oscillation cycle using helium at 1000 RPM with the velocity in axial direction u_z superimposed as a contour plot. Lekic and Kok [99] observed similar lflow fields. The images show that the flow during expansion and compression is stratified with no significant velocity gradient in radial direction. The fluid flow follows the dominant axial displacement of the piston, while near the static cylinder head the flow exhibits some curving. Towards the wall and the cylinder head the fluid velocity reduces due to the no-slip condition. We can infer from this that during expansion and compression the heat transfer is dominated by conduction. As the piston reaches top or bottom dead centre and changes direction, local vortices arise and three main recirculation areas appear. The gas in the thermal boundary layer near the wall and the bulk gas are mixed producing convective heat transfer [99].

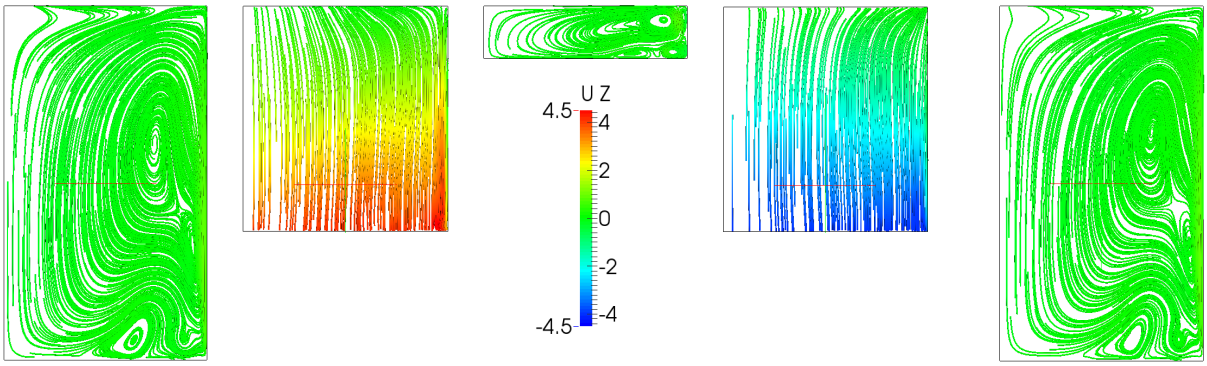


Figure VII.4: Streamlines with contours of the axial velocity u_z during compression and expansion. The centre plot is at TDC, while the plots at the very left and very right are at BDC.

VII.3 Influence of Real-Gas on Effects Temperature and Pressure

Three gases are considered here: helium, nitrogen and propane. For all the simulations in Sections VII.3 and VII.4, the wall temperature (and time-averaged temperature of the gas) is set to 350 K and the initial pressure of the gas at BDC is 3 bar. It is not possible to define an exact Peclet number for a given simulation run. The Peclet number can only be calculated after the time-averaged thermal diffusivity α_0 – which depends on the pressure and temperature – is known. A similar Peclet number ranging from $Pe \approx 360$ to $Pe \approx 540$ was adopted for all three gases. The Peclet number of a simulation run is only known after a simulation because the time-averaged thermal diffusivity α_0 is pressure and temperature-dependent. Therefore, when comparing different fluid models, identical simulation runs (same gas, same boundary and initial conditions, same speed) will produce different, but nonetheless similar, Peclet numbers. The rotational speeds considered were 250 RPM for helium, 25 RPM for nitrogen and 10 RPM for propane. Figures VII.5–VII.7 show: (a) T–V and (b) P–V curves for the three substances when modelled as ideal gases with (1) constant (solid blue) and (2) temperature-dependent thermodynamic/transport properties (dashed red) and (3) as real gases with density and temperature-dependent properties (dotted green). Additionally, nitrogen and propane are also simulated with (4) real gas property look-up tables (dash-dotted yellow).

As expected, nitrogen and helium behave similarly regardless of the model applied, although, the temperatures are slightly overestimated when assuming constant thermophysical properties compared to the real-gas model. Propane, on the other hand, shows non-negligible deviations (Fig. VII.7). The simulations which use real-gas property look-up tables (yellow in Fig. VII.7) are used as a reference for comparison. Both ideal-gas models overestimate the pressure, especially at TDC, while the Peng-Robinson model underestimates the pressure at TDC. The look-up table simulation calculates a pressure at TDC of approximately 20.6 bar, while the ideal-gas models predict a pressure of 24.1 bar (constant properties) and 23.4 bar (temperature dependent) and the Peng-Robinson simulation calculates 18.0 bar. All four models predict similar pressures at BDC.

As for the temperature in Fig. VII.7(a), all models predict very similar values. The look-up table simulations predict a maximum temperature 393 K at TDC. The Peng-Robinson simulation predicts 388 K, the ideal-gas model with varying properties predicts 389 K, and the ideal-gas model with constant properties predicts 401 K. At BDC, both ideal-gas models are consistent in predicting the temperature, while the Peng-Robinson

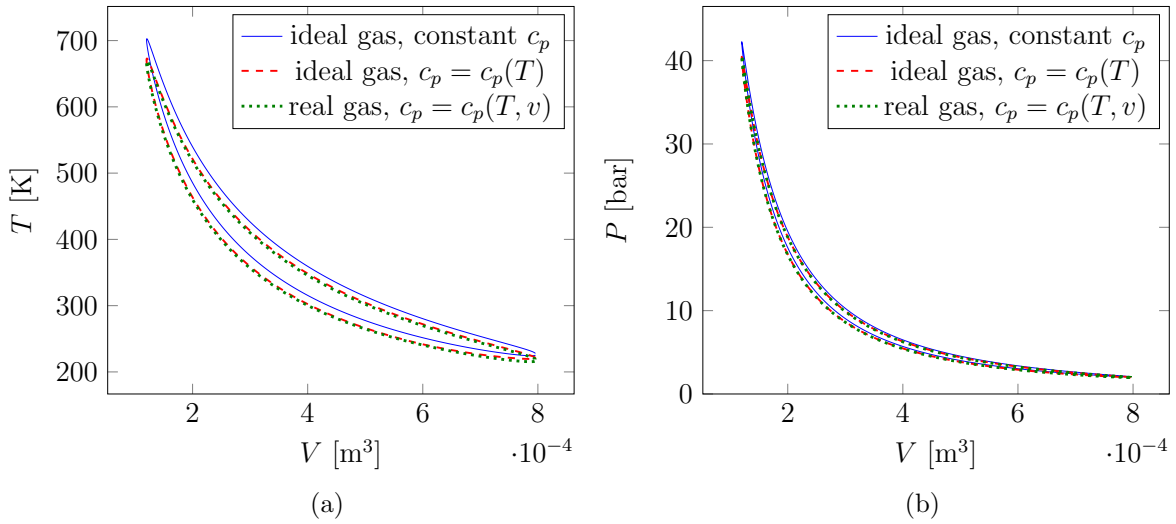


Figure VII.5: (a): T–V diagram and (b): P–V diagram for helium at 250 RPM for the ideal-gas model with constant thermophysical properties, $Pe = 446$ (solid blue); ideal-gas model with temperature-dependent properties, $Pe = 502$ (dashed red); and real-gas model with temperature and density dependent properties $Pe = 457$ (dotted green).

model deviates slightly more. The look-up table simulation temperature at BDC is 320 K, the ideal gas model with varying properties predicts 322 K, the ideal gas model with constant properties is 320 K and the Peng-Robinson simulation predicts 315 K. All four simulation models predict average temperatures (and pressures) which are higher during the compression stroke than during the expansion stroke.

Generally speaking, the Peng-Robinson model underestimates pressure and temperature, while the ideal gas models both overestimate the pressure. The ideal gas model with constant properties overestimates the temperature at TDC while predicting very accurate values at BDC. The ideal gas model with varying properties shows the best agreement in temperature with the look-up table simulation. Thus, while the ideal-gas models predict the temperature accurately, the predictions of pressure are not reliable.

Discrepancies between ideal and real gases can be understood via the compressibility factor Z:

$$Z = Pv/RT \tag{VII.1}$$

which is plotted in Fig. VII.8. By definition, $Z = 1$ for ideal gases. Values deviating from unity provide a measure for the magnitude of the real-gas effects. These tend to increase when one is close to the critical point or the saturation curves which – relative to the cases considered – corresponds to low temperatures and high pressures. Figure VII.8

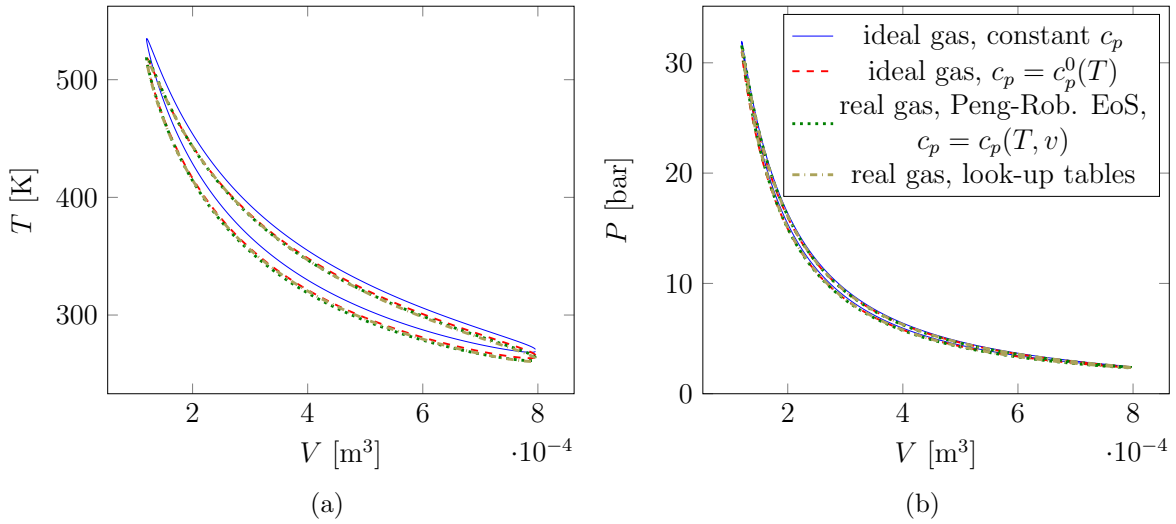


Figure VII.6: (a): T–V diagram and (b): P–V diagram for nitrogen at 25 RPM for the ideal-gas model with constant thermophysical properties, $Pe = 371$ (solid blue); ideal-gas model with temperature-dependent properties, $Pe = 355$ (dashed red); real-gas model using Peng-Robinson equation of state with temperature and density dependent properties and , $Pe = 355$ (dotted green); and model which uses empirical data tables for temperature, pressure, density, and physical properties, $Pe = 368$ (dash-dotted yellow).

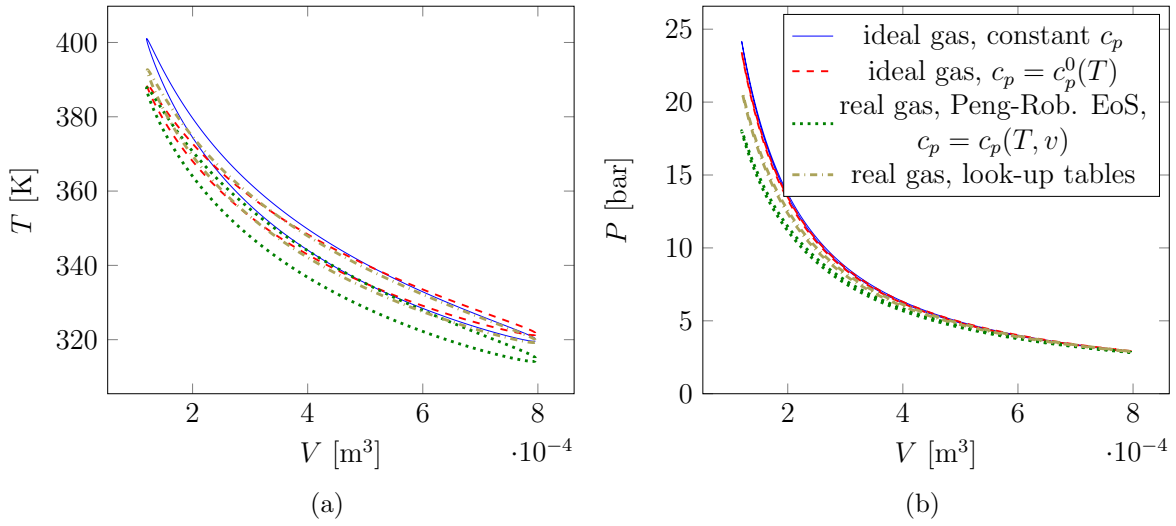


Figure VII.7: (a): T–V diagram and (b): P–V diagram for propane at 10 RPM for the ideal-gas model with constant thermophysical properties, $Pe = 545$ (solid blue); ideal-gas model with temperature-dependent properties, $Pe = 442$ (dashed red); real-gas model with temperature and density dependent properties, $Pe = 382$ (dotted green); and model which uses empirical data tables for temperature, pressure, density, and physical properties, $Pe = 506$ (dash-dotted yellow).

shows that Z is almost always equal to or very slightly greater than 1 at all crank angles for nitrogen. When propane is used, Z moves away from unity, especially at TDC where it can go as low as 0.75 for the Peng-Robinson simulations and 0.85 for the simulations with look-up tables. Simulations using the Peng-Robinson equation of state predict the gas to behave more non-ideal than the simulations which use look-up tables.

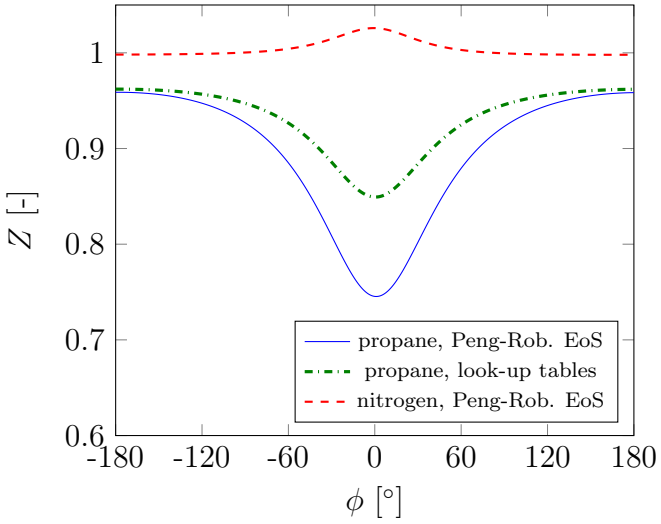


Figure VII.8: Compressibility Z over a cycle for nitrogen and propane for the case of maximum loss at $Pe \approx 10$.

VII.4 Influence of Real-Gas Effects on Thermally Induced Losses

Figures VII.9–VII.11 show the loss parameters (a) ψ and (b) ψ_{k} for helium, nitrogen and propane for varying Peclet numbers. The general trend which has been reported in previous work [88–91, 99–101] is also observed here: at low and high Pe the loss is low, and a maximum is observed at an intermediate value which is around $Pe \approx 10$. The losses normalized by the compression work ψ are as high as 28.0% for helium, 18.6% for nitrogen and 7.7% for propane. The losses normalized by the adiabatic compression work exhibit the same trends, although the values are less by a factor of about 1.5. This underlines the fact that thermally induced losses are not negligible in reciprocating machines. At low Peclet numbers, the oscillation frequency is small, and there is enough time for any work done by the gas to be exchanged in the form of heat with the solid walls. The gas temperature remains constant and equal to the wall temperature, and therefore the

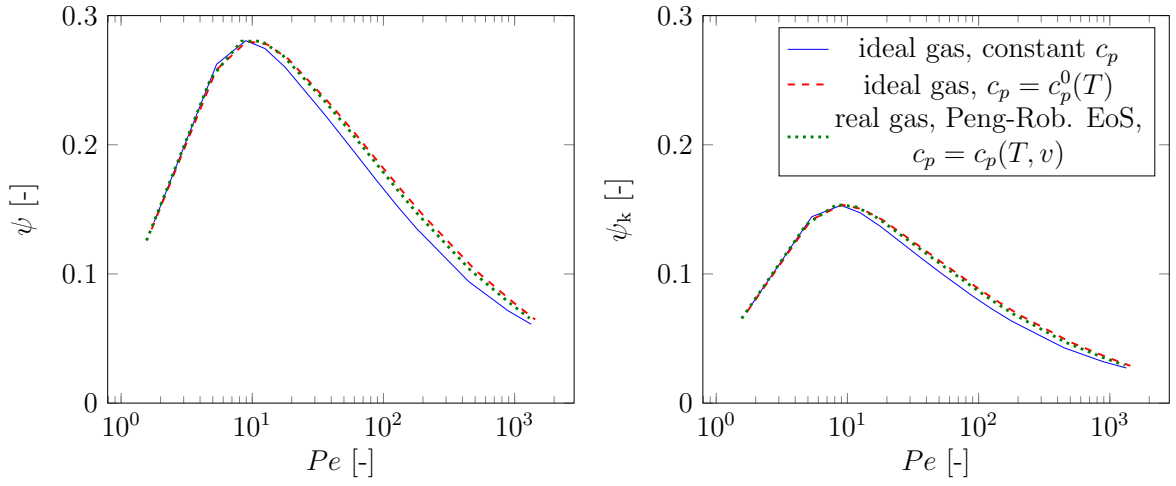


Figure VII.9: (a) Loss parameter ψ as defined in Eq. VI.34 and (b) loss parameter ψ_k as defined in Eq. VI.35 as a function of Pe for a helium gas spring.

system undergoes isothermal compression. On the other hand, the oscillation frequency is high at elevated Peclet numbers. The variation between compression and expansion occurs too quickly for significant heat transfer to take place, and the system experiences adiabatic compression and expansion. At intermediate Peclet numbers, a (net) work results from the interplay between both the non-zero internal energy of the gas and the non-zero heat transfer to the solid, leading to a net loss of work during the cycle.

All three models predict similar loss values for helium and nitrogen over the whole number range. As for propane in Fig. VII.11(a) and (b), both ideal-gas models underestimate the thermal loss compared to the real-gas model with look-up tables. On the other hand, the real gas model which uses the Peng-Robinson equation of state overestimates the loss. At $Pe \approx 10$ (where the losses peak), the differences between the models are greatest. The temperature-dependent ideal-gas model predicts a peak loss ψ of 0.057 and the constant-property ideal-gas model predicts a peak loss of 0.068. The Peng-Robinson real-gas model shows a peak loss of 0.089 while the look-up table model predicts a peak loss of 0.077.

Figure VII.12 shows the absolute heat transfer loss calculated by real-gas simulations ($\oint P\mathrm{d}V|_{\mathrm{RG}}$) divided by the absolute heat transfer loss calculated by the temperature-dependent ideal-gas model ($\oint P\mathrm{d}V|_{\mathrm{IG}}$). From Fig. VII.12, we can see that real-gas effects increase the thermally induced losses by a factor as high as 1.3 or 1.4 regardless of the Peclet number.

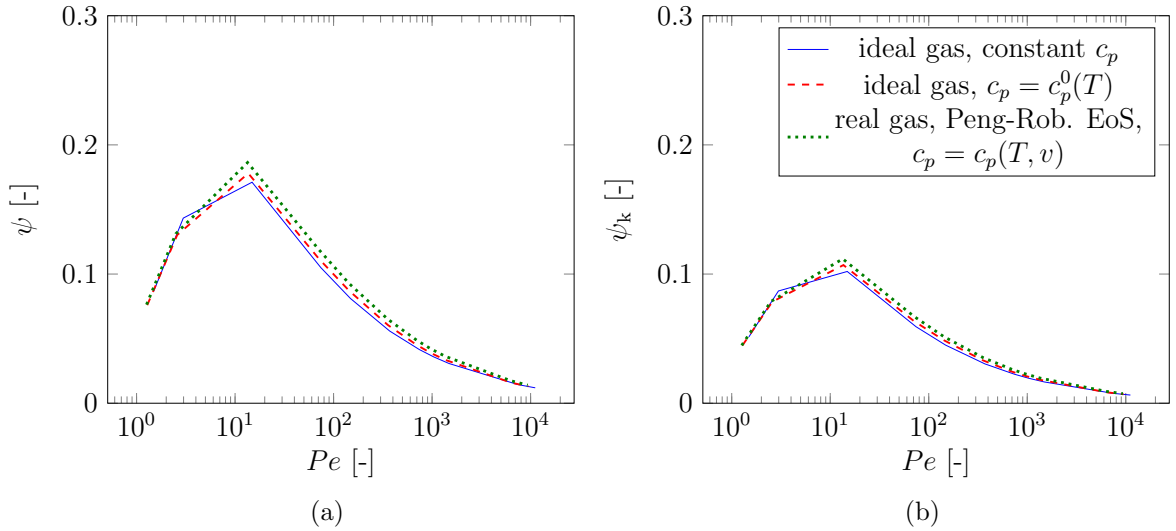


Figure VII.10: (a) Loss parameter ψ as defined in Eq. VI.34 and (b) loss parameter ψ_k as defined in Eq. VI.35 as a function of Pe for a nitrogen gas spring.

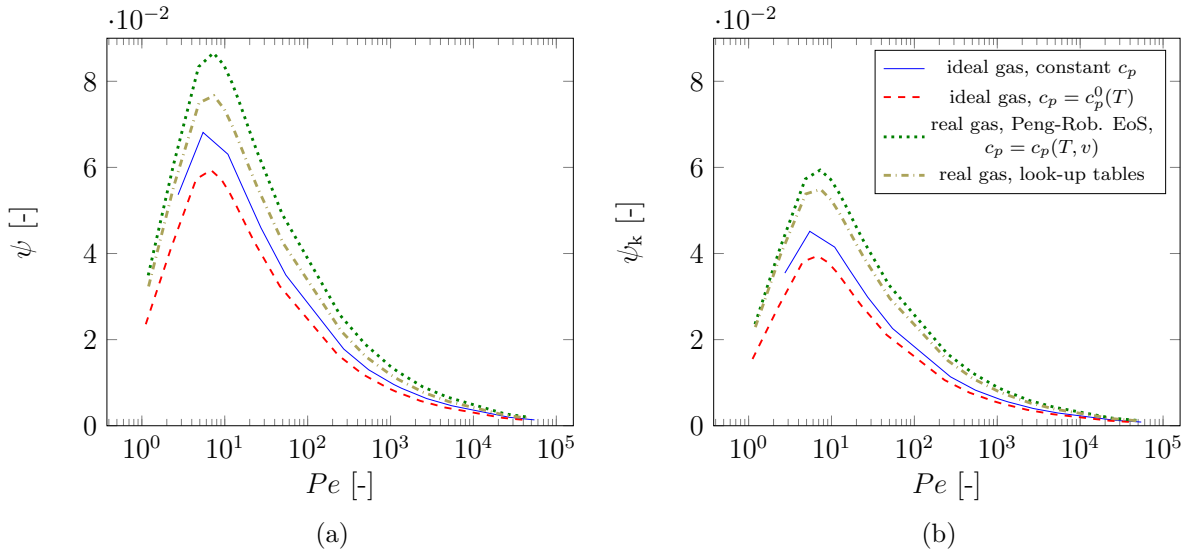


Figure VII.11: (a) Loss parameter ψ as defined in Eq. VI.34 and (b) loss parameter ψ_k as defined in Eq. VI.35 as a function of Pe for a propane gas spring.

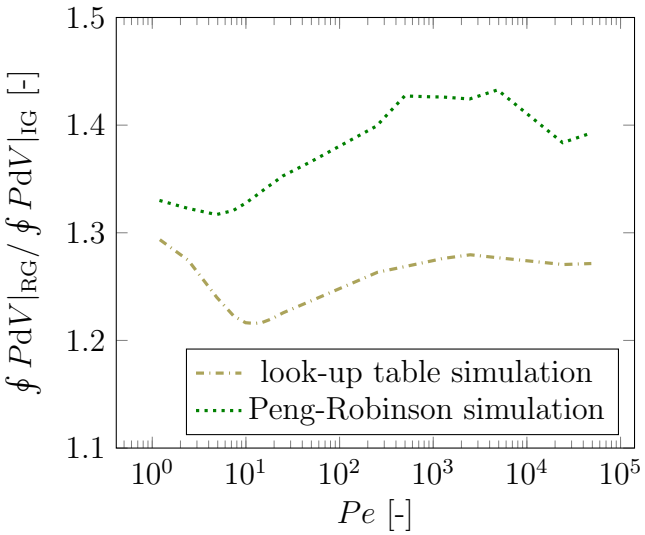


Figure VII.12: Ratio of real-gas model heat-transfer loss to ideal-gas model heat-transfer loss $\oint P\mathrm{d}V|_{\mathrm{RG}}/\oint P\mathrm{d}V|_{\mathrm{IG}}$ for varying Peclet numbers for the propane gas spring. The two real gas models are considered (look-up tables and Peng-Robinson).

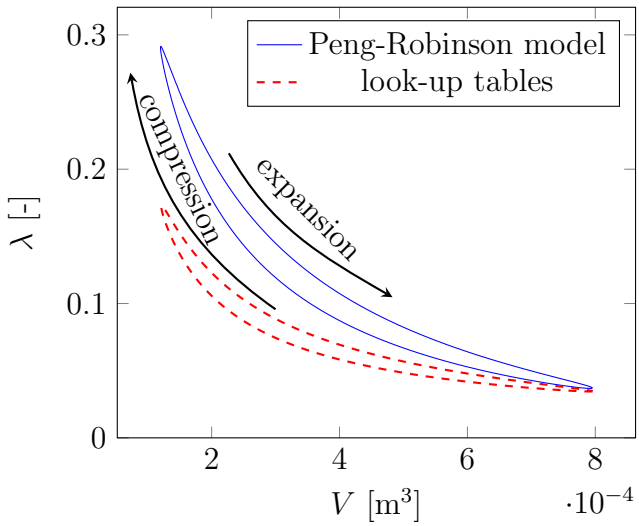


Figure VII.13: Plot of $\lambda = 1 - Z$ against volume over a cycle with propane ($Pe \approx 10$).

We now define parameter λ as:

$$\lambda = 1 - Z\,, \tag{VII.2}$$

which is a measure of how non-ideally a gas behaves. It is higher during the expansion stroke than during compression meaning that the gas is less ideal during expansion. This is shown in Fig. VII.13 where λ is plotted against the cylinder volume in one oscillation cycle for the Peng-Robinson model and look-up table model. This "asymmetry" between expansion and compression for real gases leads to an increased loss compared to ideal gases. For the Peng-Robinson case from Fig. VII.13 ($Pe \approx 10$), for example, the mean value for λ during compression is 0.09 while during expansion it is 0.11. For the look-up table case, it is 0.06 and 0.09. Integrating λ with respect to the instantaneous volume of the cylinder provides a good measure of the asymmetry in gas behaviour between expansion and compression:

$$\Lambda_i = \frac{1}{V_{\text{TDC}}} \oint \lambda \mathrm{d}V\,. \tag{VII.3}$$

The integrals $\Lambda_i = \Lambda_{\text{PR}}$ for Peng-Robinson simulations or $\Lambda_i = \Lambda_{\text{LT}}$ for look-up table simulations give the (non-dimensionalized) area enclosed within the curves of Fig. VII.13. If $\Lambda > 0$, then the mean compressibility factor is lower during expansion than compression (the gas is more non-ideal during expansion). The higher the value of Λ, the larger the "asymmetry" in compressibility factor between the expansion and compression strokes. We compare the values of Λ to the normalized difference between the real gas and ideal-gas loss $\Delta\psi_i$ defined as:

$$\Delta\psi_i = \frac{\oint P\mathrm{d}V\big|_{\text{RG}} - \oint P\mathrm{d}V\big|_{\text{IG}}}{\int_{\text{BDC}}^{\text{TDC}} P\mathrm{d}V\Big|_{RG}}\,, \tag{VII.4}$$

where $\oint P\mathrm{d}V$ is the absolute heat transfer loss during one cycle, and $\int_{\text{BDC}}^{\text{TDC}} P\mathrm{d}V$ is the work the piston does on the gas during compression. The subscript $|_{\text{RG}}$ denotes calculations from a real-gas simulation, and $|_{\text{IG}}$ denotes the use of an ideal-gas simulation. The parameter $\Delta\psi_i$ thus calculates the difference in absolute heat transfer loss between the real gas and ideal gas model and normalizes that value by the compression work of the real gas. If the Peng-Robinson model is considered, then $\Delta\psi_i = \Delta\psi_{\text{PR}}$; if the look-up table model is used, then $\Delta\psi_i = \Delta\psi_{\text{LT}}$.

In Fig. VII.14, we plot $\Delta\psi_{\text{LT}}$ and $\Delta\psi_{\text{PR}}$ as a function of Λ for all considered frequencies of the propane gas spring when using the Peng-Robinson and look-up table simulation.

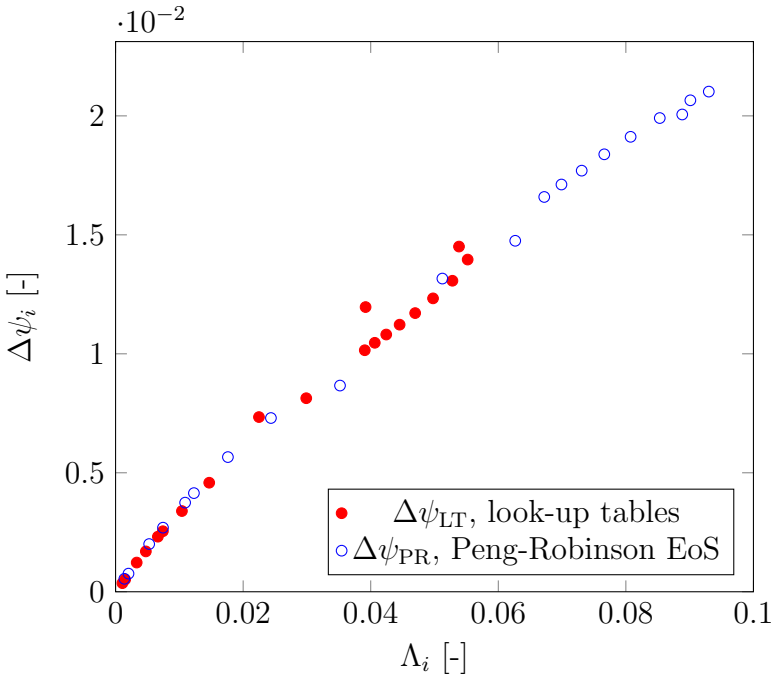


Figure VII.14: Plot of normalized loss difference between real and ideal-gas simulations of the propane gas-spring plotted as a function of the integral Λ_i as a measure of the asymmetry in gas behaviour between compression and expansion.

The linear relationship between $\Delta\psi$ and Λ is a good approximation for the range considered, indicating that firstly the higher the real gas-effects are, the higher the increase in loss is relative to the ideal gas assumption; and secondly the higher the asymmetry in non-ideality between expansion and compression, the higher the loss increase between ideal and real-gas models. The increase in real-gas behaviour during expansion means that less work can be recovered. Since the non-ideality is higher during expansion than during compression, the losses incurred during expansion are also higher.

Finally, the Peng-Robinson model predicts more non-ideality in the gas behaviour than the look-up table model. Taking the case from Fig. VII.8 as an example, one can see that during the whole cycle the compressibility factor Z is farther away from unity for the Peng-Robinson model. The maximum difference in compressibilities is attained at TDC where $Z_{\mathrm{PR}} = 0.75$ and $Z_{\mathrm{LT}} = 0.85$. One can also see from Figs. VII.13 and VII.14 that the "asymmetry" (enclosed area in Fig. VII.13) between compression and expansion is greater in the Peng-Robinson model. This is why the thermally induced losses are predicted to be higher when using the Peng-Robinson model compared to the look-up table model.

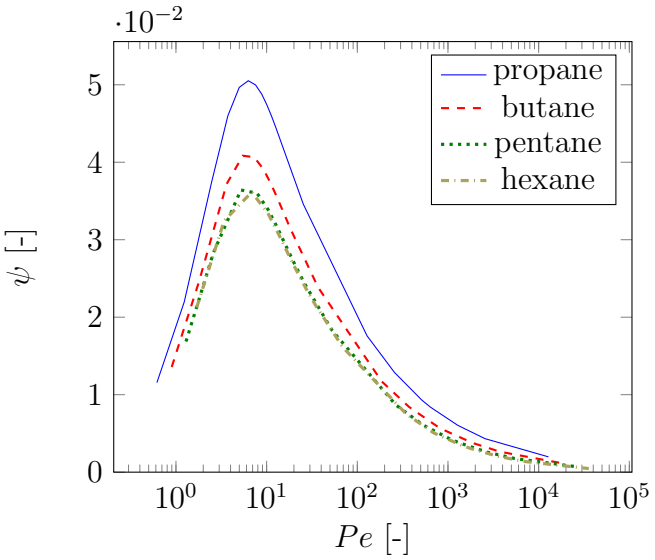


Figure VII.15: Loss ψ as a function of Pe for the alkanes propane (blue, solid), butane (red, dashed), pentane (green, dotted) and hexane (yellow, dash-dotted). The predictions were calculated with simulations using look-up tables.

VII.5 Comparison of Thermally Induced Losses of Alkanes

In Fig. VII.15, we show thermally induced losses ψ for simulations using the alkanes propane (C_3H_8), butane (C_4H_{10}), pentane (C_5H_{12}) and hexane (C_6H_{14}). Once again, the losses are plotted as functions of the Péclet number. The wall temperature is set to 485 K and the initial pressure at BDC is set at a pressure of 3 bar for all alkanes

What Fig. VII.15 shows us is that the losses decrease when moving to heavier alkanes. The peak losses for the alkanes are 0.051 for propane, 0.041 for butane, and 0.036 for both pentane and hexane. The loss correlates with the absolute heat capacity of the gas volume. With increasing heat capacity, the loss decreases. The time-averaged heat capacities for the peak loss cases at $Pe \approx 10$ are 7.22 J/K for propane, 9.76 J/K for butane, 12.64 J/K for pentane and 15.18 J/K for hexane. This is illustrated in Fig. VII.16. A low heat capacity results in higher temperature amplitudes during the oscillation. The fluctuating components of the temperature during one cycle can be seen in Fig. VII.17 for the four alkanes, and it is clear that the propane gas spring has the highest temperature amplitude while the hexane one has the lowest. Higher temperature amplitudes lead to larger temperature differences between the wall and the gas which in turn lead to higher

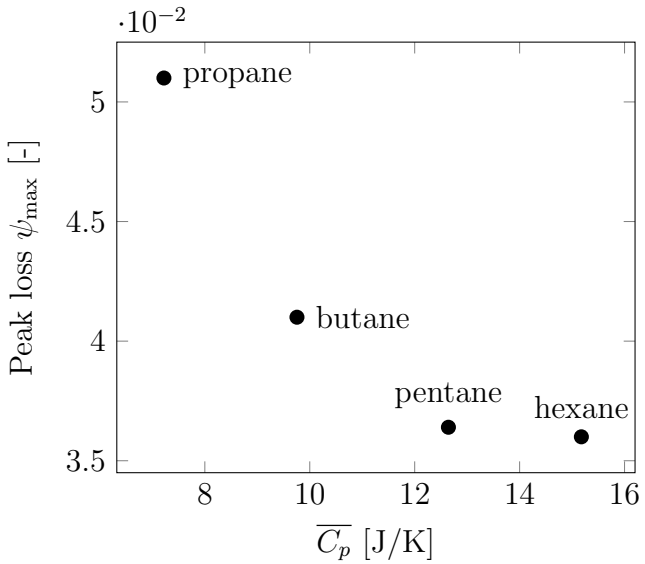


Figure VII.16: Peak loss for different alkanes as a function of the time-averaged absolute heat capacity $\overline{C_p}$.

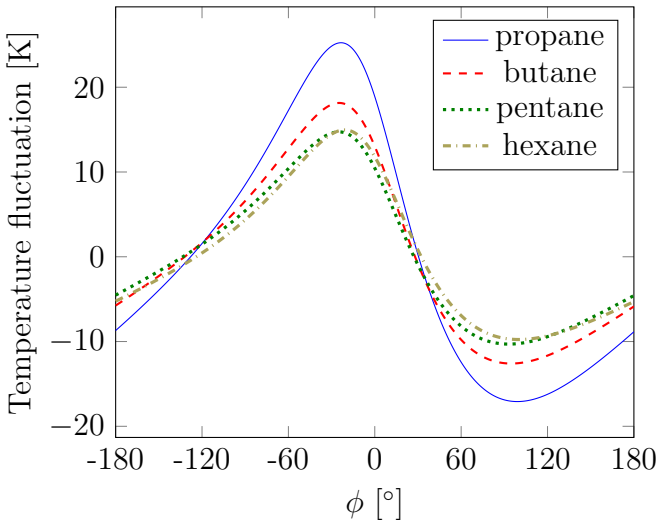


Figure VII.17: Fluctuating component of the temperature over one cycle for the alkanes propane (blue, solid), butane (red, dashed), pentane (green, dotted) and hexane (yellow, dash-dotted) for $Pe \approx 10$ (peak loss). The predictions were calculated with simulations using look-up tables.

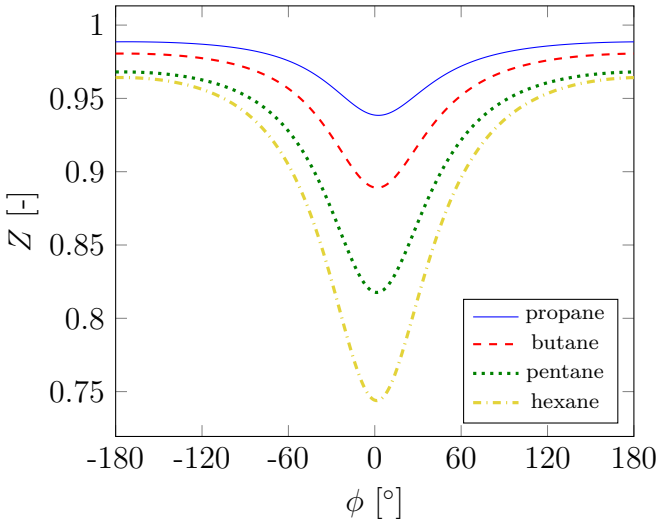


Figure VII.18: Compressibility Z over a cycle for the alkanes propane, butane, pentane and hexane for the case of maximum loss at $Pe \approx 10$, time-averaged temperature 485 K, time-averaged pressure 7.5 bar.

heat transfer rates. Therefore, the loss is higher for lower average heat capacities and higher temperature amplitudes.

The peak loss of the hexane gas-spring shown in Fig. VII.15 is unexpectedly high compared to the other alkanes considering its high heat capacity. Since the temperature amplitude of hexane is almost equal to that of pentane, their losses are also almost identical. The reason for the high peak loss of hexane in this case could be the increased real-gas effects. Hexane has a relatively low critical point in terms of pressure and temperature and, therefore, the compressibility is lower for hexane than for the other alkanes. The compressibility factor is plotted for all alkanes at the peak loss case in Fig. VII.18. For hexane, Z falls below 0.75 at TDC while for pentane it remains above 0.8. The increase of real-gas effects in hexane lead to its comparably high loss parameter value relative to the other considered alkanes.

VII.6 Thermally Induced Losses of Real-gas Mixtures

Additionally, look-up table simulations are carried out with mixtures of propane and hexane. The same initial and boundary conditions are defined as in the previous section. The wall temperature is once again 485 K and the initial pressure at BDC is 3 bar. Three

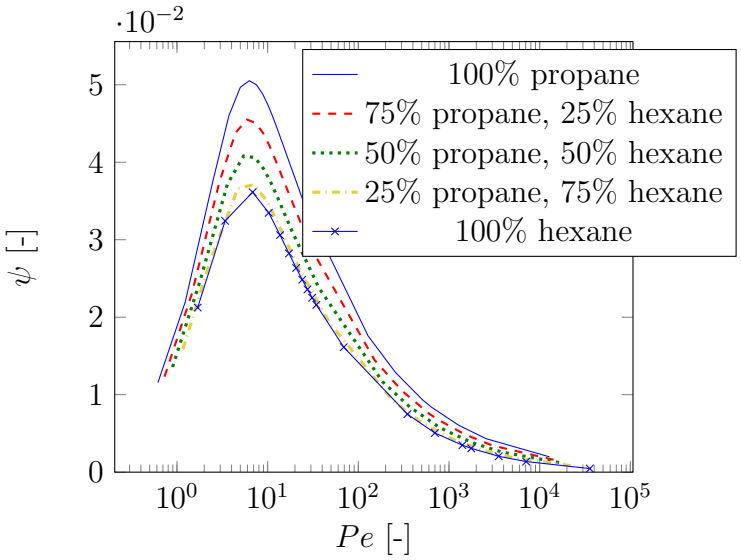


Figure VII.19: Loss ψ as a function of Pe for the alkanes propane (blue, solid), butane (red, dashed), pentane (green, dotted) and hexane (yellow, dash-dotted). The predictions were calculated with simulations using look-up tables.

mixtures were calculated: 25% propane and 75% hexane; 50% propane and 50% hexane; and 75% propane and 25% hexane (mass ratios). The simulations were carried out using look-up tables, where the data were taken from REFPROP. As seen previously, propane has the highest loss and hexane has the lowest. The peak losses of the mixtures decrease with increasing hexane or decreasing propane ratio as can be seen in Fig. VII.20. The same correlation between the loss and the heat capacity is observed as in the previous section with pure alkanes. Low heat capacities lead to high temperature amplitudes which in turn result in high loss values.

VII.7 Summary

Devices which use reciprocating motion to convert heat suffer from unsteady heat transfer loss. Gas springs are a good approximation of the expansion and compression processes occurring in reciprocating energy-conversion devices and are an appropriate model to quantify unsteady heat transfer losses in these machines. A two-dimensional CFD model of a gas-spring wedge has been developed to simulate the compression/expansion processes and calculate thermally induced thermodynamic losses in gas springs. The model can also take real-gas effects into account through two separate methods: (1) calculating pressure and temperature-dependent thermodynamic and transport properties in addition

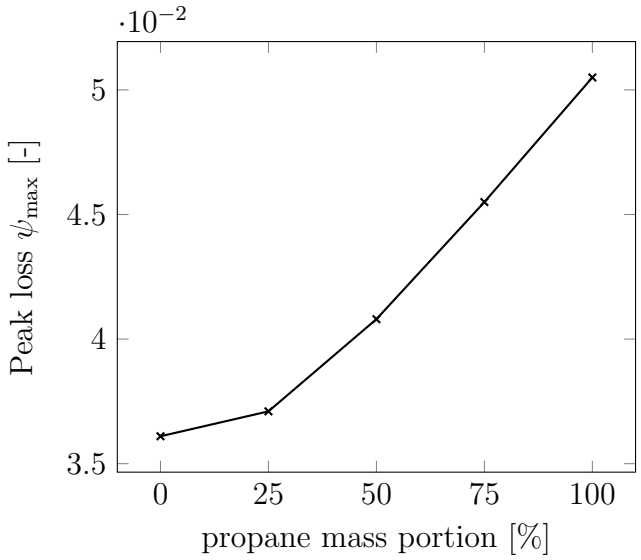


Figure VII.20: Peak loss as a function of the mass ratio of propane in propane-hexane mixtures.

to using the Peng-Robinson equation-of-state or (2) extracting data from look-up tables which list thermodynamic and transport properties of fluids as functions of pressure and temperature. Due to the low velocity of the flow and piston, the Reynolds numbers were well below the critical Reynolds numbers for the transition to turbulence in the boundary layer thereby allowing a laminar model to be used. The wall temperatures surrounding the gas were set to be uniform and constant. Four different gas models were compared: (1) an ideal-gas model with constant thermodynamic and transport properties, (2) an ideal model with temperature-dependent properties, (3) a real-gas model based on the Peng-Robinson equation-of-state with pressure and temperature-dependent properties, and finally (4) a gas model which uses empirical data in look-up tables of thermodynamic and transport properties as functions of temperature and pressure. The solver estimates properties through bilinear interpolation. The most accurate simulation is the one which uses the real gas property tables. However, it is also the most computationally demanding. The other gas models can cut computational time by almost an order of magnitude, especially the ideal gas models.

Initially, the three gases helium, nitrogen and propane are considered. One of the first observations is that thermally induced losses in reciprocating machines are not negligible. They may reach values from 10 to 30% for some gases. The losses were higher for helium than for nitrogen or propane.

Summary

When comparing helium and nitrogen, all gas models show similar variations in pressure and temperature over the cycle. Thus, helium and nitrogen can be accurately modelled as ideal gases. For propane, the ideal-gas models deviate from real-gas models especially at the higher pressures occurring at and near TDC where the deviation was as high as 20% for pressure between ideal gas values and the real gas values calculated with look-up table simulations. The ideal-gas models overestimate the pressures and to a lesser extent the temperatures in these conditions compared to the look-up table simulations, while the Peng-Robinson real-gas model generally underestimates the pressure (especially at TDC by 10%) and the temperature. The compressibility factor Z, which is used here to quantify deviations from ideality, is almost always 1, but for propane Z falls down to 0.75 at TDC in the Peng-Robinson model and 0.85 at TDC for the look-up table simulation. This explains the discrepancies between the ideal and real-gas models of propane.

Thermally induced losses were evaluated and compared for the gases over a range of Peclet numbers. Significant differences between the models were only observed for propane: both ideal-gas models underestimate the thermal loss compared to the real-gas models of this gas. This occurs over the entire Peclet number range investigated indicating that real-gas effects can increase the thermally induced losses in gas springs. The highest difference between loss values was observed at peak loss ($Pe \approx 10$) where the real-gas loss was 7.7% (property tables) and 8.9% (Peng-Robinson EoS) of the compression work and the ideal-gas loss was only 5.7% of the compression work. The reason for the difference in the predicted losses is the different gas behaviour during compression and expansion. Propane has a lower compressibility factor during expansion than compression, making it behave even more like a real gas during the expansion stroke. For ideal-gas models, the compressibility factor is by definition always equal to unity. This increase in real-gas behaviour during expansion means less work is recovered and therefore higher losses over the cycle. There is a linear correlation between the normalized increase in loss and the asymmetry in the ideality behaviour of the gas during compression and expansion. The Peng-Robinson simulations predict a higher loss due to the fact that the non-ideality during expansion is higher.

Thermally induced losses of different alkanes and alkane mixtures have also been investigated with real gas property table simulations. Heavier alkanes show lower losses than lighter ones if the operating parameters of compression and expansion are similar (same geometry, volume ratio, and initial and boundary conditions). This is because the absolute heat capacity of the gas spring volume is higher for the heavier gases. High

heat capacities lead to lower temperature fluctuations and amplitudes which result in turn in lower heat transfer to and from the walls. Hexane shows unexpectedly high losses similar to those predicted for pentane. This is due to the real gas effects which are especially prevalent with hexane at the temperatures and pressures considered. Mixtures of propane and hexane show similar behaviour to that of the different alkanes. Pure hexane gas springs have lower losses than pure propane gas springs. The losses increase with the propane mass portion.

We can summarize the main findings of this study in the following three points: (1) thermally induced losses in reciprocating are not negligible They can reach proportions as high as 30% of the compression work or adiabatic compression work. This has been concluded in all previous studies of gas springs as well. Our study has also confirmed the observations made in the publication by Lekic and Kok [99] where they simulated a gas spring in CFD. (2) Real-fluids experience even higher heat transfer losses. When taking real-gas effects into account, absolute losses are higher by a factor of 1.3–1.5 for all oscillation frequencies compared to calculations where one assumes the fluid is an ideal gas. There is a direct correlation between normalized loss increase and the degree of asymmetry of the compressibility factor. The fluid is less ideal during expansion. Therefore, expanders are more affected than compressors by real-gas effects. (3) Gases with low (absolute) heat capacities will have higher temperature amplitudes which lead to high temperature differences to the wall. The increased heat flux will increase the heat transfer losses.

Chapter VIII

Summary of Thesis Findings

Reducing emissions from energy production, especially those associated with climate change, is a major scientific, political, and economic challenge of the 21st century. Several governments are pursuing the move to a more dencentralized or distributed power generation network. In such a scenario, using small- to medium-scale systems to convert low- and medium-grade heat, especially from waste-heat sources, is one component of a sustainable energy future. Therefore, novel and cost-efficient technologies are needed to address the challenge of increasing emissions and fuel costs. Technologies which use reciprocating motion are promising candidates for low- and medium-grade heat conversion. Three main areas related to heat conversion using reciprocating motion have been investigated as part of this work: (1) the Evaporative Reciprocating-Piston Engine (ERPE), (2) working-fluid mixtures in organic Rankine cycles (ORCs), and (3) unsteady heat-transfer losses in reciprocating machines.

VIII.1 Evaporative Reciprocating-Piston Engine

The ERPE is a theoretical two-phase Thermofluidic Oscillator (TFO) which was developed and derived with a first-order linearized, spatially lumped dynamic model. The model applied electrical analogies in order to represent the operation of physical TFO with passive electrical components. The ERPE was developed by neglecting or linearizing non-linear effects occurring in an existing experimental TFO prototype. The linear model was not only developed to provide suggestions on how to improve the performance of the ERPE and the original prototype, but also to advance the overall knowledge and understanding of the nascent technology that is the TFO engine.

Measurements of the frequency, temperature gradients and heat input rate gradient in the prototype were used as indicative values for the calculations of the model. The developed model contained two sub-models of the heat transfer process. One allowed for a 'Dynamic Heat Exchange' (DHX) process to take place at the heat exchangers which accounted for the capacity of the heat exchanger walls to store and release heat. The other sub-model assumed a 'Linear Temperature Profile' (LTP) along the height of the heat exchanger walls. The models, in all cases, overestimated the frequency, but the DHX model predicted realistic frequencies in the load-free case. The temperature and heat-input gradient predictions, on the other hand, were all within acceptable ranges.

Parametric studies have shown that for the load-free case, the argon gas spring compressibility, vapour gas spring compressibility, and connection tube inductance – if kept at a minimum – have the highest effect on increasing the frequency. Additionally, to minimize the heat input rate gradient, the thermal resistance, heat exchanger capacitance, displacer cylinder hydrostatic capacitance, and vapour gas spring compressibility should be low, while the connection tube inductance should be high.

In an engine equipped with a load, only five parameters have proven to affect the frequency, exergy efficiency, heat-input rate gradient, or power output significantly: the thermal resistance, the heat exchanger capacitance, the vapour compressibility, the connection tube inductance, and the hydrostatic capacitance of the displacer cylinder. The most influential parameter was the vapour gas spring capacitance. To increase the power output, exergy efficiency and frequency, the vapour compressibility must be as low as possible while the connection tube inductance should be kept moderately high. This can be achieved by decreasing the time-averaged vapour space, increasing the mean pressure, reducing the diameter of the connection tube or increasing its length. Additionally, keeping the thermal resistance and heat exchanger capacitance at intermediate (nominal) levels further increased power output and efficiency. The resistance was inversely proportional to the heat transfer coefficient and heat transfer area, while the capacitance was proportional to the heat capacity of the walls and their mass. Finally, the parameters were optimal around their nominal values with regards to the necessary heat input. However, the connection tube inductance should be moderately high (as before for the efficiency), and the hydrostatic capacitance in the displacer cylinder should be as small as possible. This can be achieved by decreasing the cross-section area of the cylinder.

The deterioration in efficiency and power output per unit heat input depending on the vapour gas spring capacitance and connection tube inductance were ascribed to an increase in required exergy input to the engine which did not translate into an increase

in work output. The exergy destruction mainly occurred at the transfer of heat to the working fluid, often due to an unfavourable phase difference. The insight from these results offered important suggestions and guidance for improving performance and for system optimization.

Future Work

To improve the accuracy of the electrical analogy model with regards to physically existing TFO engines, non-linear effects should be taken into account. This is because several components exhibit non-linear effects when they are actually designed and operated in a prototype. The gas springs, for example, can only be considered to behave linearly if the fluctuations are small compared to the average value of the pressure. There are some operating conditions where this may no longer be the case. Furthermore, there are several non-linearities associated with the heat addition and rejection processes. The temperature or heat-flux profile along the height of the heat exchangers has been observed to be non-linear in other TFO prototypes such as the NIFTE. Additionally, we assumed a constant heat transfer coefficient for the evaporation and condensation, which was calculated based on correlations for steady-state pool boiling. A varying heat transfer coefficient – with at least two different values for evaporation and condensation – is non-linear. There are also many non-linear effects related to the piston and the leakage flow.

Some of the aforementioned aspects have been implemented successfully [28, 33]. However, it must be taken into account that non-linear calculations increase the computational time by a few orders of magnitude. Part of the intention behind developing a linear model is the fact that it completes calculations quickly, which facilitates parametric studies and optimization routines. The same claim cannot be made for non-linear models. Therefore, a linear and non-linear model are complimentary to each other, where the linear model can be used to understand general trends of the behaviour of a TFO, while a non-linear model would deliver more accurate results of a specific TFO configuration. An even more accurate model would be one that takes spatial effects into account, i.e. one that moves away from the lumped approach. A CFD simulation, for example, will be much more accurate than the discussed approach and would provide valuable insight into the behaviour of this type of engine. However, developing such a simulation is significant effort and running it will require very powerful computing resources.

Other phenomena which may influence physical TFO engines are loss mechanisms which occur due to the oscillatory nature of the engine. Examples for such losses include

phase change, which occurs out-of-phase with the position of the liquid vapour interface (e.g., if vapour condenses at colder parts of the vapour space while the vapour-liquid interface is in contact with the hot heat exchanger), or unsteady heat transfer associated with reciprocating motion as discussed in Chapters VI and VII. There are already existing correlations and analytical models for such losses which could be incorporated into a dynamic TFO model, however they are not widely applicable to different (non-ideal) working fluids and geometries. Further work is required to understand how these loss mechanisms behave and how they can be modelled analytically.

One study which can already be performed with the current model is to examine the performance of the engine when using different working fluids or working fluid mixtures. Working fluid studies have been carried out for the NIFTE and for the NIFTE [29] and for the UpTHERM [34]. However, no study has investigated using mixtures in TFOs. For such a study the required thermodynamic data for the fluids can be calculated with SAFT-VR Mie.

VIII.2 Organic Working-Fluid Mixtures in ORCs

The aim of the research in this area was to assess the potential of working-fluid mixtures, specifically alkane and perfluoroalkane mixtures, in ORCs for low to medium grade heat conversion. We modelled a sub-critical, non-regenerative ORC which uses binary mixtures of fluorocarbons or alkanes as a working fluid with a view towards affordable, low complexity, and high power output ORC plants. SAFT-VR Mie was used to acquire accurate thermodynamic and phase-change property values of the working-fluid mixtures. Mixtures of *n*-perfluorobutane and *n*-perfluorodecane were chosen as they are dissimilar which allows for a large temperature glide during phase change. However, predicting properties of mixtures with dissimilar components is more challenging.

The case study considered was an ORC driven by a flue gas stream at 330 °C and a cooling stream with a large flow-rate. We used SAFT-VR Mie to predict property values which were not available in the literature or property databases. Cycles running with pure working fluids exhibited higher thermal efficiencies than mixtures. However, for waste heat conversion, net power output is the most significant performance indicator. Our results have shown that superheating should be avoided in order to maximize output. Cycles using the pure lighter component (butane/perfluorobutane) produced the highest power outputs for all cases and the highest efficiencies for high evaporation pressures. At low pressures, mixtures with low butane or perfluorobutane proportions also produced

high power outputs. But overall, working-fluid mixtures were inferior to pure fluids apart from certain cycle configurations.

Total costs of the cycles correlated with mole fraction of the lighter components due to the associated increase in power output. Specific cost per unit power output also increased with the proportion of the lighter component. However, they fell sharply for pure butane and perfluorobutane. In general, we observed that cycles using pure fluids were more cost-efficient per unit power output than those using mixtures.

In the above described case, the temperature of the unconstrained cooling stream is constant. Therefore a mixture will have a higher average temperature difference with the cooling stream than the pure fluid because it exhibits a temperature glide during condensation. However, when the cooling stream is constrained and the temperature of the cooling stream changes, mixtures become the optimal working fluids. This is thanks to the improved thermal match to the temperature profile of the heat sink. The optimal mixture composition depends mainly on the gradient of the temperature rise in the cooling stream.

In conclusion, it is important to consider the use of working-fluid mixtures depending on the specific application. Working fluid design must therefore be fully integrated in the design of the whole cycle to exploit the full potential of the desired application.

Future Work

Working fluid mixtures were examined here from a thermodynamic and cost perspective. Detailed heat transfer characteristics were not considered. In practice, however, the literature suggests that the heat transfer coefficient of mixtures is considerably inferior to those of either of the constituent pure fluids. Therefore, the understanding of the heat transfer characteristics of mixtures must be improved. The extent and effect of this on the size and cost of heat exchangers must be ascertained before ORC systems with mixtures can be implemented on a large scale. Other future research work can investigate pathways in improving ORC performance by incorporating alternative cycle architectures, such as transcritical or supercritical cycles or internal regeneration.

A major goal in ORC research is to further develop computer aided molecular design and integrate it into a whole-system optimization platform or ORCs. Such a package would include the design of the working-fluid molecule in the overall optimization routine which will take several interdependencies and coupling effects into account.

VIII.3 Unsteady Heat-Transfer Losses Associated with Reciprocating Motion

Reciprocating machines can achieve higher efficiencies if the exergy losses associated with oscillating heat transfer between the working fluid and cylinder solid walls can be reduced. This loss also occurs in the gas springs of Thermofluidic Oscillators. A two-dimensional CFD model of a gas-spring wedge was developed to simulate the compression/expansion process and calculate thermally induced thermodynamic losses. Gas springs do not include the complex effects of valve timing and gas exchange of reciprocating-piston devices while they retain the fluctuating heat exchange phenomena between the cylinder walls and gas.

The aim of the research was to investigate the influence of real-gas effects on thermally induced losses. The model takes real-gas effects into account either (1) by using the Peng-Robinson equation of state and temperature and density dependent fluid properties or (2) by extracting data from look-up table which list fluid properties as functions of pressure and temperature.

The three gases, helium, nitrogen, and propane were compared. Heat transfer losses can be as high as 30% of the compression work of the gas spring. The maximum loss occurred at intermediate speeds. Ideal-gas and real-gas models provided the same predictions for helium and nitrogen, however they differed considerably for propane. The ideal-gas model overestimated the maximum pressure by 20% and underestimated the thermally induced loss by 30%. There is a linear relationship between the normalized loss increase due to real gas effects and the degree of asymmetry of the compressiblity factor during compression and expansion. Thus, when considering fluid states which are close to the critical point or saturation curves, real-gas behaviour must be taken into account.

Future Work

Future work in the area of unsteady heat-transfer losses will involve models which reflect the behaviour of actual engines more accurately by taking more application-specific effects into account. For TFOs, it would be beneficial to simulate a gas spring where the mass of the gas increases as the piston moves up and decreases as the piston moves down. This would mimic the evaporation and condensation of the working fluid in the TFO as the liquid-vapour interface comes into contact with the cold and hot heat exchanger. To

investigate thermally induced losses in reciprocating-piston expanders and compressors more closely, the effects of valve flow and mass exchange must be added to the simulation. This will inevitably lead to the emergence of secondary flow structures and turbulence which will increase the heat transfer due to convection and therefore possibly increase the oscillating heat transfer losses.

References

[1] European Environment Agency. Overview of the European energy system, 2015. URL http://www.eea.europa.eu/data-and-maps/indicators/overview-of-the-european-energy-system-3. [Online; accessed 21-August-2016].

[2] T. R. Karl and K. E. Trenberth. Modern global climate change. *Science*, 302(5651): 1719–1723, 2003.

[3] European Environment Agency. EEA greenhouse gas - data viewer, June 2016. URL http://www.eea.europa.eu/data-and-maps/data/data-viewers/greenhouse-gases-viewer. [Online; accessed 22-August-2016].

[4] United Nations Framework Convention on Climate Change. Paris Agreement, FCCC/CP/2015/L.9/Rev.1, December 2015. URL https://unfccc.int/resource/docs/2015/cop21/eng/l09r01.pdf. [Online; accessed 21-August-2016].

[5] J. Rogelj, M. den Elzen, N. Höhne, T. Franssen, H. Fekete, H. Winkler, R. Schaeffer, F. Sha, K. Riahi, and M. Meinshausen. Paris agreement climate proposals need a boost to keep warming well below 2 °C. *Nature*, 534(7609):631–639, 2016.

[6] L. Jeffery, C. Fyson, R. Alexander, J. Gütschow, M. Rocha, J. Cantzler, M. Schaffer, B. Hare, M. Hagemann, N. Höhne, P. van Breevort, and K. Blok. 2.7 °C is not enough – we can get lower, December 2015. URL http://climateactiontracker.org/assets/publications/briefing_papers/CAT_Temp_Update_COP21.pdf. [Online; accessed 21-August-2016].

[7] M. Altmann, A. Brenninkmeijer, J.-C. Lanoix, D. Ellison, A. Crisan, A. Hugyecz, G. Koreneff, and S. Hänninen. Decentralized energy systems. Technical report, European Parliament's Committee on Industry, Research and Energy

(ITRE), 2010. URL http://www.europarl.europa.eu/document/activities/cont/201106/20110629ATT22897/20110629ATT22897EN.pdf.

[8] J. Banks, K. Massy, L. Wood, J. Carl, A. G. Wagner, P. Mokrian, J. Simjanovic, and D. Slayton. Assessing the role of distributed power systems in the U.S. power sector. Technical report, Brookings Institution and Hoover Institution, 2011. URL http://www.hoover.org/sites/default/files/uploads/documents/Distributed-Energy.pdf.

[9] Lawrence Livermore National Laboratory. Energy flow charts, 2016. URL https://flowcharts.llnl.gov/commodities/energy. [Online; accessed 3-August-2016].

[10] C. N. Markides. Distributed heat conversion technologies based on organic fluid cycles for a high-efficiency and sustainable energy future. In *10th International Conference on Heat Transfer, Fluid Mechanics and Thermodynamics*, 2014.

[11] Oxford English Dictionary Online. "fluidics, n.". URL http://www.oed.com/view/Entry/72090?redirectedFrom=fluidics&. [Online; accessed 28-July-2016].

[12] J. W. Joyce. Fluidics—basic components and applications. Technical Report HDL-SR-83-9, U.S. Army Harry Diamond Laboratories, 1983.

[13] T. C. B. Smith. *Thermally driven oscillations in dynamic applications*. PhD thesis, University of Cambridge, 2006.

[14] S. Backhaus and G. W. Swift. A thermoacoustic-Stirling heat engine: Detailed study. *Journal of the Acoustical Society of America*, 107(6):3148–3166, February 2000.

[15] J. Wheatley, T. Hofler, G. W. Swift, and A. Migliori. An intrinsically irreversible thermoacoustic heat engine. *Journal of the Acoustical Society of America*, 74(1): 153–170, 1983.

[16] P. H. Ceperley. A pistonless Stirling engine—The traveling wave heat engine. *Journal of the Acoustical Society of America*, 66(5):1508–1513, 1979.

[17] C. D. West and R. B. Pandey. Laboratory prototype Fluidyne water pump. In *Proceedings of the 16th Intersociety Energy Conversion Engineering Conference*, pages 1916–1918, 1981. Atlanta, USA.

[18] C. D. West. Dynamic analysis of the Fluidyne. In *Proceedings of the 18th Intersociety Energy, Conversion Engineering Conference*, pages 779–784, 1983.

[19] C. W. Stammers. The operation of the Fluidyne heat engine at low differential temperatures. *Journal of Sound and Vibration*, 63(4):507–516, 1979.

[20] R. W. Redlich and D. M. Berchowitz. Linear dynamics of free-piston Stirling engines. In *Proceedings of the Institution of Mechanical Engineers, Part A: Journal of Power and Energy*, 1985.

[21] G. Walker and J. R. Senft. *Free Piston Stirling Engines*. Springer-Verlag, 1985.

[22] J. W. Mason and J. W. Stevens. Characterization of a solar-powered Fluidyne test bed. *Sustainable Energy Technologies and Assessments*, 8:1–8, 2014.

[23] B. J. Huang and M. D. Chuang. System design of orifice pulse-tube refrigerator using linear flow network analysis. *Cryogenics*, 36(11):889–902, 1996.

[24] R. Radebaugh. The development of the pulse tube refrigerator as an efficient and reliable cryocooler. In *IOR Proceedings*, volume 96, 1999.

[25] T. C. B. Smith. Power dense thermofluidic oscillators for high load applications. In *Proceedings of the 2nd International Energy Conversion Engineering Conference*, pages 1–15, 2004. Providence, USA.

[26] R. Solanki, A. Galindo, and C. N. Markides. Dynamic modelling of a two-phase thermofluidic oscillator for efficient low grade heat utilization: Effect of fluid inertia. *Applied Energy*, 89:156–163, 2012.

[27] R. Solanki, R. Mathie, A. Galindo, and C. N. Markides. Modelling of a two-phase thermofluidic oscillator for low-grade heat utilisation: Accounting for irreversible thermal losses. *Applied Energy*, 106:337–354, 2013.

[28] C. N. Markides, A. Osuolale, R. Solanki, and G.-B. V. Stan. Nonlinear heat transfer processes in a two-phase thermofluidic oscillator. *Applied Energy*, 104:958–977, 2013.

[29] C. N. Markides, R. Solanki, and A. Galindo. Working fluid selection for a two-phase thermofluidic oscillator: Effect of thermodynamic properties. *Applied Energy*, 124: 167–185, 2014.

[30] R. Solanki, A. Galindo, and C. N. Markides. The role of heat exchange on the behaviour of an oscillatory two-phase low-grade heat engine. *Applied Thermal Engineering*, 53:177–187, 2013.

[31] R. Solanki. *Modelling of a Two-Phase Thermofluidic Oscillator for Low-Grade Heat Utilisaiton*. PhD thesis, Imperial College London, 2014.

[32] A. I. Taleb, M. A. G. Timmer, M. Y. El-Shazly, A. Samoilov, V. A. Kirillov, and C. N. Markides. A single-reciprocating-piston two-phase thermofluidic prime-mover. *Energy*, 104:250–265, 2016.

[33] C. J. W. Kirmse, O. A. Oyewunmi, A. I. Taleb, A. J. Haslam, and C. N. Markides. A two-phase single-reciprocating-piston heat conversion engine: Non-linear dynamic modelling. *Applied Energy*, 186(3):359–375, 2017.

[34] O. A. Oyewunmi, C. J. W. Kirmse, A. J. Haslam, E. A. Müller, and C. N. Markides. Working-fluid selection and perfomance investigation of a two-phase single-reciprocating-piston heat conversion engine. *Applied Energy*, 186(3):376–395, 2017.

[35] T. Tartière. Orc market: A world overview, 2016. URL `http://orc-world-map.org/analysis.html`. [Online; accessed 4-August-2016].

[36] J. Freeman, K. Hellgardt, and C. N. Markides. An assessment of solar-powered organic Rankine cycle systems for combined heating and power in UK domestic applications. *Applied Energy*, 138:605–620, 2015.

[37] Y. Dai, J. Wang, and L. Gao. Parametric optimization and comparative study of organic Rankine cycle (ORC) for low grade waste heat recovery. *Energy Conversion and Management*, 50(3):576–582, 2009.

[38] O. Badr, P. W. O'Callaghan, M. Hussein, and S. D. Probert. Multi-vane expanders as prime movers for low-grade energy organic rankine-cycle engines. *Applied Energy*, 16:129–146, 1984.

[39] G. Qiu, H. Liu, and S. Riffat. Expanders for micro-CHP systems with organic Rankine cycle. *Applied Thermal Engineering*, 31(3301–3307), 2011.

[40] H. M. Curran. Use of organic working fluids in Rankine engines. *Journal of Energy*, 5(4):218–223, 1981.

[41] J. Bao and L. Zhao. A review of working fluid and expander selection for organic Rankine cycle. *Renewable and Sustainable Energy Reviews*, 24:325–342, 2013.

[42] R. Zahoransky, P. Knöringer, U. Schelling, and S. Wittig. Anmerkungen zum Einsatz und Wirkungsgrad kleiner Kraftmaschinen - Turbinen, Dampfmotor und Schraubenexpander. *Wärme*, 91(4):43–53, 1983.

[43] C. N. Markides. The role of pumped and waste heat technologies in a high-efficiency sustainable energy future for the UK. *Applied Thermal Engineering*, 53(2):197–209, 2013.

[44] M. Glushenkov, M. Sprenkeler, A. Kronberg, and V. Kirillov. Single-piston alternative to Stirling engines. *Applied Energy*, 97:743–748, 2012.

[45] V. A. Kirillov, V. V. Kireenkov, N. A. Kuzin, A. V. Samoilov, and A. B. Shigarov. Catalytic external combustion engine. *Theoretical Foundations of Chemical Engineering*, 49(4):375—387, 2015.

[46] C. N. Markides and T. C. B. Smith. A dynamic model for the efficiency optimization of an oscillatory low grade heat engine. *Energy*, 36(12):6967–6980, 2011.

[47] Thermofluidics Ltd. URL `http://www.thermofluidics.co.uk/`. [Online; accessed 24-September-2016].

[48] S. Backhaus and G. W. Swift. A thermoacoustic Stirling heat engine. *Letters to Nature*, 399:335–338, 1999.

[49] D. A. P. Jayasinghe, M. S. Letelier, and H. J. Leutheusser. Frequency-dependant friction is oscillatory laminar pipe flow. *International Journal of Mechanical Sciences*, 16:819–827, 1974.

[50] B. Ünsal, S. Ray, F. Durst, and O. Ertunc. Pulsating laminar pipe flow with sinusoidal mass flux variations. *Fluid Dynamics Research*, 37:371–333, 2005.

[51] C. K. Alexander and M. N. O. Sadiku. *Fundamentals of Electric Circuits*. McGraw Hill, 2006.

[52] B. C. K. Farid Golnaraghi. *Automatic Control Systems*. John Wiley & Sons, Inc., 2010.

[53] K. Palanisamy, A. I. Taleb, and C. N. Markides. Optimizing the non-inertive-feedback thermofluidic engine for the conversion of low-grade heat to pumping work. *Heat Transfer Engineering*, 36(14–15):1304–1321, 2015.

[54] E. H. Wang, H. G. Zhang, B. Y. Fan, M. G. Ouyang, Y. Zhao, and Q. H. Muc. Study of working fluid selection of organic Rankine cycle (ORC) for engine waste heat recoveryq. *Energy*, 36, 2011.

[55] G. Angelino and P. Colonna di Paliano. Multicomponent working fluids for organic Rankine cycles (ORCs). *Energy*, 23(6):449–463, 1998.

[56] M. Chys, M. van den Broek, B. Vanslambrouck, and M. De Paepe. Potential of zeotropic mixtures as working fluids in organic Rankine cycles. *Energy*, 44:623–632, 2012.

[57] J. L. Wang, L. Z. L., and X. D. Wang. A comparative study of pure and zeotropic mixtures in low-temperature solar Rankine cycle. *Applied Energy*, 87(11):3366–3373, 2010.

[58] F. Heberle, M. Preißinger, and D. Brüggemann. Zeotropic mixtures as working fluids in organic Rankine cycles for low-enthalpy geothermal resources. *Renewable Energy*, 37(1):364–370, 2012.

[59] S. Lecompte, B. Ameel, D. Ziviani, M. van den Broek, and M. D. Paepe. Exergy analysis of zeotropic mixtures as working fluids in organic rankine cycles. *Energy Conversion and Management*, 85, 2014.

[60] O. Odele and S. Macchietto. Computer aided molecular design: A novel-method for optimal solvent selectrion. *Fluid Phase Equilibria*, 82:47–54, 1993.

[61] J. Gross and G. Sadowski. Application of the perturbed-chain SAFT equation of state to associating systems. *Industrial and Engineering Chemistry Research*, 41 (22), 2002.

[62] M. Lampe, M. Stavrou, H. M. Bücker, J. Gross, and A. Bardow. Simultaneous optimization of working fluid and process for organic Rankine cycles using PC-SAFT. *Industrial and Engineering Chemistry Research*, 53(21):8821–8830, 2014.

[63] Inventory of U.S. greenhouse gas emissions and sinks: 1990–2014, annex 6. Technical report, U.S. Environmental Protection Agency, 2016.

[64] Sigma-Aldrich. Butane. URL http://www.sigmaaldrich.com/catalog/product/aldrich/494402. [Online; accessed 11-November-2016].

[65] Matrix Scientific. Perfluoro-n-butane. URL http://www.matrixscientific.com/001836.html. [Online; accessed 11-November-2016].

[66] S. Köhler. *Geothermisch angetriebene Dampfkraftprozesse: Analyse und Prozessvergleich binärer Kraftwerke*. PhD thesis, Technische Universität Berlin, 2005.

[67] G. F. Hewitt and S. J. Pugh. Approximate design and costing methods for heat exchangers. *Heat Transfer Engineering*, 28(2):76–86, 2007.

[68] W. D. Seider, J. D. Seader, and D. R. Lewin. *Product and Process Design Principles: Synthesis, Analysis and Evaluation*. John Wiley & Sons, 2009.

[69] Chemical engineering plant cost index. URL http://www.chemengonline.com/pci. [Online; accessed 10-December-2016].

[70] E. W. Lemmon, M. O. McLinden, and D. G. Friend. Thermophysical properties of fluid systems. In P. J. Linstrom and W. G. Mallard, editors, *NIST Chemistry webbook, NIST Standard reference database*, volume 69. National Institute of Standards and Technology, Gaithersburg MD, 20899, USA, 1998. URL http://webbook.nist.gov/chemistry/.

[71] E. W. Lemmon, M. L. Huber, and M. O. McLinden. *NIST Standard Reference Database 23: Reference Fluid Thermodynamic and Transport Properties - REFPROP*. National Institute of Standards and Technology, Standard Reference Data Program, Gaithersburg, 9.0 edition, 2010. URL http://www.nist.gov/srd/nist23.cfm.

[72] I. H. Bell, J. Wronski, S. Quoilin, and V. Lemort. Pure and pseudo-pure fluid thermophysical property evaluation and the open-source thermophysical property library coolprop. *Industrial & Engineering Chemistry Research*, 53(6):2498–2508, 2014. doi: 10.1021/ie4033999. URL http://pubs.acs.org/doi/abs/10.1021/ie4033999.

[73] D.-Y. Peng and D. B. Robinson. A new two-constant equation of state. *Industrial & Engineering Chemistry Fundamentals*, 15(1):59–64, 1976.

[74] G. Soave. Equilibrium constants from a modified redlich-kwong equation of state. *Chemical Engineering Science*, 72:1197–1203, 1972.

[75] T. Lafitte, A. Apostolakou, C. Avendaño, A. Galindo, C. S. Adjiman, E. A. Müller, and G. Jackson. Accurate statistical associating fluid theory for chain molecules formed from mie segments. *Journal of Chemical Physics*, 139(15), 2013.

[76] O. A. Oyewunmi, A. I. Taleb, A. J. Haslam, and C. N. Markides. On the use of SAFT-VR Mie for assessing large-glide fluorocarbon working-fluid mixtures in organic Rankince cycles. *Applied Energy*, 163:263–282, 2016.

[77] B. E. Poling, J. M. Prausnitz, and J. P. O'Connell. *The Properties of Gases and Liquids*. McGraw Hill, 2001.

[78] A. Burcat and B. Ruscic. Third millennium ideal gas and condensed phase thermochemical database for combustion with updates from active thermochemical tables. Technical Report ANL-05/20, Argonne National Laboratory, 2005.

[79] E. Goos and A. Burcat. *Overview of Thermochemistry and its Application to Reaction Kinetics*, chapter 1, pages 1–32. John Wiley & Sons, Inc., 2011. ISBN 9781118166123. doi: 10.1002/9781118166123.ch1. URL `http://dx.doi.org/10.1002/9781118166123.ch1`.

[80] H. H. Reamer and B. H. Sage. Phase equilibria in hydrocarbon systems. n-butane - decane system in the condensed region. *Industrial and Engineering Chemistry*, 38 (10):986–989, 1946.

[81] A. Shariati, L. J. Florusse, and C. J. Peters. Phase behavior of the butane + decane binary system. *Journal of Chemical and Engineering Data*, 56:920–922, 2011.

[82] H. H. Reamer and B. H. Sage. Phase equilibria in hydrocarbon systems. phase behavior in the n-butane–n-decane system. *Journal of Chemical and Engineering Data*, 9(1):24–28, 1964.

[83] E. Forte, F. Llovell, L. F. Vega, J. P. M. Trusler, and A. Galindo. Application of a renormalization-group treatment to the statistical associating fluid theory for potentials of variable range (SAFT-VR). *Journal of Chemical Physics*, 134, 2011.

[84] Y. Chen, P. Lundqvist, A. Johansson, and P. Platell. A comparative study of the carbon dioxide transcritical power cycle compared with an organic Rankine cycle

with R123 as working fluid in waste heat recovery. *Applied Thermal Engineering*, 26:2142–2147, 2006.

[85] C. J. W. Kirmse, O. A. Oyewunmi, A. J. Haslam, and C. N. Markides. Comparison of a novel organic-fluid thermofluidic heat converter and an organic Rankine cycle heat engine. *Energies*, 9(479), 2016.

[86] B. Peris, J. Navarro-Esbri, F. Moles, J. P. Marti, and A. Mota-Babiloni. Experimental characterization of an Organic Rankine Cycle (ORC) for micro-scale CHP applications. *Applied Thermal Engineering*, 79:1–8, 2015.

[87] D. Prando, M. Renzi, A. Gasparella, and M. Baratieri. Monitoring of the energy performance of a district heating CHP plant based on biomass boiler and ORC generator. *Applied Thermal Engineering*, 79:98–107, 2015.

[88] K. P. Lee. A simplistic model of cyclic heat transfer phenomena in closed spaces. In *Proceedings of the 18th Intersociety Energy Conversion Engineering Conference*, pages 720–723, 1983.

[89] A. A. Kornhauser and J. L. Smith. Application of a complex nusselt number to heat transfer during compression and expansion. *Fluid Flow and Heat Transfer in Reciprocating Machinery*, pages 89–96, 1987.

[90] A. A. Kornhauser and J. L. Smith. The effects of heat transfer on gas spring performance. *Journal of Energy Resources Technology*, 115:70–75, 1993.

[91] A. A. Kornhauser and J. L. Smith. Application of a complex nusselt number to heat transfer during compression and expansion. *Transactions of the American Society of Mechanical Engineers, Journal of Heat Transfer*, 116:536–542, 1994.

[92] H. Chen, Y. G. Goswami, and E. K. Stefanakos. A review of thermodynamic cycles and working fluids for the conversion of low-grade heat. *Renewable and Sustainable Energy Reviews*, 14(9):3059–3067, 2010.

[93] S. Quoilin, M. V. D. Broek, S. Declaye, P. Dewallef, and V. Lemort. Techno-economic survey of organic rankine cycle (orc) systms. *Renewable and Sustainable Energy Reviews*, 22:168–186, 2013.

[94] H. Pfriem. Periodic heat transfer at small pressure fluctuations. Technical report, National Advisory Committee for Aeronautics, 1943.

[95] V. D. Overbye, J. E. Bennethum, O. Uyehara, and P. Myers. Unsteady heat transfer in engines. In *SAE Technical Paper*. SAE International, 01 1961. doi: 10.4271/610041. URL http://dx.doi.org/10.4271/610041.

[96] W. J. D. Annand. Heat transfer on the cylinder of reciprocating internal combustion engines. *Proceedings of the Institution of Mechanical Engineers*, 177(1):973–996, 1963.

[97] B. Lawton. Effect of compression and expansion on instantaneous heat transfer in reciprocating internal combustion engines. *Proceedings of the Institution of Mechanical Engineers, Part A: Journal of Power and Energy*, 201(3):175–186, 1987.

[98] A. G. Catto and A. T. Prata. A numerical study of instantaneous heat transfer during compression and expansion in piston-cylinder geometry. *Numerical Heat Transfer, Part A: Applications*, 38(3):281–303, 2000.

[99] U. Lekić and J. B. W. Kok. Heat transfer and fluid flows in gas springs. *Open Thermodynamics Journal*, 4:13–26, 2010.

[100] R. Mathie, C. N. Markides, and A. J. White. A framework for the analysis of thermal losses in reciprocating compressors and expanders. *Heat Transfer Engineering*, 35(16–17):1435–1449, 2014.

[101] C. Willich, C. N. Markides, and A. J. White. An investigation of heat transfer losses in reciprocating devices. *Applied Thermal Engineering*, 111:903–913, 2017.

[102] H. Jasak. *Error Analysis and Estimation for the Finite Volume Method with Application to Fluid Flows*. PhD thesis, Imperial College London, June 1996.

[103] J. H. Ferziger and M. Perić. *Computational Methods for Fluid Dynamics*. Springer, 2002.

[104] S. V. Patankar. *Numerical Heat Transfer and Fluid Flow*. 1980.

[105] P. Sapin, A. I. Taleb, C. Barfuß, A. J. White, D. Fabris, and C. N. Markides. Thermodynamic losses in a gas spring: Comparison of experimental and numerical results. In *12th International Conference on Heat Transfer, Fluid Mechanics and Thermodynamics*, 2016.

[106] P. Sapin, A. I. Taleb, A. J. White, D. Fabris, and C. N. Markides. Experimental analysis of loss mechanisms in a gas spring. In *ASME Power and Energy Conference*, 2016.

[107] A. I. Taleb, P. Sapin, C. Barfuß, A. J. White, D. Fabris, and C. N. Markides. Wall temperature and system mass effects in a reciprocating gas spring. In *Efficiency, Cost, Optimizationation, Simulation and Environmental Impact of Energy Systems*, 2016.

[108] H. B. Faulkner. *An Investigation of Instantaneous Heat Transfer during Compression and Expansion in Reciprocating Gas Handling Equipment.* PhD thesis, Massachusetts Institute of Technology, 1983.

[109] A. A. Kornhauser. *Gas-Wall Heat Transfer During Compression and Expansion.* PhD thesis, Massachusetts Institute of Technology, 1989.

[110] U. Lekic. *Fluid Flow and Heat Transfer in a Helium Gas Spring - Computational Fluid Dynamics and Experiments* -. PhD thesis, University of Twente, 2011.

[111] R. P. Adair, E. B. Qvale, and J. T. Pearson. Instantaneous heat transfer to the cylinder wall in reciprocating compressors. In *International Compressor Engineering Conference*, 1972.

[112] P. J. Roache. *Verification and Validation in Computational Science and Engineering.* Hermosa Publishers, 1998.

[113] P. Merkli and H. Thomann. Transition to turbulence in oscillating pipe flow. *Journal of Fluid Mechanics*, 68(3):567–575, 1975.

[114] W. Sutherland. The viscosity of gases and molecular force. *Philosophical Magazine*, 36(223):507–531, 1893.

[115] S. Bretsznajder. *Prediction of Transport and Other Physical Properties of Fluids*, chapter 3, pages 141–188. Pergamon Press, 1971.